AIX-MARSEILLE UNIVERSITÉ
ECOLE DOCTORALE ED 353
CNRS-ECOLE CENTRALE MARSEILLE
LABORATOIRE DE MÉCANIQUE, MODÉLISATION & PROCÉDÉS
PROPRES (M2P2) UMR 7340

Thèse présentée pour obtenir le grade universitaire de docteur

Discipline - Sciences pour l'ingénieur : Mécanique, Physique et Nanoélectronique
Spécialité - Mécanique et Physique des Fluides

Adithya RAMANATHAN KRISHNAN

Explicit algebraic subfilter scale modeling for DES-like methods and extension to variable density flows

Soutenue le 3 avril 2019 devant le jury composé de

M. Rémi MANCEAU	DR CNRS - Université de Pau	Rapporteur
Mme. Anne TANIERE	Prof. Université de Lorraine	Rapporteur
M. Thomas GOMEZ	Prof. Université de Lille	Président du jury
M. Christophe FRIESS	MCF Université Aix-Marseille	Co-directeur de thèse
M. Pierre SAGAUT	Prof. Université Aix-Marseille	Directeur de thèse
M. Fabien DUVAL	Ing. IRSN	Tuteur

Contents

List of Figures

List of Tables

Résumé en français : Modélisation de sous-filtre algébrique explicite pour des méthodes de type DES et extension aux écoulements à masse volumique variable

1.1 Contexte et objectifs

La prédiction des écoulements turbulents évoluant dans un milieu où une stratification stable est présente (gradient de température, concentration) intéresse un grand nombre de domaines pour des problématiques de sûreté dans des situations aussi bien naturelles qu'industrielles (conséquences des éruptions volcaniques, pollution atmosphérique associée aux rejets des cheminées, ...). Dans le cadre des études de sûreté menées par l'IRSN, une problématique importante concerne le risque de formation d'une atmosphère explosive dans les locaux où une source d'hydrogène est présente (conduit ou capacité) ainsi que dans l'enceinte de confinement en situation accidentelle. Dans la deuxième situation, une quantité importante d'hydrogène provenant principalement de la réaction d'oxydation des gaines en zircaloy peut en effet s'accumuler en partie supérieure de l'enceinte sous l'effet des forces de flottabilité. La persistance d'une couche riche en hydrogène dans l'enceinte de confinement est donc l'une des questions majeures dans l'évaluation du risque d'inflammation et d'explosion.

Dans ces conditions, l'objectif de ce travail est de contribuer à l'amélioration des performances prédictives des outils CFD dédiés au risque d'explosion, plus particulièrement au risque de formation d'une atmosphère explosive. Les développements, réalisés dans le code de calcul P^2REMICS (Partially PREMixed Combustion Solver) développé à l'IRSN, s'articulent autour de deux axes complémentaires. Il s'agit d'une part d'améliorer les prédictions des approches RANS au travers d'une fermeture algébrique des tensions de Reynolds et du flux de masse turbulent obtenue à partir d'une hypothèse d'équilibre faible d'une modélisation au second ordre. La modélisation algébrique retenue pour les tensions de Reynolds et le flux de masse turbulent est celle proposée par Wallin *et al.* [22, 37, 82]. Ce choix a été motivé par la possibilité d'obtenir une solution directe pour le tenseur d'anisotropie ainsi que pour le flux turbulent adimensionné et de proposer une méthode naturelle de résolution du couplage dans le cas des écoulements où les effets de la flottabilité ne peuvent pas être négligés. Par ailleurs, l'intérêt de cette approche réside également dans sa formulation qui peut être étendue aux écoulements avec de forts écarts de masse volumique où le champ de vitesse n'est plus à divergence nulle [22].

D'autre part, devant la faible prédictivité des approches RANS observée pour certains écoulements et des limitations en termes de coût pour la simulation des grandes échelles, il s'agit de développer une approche hybride RANS-LES non-zonale de type DES équivalente s'appuyant sur une fermeture algébrique analogue pour les tensions et le flux de masse de sous-filtre.

Les problématiques de sûreté mentionnées précédemment correspondent à une classe d'écoulements turbulents à masse volumique variable sans effet de compressibilité. On se limite dans ce travail dans un premier temps à des écoulements sans variation de masse volumique puis, dans le cas d'une stratification stable, à des écoulements avec de faibles écarts de masse volumique pour lesquels l'approximation de Boussinesq est justifiée.

1.2 Modélisation RANS et fermeture algébrique des flux turbulents

Les fermetures algébriques s'appuyant sur une hypothèse d'équilibre faible d'une modélisation au second ordre des flux turbulents (tensions de Reynolds et flux turbulent d'un scalaire passif ou actif) constituent une alternative attractive vis-à-vis des modèles au premier ordre basés sur une fermeture de type loi de gradient et des modèles au second ordre pour lesquels les flux sont solutions d'une équation de transport. Il s'agit d'améliorer les prédictions des modèles au premier ordre avec des performances proches de celles d'une modélisation au second ordre, tout du moins lorsque l'hypothèse d'équilibre faible n'est pas mise en défaut, tout en conservant la robustesse des modèles à viscosité turbulente. On peut signaler dès à présent que cette alternative est particulièrement attractive dans un contexte hybride RANS/LES étant donné le surcoût engendré la résolution d'équations de transport pour chaque composante du flux de sous-filtre.

1.2.1 Ecoulements incompressibles

L'hypothèse d'équilibre faible [59], initialement proposée pour les tensions de Reynolds, revient à négliger le transport et la diffusion du tenseur d'anisotropie $\boldsymbol{a}$ défini par

$$\boldsymbol{a} = \frac{\overline{u_i' u_j'}}{k} - \frac{2}{3}\boldsymbol{\delta} \tag{1.1}$$

Afin d'obtenir une relation algébrique pour les tensions de Reynolds, la première étape consiste à écrire le modèle au second ordre pour les tensions de Reynolds en fonction du tenseur d'anisotropie

$$k\frac{D\boldsymbol{a}}{Dt} - \left(\boldsymbol{\mathcal{D}} - \frac{\overline{u_i' u_j'}}{k}\mathcal{D}\right) = -\frac{\overline{u_i' u_j'}}{k}\left(\mathcal{P} - \epsilon\right) + \boldsymbol{\mathcal{P}} - \boldsymbol{\varepsilon} + \boldsymbol{\Pi} \tag{1.2}$$

où $\boldsymbol{\mathcal{D}}$, $\boldsymbol{\mathcal{P}}$, $\boldsymbol{\Pi}$ et $\boldsymbol{\varepsilon}$ désignent respectivement les termes de diffusion, production, redistribution et de dissipation des tensions de Reynolds. Les quantités scalaires $\mathcal{D}$, $\mathcal{P}$ et ε correspondent à la demi-trace des tenseurs et correspondent respectivement aux termes de diffusion, production et dissipation d'énergie cinétique turbulente. L'hypothèse d'équilibre faible revient à négliger le membre de gauche de l'équation précédente et conduit donc à la relation algébrique suivante

$$\frac{\overline{u_i' u_j'}}{k}\left(\mathcal{P} - \varepsilon\right) = \boldsymbol{\mathcal{P}} + \boldsymbol{\Pi} - \boldsymbol{\varepsilon} \tag{1.3}$$

En adoptant l'hypothèse classique d'isotropie de la dissipation, on peut montrer que la plupart des modèles proposés pour le terme de redistribution permettent d'écrire la relation algébrique

précédente sous la forme

$$\left(c_1 - 1 + \frac{\mathcal{P}}{\varepsilon}\right)\boldsymbol{a} = -\frac{8}{15}\boldsymbol{S} + \frac{7c_2+1}{11}\left(\boldsymbol{a\Omega} - \boldsymbol{\Omega a}\right) - \frac{5-9c_2}{11}\left(\boldsymbol{aS} + \boldsymbol{Sa} - \frac{2}{3}\boldsymbol{aS\delta}\right) \tag{1.4}$$

où $\boldsymbol{S}$ et $\boldsymbol{\Omega}$ désignent respectivement les tenseurs de cisaillement et de rotation moyens adimensionnés par une échelle caractéristique de temps de la turbulence $\tau = k/\epsilon$

$$\boldsymbol{S} = \frac{\tau}{2}\left(\frac{\partial \overline{u}_i}{\partial x_j} + \frac{\partial \overline{u}_j}{\partial x_i}\right), \quad \boldsymbol{\Omega} = \frac{\tau}{2}\left(\frac{\partial \overline{u}_i}{\partial x_j} - \frac{\partial \overline{u}_j}{\partial x_i}\right) \tag{1.5}$$

En supposant connu le ratio $\mathcal{P}/\varepsilon$, une solution algébrique explicite pour $\boldsymbol{a}$ peut être obtenue à partir de la méthode directe proposée par Grigoriev et Lazeroms [28]. Afin de simplifier les développements, on adopte ici la valeur $c_2 = 5/9$ et on peut montrer que le tenseur d'anisotropie s'écrit sous la forme initialement proposée par Wallin and Johansson [82] obtenue à partir de la projection du tenseur d'anisotropie dans une base tensorielle. Dans le cas bidimensionnel, la relation algébrique s'écrit

$$\boldsymbol{a} = \beta_1 \boldsymbol{S} + \beta_4(\boldsymbol{S\Omega} - \boldsymbol{\Omega S}) \tag{1.6}$$

Les coefficients β_1 et β_4 sont fonction du ratio $\mathcal{P}/\varepsilon = -tr\{\boldsymbol{aS}\}$ pour lequel une solution analytique peut être obtenue dans le cas bidimensionnel en résolvant l'équation non-linéaire obtenue en substituant $\boldsymbol{a}$ par son expression dans la définition du ratio. Dans le cas tridimensionnel, il n'est plus possible d'obtenir une solution analytique pour le ratio $\mathcal{P}/\varepsilon$ et on adopte généralement en première approximation la solution obtenue dans le cas bidimensionnel afin de conserver une relation explicite.

Si la modélisation algébrique fournit une fermeture pour le tenseur d'anisotropie, elle nécessite également comme les modèles de viscosité turbulente une fermeture pour l'énergie cinétique turbulente k et l'échelle de temps τ. Ces deux échelles caractéristiques de la turbulence sont déterminées ici à partir d'un modèle à deux équations de transport pour k et $\omega = \varepsilon/(\beta^* k)$, le modèle k-ω BSL [44]

$$\frac{dk}{dt} = \mathcal{P} - \beta^*\omega k + \frac{\partial}{\partial x_j}\left[(\nu + \sigma_k \frac{k}{\omega})\frac{\partial k}{\partial x_j}\right] \tag{1.7}$$

$$\frac{d\omega}{dt} = \frac{\gamma\omega}{k}\mathcal{P} - \beta\omega^2 + \frac{\partial}{\partial x_j}\left[(\nu + \sigma_\omega \frac{k}{\omega})\frac{\partial \omega}{\partial x_j}\right] + 2(1-F_1)\sigma_{\omega_2}\frac{1}{\omega}\frac{\partial k}{\partial x_j}\frac{\partial \omega}{\partial x_j} \tag{1.8}$$

Nous avons adopté ici la méthodologie proposée par Wilcox [86] consistant à ne pas modifier la modélisation initiale des flux de diffusion permettant ainsi de conserver les constantes de calibration du modèle contrairement aux développements proposés par Hellsten [23].

Les performances du modèle ont été évaluées sur des cas classiques de la littérature de l'écoulement turbulent pleinement développé entre deux plaques planes puis dans une conduite à section carrée. Les résultats obtenus dans le premier cas sont quasi-identiques aux résultats obtenus à partir du même modèle pour k et ω et une fermeture de type loi de gradient pour les tensions de Reynolds. En revanche, les résultats obtenus dans le deuxième cas révèlent clairement la supériorité d'une modélisation algébrique puisque dans ce cas un écoulement secondaire dû à l'anisotropie des tensions de Reynolds est prédit par le modèle algébrique contrairement à son homologue basé sur une fermeture de type loi de gradient.

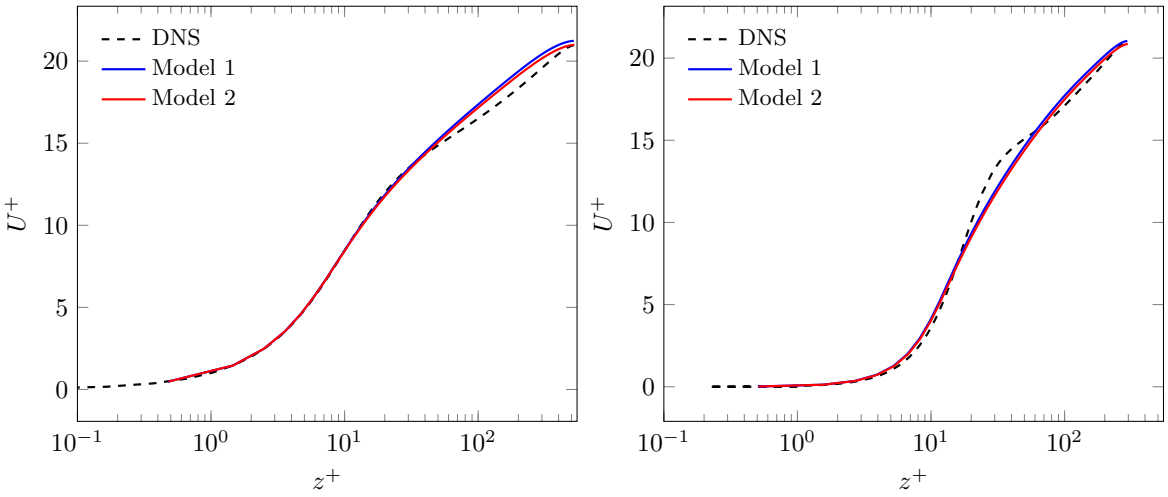

FIGURE 1.1. Profils de vitesse moyenne dans le cas du canal plan turbulent $Re_\tau = 550$ (gauche) et de la conduite à section carrée $Re_\tau = 600$ (droite) pour deux valeurs de la constante c_2.

1.2.2 Extension au cas des écoulements à masse volumique variable

La modélisation algébrique des flux turbulents dans le cas des écoulements à masse volumique variable s'appuie sur la même méthodologie que celle adoptée précédemment pour les tensions de Reynolds dans le cas où les effets de flottabilité sont négligés. L'hypothèse d'équilibre faible pour les tensions de Reynolds est complétée ici par une hypothèse d'équilibre faible pour le flux turbulent adimensionné du scalaire défini par

$$\xi_i = \frac{\overline{u_i'\theta'}}{\sqrt{k k_\theta}} \tag{1.9}$$

où θ désigne le scalaire responsable des effets de flottabilité (concentration, température) et k_θ sa demi-variance. L'hypothèse d'équilibre faible pour les tensions de Reynolds et le flux turbulent adimensionné du scalaire conduit ainsi aux relations algébriques suivantes

$$\frac{\overline{u_i'u_j'}}{k}\left(\mathcal{P} - \varepsilon + \mathcal{G}\right) = \mathcal{P}_{ij} + \Pi_{ij} - \varepsilon_{ij} + \mathcal{G}_{ij} \tag{1.10}$$

$$\frac{\overline{u_i'\theta'}}{2}\left(\frac{\mathcal{P} - \varepsilon + \mathcal{G}}{k} + \frac{\mathcal{P}_\theta - \varepsilon_\theta}{k_\theta}\right) = \mathcal{P}_{\theta i} + \Pi_{\theta i} - \varepsilon_{\theta i} + \mathcal{G}_{\theta i} \tag{1.11}$$

où $\mathcal{D}_{\theta i}$, $\mathcal{P}_{\theta i}$, $\Pi_{\theta i}$ et $\varepsilon_{\theta i}$ désignent respectivement les termes de diffusion, production, redistribution et de dissipation du flux turbulent associé au scalaire et où $\boldsymbol{\mathcal{G}}$ et $\mathcal{G}_{\theta i}$ désignent les termes de production/destruction par les effets de flottabilité. Comme précédemment, en adoptant l'hypothèse classique d'isotropie des dissipations, on peut montrer que la plupart des modèles proposés pour les

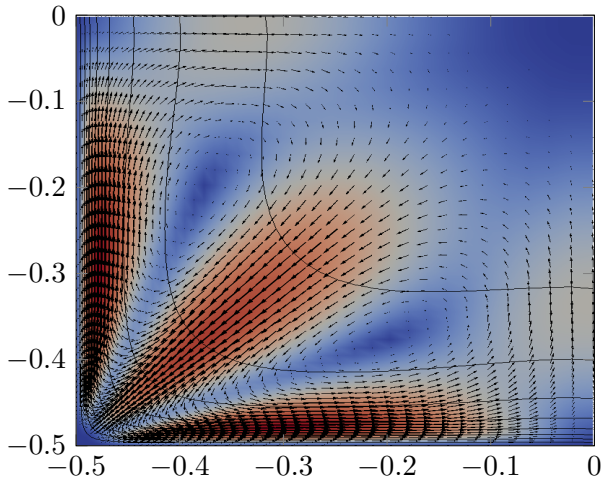

FIGURE 1.2. Ecoulement secondaire prédit par le modèle algébrique dans un quadrant de la section droite de la conduite à section carrée.

termes de redistribution conduisent aux relations algébriques suivantes

$$\begin{aligned} N a_{ij} = &- \frac{8}{15} S_{ij} + \frac{7c_2 + 1}{11} \left(a_{ik}\Omega_{kj} - \Omega_{ik} a_{kj} \right) \\ &- \frac{5 - 9c_2}{11} \left(a_{ik} S_{kj} + S_{ik} a_{kj} - \frac{2}{3} a_{km} S_{mk} \delta_{ij} \right) \\ &- (1 - c_g) \left(\Gamma_i \xi_j + \Gamma_j \xi_i - \frac{2}{3} \Gamma_k \xi_k \delta_{ij} \right) \end{aligned} \tag{1.12}$$

$$\begin{aligned} N_\theta \xi_i = &- \left((1 - c_{\theta 2} - c_{\theta 3}) S_{ik} + (1 - c_{\theta 2} + c_{\theta 3}) \Omega_{ik} \right) \xi_k \\ &- (1 - c_{\theta 4}) \left(a_{ik} + \frac{2}{3} \delta_{ik} \right) \Theta_k - (2 - c_{\theta g}) \Gamma_i \end{aligned} \tag{1.13}$$

où les vecteurs Θ_i et Γ_i sont définis par

$$\Theta_i = \tau \sqrt{\frac{k}{k_\theta}} \frac{\partial \bar{\theta}}{\partial x_i}, \quad \Gamma_i = \tau \sqrt{\frac{k_\theta}{k}} \beta_\theta g_i \tag{1.14}$$

Dans les relations algébriques précédentes, les coefficients N et N_θ sont donnés par

$$\begin{aligned} N &= c_1 - 1 + \frac{\mathcal{P} + \mathcal{G}}{\varepsilon} \\ &= c_1 - 1 - a_{km} S_{km} - \Gamma_k \xi_k \end{aligned} \tag{1.15}$$

$$\begin{aligned} N_\theta &= c_{\theta 1} + c_{\theta 5} \xi_k \Theta_k + \frac{1}{2} \left(\frac{\mathcal{P} + \mathcal{G}}{\varepsilon} - 1 + \frac{1}{r} \left(\frac{\mathcal{P}_\theta}{\varepsilon_\theta} - 1 \right) \right) \\ &= c_{\theta 1} + \frac{1}{2} \left(\frac{\mathcal{P} + \mathcal{G}}{\varepsilon} - 1 - \frac{1}{r_\tau} \right) + \left(c_{\theta 5} - \frac{1}{2} \right) \xi_k \Theta_k \end{aligned} \tag{1.16}$$

Afin de simplifier les développements, on adopte ici les valeurs $c_2 = 5/9$ et $c_{\theta 5} = 1/2$. Néanmoins, les développements proposés dans ce travail ne se restreignent pas à ce choix particulier de valeurs.

Comme précédemment, en suivant la méthodologie proposée par Grigoriev et Lazeroms [28], on

montre que l'on peut obtenir une relation algébrique explicite pour a_{ij} et ξ_i si on suppose que le ratio $(\mathcal{P}+\mathcal{G})/\epsilon$ est connu. Dans le cas où les effets de flottabilité peuvent être négligés, c'est-à-dire $\Gamma_i = 0$, les développements proposés sont formellement équivalents au modèle proposé par Wikström *et al.* [85] pour le cas du scalaire passif. Dans le cas du scalaire actif, on propose de résoudre le couplage entre a_{ij} et ξ_i de manière itérative à partir de la relation

$$N_n = c_1 - 1 - a_{km}(N_{n-1})S_{km} - \xi_k(N_{n-1})\Gamma_k \tag{1.17}$$

En pratique, la première itération est initialisée avec la solution analytique obtenue dans le cas bidimensionnel sans effets de flottabilité et les configurations étudiées révèlent qu'une solution convergée est rapidement atteinte après trois itérations. L'intérêt de cette stratégie de résolution est triple : *(i)* elle n'est pas restreinte à un choix particulier des constantes du modèles, *(ii)* elle conduit à une solution consistante pour le ratio $(\mathcal{P}+\mathcal{G})/\epsilon$ dans les cas bi- et tridimensionnels et *(iii)* elle peut être étendue à des écoulements où la vitesse n'est plus nécessairement à divergence nulle (écarts de masse volumique importants, ...) [22].

La mise en oeuvre de la fermeture algébrique s'appuie comme précédemment sur le modèle k-ω BSL en adoptant la méthodologie proposée par Wilcox [86] pour la modélisation des flux de diffusion pour k et ω. On adopte la même méthodologie pour l'équation de transport de la demi-variance du scalaire, c'est-à-dire

$$\frac{dk_\theta}{dt} = \mathcal{P}_\theta - \varepsilon_\theta + \frac{\partial}{\partial x_j}\left[(\kappa + \frac{1}{\sigma_{k_\theta}}\frac{k}{\omega})\frac{\partial k_\theta}{\partial x_j}\right] \tag{1.18}$$

La dissipation ε_θ est estimée ici en adoptant l'hypothèse classique sur la donnée du rapport des échelles de temps caractéristiques thermique et dynamique $r_\tau = \tau_\theta/\tau$. Dans ce travail, la valeur classique $r_\tau = 0.55$ a été retenue.

Les performances du modèle ont dans un premier temps été estimées dans le cas du scalaire passif sur le cas de l'écoulement turbulent pleinement développé entre deux plaques planes. Les résultats obtenus illustrent la supériorité d'une modélisation algébrique devant une modélisation de type loi de gradient puisque dans ce cas, même si elle reste sous-estimée, la composante longitudinale du flux turbulent du scalaire passif n'est pas identiquement nulle. Cette sous-estimation, particulièrement marquée en proche paroi, est principalement le résultat d'absence d'une modélisation spécifique en proche paroi, tant d'un point de vue des variances k et k_θ que l'anisotropie des flux. Ce premier cas a également permis d'estimer la validité de la correction proposée pour prendre en compte les termes de diffusion dans la région centrale du canal où l'hypothèse d'équilibre faible est mis en défaut.

Dans un deuxième temps, les performances du modèle dans le cas où les effets de flottabilité ne peuvent plus être négligés ont été estimées sur la même configuration dans le cas de stratifications stables. Si les résultats obtenus ne montrent pas clairement l'intérêt de la correction pour prendre en compte les termes de diffusion en raison d'une laminarisation de l'écoulement au centre du canal [37], la méthode de couplage proposée s'est avérée robuste et les effets de la stratification sont qualitativement bien reproduits. La méthodologie et les résultats encourageants obtenus restent à étendre à d'autres types de configuration, en particulier des configurations de type convection naturelle avec une modélisation dédiée en proche paroi (pondération elliptique, ...).

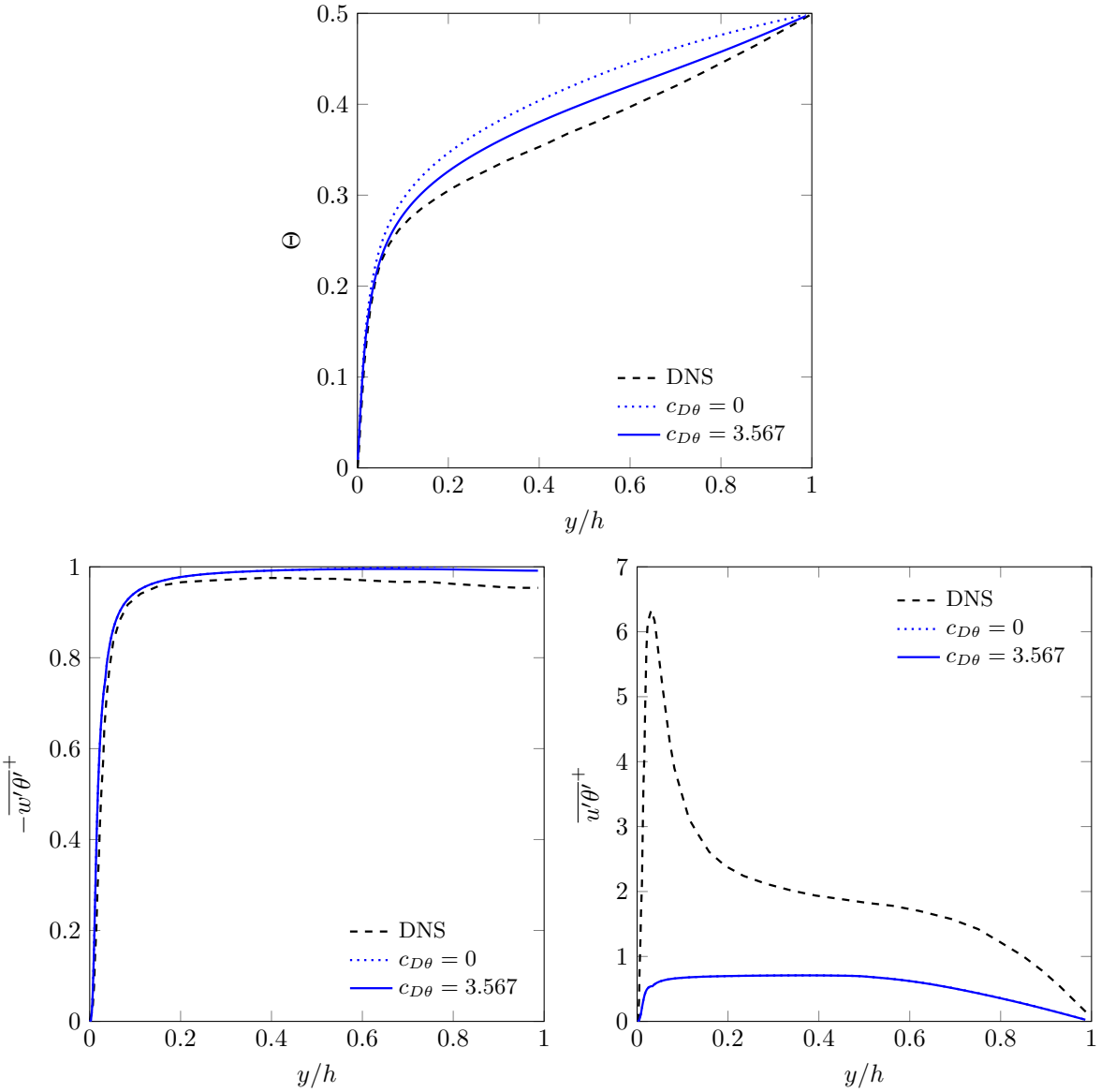

FIGURE 1.3. Profils du scalaire passif (haut), de la composante normale aux parois (bas-gauche) et longitudinale (bas-droite) du flux turbulent.

1.3 Modélisation hybride RANS/LES et fermeture algébrique des tensions de sous-filtre et du flux de masse de sous-filtre

Les approches hybrides RANS/LES constituent une alternative à la LES, moins gourmande en termes de coût de calcul. En effet, elles permettent une coupure spectrale à des échelles plus grandes que celles de la zone inertielle du spectre turbulent.

Nous nous focalisons ici sur les méthodes non-zonales, à transition continue. Il en existe pléthore, dont le principe global est de s'appuyer sur un modèle RANS, auquel on apporte une modification pour faire intervenir la coupure spectrale associée au maillage, afin de réduire la viscosité turbulente. Cette modification sera appelée ci-après "fonction d'hybridation". Ceci afin de permettre au terme convectif des équations du mouvement, de transporter les fluctuations de grande échelle.

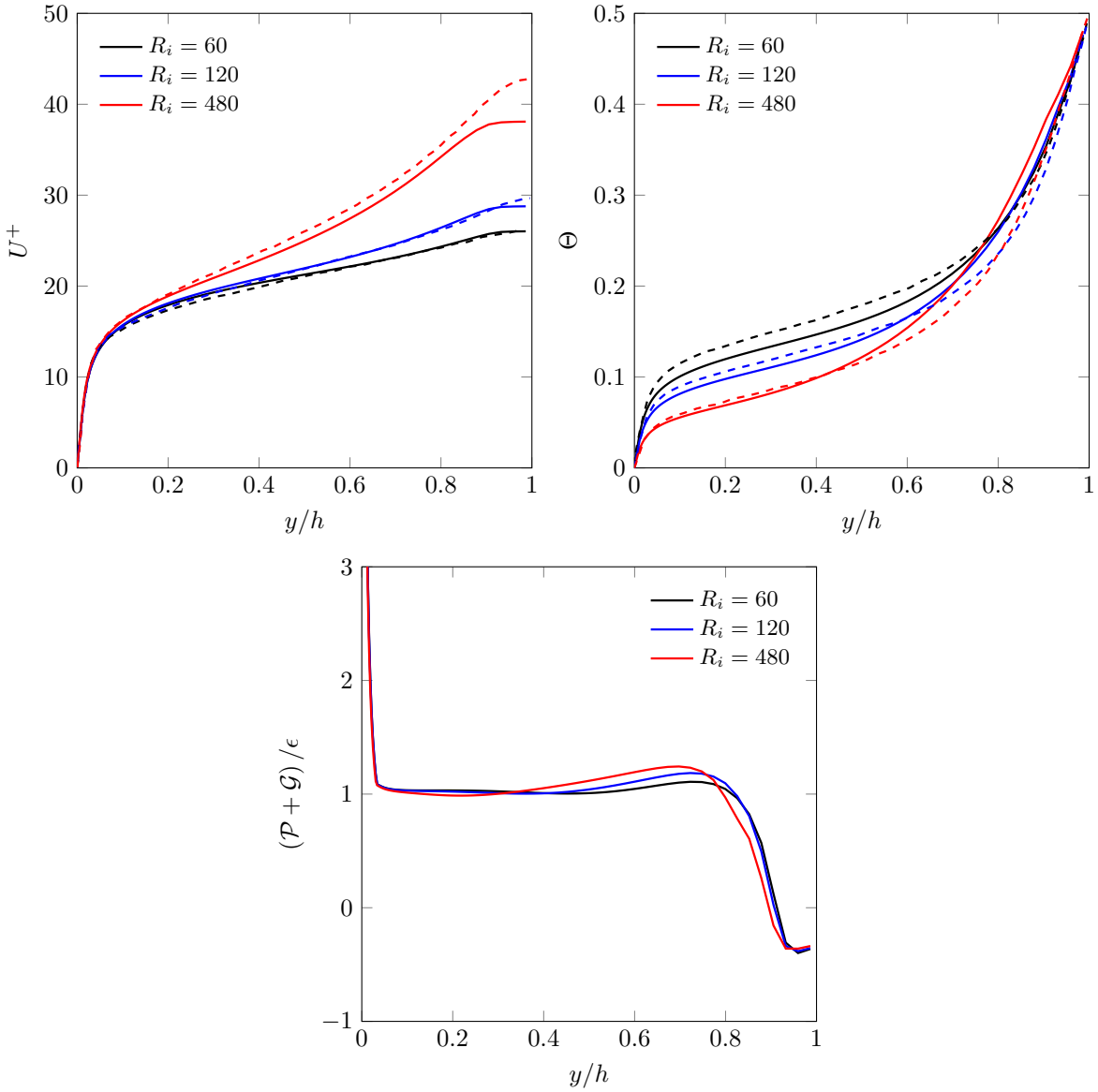

FIGURE 1.4. Profils de vitesse moyenne (haut-gauche), de température moyenne (haut-droite) et rapport production sur dissipation pour trois nombres de Richardson.

L'avantage de ces méthodes, est qu'outre la modification évoquée ci-dessus pour tenir compte de la coupure spectrale, le modèle de fermeture turbulente est formellement identique à sa version RANS. Les grandeurs transportées par le modèle de fermeture (par exemple énergie cinétique turbulente, dissipation...) changent alors quelque peu de sens physique, pour devenir des grandeurs de *sous-filtre*.

1.3.1 DES équivalente

Notre choix se tourne vers la DES équivalente, qui constitue un compromis entre la robustesse de la DES et la justification théorique du PITM. Pour rappel, le principe de la DES est de modifier

le terme puits (dissipation) de l'équation de transport de l'énergie cinétique turbulente, pour le rendre sensible à la coupure spectrale : De son côté, la théorie du PITM a été développée dans l'espace spectral et, dans le cas d'une fermeture de type $k-\varepsilon$, c'est le cœfficient $C_{\varepsilon 2}$ de l'équation de transport de la dissipation, qui est rendu sensible à la coupure : via le ratio d'énergie r, qui est le rapport de l'énergie cinétique turbulente modélisée sur l'énergie cinétique turbulente totale : $r = k_m/k$, et qui est une fonction (subjective) de la coupure spectrale, qui vaut théoriquement 1 à la limite RANS et 0 à la limite DNS.

Friess *et al.* [14] ont établi un critère d'équivalence statistique entre la DES et le PITM, aboutissant sur la méthode hybride RANS/LES appelée DES équivalente. En bref, il s'agit d'une DES pour laquelle on emploie non pas explicitement la taille de maille, mais le ratio d'énergie r :

$$\frac{Dk_s}{Dt} = \text{production} + \text{diffusion} - \underbrace{\max\left(1; \Psi(r)\frac{k_s^{3/2}}{(rk_{tot})^{3/2}}\right)}_{\psi}\varepsilon_s \tag{1.19}$$

avec

$$\Psi(r) = 1 + \left(\frac{C_{\varepsilon 2}}{C_{\varepsilon 1}} - 1\right)\left(1 - r^{C_{\varepsilon 1}/C_{\varepsilon 2}}\right) \tag{1.20}$$

Dans la présente thèse, le modèle de fermeture $k-\omega$ BSL de Menter [46] est étendu au contexte hybride. La fonction d'hybridation ψ apparaissant dans l'équation (1.19) est alors le fruit d'une pondération entre les fonctions ψ de chacune des branches $k-\varepsilon$ et $k-\omega$.

1.3.2 Fermeture algébrique en contexte hybride RANS/LES

Cas général

En contexte hybride RANS/LES, se pose la question de l'applicabilité de l'hypothèse d'équilibre faible sur la turbulence de sous-filtre.

Récemmment, Marstorp *et al.* [41] ont développé un modèle anisotrope de sous-maille, pour la LES, en s'inspirant des travaux en RANS de Wallin et Johansson [82], aboutissant à une approche nommée "explicit algebraic subgrid scale model (EASSM)", donnant des résultats prometteurs, notamment sur l'écoulement en conduite à section carrée.

Aussi, si l'hypothèse d'équilibre faible est une approximation raisonnable à la fois à la limite RANS, et en LES, on peut alors présumer par interpolation qu'elle est acceptable entre ces deux limites, bien que cela mériterait d'être démontré. C'est en tout cas l'hypothèse implicitement faite dans les travaux de Weatheritt *et al.* [83] et de Weinmann *et al.* [84].

Cette hypothèse, associée à celle supposant l'identité formelle entre modèle RANS et fermeture de sous-filtre, permet d'exploiter les résultats présentés en section 1.2.1, avec les nuances suivantes :

- les quantités moyennées du type $\overline{\phi}$ sont remplacées par leurs équivalentes filtrées $\widetilde{\phi}$,
- les variables des modèles de fermeture turbulente (par exemple k) sont remplacées par leur équivalent de sous-filtre (par exemple k_s).

En effet, la fonction d'hybridation n'intervient que dans l'équation de transport de l'échelle caractéristique de temps de la turbulence de sous-filtre τ_s.

Cas avec scalaire

Lorsqu'un scalaire est transporté, en modélisation RANS il faut transporter sa demi-variance. En hybride RANS/LES, c'est sa demi-variance de sous-filtre qui est transportée :

$$k_{\theta s} = \widetilde{\theta'\theta'} \ . \tag{1.21}$$

Comme en dynamique pure, il faut insérer une fonction d'hybridation dans l'équation de transport de $k_{\theta s}$. Ceci soulève la question d'un ratio d'énergie pour la turbulence scalaire. Or cela reviendrait à construire des échelles supplémentaires de sous-filtre, ce qui alourdirait le modèle. Par souci de simplicité, nous utilisons donc le même ratio d'énergie r qu'en dynamique.

En outre, similairement à ce qui est fait en RANS (voir section 1.2.2), on détermine la dissipation scalaire de sous-filtre $\varepsilon_{\theta s}$ via le rapport des échelles de temps caractéristiques scalaire et dynamique (de sous-filtre), dont la valeur est discutée ci-dessous.

La fonction d'hybridation ψ_θ pour le scalaire, est un peu plus complexe à construire que son homologue dynamique. En effet, en dynamique, on construit aisément une échelle de longueur (et de temps) à partir de k_s et ε_s. Mais selon la nature du scalaire θ, il peut être dimensionnellement impossible de construire une échelle de longueur à partir de $k_{\theta s}$ et $\varepsilon_{\theta s}$. Par contre, il est toujours possible de construire une échelle de temps. On peut alors s'appuyer sur les travaux de Tran *et al.* [76] en dynamique :

$$\psi_\theta = \max\left(1; \frac{t_{\theta,S}}{t_{\theta,LES}}\right) , \tag{1.22}$$

avec :

$$t_{\theta s} = \frac{k_{\theta s}}{\varepsilon_{\theta s}} \quad \text{and} \quad t_{\theta LES} = \frac{r k_{\theta,tot}}{\Psi(r)\varepsilon_{\theta,tot}} \ . \tag{1.23}$$

On fait l'hypothèse heuristique que le cœfficient $\Psi(r)$ utilisé en dynamique, peut être utilisé en turbulence. En utilisant le rapport des échelles de temps scalaire et dynamique r_τ et sa valeur de sous-filtre $r_{\tau s}$, on peut définir $t_{\theta s}$ et $t_{\theta LES}$ à partir des variables turbulentes dynamique (en supposant $\varepsilon_{tot} \approx \varepsilon_s$):

$$\psi_\theta = \max\left(1; \frac{r_{\tau s}}{r_\tau}\frac{k_s}{r k_{tot}}\Psi(r)\right) . \tag{1.24}$$

Le rapport de sous-filtre des échelles de temps $r_{\tau,S}$ peut par exemple être défini comme dans les travaux de Jimenez *et al.* (2015) [30] en LES :

$$r_{\tau s} \approx Pr \tag{1.25}$$

ou à l'aide d'une pondération entre r_τ et l'expression ci-dessus, faisant intervenir le ratio d'énergie r.

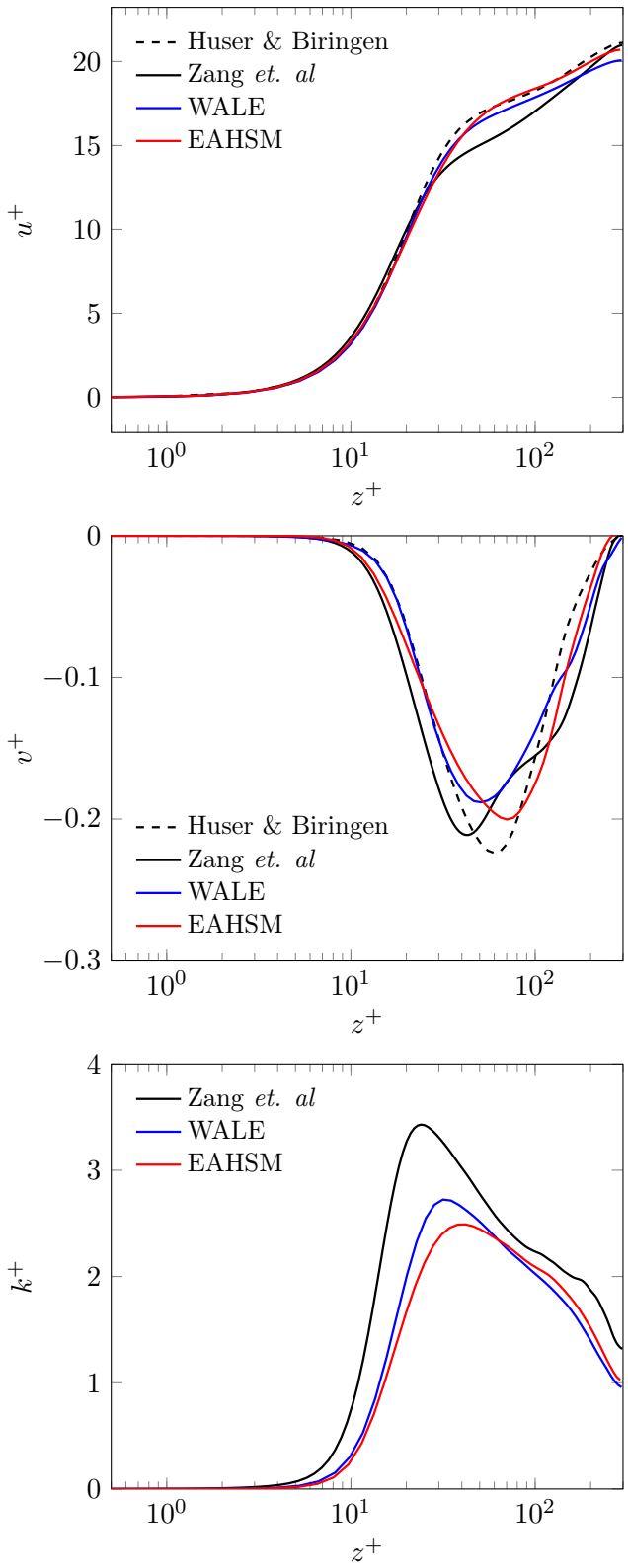

FIGURE 1.5. Ecoulement périodique dans un canal à section carrée à $\mathrm{Re}_\tau = 600$. Maillage grossier, modèles WALE et EAHSM.

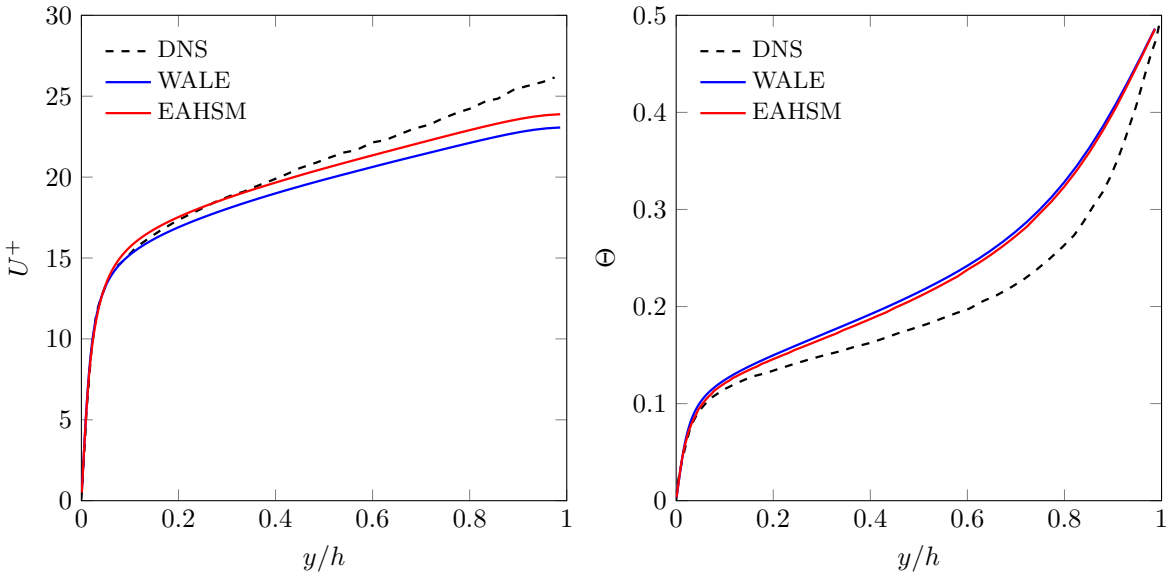

FIGURE 1.6. Vitesse (gauche) et température (droite) moyennes - $R_i = 60$.

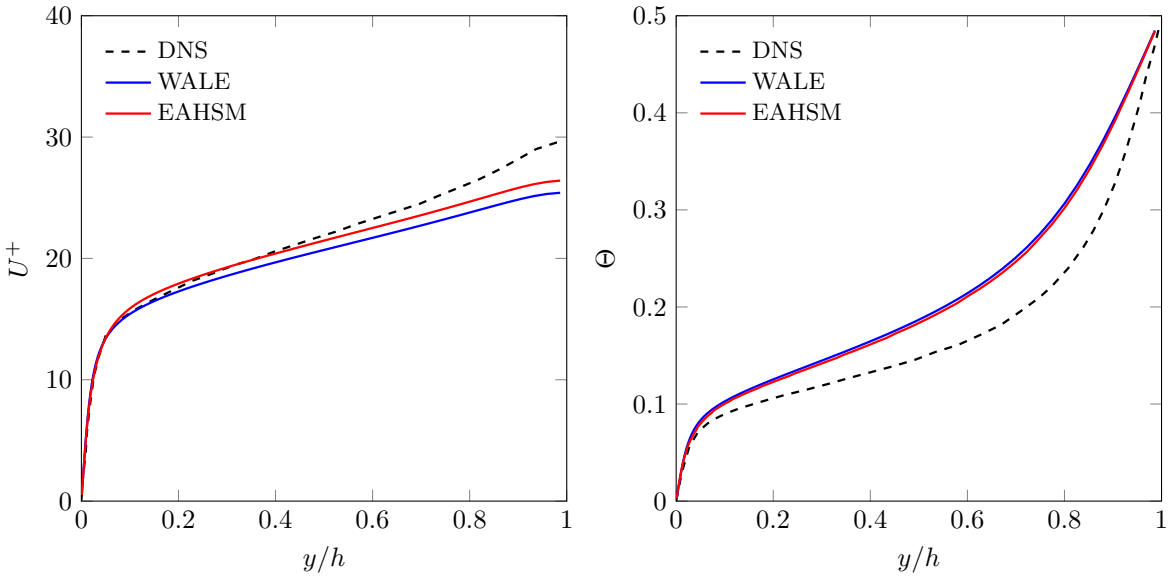

FIGURE 1.7. Vitesse (gauche) et température (droite) moyennes - $R_i = 120$.

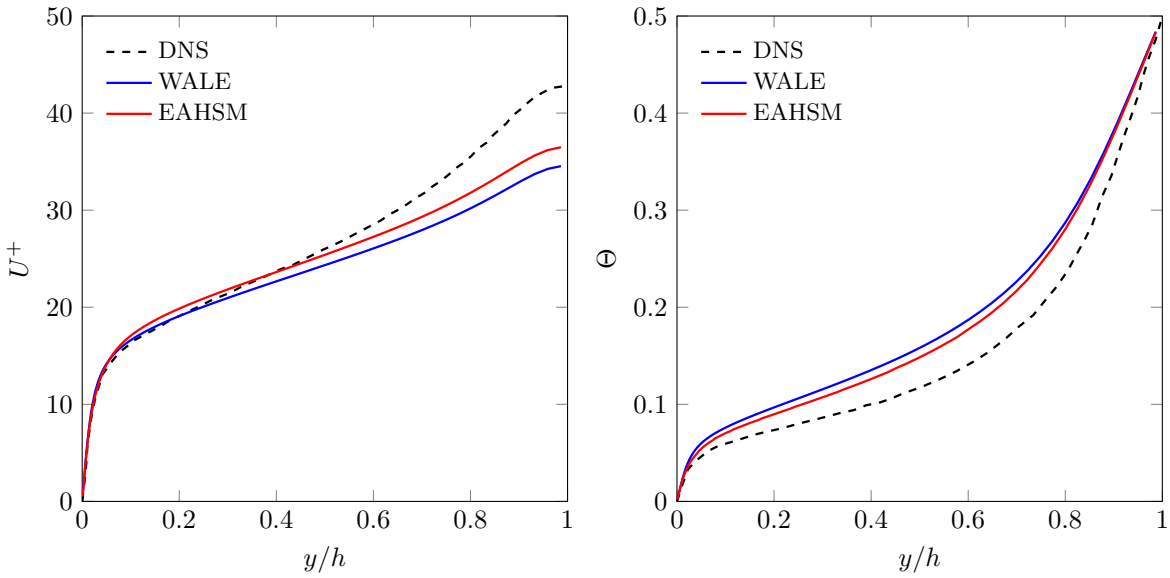

FIGURE 1.8. Vitesse (gauche) et température (droite) moyennes - $R_i = 480$.

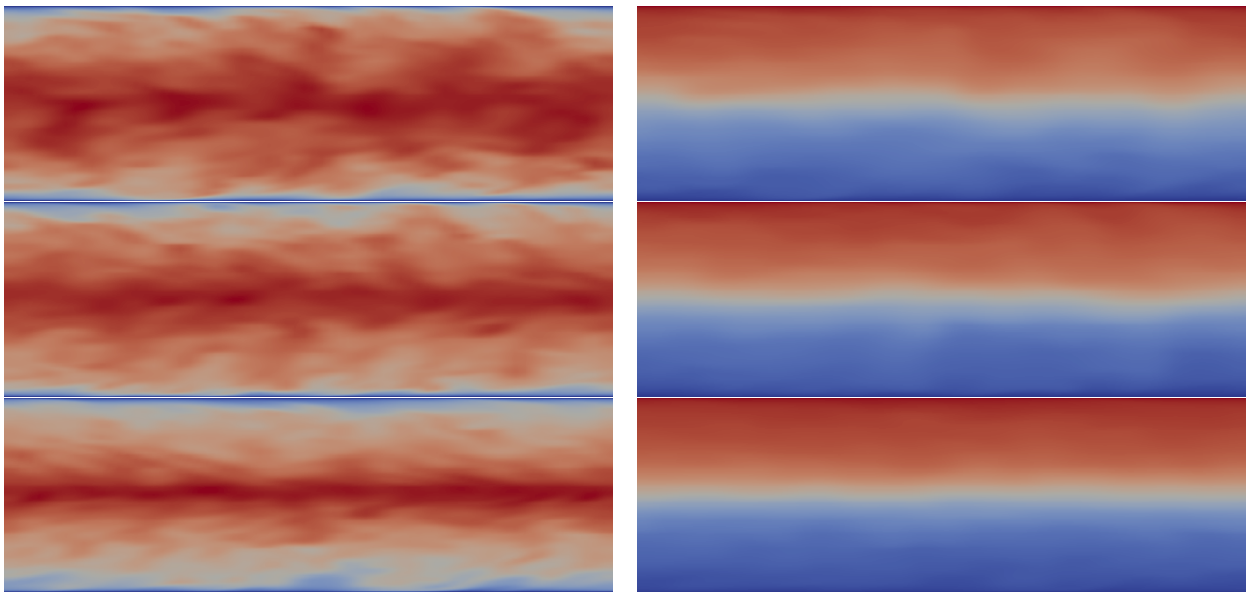

FIGURE 1.9. Champs instantanés de vitesse longitudinale (gauche) et température (droite) filtrées, prédites par le modèle EAHSM, pour les nombres de Richardson $R_i = 60$ (haut), 120 (milieu) and 480 (bas).

Chapter 1

Introduction and Preliminaries

In this chapter, the need of using Computational Fluid Dynamics (CFD) tools for safety studies dealing with hydrogen hazard related problems is presented. This is followed by an introduction to the various levels of turbulence modeling present in the literature. The underlying principle of DNS, RANS, LES and Hybrid RANS/LES methods along with their advantages and weaknesses are briefly discussed. We then conclude by the structure of the proposed work that is interested in the development of hybrid methods for the P^2REMICS CFD software developed at IRSN.

1.1 Hydrogen hazard and the need of reliable CFD tools

As an energy carrier for many increasingly application-based processes, hydrogen is likely to gain prominence especially if it facilitates the reduction of greenhouse gas emissions given that renewable primary energy sources are employed to produce hydrogen in the first place. The safety issues associated with hydrogen applications thus have to be investigated and fully understood for a safe transition to their usage in public sector. The nature of hydrogen based reactions in industrial applications where hydrogen may be present directly or indirectly as a product of a preceding reaction, and subsequent methods to control its accumulation and prevention of return to critically are studied with interest by the scientific community (e.g. [4, 72]). Of pertinent interest is the maintenance of the local concentration levels of hydrogen well below its flammable limit which if not paid specific attention to, might lead to unforeseen disasters.

The 1983 Stockholm hydrogen accident [80] in central Stockholm, Sweden is a major example of an explosion incident where hydrogen was involved. The accidental release of approximately 13.5 kg of hydrogen from a rack of 18 interconnected industrial pressure vessels being transported by a delivery truck led to an explosion. Similarly, the hazards associated with hydrogen gas leakage within a building, for instance as in a vehicle parked in a residential garage, would lead to the mixing of the leaked unignited hydrogen with indoor air forming a flammable mixture which might cause an explosion [1]. A recent reminder of the potential consequences of the release and ignition of hydrogen during severe accident conditions in a nuclear power plant is the Fukushima Daiichi accident [5]. During the course of this severe accident, chemical reactions between the fuel cladding, in this case the Zirconium alloy and water generated large quantities of hydrogen, which from the containment escaped into reactor's primary containment vessel and then further into the reactor building where it mixed with air. This subsequently raised a combustion hazard and ultimately led

to a series of explosions, damaging the reactor containment and leading to the release of radioactive materials into the reactor building and eventually to the environment.

The role of IRSN is to carefully analyze and understand the risk of hydrogen explosion in nuclear facilities as it poses a potential threat to the reactor (breakdown of safety equipments, failure of containment) and the environment (diffusion of radioactive materials in the environment) which can be catastrophic. Fukushima Daiichi nuclear disaster also led to complementary research and development projects [4, 5] to better understand the phenomena associated with the combustion hazard and to address issues such as explosion hazard in the venting system, dispersion of the radioactive particles beyond the primary containment and motivated further work to develop and validate Computational Fluid Dynamics (CFD) tools [3], which are growing into useful analysis tools for supporting safety management. The safety issues related to the explosion hazards are usually segregated into three linked yet separate phases

(i) The first phase corresponds to the release and dispersion of the explosive gases leading to a partially premixed explosive atmosphere from the turbulent mixing of the gases,

(ii) A possible chemical reaction between the gases could lead to an explosion, regarded as the second phase. The challenges posed here constitute the understanding of the rate of combustion and of the flame-front structure along with turbulence coupling,

(iii) The final phase involve the propagation of the blast wave and its effects on the structural integrity of the reactor facility.

The P^{2}REMICS (Partially PREMixed Combustion Solver) is an in-house CFD software developed at IRSN dedicated to the computation of the three phases listed above, the formation of explosive atmospheres *(i)*, their deflagration or detonation *(ii)* and the subsequent propagation of blast waves *(iii)*. Phase one addressing the release and dispersion of the explosive gases is focused in this work where turbulence modeling plays a central role as discussed in the next section. As a first step, the following thesis focuses on slightly variable density flows that reflect most of the phenomena involved in variable density flows with large density differences and deals with the predictive capability of hybrid RANS-LES approaches.

1.2 Governing Equations and turbulence modeling approaches

The Navier-Stokes equation, representing the conservation of momentum, governs the motion of fluids and can be interpreted as Newton's second law of motion for fluids. For an incompressible Newtonian fluid, the conservation of momentum for an instantaneous local velocity field, $\boldsymbol{u}(x, y, z, t)$ is

$$\frac{\partial u_i}{\partial t} + u_j \frac{\partial u_i}{\partial x_j} = -\frac{1}{\rho}\frac{\partial p}{\partial x_i} + \nu \frac{\partial^2 u_i}{\partial x_j \partial x_j} + f_i. \tag{1.1}$$

where u_i is the i-th component of the velocity vector, p is the fluid pressure, ρ and ν are the density and the kinematic viscosity of the fluid respectively, and f_i is an external bulk force acting on the fluid, e.g. gravity. The set of Navier-Stokes equations along with the mass-conservation equation for an incompressible flow

$$\nabla \cdot \boldsymbol{u} = \frac{\partial u_i}{\partial x_i} = 0. \tag{1.2}$$

form a closed system for the evolution of velocity and pressure, provide the starting point of any journey into turbulence.

In the present context, the mixing process associated in the release and dispersion of explosive gases is to be studied and an analytical solution do not exist to properly deal with such complex phenomena. Further, the governing set of equations can only be solved for very simple cases of flow in the computational standpoint. Hence, for most of the cases, to predict the evolution of turbulence flows and the phenomenon attributed to it, one uses CFD tools consisting of turbulence models. These models are simplified constitutive equations that predict the evolution (depending on the modeling technique) of certain quantities of turbulent flows. The construction and use of a model to predict the effects of turbulence is dealt under the subject turbulence modeling. In this thesis, the first three chapters strictly deal with incompressible flows. Effects of compressibility will be addressed in Chapter 4.

Before plunging into the mathematics of turbulence, it is worthwhile to discuss some physical aspects of turbulence. Turbulence is not easy to define but not hard to find examples. The flow of the smoke arising from a cigarette, the whirl of the milk added to a cup of tea and external flow over vehicles are some examples of turbulent flows. Also, all flows of practical engineering interest are turbulent. From these examples, certain common characteristics[1] of a turbulent flow persists:

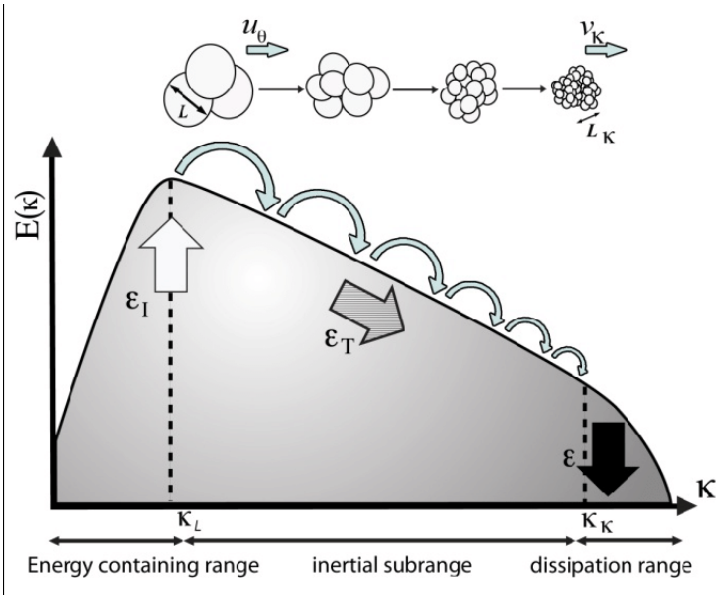

FIGURE 1.1. The turbulence energy cascade [62]. The large energy containing eddies, given by lengthscale L break down into smaller eddies down until a length scale (Kolmogorov microscale, L_κ) at which point the energy is converted into heat under the effect of molecular viscosity.

(i) Disorder: The flow is never reproducible in detail. Although, averages over a suitably large space or time may be well defined.

(ii) Efficient mixing: It is an essential feature of a turbulent motion. Mixing can either lead to a complete blending of the fluids in a confined volume (milk + tea) or dilution (smoke arising from a cigarette).

(iii) Vorticity: Irregularly distributed in $3D$.

[1]Refer [75] for a more detailed explanation on the various characteristics of a turbulent flow.

The irregular nature of turbulence is characterized by the presence of a continuous spectrum of scales ranging from largest to smallest length scales. Figure. 1.1 show the various length scales in a turbulent flow and also the energy cascade. The large-scale vortices of characteristic length L (in Figure. 1.1) are created by the flow and influenced by the geometry the flow is engaged with. They are the energy-containing vortices, which contain the highest part of the turbulent kinetic energy, described by the Taylor scale.
The Taylor microscale, named after Geoffrey Ingram Taylor, is sometimes called the turbulence length scale, is a length scale used to characterize a turbulent fluid flow. The Taylor microscale is the intermediate length scale at which fluid viscosity significantly affects the dynamics of turbulent eddies in the flow. This length scale is traditionally applied to turbulent flow which can be characterized by a Kolmogorov spectrum of velocity fluctuations. In such a flow, length scales which are larger than the Taylor microscale are not strongly affected by viscosity. These larger length scales in the flow are generally referred to as the inertial range. Below the Taylor microscale the turbulent motions are subject to strong viscous forces and kinetic energy is dissipated into heat. These shorter length scale motions are generally termed the dissipation range.
These large-scale vortices are broken down into smaller vortices through the process of vortex stretching. This moves the energy from large-scale vortices to small-scale vortices and further to smaller-scales. This region corresponds to the inertial range, where vortex stretching can be described by inertial effects of the vortex breakup with negligibble viscous effects. The energy cascade continues until the length-scale is of the order of Kolmogorov microscales (L_κ). Although the small vortices contain low proportion of overall kinetic energy, they contribute to most of dissipation of the kinetic energy into heat through the action of molecular viscosity. The Kolmogorov microscale is the smallest relevant scale in turbulence. Due to this nature of turbulence, we say that turbulent flows are always dissipative.

Direct Numerical Simulation (DNS)
In principle, the governing equations (Eqs. 1.1-1.2) contains all of the physics of a given turbulent flow. Unfortunately, no known analytical solution exist in turbulent regime. This is why engineers need computation codes, in which the problem is discretized and solved numerically. The approach of solving directly the set of equations of motion with initial and boundary conditions appropriate to the flow considered without any use of a turbulence model is termed as DNS. The whole range of scales is solved explicitly.
It is the simplest approach and when it can be applied, it is unrivaled in accuracy and the level of description achieved. However, it is an exceedingly expensive method for any but simple, low-speed flows because the range of eddy size broadens in proportion to the Reynolds number, given by $Re^{3/4}$. Here, $Re = UL/\nu$ being the Reynolds number, based on a mean flow velocity U and a length scale L characteristic of the flow in question ($\nu = \mu/\rho$ is the kinematic viscosity). When performing a numerical simulation, analysis has shown that the number of computational grid points required increases as $Re^{9/4}$ and the number of time-steps in proportion to $Re^{3/4}$ [54]. As a result, performing DNS of turbulent flows with the complete details of different turbulence length scales (from the largest turbulent structures down to the smallest structures) is beyond reach for industrial applications which mostly deal with high Reynolds number flows.

1.3 Statistical modeling: Reynolds Averaged Navier-Stokes

Statistical approaches are used in an attempt to reduce the complexity and cost of the numerical simulation by focusing the attention on the velocity and pressure at any one spatial location,

averaged over some period of time, yielding averaged equivalents of the respective instantaneous variables. Thus, if the mean/averaged velocity is denoted by U_i, then the instantaneous velocity is represented as $u_i = U_i + u_i'$. Here, u_i' denotes the fluctuating part of the velocity. This procedure of expressing the instantaneous quantity is called as Reynolds averaging, initially introduced by Reynolds [58].
The Reynolds averaging operator for an instantaneous quantity a is

$$A = \overline{a} = \lim_{N\to\infty} \left(\frac{1}{N} \sum_{k=1}^{N} a_k \right). \tag{1.3}$$

Here, N corresponds to the sample size. Reynolds average operation is usually performed over a period of time but it may be taken over space or over an ensemble of realizations, denoted by N.
To derive a mathematical framework for determining the time-averaged velocity, the Reynolds decompositions $u_i = U_i + u_i'$ and $p = P + p'$ are inserted into the Navier–Stokes (1.1) and mass-conservation (1.2) equations. Further, time averaging the equations lead to:

$$\frac{\partial U_i}{\partial t} + U_j \frac{\partial U_i}{\partial x_j} = -\frac{1}{\rho}\frac{\partial P}{\partial x_i} + f_i + \nu \frac{\partial^2 U_i}{\partial x_j \partial x_j} - \underbrace{\frac{\partial \overline{u_i' u_j'}}{\partial x_j}}. \tag{1.4}$$

$$\frac{\partial U_i}{\partial x_i} = 0. \tag{1.5}$$

Through Reynolds averaging, the interest from the instantaneous behavior (u_i, p) of the flow is shifted to its mean behavior (U_i, P). Looking at turbulent flow, it may be steady in the mean in spite of turbulent fluctuations.
In Eq. 1.4, an additional term (the underbraced term) in the form of the divergence of a tensor arises from the influence of the averaging operator on the non-linear term. The correlation $\boldsymbol{R} = \overline{u_i' u_j'}$ is called the turbulent stresses or the Reynolds stresses, which is a new unknown. It is a second rank symmetric tensor, interpreted as the turbulence equivalent of the viscous stress term in a Newtonian fluid.
In order to compute the mean-flow properties, we need to prescribe $\overline{u_i' u_j'}$, which is an unknown. This is the 'Closure problem': with 10 unknowns (three velocity components, pressure and six stresses) larger than the number of equations; four (continuity equation and three components of the Navier-Stokes equations).

1.3.1 Boussinesq hypothesis

In order to tackle the closure problem, Joseph Valentin Boussinesq in 1877 introduced the concept of an eddy viscosity by developing a mathematical description of turbulent stresses to the mean flow following the gradient-diffusion hypothesis.

$$\overline{u_i' u_j'} = -2\nu_t \boldsymbol{S} + \frac{2}{3} k \boldsymbol{\delta}. \tag{1.6}$$

ν_t is the turbulent viscosity, $\boldsymbol{S}$ is the mean rate of strain tensor, $k = \frac{1}{2}\overline{u_i' u_i'}$ is the turbulent kinetic energy (half trace of the Reynolds stress tensor) and $\boldsymbol{\delta}$ is the Kronecker delta.

$$\boldsymbol{S} = \frac{1}{2}\left(\frac{\partial U_i}{\partial x_j} + \frac{\partial U_j}{\partial x_i}\right). \tag{1.7}$$

Unlike laminar viscosity, the turbulent viscosity is a flow property which remains to be specified. The problem reduces to finding ν_t as a function of the solution. Based on the number of additional transport equations utilized, the models can be classified into three popular categories constructed on the Boussinesq closure.

Algebraic models

The simplest of all models are the algebraic models because they are constructed using basic algebraic relationships for turbulent viscosity. These models do not require additional transport equations other than the NS equations. Prandtl put forth the mixing-length model of the following form:

$$\nu_t = l_{mix}^2 \left|\frac{\partial U_i}{\partial x_j}\right|, \tag{1.8}$$

where l_{mix} is the empirical mixing length, in the case of a channel flow given by:

$$l_{mix} = \min(\kappa y; 0.1h). \tag{1.9}$$

The mixing length model fails to provide close agreement with measured skin friction for boundary layer flows following which several key modifications have been performed. See [88] for a more-complete history of the mixing length model.

One equation model

A popularly utilized model is the one equation model developed by Spalart and Allmaras [69] which was originally developed to tackle aerodynamic flows. A modeled transport equation for the kinematic turbulent viscosity is solved in this model:

$$\frac{\partial \tilde{\nu}}{\partial t} + U_j \frac{\partial \tilde{\nu}}{\partial x_j} = c_{b1}\boldsymbol{S}\tilde{\nu} - c_{w1} f_w \left(\frac{\tilde{\nu}}{d}\right)^2 + \frac{1}{\sigma}\frac{\partial}{\partial x_j}\left[(\nu + \tilde{\nu})\frac{\partial \tilde{\nu}}{\partial x_j}\right] + \frac{c_{b2}}{\sigma}\frac{\partial \tilde{\nu}}{\partial x_j}\frac{\partial \tilde{\nu}}{\partial x_j}, \tag{1.10}$$

with the kinematic turbulent viscosity given by

$$\nu_t = f_{\nu 1}\tilde{\nu}. \tag{1.11}$$

with the following relationships:

$$f_{\nu 1} = \frac{\xi^3}{\xi^3 + c_{\nu 1}^3}, \quad f_{\nu 2} = 1 - \frac{\xi}{1 + \xi f_{\nu 1}}, \quad f_w = g\left[\frac{1 + c_{w3}^6}{g^6 + c_{w3}^6}\right]^{1/6}$$

$$\xi = \frac{\tilde{\nu}}{\nu}, \quad g = r + c_{w2}(r^6 - r), \quad r = \frac{\tilde{\nu}}{\tilde{\boldsymbol{S}}\kappa^2 d^2}$$

$$\tilde{\boldsymbol{S}} = \boldsymbol{S} + \frac{\tilde{\nu}}{\kappa^2 d^2} f_{\nu 2}, \quad \boldsymbol{S} = \sqrt{2\boldsymbol{\Omega}\boldsymbol{\Omega}}$$

along with the closure coefficients

$$c_{b1} = 0.1355, \quad c_{b2} = 0.622, \quad c_{\nu 1} = 7.1, \quad \sigma = 2/3$$

$$c_{w1} = \frac{c_{b1}}{\kappa^2} + \frac{1 + c_{b2}}{\sigma}, \quad c_{w2} = 0.3, \quad c_{w3} = 2, \quad \kappa = 0.41$$

Here, d is the distance to the closest wall which plays a major role in determining the level of production and destruction of turbulent viscosity. $\boldsymbol{\Omega}$ corresponds to the rotation tensor which is given by

$$\boldsymbol{\Omega} = \frac{1}{2}\left(\frac{\partial U_i}{\partial x_j} - \frac{\partial U_j}{\partial x_i}\right). \tag{1.12}$$

To enhance the model prediction for industrial flows, several improvements have been performed [88]. To have a more universal model, transport effects on the turbulence length scale must also be accounted for.

Two equation model

Two-equation models has been extensively used for much of the turbulence model research. This approach consists of solving transport equations for the turbulence lengthscale (l) and a timescale (τ).

The first model of this type was introduced by Kolmogorov. One transport equation for the turbulent kinetic energy (k) and a second transport equation to compute the specific dissipation rate (ω) was utilized with

$$\nu_t = \frac{k}{\omega}. \tag{1.13}$$

to close the system of equations.

Most of the commercially available CFD codes at present have a broad range of two equation models. A brief description of the most widely utilized models are presented here.

Standard k-ϵ model

This model includes two additional transport equations to represent the turbulent properties of flow. The two transported variables are turbulent kinetic energy (k) and the dissipation rate (ϵ). The transport equations of the standard k-ϵ model by Launder and Sharma [36] is presented below.

$$\frac{\partial k}{\partial t} + U_j \frac{\partial k}{\partial x_j} = P - \epsilon + \frac{\partial}{\partial x_j}\left[(\nu + \sigma_k \nu_t)\frac{\partial k}{\partial x_j}\right] \tag{1.14}$$

$$\frac{\partial \epsilon}{\partial t} + U_j \frac{\partial \epsilon}{\partial x_j} = \frac{\epsilon}{k}\left(C_{\epsilon 1} P - C_{\epsilon 2}\epsilon\right) + \frac{\partial}{\partial x_j}\left[(\nu + \sigma_\epsilon \nu_t)\frac{\partial \epsilon}{\partial x_j}\right] \tag{1.15}$$

where the turbulent eddy viscosity ν_t is,

$$\nu_t = C_\mu \frac{k^2}{\epsilon} \tag{1.16}$$

The production term P is

$$P = 2\nu_t \boldsymbol{S}\boldsymbol{S} \tag{1.17}$$

with the model constants[2]

$$C_{\epsilon 1} = 1.44, C_{\epsilon 2} = 1.92, \sigma_k = 1.0, \sigma_\epsilon = 0.769, C_\mu = 0.09 \tag{1.18}$$

In spite of the success of the k-ϵ model, this model has a number of well known shortcomings. It performs poorly, for example, flows with adverse pressure gradient and flows involving separation. Another shortcoming is the numerical stiffness of the model arises when equations are integrated through the viscous sub-layer which are treated with damping functions that have stability issues.

Distinct k-ω models

Alternative models have been developed to overcome some of the shortcomings of the k-ϵ model. One such model is Wilcox's k-ω model [88]. Similar to the k-ϵ model, the first transported variable is the turbulent kinetic energy, k. The second transported variable in this case is the specific dissipation rate, ω which determines the scale of the turbulence, whereas k determines the energy in the turbulence. The transport equations for Wilcox's k-ω model [88] are (excluding the $CD_{k\omega}$ term in Eq. 1.20).

$$\frac{dk}{dt} = P - \beta^* \omega k + \frac{\partial}{\partial x_j}\left[(\nu + \sigma_k \nu_t)\frac{\partial k}{\partial x_j}\right] \tag{1.19}$$

$$\frac{d\omega}{dt} = \gamma \frac{\omega}{k} P - \beta \omega^2 + \frac{\partial}{\partial x_j}\left[(\nu + \sigma_\omega \nu_t)\frac{\partial \omega}{\partial x_j}\right] + \underbrace{2(1 - F_1)\sigma_{\omega_2}\frac{1}{\omega}\frac{\partial k}{\partial x_j}\frac{\partial \omega}{\partial x_j}}_{CD_{k\omega}} \tag{1.20}$$

with the model constants

$$\sigma_{k_1} = 0.4968, \sigma_{\omega_1} = 0.5, \beta_1 = 0.075, \beta^* = 0.09, \gamma_1 = 0.55 \tag{1.21}$$

The production term P is specified by Eq. 1.17. The turbulent eddy viscosity ν_t is defined as,

$$\nu_t = \frac{C_\mu}{\beta^*}\frac{k}{\omega} \tag{1.22}$$

Inspite of its success, the major shortcoming of the k-ω model is its sensitivity to freestream boundary conditions for free shear flows [43]. This has motivated the development of Menter's Baseline (BSL) k-ω model [43] which is analogous to Wilcox's k-ω model [87] in the inner 50% of the boundary-layer and changes progressively to the standard k-ϵ model (in a k-ω formulation) towards the boundary-layer edge (outer wake region). This is achieved by first transforming the standard k-ϵ model into a k-ω formulation, giving rise to an additional term in the k-ω equation ($CD_{k\omega}$ term in Eq. 1.20). This allows one to perform the computations with a single set of equations (k-ω). Following which a blending function F_1 is utilized to perform a blend between the two regions. The original k-ω model is multiplied by F_1 and the transformed model by the function $F_2 = 1 - F_1$. Adding both equation gives rise to Menter's BSL model, Eqs. 1.19-1.20. The model constants are given through the equation

$$\phi = F_1 \phi_1 + F_2 \phi_2 \tag{1.23}$$

where, ϕ_1 represents any constant in the original model, ϕ_2 represents its counterpart constant in the transformed model and ϕ is the corresponding constant in the new model. The function F_1 is designed to take a value of one in the near wall region (activating the original k-ω model) and zero

[2] Arguments based on physical reasoning are involved in the determination of the value of these constants.

away from the wall, usually in the outer wake region. F_1 is written as

$$F_1 = tanh(arg_1^4) \tag{1.24}$$

with,

$$arg_1 = min\left(max\left(\frac{\sqrt{k}}{\beta^*\omega y}; \frac{500\nu}{y^2\omega}\right); \frac{4\rho\sigma_{\omega_2}k}{CD_{k\omega}y^2}\right) \tag{1.25}$$

The first term in Eq. 1.25 corresponds to the ratio of turbulent length scale, L_t to the shortest distance to the wall, y. In the logarithmic region, the ratio L_t/y is found to be 2.5. It is found by using the relations, $k = u_\tau^2/\sqrt{\beta^*}$ and $\omega = u_\tau/\sqrt{\beta^*}\kappa y$ which is applicable in the logarithmic region.

$$\frac{L_t}{y} = \frac{k^{\frac{1}{2}}}{\beta^*\omega y} = \frac{\kappa}{(\beta^*)^{\frac{3}{4}}} = 2.5 \tag{1.26}$$

As we move farther from the logarithmic region of the boundary-layer to the boundary-layer edge, this ratio goes from 2.5 to zero (the ratio becomes smaller and smaller with increasing y). The second argument provides a lower limit for the function F_1 ensuring that this function does not go to zero in the viscous sublayer. The third argument is an additional safeguard against the "degenerate" solution of the original k-ω model with small freestream values for ω in free shear flows where the inclusion of a lower limit for ω is impossible [45].

$$CD_{k\omega} = max\left(2\sigma_{\omega_2}\frac{1}{\omega}\frac{\partial k}{\partial x_j}\frac{\partial \omega}{\partial x_j}, CD_{k\omega,min}\right) \tag{1.27}$$

$CD_{k\omega}$ is the positive portion of the cross-diffusion term present in the transformed ϵ equation. Menter has used 10^{-20} as the value for $CD_{k\omega,min}$. Hellsten [23] states that the choice of having such a small value for $CD_{k\omega,min}$ may lead to a bad numerical behavior of $CD_{k\omega}$ and can introduce undesirable rise of the blending function F_1 back to a value of 1 around the outer edge of the boundary layer. To obtain a better behavior Hellsten has made $CD_{k\omega,min}$ proportional to the maximum value of the cross-diffusion term in each grid-block instead of the maximum value of the whole flow field. This maximum value is multiplied by a factor of 10^{-8} to obtain a proper value for $CD_{k\omega,min}$.

The performance of this model is similar to that of the Wilcox's k-ω model for flows with adverse pressure gradient, without the undesirable freestream dependency of Wilcox's k-ω model. Also, damping functions are not necessary in comparison to the standard k-ϵ model. For free shear layers, the BSL model is identical to the k-ϵ model and significantly better than k-ω model in predicting spreading rates thereby keeping advantages of both k-ϵ and k-ω models. The BSL model is not more complicated than the other existing two equation eddy-viscosity models and requires only a small additional computational time. Furthermore, this model has shown to have the same numerical robustness as the original model [45].
Although Menter's BSL model outperforms the original k-ϵ model in predicting flows with adverse pressure gradient, they still underpredict the flow separation for severe adverse pressure gradient flows. The levels of principal turbulent shear-stress is overpredicted by the LEVMs (the ratio $P/\epsilon >> 1$).
Thus, Menter in his Shear Stress Transport (SST) formulation introduces an upper bound for the principal shear-stresses. The SST model is similar to the BSL model except for a limiter introduced in the SST formulation. The limiter is based on Bradshaw's assumption, i.e., the shear stress (τ)

in a boundary layer is proportional to the turbulent kinetic energy (k).

$$\tau = \rho a_1 k \implies |\overline{u'v'}| = a_1 k \tag{1.28}$$

a_1 being a constant. Usually in two-equation models, the shear-stress is computed by

$$|\overline{u'v'}| = \nu_t \boldsymbol{S} \tag{1.29}$$

with $S = \sqrt{2\boldsymbol{S}\boldsymbol{S}}$ for simple shear flows with $\boldsymbol{S}$ being the strain-rate tensor. Rearranging the above equation gives

$$\nu_t = \frac{|\overline{u'v'}|}{S} = \frac{a_1 k}{\boldsymbol{S}} = \frac{a_1 k}{\sqrt{2\boldsymbol{S}\boldsymbol{S}}} \tag{1.30}$$

Eq. 1.30 is called the SST limitation for ν_t. The SST limitation is suitable only for wall-bounded flows, i.e., for high values of S. But in case of free shear flows, the SST limitation has to be switched off. Similar to F_1, a blending function F_2 is used in the SST model. F_2 is given by

$$F_2 = tanh(arg_2^2) \tag{1.31}$$

with,

$$arg_2 = max\left(\frac{2\sqrt{k}}{\beta^*\omega y}; \frac{500\nu}{y^2\omega}\right) \tag{1.32}$$

with ν_t given as,

$$\nu_t = \frac{a_1 k}{max(a_1\omega; F_2\boldsymbol{S})} \tag{1.33}$$

The SST model is the most widely utilized k-ω model.

Defects of linear Eddy viscosity models

The deficiencies of the two-equation models mostly come from the linear stress-strain relationship, the Boussinesq hypothesis. The dependence of anisotropy on system rotation is also excluded by considering this linear relationship. Moreover, the eddy-viscosity assumption completely fails in predicting all but one of the components in the Reynolds stress anisotropy tensor in the simplest possible equilibrium shear flows, or in the logarithmic region of the boundary layer. For shear flows, in order to properly capture the near wall behavior, certain limiters or damping functions are necessary, e.g. the SST limiter.

These models lack realizability of the normal stresses. For flows with strong acceleration, this results in negative normal stresses prediction. The normal stresses should always be positive which is one of the necessary constraint according to the Schwarz' inequality.

In case of the scalar fluxes, the linear models does not capture the scalar fluxes, even in a simple shear layer.

1.3.2 Reynolds stress models

Instead of depending on the Boussinesq hypothesis for the Reynolds stresses, the most accurate way of finding the Reynolds stress tensor is by solving transport equation for the same. Transport

equation for Reynolds stress is derived in a manner similar to the derivation of the Reynolds-averaged Navier-Stokes equation. However, it introduces six additional transport equations describing Reynolds stress and one additional equation describing the turbulence length scale. The equation for the Reynolds stress tensor ($\boldsymbol{R} = \overline{u_i' u_j'}$) is derived from the fluctuating momentum equation and is given by

$$\frac{\partial \overline{u_i' u_j'}}{\partial t} + U_j \frac{\partial \overline{u_i' u_j'}}{\partial x_j} = \boldsymbol{P} - \boldsymbol{\varepsilon} + \boldsymbol{\Pi} + \frac{\partial \boldsymbol{T}}{\partial x_j}, \tag{1.34}$$

where $\boldsymbol{P}$ is the production of the Reynolds stress, $\boldsymbol{\varepsilon}$ is the dissipation rate tensor, $\boldsymbol{\Pi}$ is the pressure strain-rate correlation and the diffusive transport of the Reynolds stress is given by $\boldsymbol{T}$. The production term requires no modeling and is given by

$$\boldsymbol{P} = -\overline{u_i' u_k'} \frac{\partial \overline{u}_j}{\partial x_k} - \overline{u_j' u_k'} \frac{\partial \overline{u}_i}{\partial x_k}. \tag{1.35}$$

Various Reynolds stress transport models have been proposed based on the closure approach used for the turbulent dissipation rate tensor $\boldsymbol{\varepsilon}$ and pressure strain-rate tensor $\boldsymbol{\Pi}$ which are represented in terms of some known mean quantities. An isotropic assumption for the dissipation rate tensor is usually assumed,

$$\boldsymbol{\varepsilon} = \frac{2}{3} \boldsymbol{\delta} \epsilon \tag{1.36}$$

Moving to the pressure strain-rate, one traditionally adopt a decomposition into two parts, the rapid and the slow part. Rapid part contains the mean flow field which enables it to respond directly to changes in the mean flow while the slow part does not contain any mean flow field information. The linear return-to-isotropy model proposed by Rotta is usually adopted for the slow part

$$\boldsymbol{\Pi}^s = -c_1 \frac{\varepsilon}{k} \left(\overline{u_i' u_j'} - \frac{2}{3} k \boldsymbol{\delta} \right) \tag{1.37}$$

On the other hand, following the general linear model of Launder, Reece and Rodi [35] known as the LRR model, the rapid part reads

$$\begin{aligned} \boldsymbol{\Pi}^r = &- \frac{c_2 + 8}{11} \left(\boldsymbol{P} - \frac{1}{3} \mathcal{P} \boldsymbol{\delta} \right) - \frac{30 c_2 - 2}{55} k \left(\frac{\partial \overline{u}_i}{\partial x_j} + \frac{\partial \overline{u}_j}{\partial x_i} \right) \\ &- \frac{8 c_2 - 2}{11} \left(-\overline{u_i' u_k'} \frac{\partial \overline{u}_k}{\partial x_j} - \overline{u_j' u_k'} \frac{\partial \overline{u}_k}{\partial x_i} - \frac{2}{3} \mathcal{P} \boldsymbol{\delta} \right) \end{aligned} \tag{1.38}$$

The set of values for the constants differ from model to model. The LRR model utilizes $c_1 = 1.8$ and $c_2 = 5/9$. The diffusive transport of the Reynolds stresses is given by

$$\boldsymbol{T} = -\frac{\partial}{\partial x_k} \left[\overline{u_i' u_j' u_k'} + p' \overline{\delta_{ij} u_i' + \delta_{ij} u_j'} \right] + \nu \frac{\partial \overline{u_i' u_j'}}{\partial x_k}. \tag{1.39}$$

Shortcoming of Reynolds stress transport models

The use of Reynolds stress models in commercial software packages has not been completely possible because of various reasons. Firstly, RSM's are mathematically complex as it involves seven coupled partial differential equations. Secondly, model coefficients have to be optimized in order to correctly represent the wall-asymptotic variations of the stresses. Apart from the complexity of the modeling

task, solving six differential transport equations for the stress components makes it computationally expensive and numerically less robust in comparison to the two-equation models. They also require the specification of boundary conditions for all stress components.

1.3.3 Non linear Eddy viscosity models

In the late 70's, the task of solving six differential transport equations for the stress components, instead of one for the turbulence energy, was considered to be too resource intensive. This could have motivated Rodi (1976) to approximate the transport of the stresses by the algebraically scaled transport of the turbulence kinetic energy, called the weak equilibrium assumption.
Making use of this assumption allows for an alternative representation of the Reynolds stress tensor. Such models retain the differential formulation of a two-equation model and also to some extent the Reynolds stress anisotropy $\boldsymbol{a}$ associated with Reynolds stress tensor. Such level of closures are termed as nonlinear eddy viscosity models(NLEVMs). Within the NLEVM lies the traditional algebraic Reynolds stress model (ARSM). The cost and effort to compute the implicit relation of $\boldsymbol{a}$ used in the ARSM model is excessively large as a result of which the advantages of using ARSM instead of the RSM is lost. Hence, an explicit expression to represent the Reynolds stress anisotropy $\boldsymbol{a}$ consisting of the mean strain rate $\boldsymbol{S}$ and rotation rate $\boldsymbol{\Omega}$ tensors is built where $\boldsymbol{a}$,$\boldsymbol{S}$ and $\boldsymbol{\Omega}$ are second-rank tensors. NLEVM models will be assessed in detail in Chapter 2.

1.4 Scale resolving simulation models

The alternative to RANS models are models that resolve at least a portion of the turbulence in the flow domain. Such models are generally termed as scale resolving models. Recent rise in the computer power has shifted the focus of researchers on methods where length scales larger than the resolution of the grid are resolved. Whereas a model is utilized for the eddies with lengthscales smaller than the grid resolution. Consequently, the turbulence model should be sensitive to the grid resolution such that on a very coarse grid the model should be capable to model all the scales. Conversely, when the grid is fine enough, all the scales should be resolved.
These models help to capture certain flow phenomena where the time dependency of the flow is important. For example, capturing the detached flow over an airfoil.

1.4.1 Large Eddy Simulation

Large Eddy Simulation (LES) is the most widely used scale resolving modeling approach. In such a method, the large, non-universal, energy containing scales of the flow are computed explicitly, as in DNS, while the small scales are modeled assuming that these scales are independent of the particular flow and isotropic enough for a single model to be able to represent them in all situations.
Large eddies are the most effective transporters of conserved quantities (mass, momentum and energy) and are anisotropic in nature. Small eddies are weaker and show a universal behavior. They are isotropic irrespective of the Reynolds number and geometry of the flow. In an LES prediction the size of the mesh defines the size of the resolved scales. Normally, LES requires lower grid resolution in comparison to DNS. We obtain accurate time history for highly separated flows. In order to resolve the large scales and model the small scales, one has to separate the two. The separation between the large scales and the small scales is achieved with the help of spatial filters.

Having a filter size smaller than the size of the mesh is meaningless. Hence the most common relationship for a structured mesh is given by

$$\Delta = \sqrt[3]{\Delta_x \Delta_y \Delta_z} \tag{1.40}$$

Here, Δ_x, Δ_y and Δ_z corresponds to the local mesh spacing along the three axes. The governing equations for the filtered quantities in LES are similar to the governing equations for the mean quantities in RANS. The filtered equations are

$$\frac{\partial \tilde{U}_i}{\partial t} + \tilde{U}_j \frac{\partial \tilde{U}_i}{\partial x_j} = -\frac{1}{\rho}\frac{\partial \tilde{P}}{\partial x_i} + f_i + \nu \frac{\partial^2 \tilde{U}_i}{\partial x_j \partial x_j} - \frac{\partial \tau_{ij,S}}{\partial x_j}. \tag{1.41}$$

$$\frac{\partial \tilde{U}_i}{\partial x_i} = 0. \tag{1.42}$$

where the tilde denotes a filtered quantity and it has been assumed that the filtering operation commutes with temporal and spatial derivatives. Here, the term $\boldsymbol{\tau}_s$ is the subgrid stress (SGS) which needs to be modeled.

$$\boldsymbol{\tau}_s = \widetilde{u_i u_j} - \tilde{u}_i \tilde{u}_j. \tag{1.43}$$

The motivation behind a SFS model is to express the subfilter stresses in terms of the resolved velocity. Analogous to the Boussinesq hypothesis (Eq.1.6), the SFS stresses can be written in terms of the resolved rate of strain tensor through the relationship:

$$\boldsymbol{\tau}_s = -2\nu_s \tilde{\boldsymbol{S}}. \tag{1.44}$$

where $\tilde{\boldsymbol{S}}$ is the resolved rate of strain tensor given by:

$$\tilde{\boldsymbol{S}} = \frac{1}{2}\left(\frac{\partial \tilde{u}_i}{\partial x_j} + \frac{\partial \tilde{u}_j}{\partial x_i}\right). \tag{1.45}$$

ν_s is the SFS turbulent viscosity and it should be sensitive to the grid resolution. Typical LES models in use are of Smagorinsky model type, with either a fixed coefficient (Smagorinsky mode) or a dynamic coefficient (Dynamic Smagorinsky mode).

Smagorinsky model

The Smgorinsky model [67] was originally proposed for simulating atmospheric flows and has become one of the most successful methodology for simulating turbulent flows with the improvement of computing power. The eddy viscosity is expressed as follows:

$$\nu_s = (c_s \Delta)^2 \sqrt{\tilde{\boldsymbol{S}}\tilde{\boldsymbol{S}}}. \tag{1.46}$$

alongwith $c_s = 0.17$, calibrated using numerical experimentation of the decay of isotropic turbulence. Lilly derived a value of 0.23 for homogeneous isotropic turbulence in the inertial subrange. However, the optimum value of c_S varies from flow to flow and its value should vary such that near solid walls, the amount of dissipation introduced by the SGS model must be reduced.

Dynamic Smagorinsky model

This model is an extension of the Smagorinsky model. The coefficient c_s[3] is no more a constant rather a parameter that is dynamically computed based on the information provided by the resolved scales of motion [62]. The dynamic procedure therefore obviates the need for users to specify the model constant in advance.

WALE model
In the Wall-Adapting Local Eddy-Viscosity (WALE) model [52], the eddy viscosity is modeled by

$$\nu_s = L_s^2(c_s\Delta)\frac{(\tilde{\boldsymbol{S}}\tilde{\boldsymbol{S}})^{3/2}}{(\tilde{\boldsymbol{S}}\tilde{\boldsymbol{S}})^{5/2} + (\tilde{\boldsymbol{S}}\tilde{\boldsymbol{S}})^{5/4}}. \tag{1.47}$$

with,

$$L_s = min(\kappa d, C_w V^{1/3}). \tag{1.48}$$

with $C_w = 0.325$ and V is the volume of the cell. The WALE model is designed to return the correct wall asymptotic behavior for wall bounded flows. Another advantage of the WALE model is that it returns a zero turbulent viscosity for laminar shear flows. The WALE model is therefore preferable compared to the Smagorinsky-Lilly model as the Smagorinsky-Lilly model produces nonzero turbulent viscosity.

LEVM as SFS models
Various SGS models have been proposed and most of them utilize the Boussinesq's hypothesis to model the SGS stress tensor as in typical RANS models. Such advanced models introduce some transport effects by either solving a transport equation for the sub-filter kinetic energy, k_s or by solving multiple transport equations like the two-equation model.
The application of LES can now be used to simulate complex engineering flows. However, its application is limited to simple geometries with low-to-moderate Reynolds number because of high demands on grid resolution for industrial computations. Further, use of LES for simulating near wall turbulence has been a problem. The reason being that near wall turbulence length scales are very small. Hence, a mesh size fine enough to capture these length scales must be utilized leading to an increase in the computational cost.

Higher order SFS models
More recent works have included a better description of the SGS model by introducing the effects of anisotropy throught the use of an explicit algebraic stress models (EASM). Marstorp *et al.* [41], developed a SGS model for simulating complex flows. They put to use an explicit algebraic model, involving the strain rate ($\tilde{\boldsymbol{S}}$) and rotation rate ($\tilde{\boldsymbol{\Omega}}$) tensors to predict the anisotropy of the SFS in a more realistic way than the models based on the eddy viscosity assumption. The authors have performed turbulent plane and rotating channel flow simulations from moderately-to-high Reynolds number. They have shown that by utilizing a higher order SFS model, the grid resolution can be $1/5th$ of the guidelines present in the literature for this test case [50].

1.4.2 Hybrid RANS/LES methods

Many approaches have been suggested to optimize the computational cost for simulating wall bounded flows. Recently, techniques have evolved to bridge RANS and LES models to maintain

[3] c_s is not a constant but ranges between $0.1 < c_s < 0.24$.

accuracy with a reduced cost of computation [15]. Such methods are termed as Hybrid RANS/LES methods (HRLM). In these methods, LES is restricted for the simulation of the outer flow eddies to circumvent the requirement of very fine grids in the near wall region. For this region, a pure RANS turbulence model is utilized. In recent years HRLM has received increased attention [62].
The Hybrid model should be capable to tend towards a RANS model when the grid resolution is very coarse. Conversely, at sufficiently high grid resolution, the model should tend towards a DNS. HRLM can be broadly classified into two categories.

Zonal hybrid RANS/LES methods (zHRLM)
The first category falls into zHRLM where a part of the domain is set to be computed using RANS equations and the rest is computed with LES (see [10, 77]). These models are complicated to use when dealing with complex geometries as the transition zone has to be specified by the user.

Seamless hybrid RANS/LES methods (sHRLM)
The second method is to make the subfilter stress model sensitive to the local grid resolution and turbulence properties. This enables to have a smooth and continuous transition from the RANS to LES regions. These methods are called sHRLM. Such methods utilize a single set of transport equations to model turbulence in the RANS and LES regions by adapting itself to the local grid resolution. A detailed description on how the turbulence model adapts itself according to the grid resolution is presented in detail in Chapter 3. Detached Eddy Simulation (DES) [68], Partially Integrated Transport Modeling (PITM) [64], Equivalent-Detached Eddy Simulation (E-DES) [14] are some examples of sHRLM.
The focus in the following thesis is on improving the predictive capabilities of the SFS model in a continuous-HRLM framework.

1.5 Thesis Outline

The demand of CFD methods for the analysis of fluid flows is increasing. Role of IRSN is to build a generic CFD code to conduct safety studies concerning hydrogen hazards. The aim of this study is to improve the predictive capabilities of hybrid RANS/LES methods through the development of a subfilter scale model which considers an explicit algebraic relation for the the non-isotropic turbulent subfilter stress and turbulent scalar fluxes thus contributing to the improvement of the safety analysis concerning hydrogen hazards. This chapter provides an introduction to the different turbulence modeling strategies available. While there are a plethora of turbulence models, emphasis is made on selected models most relevant to this work. Chapters 2 and 3 are limited to incompressible flows while chapter 4 deals with variable density flows.

The development of an explicit algebraic Reynolds stress model in a RANS framework is presented in Chapter 2 arrived at through a direct solution method. The coupling between the explicit algebraic model and Menter's BSL model is achieved without the need of a full recalibration. The performance of the developed model is accessed on the flow in a fully developed turbulent channel and the flow in a pipe of square cross-section.

Chapter 3 is precisely dedicated to seamless hybrid RANS/LES methods. Starting from E-DES k_s-ϵ_s, E-DES based on Menter's BSL-like model is developed. For the closure, the explicit algebraic model developed in Chapter 2 is extended within a seamless hybrid RANS/LES framework. A calibration of the model on the decaying isotropic turbulence is conducted to find the optimum

value of the model coefficient. Following which, three-dimensional simulations are performed using the EAHSM on two grids: 'fine' and 'coarse'.

In continuation to what is developed in Chapter 2 for an incompressible flow, the first part of Chapter 4 deals with the development of an explicit algebraic model for slightly variable density flows in a RANS framework. The development of an explicit algebraic model for the Reynolds stresses and the scalar flux is performed using the direct solution method. The model is accessed on the stably stratified homogeneous shear and the stably stratified channel flow. In the latter half of this chapter the resulting explicit algebraic model is extended to a seamless hybrid RANS/LES method following Chapter 3. Performance of the model is accessed on the two test cases like for RANS.

Finally the open ends within the scope of this work is presented with certain solution strategies.

Chapter 2

Explicit Algebraic Reynolds Stress Modeling

In this chapter, the development of the EARSM model is presented starting from the transport equation for the Normalized Reynolds stresses followed by the weak equilibrium assumption which provides the foundation for the development of the algebraic models. One arrives at the Implicit Algebraic Reynolds Stress Models through the utilization of this assumption on the transport of the Normalized Reynolds stresses. Rather than using a particular tensor basis projection method as used in the primary work [53] and most of the contributions that followed (e.g [24, 82]), we follow here the direct solution method proposed by Grigoriev [28] to arrive at an explicit algebraic relationship from the implicit relationship. The interest of using such a direct solution method will be highlighted in Chapter 4 when dealing with variable density flows.
Coupling EARSM with any of the existing two-equation models usually requires a full calibration of the coefficients (e.g Hellsten [24]). As a result, the generality of the platform two-equation model is lost. Instead, we follow a very simple procedure for adapting EARSM with the k-ω model following Wilcox [86] thereby eliminating the need for a complete recalibration of the model coefficients. Validation is performed on the canonical test case of the fully developed channel flow at $Re_\tau = 550$ and a more challenging case of the fully developed flow in a square pipe at $Re_\tau = 600$.

2.1 Transport equation for the Normalized Reynolds stresses

Following the exposition on various levels of turbulence modeling approaches in Chapter 1, the Second Moment Closures, in general distinguished as the Reynolds stress models (RSM) are at par better in comparison to the Linear Eddy Viscosity Models (LEVM). The advection and diffusion terms in RSM account for the transport effects of the individual stress components whereas the LEVM address such effects for the trace of the Reynolds stress tensor. Yet, RSM have not received much attention for industrial applications in comparison to the LEVM due to their mathematical complexity (the task of solving six differential transport equations for the stress components complemented by closure models for pressure-strain rate correlation and triple-velocity correlations, instead of one for the turbulence energy) and the consequential cost of computation.

Inevitably, in the late 60s, when computer power was a tiny fraction of what it is today, it was considered inappropriate to apply emerging RSMs (e.g. Launder, Reece and Rodi [35]) to anything more complex than two-dimensional boundary layers. This motivated Rodi [59] to make the pioneering proposal to approximate the transport of the stresses by the algebraically scaled transport of the turbulence energy leading to an alternative representation of the Reynolds stress tensor. Such

models retain the differential formulation of a two-equation model and also include the Reynolds stress anisotropy effects associated with the Reynolds stress tensor.

The first step in the development of the algebraic models consists thus writing the transport equations for the Reynolds stresses in terms of the dimensionless anisotropy tensor defined by

$$\boldsymbol{a} = \frac{\overline{u_i' u_j'}}{k} - \frac{2}{3}\boldsymbol{\delta} \tag{2.1}$$

The LHS of Reynolds stress transport equation minus the turbulent transport term (Eq. 1.34) along with Eq. 1.14 can be written as

$$\begin{aligned} \frac{D\overline{u_i' u_j'}}{Dt} - \boldsymbol{\mathcal{D}} &= k\frac{D}{Dt}\left(\frac{\overline{u_i' u_j'}}{k}\right) + \frac{\overline{u_i' u_j'}}{k}\frac{Dk}{Dt} - \boldsymbol{\mathcal{D}} \\ &= k\frac{D}{Dt}\left(\frac{\overline{u_i' u_j'}}{k}\right) + \frac{\overline{u_i' u_j'}}{k}\frac{Dk}{Dt} - \boldsymbol{\mathcal{D}} \\ &= k\frac{D}{Dt}\left(\frac{\overline{u_i' u_j'}}{k}\right) + \frac{\overline{u_i' u_j'}}{k}\left(\mathcal{P} - \epsilon + \mathcal{D}\right) - \boldsymbol{\mathcal{D}} \end{aligned} \tag{2.2}$$

Substituting Eq. 2.2 in Eq. 1.34 and utilizing Eq. 2.1 leads to

$$k\frac{D\boldsymbol{a}}{Dt} - \left(\boldsymbol{\mathcal{D}} - \frac{\overline{u_i' u_j'}}{k}\mathcal{D}\right) = -\frac{\overline{u_i' u_j'}}{k}\left(\mathcal{P} - \epsilon\right) + \boldsymbol{\mathcal{P}} - \boldsymbol{\varepsilon} + \boldsymbol{\Pi} \tag{2.3}$$

where $\boldsymbol{\mathcal{D}}$, $\boldsymbol{\mathcal{P}}$, $\boldsymbol{\Pi}$ and $\boldsymbol{\varepsilon}$ refer respectively to diffusion, production, pressure redistribution and dissipation of the Reynolds stresses and given by Eqs. 1.35 - 1.39.

2.2 Weak Equilibrium assumption

The classical assumption on which the algebraic models are built is the weak equilibrium assumption by Rodi [59].

$$\frac{D\boldsymbol{a}}{Dt} - \left(\boldsymbol{\mathcal{D}} - \frac{\overline{u_i' u_j'}}{k}\mathcal{D}\right) = \frac{\partial \boldsymbol{a}}{\partial t} + u_j\frac{\partial \boldsymbol{a}}{\partial x_j} - \left(\boldsymbol{\mathcal{D}} - \frac{\overline{u_i' u_j'}}{k}\mathcal{D}\right) = 0 \tag{2.4}$$

This is to say that the advection and diffusion terms in the exact transport equation for the Reynolds stress anisotropy $\boldsymbol{a}$, are neglected, i.e., the LHS of Eq. 2.3 is neglected. The dimensionless quantities only vary slowly in space and time.

The assumption is based on the expectation that the transport of the Reynolds stresses occurs at the same rate as the transport of the turbulent energy. This may be a reasonable assumption for the normal-stress components — which are, after all, components of the turbulence energy. This might appear to be on weaker ground for the shear-stress components. Using the weak-equilibrium

assumption, the resulting algebraic equation read

$$\frac{\overline{u_i' u_j'}}{k}\left(\mathcal{P}-\varepsilon\right) = \boldsymbol{\mathcal{P}} + \boldsymbol{\Pi} - \frac{2}{3}\varepsilon\boldsymbol{\delta} \tag{2.5}$$

The above class of models are termed as algebraic stress models as it only requires the solution of an implicit algebraic equation for the Reynolds stresses. The production and pressure-strain terms on the right hand side of the above equation can be expressed in terms of $\boldsymbol{a}$, $\boldsymbol{S}$ and $\boldsymbol{\Omega}$ where $\boldsymbol{S}$ and $\boldsymbol{\Omega}$ are the normalized mean strain tensor and the normalized mean rotation tensor respectively given as

$$\boldsymbol{S} = \frac{\tau}{2}\left(\frac{\partial \overline{u}_i}{\partial x_j} + \frac{\partial \overline{u}_j}{\partial x_i}\right), \quad \boldsymbol{\Omega} = \frac{\tau}{2}\left(\frac{\partial \overline{u}_i}{\partial x_j} - \frac{\partial \overline{u}_j}{\partial x_i}\right) \tag{2.6}$$

Where $\tau = (k/\epsilon)$ is the turbulent time scale used to normalize the velocity gradients. The turbulence properties of a flow are profoundly influenced under the presence of a wall. In this work the attention given to the near-wall region has been peripheral. Following [82], we introduce here a lower bound for the turbulent time scale which goes to zero as the wall is approached. The limiter proposed by Durbin[12] reads

$$\tau = \left(\frac{k}{\epsilon}, C_\tau\sqrt{\frac{\nu}{\epsilon}}\right) \tag{2.7}$$

with $C_\tau = 6$. This limiter is active in the near-wall regions through the viscous time scale

Inserting $\boldsymbol{a}$, $\boldsymbol{S}$ and $\boldsymbol{\Omega}$ in the definition of the production and redistribution terms leads to the following expressions

$$\frac{\boldsymbol{\mathcal{P}}}{\varepsilon} = -\frac{4}{3}\boldsymbol{S} - (\boldsymbol{aS} + \boldsymbol{Sa}) + \boldsymbol{a\Omega} - \boldsymbol{\Omega a} \tag{2.8}$$

$$\begin{aligned}\frac{\boldsymbol{\Pi}}{\varepsilon} &= -c_1\boldsymbol{a} + \frac{4}{5}\boldsymbol{S} + \frac{9c_2+6}{11}\left(\boldsymbol{aS} + \boldsymbol{Sa} - \frac{2}{3}\boldsymbol{aS\delta}\right) \\ &\quad + \frac{7c_2-10}{11}\left(\boldsymbol{a\Omega} - \boldsymbol{\Omega a}\right)\end{aligned} \tag{2.9}$$

Resulting in an algebraic equation for the Reynolds stress anisotropy tensor that reads

$$\begin{aligned}\left(c_1 - 1 + \frac{\mathcal{P}}{\varepsilon}\right)\boldsymbol{a} = &-\frac{8}{15}\boldsymbol{S} + \frac{7c_2+1}{11}\left(\boldsymbol{a\Omega} - \boldsymbol{\Omega a}\right) \\ &- \frac{5-9c_2}{11}\left(\boldsymbol{aS} + \boldsymbol{Sa} - \frac{2}{3}\boldsymbol{aS\delta}\right)\end{aligned} \tag{2.10}$$

2.3 Development of EARSM

The advantage of such a manipulation done in the previous section to the 'parent RSM' is to reduce the complexity of using the differential terms. Further the absence of any differential terms in the Reynolds-stress equations implies that no boundary conditions are necessary for the stresses. Nevertheless, the implicit relationship still requires excessive computational efforts and as a result

the benefits of using ARSM instead of RSM may be somewhat negligible and especially when moving to seamless hybrid methods.

To tackle this issue, an explicit expression to represent the Reynolds stress anisotropy $\boldsymbol{a}$ consisting of the mean strain rate ($\boldsymbol{S}$) and rotation rate ($\boldsymbol{\Omega}$) tensors is built, the explicit algebraic Reynolds stress model (EARSM). In simple terms, the nature of deriving an EARSM can be described as a purely mathematical process of inverting the implicit algebraic relation (Eq. 2.10) to arrive at explicit relationships that link the stresses to the strains and other known or determinable quantities (k, ϵ, ω). The advantages of using this model over its parent model is its improved numerical robustness and also the required computational effort is less due to its simplicity while keeping its most important physical modeling. Since we include the Reynolds stress anisotropy, we can expect the EARSM model to perform better than the general LEVM in predicting turbulent flows.

The most general explicit formalism for $\boldsymbol{a}$ in terms of $\boldsymbol{S}$ and $\boldsymbol{\Omega}$, restricted for 2D flows consisted of ten tensorially independent groups, provided by Pope [53]. The higher order terms can be reduced to these ten terms with the aid of Cayley-Hamilton theorem. Gatski and Speziale [19] derived a 3D EARSM based on the general quasi-linear RSM of Speziale, Sarkar and Gatski [70]. The authors point out that the model requires a regularization technique in order to obviate unreasonable solutions. In particular, the production to dissipation ratio ($\mathcal{P}/\epsilon$ in Eq. 2.10) was considered to be a constant and such an imposition resulted in an internal inconsistency in conditions other than equilibrium. By utilizing the LRR model with the approximation ($c_2 = 5/9$ in Eq. 2.10), Taulbee [73] provided an extension of the formalism by Pope for 2D flows to 3D conditions. That same model has been utilized by Wallin and Johansson [82], but with an explicit treatment of the production to dissipation ratio in contrary to other models.

Of all the models, the model by Wallin and Johansson [82] probably constitutes the best compromise between completeness and simplicity. In the following work, this model is put to use. We further follow in this work the direct solution method proposed by Grigoriev [28] to arrive at an explicit algebraic relationship from the implicit relationship. The interest of using such a direct solution method will be highlighted in Chapter 4 when dealing with variable density flows.

2.3.1 Explicit algebraic relation

As pointed out by Wallin and Johansson [82], the value of c_2 close to 5/9 suggested by some studies allows to neglect the last term in the right hand side of Eq. 2.10 and this greatly simplify the algebraic equation. Adopting this value leads to the following simplified yet an implicit algebraic relation for the Reynolds stress anisotropy tensor

$$N\boldsymbol{a} = -A_1\boldsymbol{S} + (\boldsymbol{a\Omega} - \boldsymbol{\Omega a}) \tag{2.11}$$

N is a function of $\boldsymbol{a}$ and reads

$$\begin{aligned} N &= A_3 + A_4\frac{\mathcal{P}}{\epsilon} \\ &= A_3 - A_4\boldsymbol{aS} \end{aligned} \tag{2.12}$$

with

$$A_1 = \frac{8}{15A_0}, \quad A_3 = \frac{c_1 - 1}{A_0}, \quad A_4 = \frac{1}{A_0}, \quad A_0 = \frac{7c_2 + 1}{11} \tag{2.13}$$

The procedure to solve the implicit equation for $\boldsymbol{a}$ consists first in assuming that the coefficient N is known. This leads to a linear equation that can be solved with the help of the Cayley-Hamilton theorem. The final step consists then in solving the nonlinear equation for N. Introducing $\boldsymbol{s} \equiv A_1\boldsymbol{S}/N$ and $\boldsymbol{o} \equiv \boldsymbol{\Omega}/N$, the implicit relation, Eq. 2.11, is first rewritten as

$$\boldsymbol{a} = -\boldsymbol{s} + (\boldsymbol{ao} - \boldsymbol{oa}) \tag{2.14}$$

The first step consist in writing the dimensionless Reynolds-stresses anisotropy tensor in terms of the dimensionless mean strain tensor $\boldsymbol{S}$ and the dimensionless mean rotation $\boldsymbol{\Omega}$ is presented below, for both two- and three-dimensional mean flows, following the direct procedure proposed by Grigoriev and Lazeroms [28]. The direct evaluation of the tensor is performed rather than a projection on a particular tensor basis. This approach is followed in this thesis as it will be a powerfull tool when dealing with buoyancy driven flows in Chapter 4.

Two-dimensional mean flows In order to derive an algebraic equation for the dimensionless Reynolds-stresses anisotropy tensor, the first step consists in writing the first recursive usage of the implicit relation, Eq. 2.10, leading to

$$\boldsymbol{a} = -\boldsymbol{s} + (\boldsymbol{so} - \boldsymbol{os}) + (\boldsymbol{ao}^2 + \boldsymbol{o}^2\boldsymbol{a} - 2\boldsymbol{oao}) \tag{2.15}$$

In order to express the last term in the right hand side of Eq. 2.15, we recall that the Cayley-Hamilton theorem for a two-dimensional traceless tensor reads

$$\boldsymbol{c}^2 = \frac{1}{2} II_c \boldsymbol{I}\,, \quad II_c = tr\{\boldsymbol{c}^2\} \tag{2.16}$$

Here, $\boldsymbol{I}$ is the three-dimensional unit tensor. Substituting $\boldsymbol{c} = \boldsymbol{a} + \boldsymbol{o}$ into Eq. 2.16 leads to

$$\boldsymbol{ao} + \boldsymbol{oa} = tr\{\boldsymbol{ao}\}\boldsymbol{I} \tag{2.17}$$

As $\boldsymbol{a}$ is symmetric and $\boldsymbol{o}$ is antisymmetric, the right hand side of Eq. 2.17 is zero and this allows to get

$$\boldsymbol{ao}^2 + \boldsymbol{o}^2\boldsymbol{a} = -2\boldsymbol{oao} \tag{2.18}$$

Finally, substituting $c = o$ into Eq. 2.16 and multiplying by a leads to

$$\boldsymbol{ao}^2 + \boldsymbol{o}^2\boldsymbol{a} = II_o\boldsymbol{a} \tag{2.19}$$

As a result, the algebraic relation reads

$$(1 - 2II_o)\,\boldsymbol{a} = -\boldsymbol{s} + (\boldsymbol{so} - \boldsymbol{os}) \tag{2.20}$$

Substituting $\boldsymbol{s} \equiv C_1\boldsymbol{S}/N$ and $\boldsymbol{o} \equiv \boldsymbol{\Omega}/N$, the resulting expression is formally equivalent to the common expression proposed by Wallin and Johansson given by

$$\boldsymbol{a} = \beta_1\boldsymbol{S} + \beta_4(\boldsymbol{S\Omega} - \boldsymbol{\Omega S}) \tag{2.21}$$

with

$$\beta_1 = -\frac{A_1 N}{N^2 - 2II_\Omega}\,, \quad \beta_4 = -\frac{A_1}{N^2 - 2II_\Omega} \tag{2.22}$$

The nonlinear equation for N can then be derived by inserting the solution of $\boldsymbol{a}$ provided by Eq. 2.21 in the definition of N. The resulting equation reads

$$N^3 - A_3 N^2 - \left(A_1 A_4 II_S - 2II_\Omega\right) N + 2A_3 II_\Omega = 0 \tag{2.23}$$

The solution of the cubic equation; Eq. 2.23 for N is

$$N = \begin{cases} \frac{c_1'}{3} + \left(P_1 + \sqrt{P_2}\right)^{\frac{1}{3}} + \text{sign}\left(P_1 - \sqrt{P_2}\right)\left|P_1 - \sqrt{P_2}\right|^{\frac{1}{3}} & P_2 \geq 0, \\ \frac{c_1'}{3} + 2(P_1^2 - P_2)^{\frac{1}{6}} \cos\left(\frac{1}{3}\arccos\left(\frac{P_1}{\sqrt{P_1^2 - P_2}}\right)\right) & P_2 < 0. \end{cases}$$

where,

$$P_1 = \left(\frac{1}{27}c_1'^2 + \frac{A_1 A_4}{6} II_S - \frac{2}{3} II_\Omega\right) c_1',$$
$$P_2 = P_1^2 - \left(\frac{1}{9}c_1'^2 + \frac{A_1 A_4}{3} II_S + \frac{2}{3} II_\Omega\right)^3$$

with $c_1' = A_3$. The first term on the RHS of Eq. 2.21 can be interpreted as a linear eddy-viscosity representation but with a variable C_μ^* coefficient given by

$$\beta_1 \boldsymbol{S} \approx \nu_t \boldsymbol{S}$$

$$\nu_t = C_\mu^* k\tau \tag{2.24}$$

$$C_\mu^* = -\frac{1}{2}\beta_1 \tag{2.25}$$

Three-dimensional mean flows As for two-dimensional mean flows, the first step consists in writing the first recursive usage of the implicit relation and this leads to Eq. 2.15. In order to express the last term in the right hand side of Eq. 2.15, we recall that the Cayley-Hamilton theorem for a three-dimensional traceless tensor reads

$$\boldsymbol{c}^3 = \frac{1}{2} II_c \boldsymbol{c} + \frac{1}{3} III_c \boldsymbol{I}\,, \quad II_c = tr\{\boldsymbol{c}^2\}\,, \quad III_c = tr\{\boldsymbol{c}^3\} \tag{2.26}$$

Substituting $\boldsymbol{c} = \boldsymbol{s} + \boldsymbol{o}$ into Eq. 2.26, taking into account that s is a symmetric traceless tensor and $\boldsymbol{o}$ is an antisymmetric traceless tensor, and equating the equal powers of $\boldsymbol{s}$ and $\boldsymbol{o}$, one gets

$$\boldsymbol{s}^3 = \frac{1}{2} II_s \boldsymbol{s} + \frac{1}{3} III_s \boldsymbol{I} \tag{2.27}$$
$$\boldsymbol{o}\boldsymbol{s}^2 + \boldsymbol{s}\boldsymbol{o}\boldsymbol{s} + \boldsymbol{s}^2\boldsymbol{o} = \frac{1}{2} II_s \boldsymbol{o} \tag{2.28}$$
$$\boldsymbol{o}^2\boldsymbol{s} + \boldsymbol{o}\boldsymbol{s}\boldsymbol{o} + \boldsymbol{s}\boldsymbol{o}^2 = \frac{1}{2} II_o \boldsymbol{s} + IV \boldsymbol{I}\,, \quad IV = tr\{\boldsymbol{s}\boldsymbol{o}^2\} \tag{2.29}$$
$$\boldsymbol{o}^3 = \frac{1}{2} II_o \boldsymbol{o} \tag{2.30}$$

As a result, using Eq. 2.29 with $\boldsymbol{s} \equiv \boldsymbol{a}$, one has

$$\boldsymbol{o}^2\boldsymbol{a} + \boldsymbol{a}\boldsymbol{o}^2 = \frac{1}{2} II_o \boldsymbol{a} + tr\{\boldsymbol{a}\boldsymbol{o}^2\}\boldsymbol{I} - \boldsymbol{o}\boldsymbol{a}\boldsymbol{o} \tag{2.31}$$

Using the implicit relation Eq. 2.14 multiplied by $\boldsymbol{o}^2$ and taking the trace of the result, the second term on the right hand side of Eq. 2.31 simplifies to

$$tr\{\boldsymbol{a}\boldsymbol{o}^2\} = tr\{(-\boldsymbol{s} + (\boldsymbol{a}\boldsymbol{o} - \boldsymbol{o}\boldsymbol{a}))\boldsymbol{o}^2\} = -IV \tag{2.32}$$

Hence, collecting Eqs. 2.31 and 2.32 allows to write Eq. 2.15 as

$$\boldsymbol{a} = -\boldsymbol{s} + (\boldsymbol{s}\boldsymbol{o} - \boldsymbol{o}\boldsymbol{s}) + (\frac{1}{2} II_o \boldsymbol{a} - IV\boldsymbol{I} - 3\boldsymbol{o}\boldsymbol{a}\boldsymbol{o}) \tag{2.33}$$

Next, the second recursive employment of the implicit relation provided by Eq. 2.15 allows to write the last term in the right hand side of Eq. 2.33 as

$$\begin{aligned} \boldsymbol{o}\boldsymbol{a}\boldsymbol{o} &= \boldsymbol{o}\left[-\boldsymbol{s} + (\boldsymbol{s}\boldsymbol{o} - \boldsymbol{o}\boldsymbol{s}) + (\boldsymbol{a}\boldsymbol{o}^2 + \boldsymbol{o}^2\boldsymbol{a} - 2\boldsymbol{o}\boldsymbol{a}\boldsymbol{o})\right]\boldsymbol{o} \\ &= -\boldsymbol{o}\boldsymbol{s}\boldsymbol{o} - \boldsymbol{o}\boldsymbol{s}\boldsymbol{o}^2 + \boldsymbol{o}^2\boldsymbol{s}\boldsymbol{o} + \boldsymbol{o}(\boldsymbol{a}\boldsymbol{o}^2 + \boldsymbol{o}^2\boldsymbol{a} - 2\boldsymbol{o}\boldsymbol{a}\boldsymbol{o})\boldsymbol{o} \end{aligned} \tag{2.34}$$

Using Eq. 2.31 together with Eq. 2.32, the last term in the right hand side of Eq. 2.34 simplifies to

$$\boldsymbol{o}(\boldsymbol{a}\boldsymbol{o}^2 + \boldsymbol{o}^2\boldsymbol{a} - 2\boldsymbol{o}\boldsymbol{a}\boldsymbol{o})\boldsymbol{o} = 3\boldsymbol{o}(\boldsymbol{a}\boldsymbol{o}^2 + \boldsymbol{o}^2\boldsymbol{a})\boldsymbol{o} - II_o\boldsymbol{o}\boldsymbol{a}\boldsymbol{o} + 2IV\boldsymbol{o}^2 \tag{2.35}$$

Then, using Eq. 2.30 to express the first term in the right hand side of Eq. 2.35, Eq. 2.34 leads to

$$(1 - 2II_o)\boldsymbol{o}\boldsymbol{a}\boldsymbol{o} = -\boldsymbol{o}\boldsymbol{s}\boldsymbol{o} - (\boldsymbol{o}\boldsymbol{s}\boldsymbol{o}^2 - \boldsymbol{o}^2\boldsymbol{s}\boldsymbol{o}) + 2IV\boldsymbol{o}^2 \tag{2.36}$$

Finally, multiplying Eq. 2.33 by $(1-2II_o)$ and using Eq. 2.29 to express $\boldsymbol{o}\boldsymbol{s}\boldsymbol{o}$, we obtain the following explicit algebraic relation

$$\begin{aligned} (1 - 2II_o)(1 - \frac{1}{2}II_o)\boldsymbol{a} = &-(1 - \frac{7}{2}II_o)\boldsymbol{s} - 6IV(\boldsymbol{o}^2 - \frac{1}{3}II_o\boldsymbol{I}) \\ &- (1 - 2II_o)(\boldsymbol{s}\boldsymbol{o} - \boldsymbol{o}\boldsymbol{s}) - 3(\boldsymbol{s}\boldsymbol{o}^2 + \boldsymbol{o}^2\boldsymbol{s} - \frac{2}{3}IV\boldsymbol{I}) - 3(\boldsymbol{o}^2\boldsymbol{s}\boldsymbol{o} - \boldsymbol{o}\boldsymbol{s}\boldsymbol{o}^2) \end{aligned} \tag{2.37}$$

Substituting $\boldsymbol{s} \equiv A_1\boldsymbol{S}/N$ and $\boldsymbol{o} \equiv \boldsymbol{\Omega}/N$, the resulting expression is formally equivalent to the common expression proposed by Wallin and Johansson given by

$$\begin{aligned} \boldsymbol{a} = &\beta_1\boldsymbol{S} + \beta_3\left(\boldsymbol{\Omega}^2 - \frac{1}{3}II_\Omega\boldsymbol{\delta}\right) + \beta_4(\boldsymbol{S}\boldsymbol{\Omega} - \boldsymbol{\Omega}\boldsymbol{S}) \\ &+ \beta_6\left(\boldsymbol{S}\boldsymbol{\Omega}^2 + \boldsymbol{\Omega}^2\boldsymbol{S} - \frac{2}{3}IV\boldsymbol{\delta}\right) + \beta_9\left(\boldsymbol{\Omega}\boldsymbol{S}\boldsymbol{\Omega}^2 - \boldsymbol{\Omega}^2\boldsymbol{S}\boldsymbol{\Omega}\right) \end{aligned} \tag{2.38}$$

where the coefficients β_i are defined according to :

$$\begin{aligned} \beta_1 &= -\frac{N\left(2N^2 - 7II_\Omega\right)}{Q}, \quad \beta_3 = -\frac{12N^{-1}IV}{Q} \\ \beta_4 &= -\frac{2\left(N^2 - 2II_\Omega\right)}{Q}, \quad \beta_6 = -\frac{6N}{Q}, \quad \beta_9 = \frac{6}{Q} \end{aligned} \tag{2.39}$$

where the denominator Q is defined by

$$Q = \frac{1}{A_1}\left(N^2 - 2II_\Omega\right)\left(2N^2 - II_\Omega\right)$$

Q always remains positive since II_Ω is negative as the trace of the square of the antisymmetric matrix is negative.

The non-linear equation for N is of sixth order for three-dimensional flows. Wallin and Johansson [82] suggest to use Eq. 2.23 as a first approximation and mention the difference between the 2D and 3D solution to be negligible. The solution of the 2D cubic equation is used for both two-dimensional and three-dimensional flows in this study.

At this stage of the developments, it is evident that the model remains incomplete without the description of k and τ. This necessitates for a platform model to obtain these turbulence properties.

2.3.2 The k-ω BSL-EARSM model

Many authors have used the BSL model as the platform for EARSM [23, 40, 31]. Whatever the existing platform model, in order to appropriately couple with a "higher order" model usually requires a partial or a full recalibration of the model coefficients in the platform model. Therefore, when combined with EARSM, some problems may arise without any recalibration of the platform model. This encouraged for instance Hellsten [23, 25] to perform a systematic calibration of both sets of model coefficients present in the BSL model.

In the following section, the goal is to combine EARSM with the k-ω BSL model keeping the BSL model unaltered. We propose to achieve this in two steps thereby enabling not to perform a detailed recalibration of the model constants. Firstly, we follow the methodology by Wilcox [86] which aids in coupling any algebraic model with a two-equation model (k-ω BSL in our case) without the need for a complete recalibration procedure. A detailed analytical study performed in section 2.3.3 on the canonical test cases will show that a slightly modification of the c_2 coefficient arising from the parent RSM model in the EARSM formulation is sufficient to successfully perform the coupling.

The governing equations for the k-ω BSL model follows Eqs. 1.19-1.20. When the k-ω BSL model is coupled with EARSM, the terms that are implicitly affected are

- The production terms via the Reynolds-stress tensor given by

$$\mathcal{P} = \boldsymbol{\tau}\frac{\partial U_i}{\partial x_j} \tag{2.40}$$

  where

$$\boldsymbol{\tau} = k\boldsymbol{a} + \frac{2}{3}k\boldsymbol{\delta} \tag{2.41}$$

  Here, $\boldsymbol{a}$ follows Eq.2.38.

- The diffusion terms via the turbulent viscosity given by

$$\nu_t = C_\mu^* k\tau \tag{2.42}$$

  with a variable C_μ^* coefficient.

This motivated Hellsten [23] to revise the complete set of model coefficients present in the parent BSL model, for the coupled system, by performing the analysis on the canonical test cases. Here, we prefer to leave the original BSL model unaltered.

We perform a simple procedure for adapting k-ω BSL with EARSM. The governing equations for the turbulent kinetic energy k-and the specific dissipation rate ω follow the set of equations given by Wilcox [86]

$$\frac{dk}{dt} = \mathcal{P} - \beta^*\omega k + \frac{\partial}{\partial x_j}\left[(\nu + \sigma_k\frac{k}{\omega})\frac{\partial k}{\partial x_j}\right] \tag{2.43}$$

$$\frac{d\omega}{dt} = \frac{\gamma\omega}{k}\mathcal{P} - \beta\omega^2 + \frac{\partial}{\partial x_j}\left[(\nu + \sigma_\omega\frac{k}{\omega})\frac{\partial \omega}{\partial x_j}\right] + 2(1-F_1)\sigma_{\omega_2}\frac{1}{\omega}\frac{\partial k}{\partial x_j}\frac{\partial \omega}{\partial x_j} \tag{2.44}$$

with the function F_1 is given by Eq. 1.24. On comparing the above set of equations and Eqs. 1.19-1.20 indicate that the influence of turbulent viscosity in the diffusion terms is absent. The diffusion terms are rather proportional to k/ω. As a result, the influence of the variable C^*_μ coefficient is absent in the diffusion terms. This provides a more general foundation model for computing the Reynolds-stress tensor such as an algebraic stress model [86] since now the diffusion terms are independent of the type of closure. Menter [47] states that such a modification for the diffusion terms avoids the problems observed and resolved by Hellsten [24] in the boundary layer edge.

The only terms in these equations that are implicitly affected by the variable C^*_μ coefficients are the production terms through Eq. 2.40. To understand this influence on the platform model, the model is thoroughly examined on the canonical cases and it is seen that the effect of the variable C^*_μ is present in the logarithmic region.

2.3.3 Calibration of the c_2 coefficient

The following section focuses on the inner region of the boundary layer. The influence of variable C^*_μ coefficient enters exclusively from the anisotropic term, a_{12} in the logarithmic region. This region is far from the wall to neglect the molecular viscosity relative to the eddy viscosity and yet close enough to neglect the convective effects relative to the rate at which the turbulence is being created and destroyed. Considering the logarithmic layer of a zero pressure gradient boundary layer, the transport equations for the kinetic energy and the specific dissipation rate equation simplify to

$$0 = \mathcal{P} - \beta^*\omega k + \sigma_{k_1}\frac{\partial}{\partial y}\left[\frac{k}{\omega}\frac{\partial k}{\partial y}\right] \tag{2.45}$$

$$0 = \gamma_1\frac{\omega}{k}\mathcal{P} - \beta_1\omega^2 + \sigma_{\omega_1}\frac{\partial}{\partial y}\left[\frac{k}{\omega}\frac{\partial \omega}{\partial y}\right] \tag{2.46}$$

In the logarithmic region, we have a constant Reynolds shear stress $-\overline{u'v'} = u_\tau^2 = -a_{12}k$, u_τ is the frictional velocity. The kinetic energy also remains constant in the log layer. As a result, from the transport equation for k, we have, $\mathcal{P} = \beta^*\omega k$.

The mean velocity gradient in this region is given by

$$\frac{dU}{dy} = \frac{u_\tau}{\kappa y} \tag{2.47}$$

Hence, P and ω become:

$$\mathcal{P} = -\overline{u'v'}\frac{dU}{dy} = \frac{u_\tau^3}{\kappa y}, \quad \omega = -a_{12}u_\tau/\kappa y\beta^*$$

Here, κ is the von Kármán constant, usually equal to 0.41. Anisotropy a_{12} is

$$a_{12} = -\frac{C_\mu^*}{\beta^*\omega}\frac{dU}{dy} = \sqrt{C_\mu^*} \tag{2.48}$$

where C_μ^* is introduced by using the non-linear constitutive relationship between the turbulent stress and the mean-strain rate tensors.

Numerical experimentation on the Channel flow reveals that the coefficient has a value of $C_\mu^* = 0.088125$ (which is close to $\beta^* = 0.09$) in the logarithmic region for the original values of the constants present in the BSL model and the LRR model. To obtain a correct behavior in the logarithmic region, or to obtain the right value for the $C_\mu^* = 0.09$ coefficient, two possibilities arise. Either the coefficients in the BSL model can be modified or the coefficients in the original LRR model from which the EARSM model is derived can be modified. Here, the coefficient from the original LRR model is modified.

By keeping the BSL model unaltered, the only way to have a value of $C_\mu^* = 0.09$ in the logarithmic region is by modifying the constants c_1 and/or c_2 that enters the EARSM formulation from the pressure-strain relationship of the Reynolds stress model. The original values used by Wallin and Johansson [82] are: $c_1 = 1.8$ and $c_2 = \frac{5}{9}$. The variable C_μ^* coefficient obtained for the original values of c_1 and c_2 in the log layer of a fully developed channel flow is 0.088125. We can see that the value of C_μ^* is slightly lower than its experimental value. This is the motivation behind the modification done to the c_2 coefficient. The value of C_μ^* is dependent on the A_1 coefficient which depends on c_2. The value of the c_2 coefficient is decreased from $\frac{5}{9}$ to 0.539166 to obtain a value close to 0.09 for the C_μ^* coefficient in the logarithmic region. Various values for the c_2 coefficient are shown in Table 2.1. Menter [47] modifies the value of A_1 alone present in the model equations with other

Model	c_2	A_1	C_μ^*
Wallin and Johansson [82]: Model 1	5/9	1.2	0.0881
Original RSS model [7]	0.52	1.26437	0.0917
Menter [47]	5/9	1.245	0.0914
Our calibration: Model 2	0.539166	1.23	0.0900

TABLE 2.1. The values of the c_2 coefficient in the various EARSM variants and the corresponding value of the C_μ^* coefficient in the logarithmic region.

coefficients left unaltered in order to match the velocity profile in the logarithmic region of a zero pressure gradient boundary layer without the need to modify the original BSL-equations.

In figure. 2.1, the β_1-coefficient is shown for various values of c_2. The iso-curves of the β_1-coefficient in the $(\sigma, \omega$-plane shows a small difference between the original value of $c_2 = 5/9$ and $c_2 = 0.52$. The behaviour is very similar and considering a value of $c_2 = 0.52$ is modest. An important point to be noted is that the substitution of c_2 coefficient might have a negative impact since the choice of $c_1 = 1.8$ and $c_2 = 5/9$ is one of combination that predicts both a_{12} and a_{22} correctly for the higher order Reynolds stress model. Therefore, modifying c_2 coefficient alone might pose a problem for other flows.

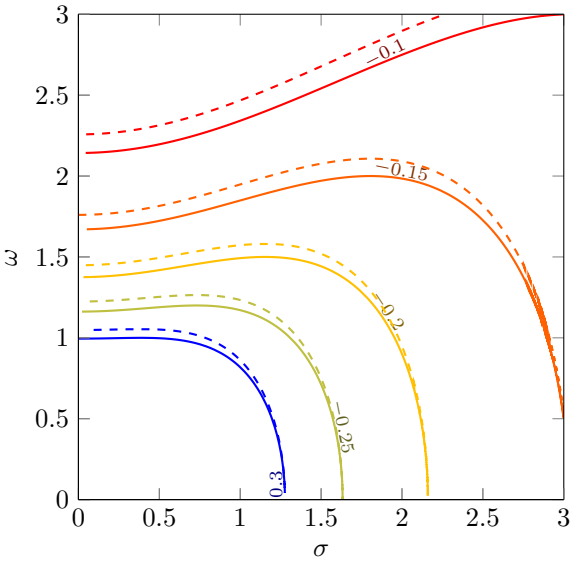

FIGURE 2.1. The behaviour of the β_1 coefficient in the σ-ω-plane. Solid lines($c_2 = 5/9$). Dashed lines($c_2 = 0.52$)

2.3.4 Diffusion correction

In some regions of the flow where the production to dissipation ratio is small, diffusion may become of the same order of magnitude as the other terms of the transport equation of the anisotropy tensor. In such a case, the weak equilibrium assumption fails to be valid and this may cause problems [73]. This is the case for example in the center of a turbulent channel flow where the magnitude of the β_1 coefficient becomes too large. This can be clarified by finding the value for C_μ^* when the strain rate goes to zero. The two-dimensional solution of the model becomes:

$$N(\sigma \to 0) = A_3, \quad \beta_1 = -\frac{A_1}{A_3}, \quad C_\mu^* = \frac{A_1}{2A_3} \tag{2.49}$$

Using the original values for the constants A_1 and A_3, the resulting value $C_\mu^* = 0.33$ is very large compared with the commonly adopted value $C_\mu = 0.09$. For this reason, Wallin and Johansson [82] include a correction introduced by an approximation for the neglected turbulent diffusion term to the ARSM equations (Eq. 2.3) arising from the weak equilibrium assumption. The proposed correction is based on the following simple model for the missing diffusion term in Eq. 2.3

$$\boldsymbol{\mathcal{D}} - \frac{\overline{u_i u_j}}{k}\mathcal{D} = -C_D \boldsymbol{a}\mathcal{D} \tag{2.50}$$

Such a model can be motivated for instance by assuming that the deviatoric part of $\boldsymbol{\mathcal{D}}$ can be neglected instead of assuming that anisotropy in $\boldsymbol{\mathcal{D}}$ is mainly related to the anisotropy in the Reynolds stresses themselves [6, 18, 57]. The diffusive flux of k is further approximated by assuming the equilibrium relation, $\mathcal{D} \simeq \epsilon - \mathcal{P}$, that neglects advection of k. This allows to express the right-hand side of Eq. 2.50 as

$$C_D \boldsymbol{a}\mathcal{D} = C_D \epsilon \boldsymbol{a}\left(1 - \frac{\mathcal{P}}{\epsilon}\right) \tag{2.51}$$

By plugging Eq. 2.51 into Eq. 2.12, c_1' becomes

$$c_1' = A_3 + \frac{C_D}{A_0} \max\left(1 - \frac{\mathcal{P}}{\epsilon}, 0\right) \tag{2.52}$$

The limiter is added to prevent the model from approaching to a singular behavior for large production to dissipation ratio. On the other hand, this limiter can also be seen as a blending between two different weak equilibrium assumptions [18].

The ratio $\mathcal{P}/\epsilon$ in the maximum function makes it impossible to be solved. The diffusion model is further approximated by using $\mathcal{P}/\epsilon = -\beta_1 II_S$ and β_1 is approximated with β_1^{eq} that corresponds to $\mathcal{P}/\epsilon = 1$. The use of β_1^{eq} assures the correction to be zero in the log-layer and for very high strain rates. Thus c_1' becomes

$$c_1' = A_3 + \frac{C_D}{A_0} \max\left(1 + \beta_1^{eq} II_S, 0\right) \tag{2.53}$$

with

$$\beta_1^{eq} = -\frac{A_1 N^{eq}}{(N^{eq})^2 - 2II_\Omega}, \quad N^{eq} = A_3 + A_4$$

The constant C_D can be estimated by looking for the effective $C_\mu^* = 0.09$ for zero strain rates. From Eq. 2.49, we get

$$C_D = \frac{A_0}{2C_\mu^*}\left(A_1 - 2C_\mu^* A_3\right)$$

This leads to $C_D = 2.163$, a value close to 2.2 considered by Wallin and Johansson [82].

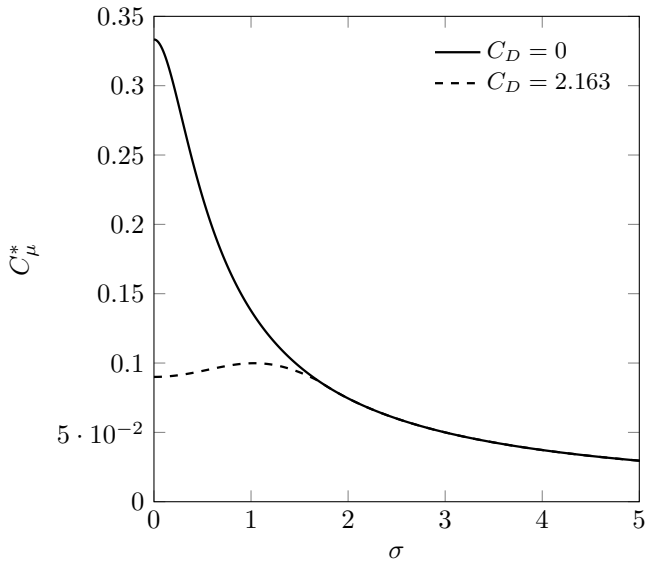

FIGURE 2.2. Behaviour of the C_μ^* coefficient for parallel shear flows using the diffusive correction

The modifications provided in this section allows one to surpass the complete recalibration procedure accomplished by Hellsten [25]. In situations where the algebraic expression reduces to the usual Boussinesq closure for the Reynolds stresses, the k-ω BSL-EARSM model behaves like the platform

two-equation k-ω BSL together with a behavior for the effective C_μ^* coefficient that mimics the shear stress transport limiter of the SST model [25].

2.4 Validation of EARSM

Two test cases are utilized to perform the validation of the implemented EARSM model. The first test case corresponds to the fully developed channel flow at a frictional Reynolds number $Re_\tau = 550$. Numerical simulations are carried out here on a moderate friction Reynolds number $\mathrm{Re}_\tau = 550$. Reference data are taken from the DNS of Lee and Moser [39].
The second test case is more challenging and deals with a fully developed turbulent flow in a pipe of square cross-section at a friction Reynolds number $\mathrm{Re}_\tau = 600$. The DNS results by Zhang *et al.* [89] is used as the reference for this case.

We acknowledge that in our proposed developments, no particular treatment except for the use of the limiter for turbulent time scale has been proposed to deal with the near-wall region. Nevertheless, these cases, especially the channel flow case, correspond to widely studied configurations of engineering interest in CFD research as both the simplicity of the geometry and the available DNS data make these cases ideal test cases for the turbulence model. Moreover, even without dedicated near-wall corrections, these studied cases allow to assess and to illustrate the potentialities of the model.

The numerical simulations are performed using the P^{2}REMICS software developed at IRSN. In the following cases, the velocity field is solved implicitly via a second-order accurate finite-volume scheme while the time advancement is accomplished by a semi-implicit Crank-Nicolson method. The numerical scheme used to solve the variables, k and ω corresponds to hybrid approximation. Implementation of the algebraic expression for the Reynolds stresses follows suggestions proposed by Wallin and Johansson [82] that consist in formulating the model in terms of an effective eddy viscosity that is treated implicitly together with an additional correction $\boldsymbol{a}^{(ex)}$ that is treated fully explicitly:

$$\overline{u_i' u_j'} - \frac{2}{3} k \delta_{ij} = -2 C_\mu^* k \tau S_{ij} + a_{ij}^{(ex)} \tag{2.54}$$

Simulations are performed for the two EARSM variants: 'Model 1' and 'Model 2'. Model 1 corresponds to the EARSM with the original c_2 coefficient and Model 2 with the modified c_2 coefficient (refer Table 2.1). For the turbulent channel flow, the performance of the EARSM model and the linear eddy viscosity models are similar (not shown here) whereas an improvement is observed for the turbulent flow in a square pipe using the EARSM. The linear eddy viscosity models are incapable of predicting the weak secondary flow.

2.4.1 Fully developed turbulent Channel flow

Fully developed turbulent channel flow constitutes a reference test case for the simulation of incompressible turbulent flows using either LES or RANS approach due to the simplicity of its geometry. It corresponds to a turbulent flow between two parallel plates separated by a distance 2δ where δ is referred to as the channel half width. Figure 2.3 shows the configuration of the flow. The flow

is homogeneous in the streamwise and spanwise directions. Simulations are performed along a two-dimensional plane (colored in grey) normal to the wall benefiting from the steady-state quantities which vary only along the wall-normal direction.

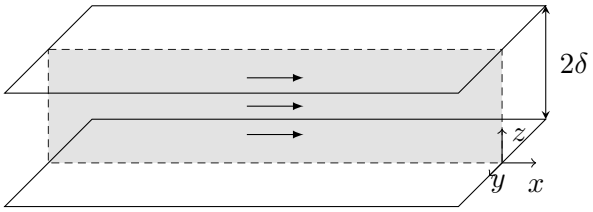

FIGURE 2.3. Configuration of the channel flow where x,y and Z are the streamwise, spanwise direction and the wall-normal direction respectively.

The available reference solutions provide direct numerical simulations at various Reynolds numbers $\mathrm{Re}_\tau = (u_\tau \delta/\nu)$ based on the friction velocity u_τ and the channel half width δ. We consider a moderate Reynolds number case corresponding to $\mathrm{Re}_\tau = 550$. The simulation results are compared with the DNS of Lee and Moser [51].

Numerical simulations are performed in a domain $[0; 2\pi\delta] \times [0; \delta]$ corresponding to the streamwise and the wall-normal direction respectively. While in the normal direction to the wall a non-uniform meshing is used according to the transformation given by Eq.2.55; the meshing in the streamwise direction is uniform.

$$\forall k \in [1, N_z]\,, z_k = \frac{\delta}{2}\left[1 + \frac{1}{a}\tanh\left[\left(-1 + \frac{2(k-1)}{N_z - 1}\right)\tanh^{-1}(a)\right]\right] \tag{2.55}$$

The parameter a is set to $a = 0.967$ to have the first dimensionless grid point location at $z_2^+ = 1$ for $N_z = 156$ where $z_2^+ = z_2 R_\tau \delta$.

The mean flow is driven by maintaining a constant flow rate $Q = \rho U_b \delta$ where U_b is the bulk velocity. A periodic boundary condition is applied assuming homogeneity in the streamwise direction whereas no-slip condition is imposed on the horizontal wall with a symmetry condition along the center of the channel. The initial velocity profile is prescribed according to:

$$\mathbf{v}(\mathbf{x}, 0) = (U(z), 0, 0), \quad U(z) = \begin{cases} u_\tau(\frac{1}{\kappa}\ln z^+ + B), & \text{if } z^+ \geq z_v \\ u_\tau z^+, & \text{otherwise} \end{cases} \tag{2.56}$$

with $B = 5.2$ and the von Kármán constant $\kappa = 0.41$. The distance from the wall where the viscous stress is predominant is given by $z_v = 10\nu/u_\tau$. The dimensional distance from the wall is given by $z^+ = z u_\tau/\nu$. For the dimensionless grid points lying in $30 < z^+ < 0.3\delta$ the law of the wall is usually valid whereas for $z^+ \leq z_v$ the linear viscous profile applies.

The mean velocity profile obtained for the EARSM is plotted in Figure. 2.4a. The plots are normalized using the friction velocity u_τ and the channel half width δ. It can be inferred that the mean velocity profile in the logarithmic region is well reproduced. The difference between the results for the two values of c_2 is negligible. The prediction of the Reynolds shear stress by both the models plotted in Fig. 2.4b is very close. The linear eddy viscosity models reproduce very similar profiles (not shown here).

The kinetic energy is underpredicted by EARSM in the near-wall region along with a shift in the

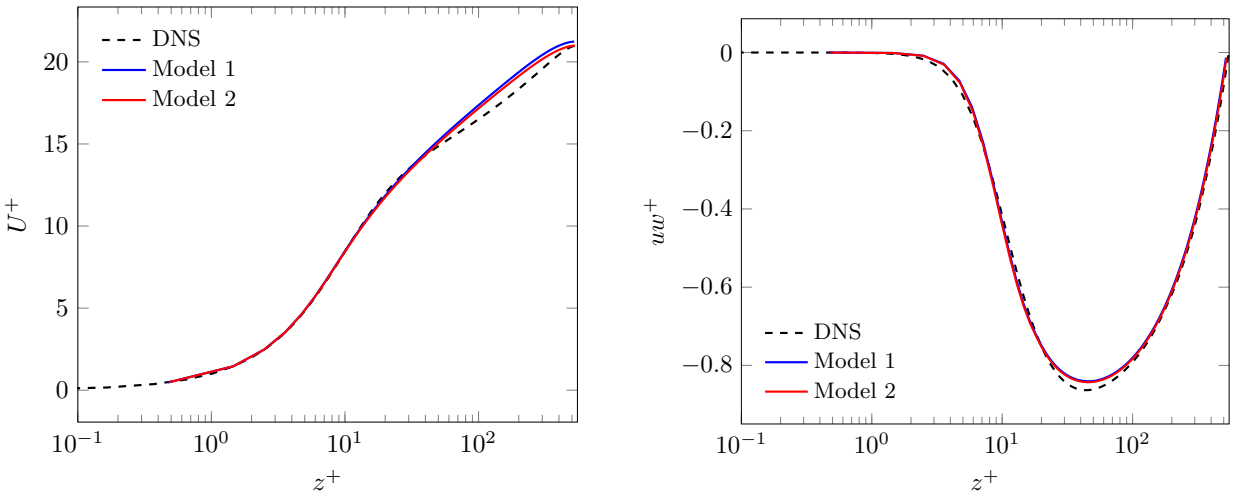

(A) Mean velocity profile

(B) Reynolds shear stress

FIGURE 2.4. Periodic channel flow simulation at $Re_\tau = 550$. Comparison between the two EARSM variants: Model 1 with the original value of $c_2 = 5/9$ and Model 2 with the Calibrated value of $c_2 = 0.539166$.

location of the peak. The profile for the kinetic energy is plotted in Fig. 2.5. As mentioned earlier, both the 'parent RSM' and the 'platform model' do not utilize any particular near-wall modeling. Introducing wall functions in the platform model and for the coefficients in the explicit algebraic relations will avail the model to better predict the location of the peak of the kinetic energy and its intensity. Secondly, two-equation models are calibrated to reproduce the correct near-wall behavior of the mean velocity profile, and not the turbulent kinetic energy.

2.4.2 Fully developed turbulent flow in a Square pipe

The fully developed turbulent flow in a straight pipe of square cross-section is a test case which constitutes an illustrative case for which the anisotropy between the Reynolds stress components is present and influences the mean flow. In this case, the anisotropy leads to a secondary flow that greatly modifies both the shear stress and the heat transfer at the walls. This may also lead to an increase in the turbulent mixing when dealing for instance with passive scalar transport or variable density flows.

The two-equation RANS turbulence models based on the linear stress strain relationship are incapable of capturing the secondary flow. This is because the secondary flow is a result of the anisotropy in the normal stresses. As a result, all turbulence models of this kind are unable to generate secondary flows. The focal point of this test case is to determine the predictive capabilities of the EARSM model (which should provide some anisotropy), to capture these secondary motion of second-kind (purely turbulence driven) which are driven by the difference of the normal Reynolds stresses $(v^2 - w^2)$ perpendicular to the principal velocity U_1. Following the approach by Rung et al [61], the coefficients which act as a crucial parameter for the evolution of the secondary flow in the current framework of the EARSM are determined. The quantity $(2\beta_4 + \beta_3)$ drives the secondary motion of second-kind.

Numerical simulations are performed here in a domain $[0; 2\pi D] \times [0; D] \times [0; D]$ where D is the

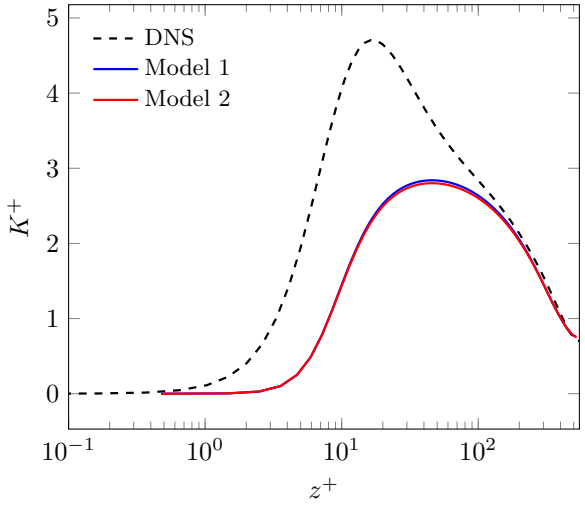

FIGURE 2.5. Periodic channel flow simulation at $Re_\tau = 550$. The turbulent kinetic energy profiles for the two EARSM variants: Model 1 with the original value of $c_2 = 5/9$ and Model 2 with the Calibrated value of $c_2 = 0.539166$.

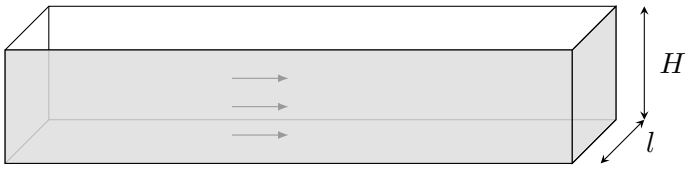

FIGURE 2.6. Configuration of the flow in a pipe of square cross-section where x,y and Z corresponds to the streamwise, spanwise and the wall-normal directions respectively.

duct width. Assuming symmetry conditions at $y = z = D/2$, the RANS numerical simulations are performed on a quarter of the pipe $[0; 2\pi D] \times [0; D/2] \times [0; D/2]$, where $D/2$ is half the pipe width, prescribing symmetry boundary conditions at $y = z = D/2$. Numerical results are compared with DNS performed by Zhang, Hao, *et al.* [89]. The Reynolds number Re_τ based on the friction velocity u_τ and the duct width D is 600 which corresponds approximately to the bulk Reynolds number $\mathrm{Re}_b = U_b D/\nu$ of 10500. The flow is sustained by prescribing a constant mass flow rate at a cross-section, given by

$$Q_{ref} = \rho U_b (D/2)^2$$

specified at each time-step.

Along the streamwise direction, the meshing is uniform with N_x number of grid points whereas a non-uniform meshing is used in the wall-normal directions for which the transformation reads:

$$\forall k \in [1, N_z], y_k, z_k = \frac{D}{2}\left[1 + \frac{1}{a}\tanh\left[\left(-1 + \frac{(k-1)}{N_z - 1}\right)\tanh^{-1}(a)\right]\right]$$

According to the number of grid points $N_y = N_z$ in the normal direction to the walls, the parameter a is calculated by setting the first dimensionless grid point locations y_2^+, z_2^+:

$$y_2^+ = \frac{y_2 R_\tau}{D}, z_2^+ = \frac{z_2 R_\tau}{D}$$

By setting $N_z = 49$ and $y_2^+ = z_2^+ = 0.2$, this leads to 0.96.
As initial conditions, the turbulence intensity is set to 0.01 and the turbulent viscosity ratio is set to 10. The time-step is provided as per $\Delta t = 0.1T_0$ with $T_0 = D/U_b$ with the final time $t = 300T_0$. The results are made dimensionless using $z^+ = zu_\tau/\nu$, $u^+ = u/u_\tau$, $v^+ = v/u_\tau$. The results presented in this section is plotted along the corner bisector $y = z$.

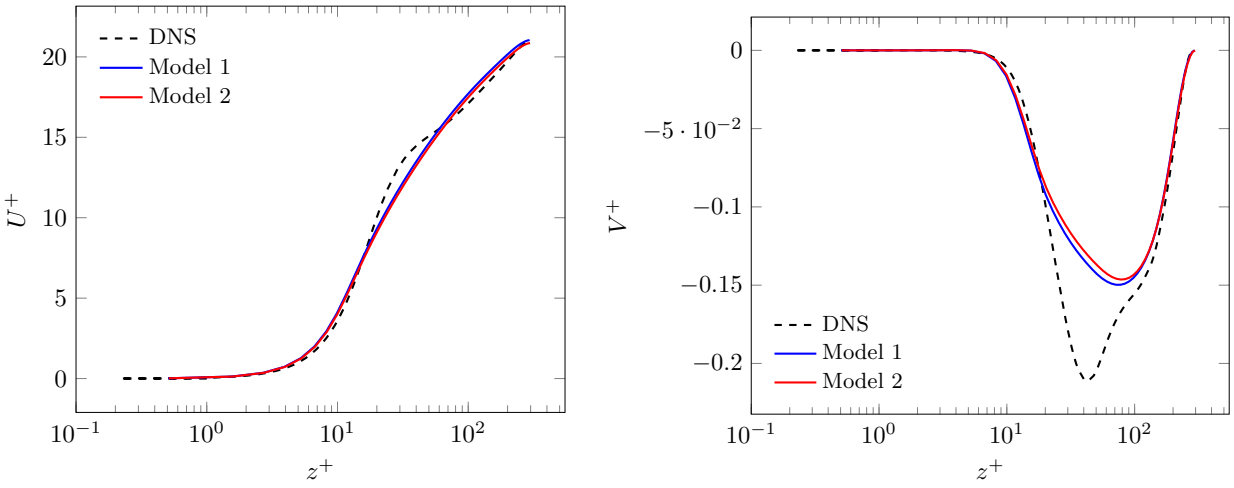

(A) Streamwise velocity profile

(B) Secondary velocity profile

FIGURE 2.7. Comparison between the two EARSM simulation results with the reference DNS by Zhang, Hao, *et al.* [89] at $\mathrm{Re}_\tau = 600$. Left: Mean streamwise velocity profile plotted along the corner bisector, Right: Secondary velocity profile plotted along the corner bisector. Model 1: Original value of $c_2 = 5/9$, Model 2: Calibrated value of $c_2 = 0.539166$

Fig. 2.7a shows the mean stream-wise velocity profile along the corner bisector which is similar to the profile obtained by Menter [47]. The increased axial momentum transfer into the corner from the duct center increases the axial velocity near the corner walls which is well captured by both the EARSM model variants. The transfer of this momentum arises due to the presence of secondary velocity field plotted in figure. 2.7b. The developed EARSM model captures the secondary flow resulting from the anisotropy of the normal stresses. On the contrary, all first order RANS models do not exhibit any secondary motion (not shown here).

With the value of the coefficient $c_2 = 0.539166$, there is a small but negligible decrease in the strength of the secondary flow. The effect of modifying the coefficient c_2 enters the anisotropic stress tensor through the β coefficients. As the value of c_2 is decreased, there is an impact on the levels of anisotropic normal stress components which results in a decreased secondary flow. The momentum transfer towards the corner of the wall from the center of the duct is decreased, resulting in a decreased axial velocity near the center of the duct.

Two counter rotating vortices near along the corner bisector are clearly visible in Fig. 2.8. The effect of the secondary motion on the mean stream-wise velocity is to convect momentum from the central region of the duct to the walls along the corner bisector which is the reason why the mean stream-wise velocity contour is bent towards the corner. Further, the secondary motion convects momentum from the corners to the center along the wall and from the wall to the center of the

duct which is the reason for the bulge of the mean velocity contour towards the center of the duct along the wall bisector. This can be easily understood by looking at the mean stream-wise velocity isotachs.

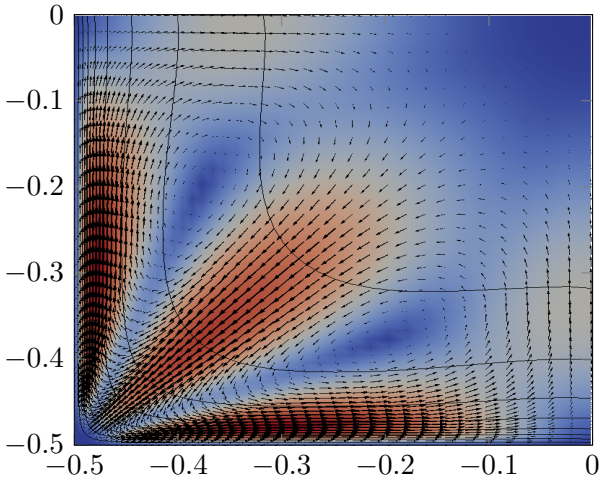

FIGURE 2.8. Cross-section of the simulation domain. Mean streamwise velocity isotachs and the secondary velocity vectors.

2.5 Conclusion

The development of explicit algebraic Reynolds stress model in a RANS framework has been the subject of this chapter. A direct solution method instead of using a particular tensor basis projection method has been put to use to arrive at an explicit algebraic relation from the implicit relation. The generality of the two-equation model is lost when coupling EARSM with it as the two-equation model usually requires a full calibration of the model coefficients. It has been shown that modifying the diffusion terms in the kinetic energy and specific dissipation rate transport equations along with the calibration of a coefficient from the parent Reynolds stress model eliminates the need for a complete recalibration of the coefficients in the platform two-equation model. In the developed model, no particular treatment of the near wall region has been considered except for the use of a Kolmogorov limiter in the turbulent time scale. Validation of EARSM has been performed on the fully developed channel flow and the fully developed flow in a pipe of square cross-section. EARSM is able to capture the secondary flow arising due to the presence of the corners unlike the linear eddy viscosity models.
The next chapter is dedicated to seamless hybrid RANS/LES methodologies. The EARSM model developed in a RANS framework in this chapter will be extended as a subfilter scale model in a hybrid RANS/LES framework in the following chapter.

Chapter 3

Explicit algebraic subfilter closure for seamless hybrid RANS-LES methods

In order to account for complex flow features (unsteadiness...), the explicit algebraic approach presented in Chapter 2 is now extended to a seamless hybrid RANS-LES framework, following the Equivalent-Detached Eddy Simulation (E-DES) methodology described in [14]. The development of a subfilter scale model is presented wherein the anisotropic effects in the subfilter scales are taken into account. Following the conventional LES practice, the model constants are calibrated on the Decay of Isotropic Turbulence. Further, the performance of the model is analyzed on the two previous flows, the fully developed channel flow and the fully developed flow in a square pipe.

3.1 Seamless Hybrid RANS/LES methods

For simulating fluid flows, hybrid methods have gained the attention of researchers for the past 20 years and it is currently under development. As discussed in section 1 of Chapter 1, hybrid RANS-LES methods can be broadly classified into two categories, zonal methods and seamless methods. In zonal methods, the RANS to LES transition is abrupt and prescribed by the user whereas in the seamless approach, a single SFS turbulence model, sensitized to the local grid properties and local turbulence level is utilized. The intention of these methods was originally to model either the complete or a part of the boundary layer with RANS and switch to a turbulence-resolving simulation state in far wall and separated regions.

Usually, the hybrid RANS-LES methods adapt a RANS model as a base model and switch to a SFS model by the adaption of a turbulent length scale. This length scale lets the hybrid RANS-LES method work in fully modeling, i.e. RANS or partly resolving mode, i.e. LES. Thus, obtaining a more accurate solution and at the same time having a reduction in the computational cost. There are a large variety of seamless hybrid RANS-LES methods. We refer to the review provided by Chaouat [8] for a detailed presentation of the most popular seamless hybrid approaches. In this section, we restrict to the main concepts of seamless methods that are relevant to the present work.

3.1.1 Detached Eddy Simulation

Among the many available seamless methods, the most widely utilized one was proposed by Spalart in the year 1997 called Detached Eddy Simulation (DES) [68]. This method was developed mainly for simulating aerodynamic flows, in particular, detached flow over airfoils with the intention to

bring down the computational cost of a true-LES for wall-bounded flows and the inability of RANS methods to capture massively-separated flows. In this method, regions near solid boundaries where the flow remains attached is modeled in RANS mode. The model transitions from a pure RANS to a subfilter scale formulation in detached regions of the flow.

The hybridization of a base model from a RANS framework to its appropriate subfilter scale (SFS) model is obtained by making the base model sensitive to the local grid resolution. Such an hybridization was originally proposed for the single transport equation Spalart-Allmaras RANS model. In the RANS model given by Eq. 1.10, the distance to the nearest wall d was replaced by a new length-scale $\tilde{d}$; sensitive to the grid spacing

$$\tilde{d} = \min\left(d, C_{\mathrm{DES}}\Delta\right)$$

where Δ is given by

$$\Delta = \max(\Delta_x, \Delta_y, \Delta_z)$$

C_{DES} is a modeling parameter which is determined by performing a model calibration, usually on the decay of isotropic turbulence [65].

The motivation behind the development of DES through the modification of the length scale was based on the fact that under local equilibrium conditions, i.e. when the production balances the dissipation, the model in its LES formulation reduces to a Smagorinsky-like model [67]. Near the wall (where the turbulence length scale is smaller than the grid size), $\tilde{d} = d$ and we obtain the original RANS Spalart-Allmaras equations. As the grid is refined below the limit $C_{\mathrm{DES}}\Delta < d$, where the distance to the nearest wall is larger than the grid size, the DES limiter is activated and the base model switches from RANS to SFS model. When the turbulence model is functioning as a SFS model, the standard DES lengthscale becomes

$$\tilde{d} = C_{\mathrm{DES}}\Delta$$

The level of production and destruction of turbulent viscosity is modified and now dependent on the grid. The SST model was hybridized in a DES framework by Strelets [71]. Just like the classical, RANS, Menter's-SST model, the DES formulation developed by Strelets has two branches. This motivated the author to introduce an empirical function to have two distinct values for the C_{DES} coefficient; one for the transformed k_s-ϵ_s branch and the other for the k_s-ω_s branch.

Problems may arise when the DES limiter gets activated inside the attached boundary layer resulting from the grid refinement, activating the LES mode inside the boundary layer, where the grid is not fine enough to sustain resolved turbulence. This is undesirable as it can lead to grid-induced separation, as discussed by Menter *et al.* [42] where the boundary layers separates at arbitrary locations based on the grid spacing. In order to avoid this, further improvements have been proposed by extending DES to Delayed-DES (DDES) [48] and Improved-DDES (IDDES) [66].

3.1.2 Partially Integrated Transport Model

The numerical method put in place is developed in a general framework of large eddy simulations and can be applied to almost all subfilter scale models based on transport equations of subfilter

scale turbulent quantities. More recently, Schiestel and Dejoan [64] developed a k_s-ϵ_s SFS model[1] that could be applied for RANS-LES in the context of seamless hybrid approach, i.e., to have a smooth transition between resolved and unresolved scales, called Partially Integrated Transport Model (PITM). The RANS model is to be made dependent on the filter width thereby being able to control the amount of resolved energy.

In order to modify and make the system of transport equations dependent on the cutoff wavenumber, the energy spectrum is partitioned into three spectral zones, such that $[0, \kappa_c]$, $[\kappa_c, \kappa_d]$, $[\kappa_d, \infty]$. This multi-scale approach is developed in spectral space, by selecting a cutoff wavenumber (κ_c) at-first located in the inertial range just as done in the case of LES. The cutoff wavenumber κ_c is usually determined by the grid size

$$\kappa_c = \frac{2\pi}{C_g \Delta} \tag{3.1}$$

C_g is a constant and in practice depends on the type of numerical scheme being used. Next, a larger wavenumber (κ_d) is introduced as:

$$\kappa_d = \kappa_c + \xi \frac{\epsilon}{k_s^{3/2}} \tag{3.2}$$

This larger wavenumber is selected such that the energy located beyond it, is negligible. The parameter ξ is sufficiently large such that the contribution of energy beyond κ_d is negligible. Therefore the energy contained between κ_c and κ_d is modeled. The system of k_s-ϵ_s SFS model in a PITM framework is given by

$$\frac{\partial k_s}{\partial t} + \tilde{U_j} \frac{\partial k_s}{\partial x_j} = \mathcal{P}_s - \epsilon_s + \frac{\partial}{\partial x_j} \left[(\nu + \frac{\nu_{t,s}}{\sigma_k}) \frac{\partial k_s}{\partial x_j} \right], \tag{3.3}$$

$$\frac{\partial \epsilon_s}{\partial t} + \tilde{U_j} \frac{\partial \epsilon_s}{\partial x_j} = \frac{\epsilon_s}{k_s} \left(C_{\epsilon 1} \mathcal{P}_s - C^*_{\epsilon 2} \epsilon_s \right) + \frac{\partial}{\partial x_j} \left[(\nu + \frac{\nu_{t,s}}{\sigma_\epsilon}) \frac{\partial \epsilon_s}{\partial x_j} \right]. \tag{3.4}$$

where $C^*_{\epsilon 2}$ is given by

$$C^*_{\epsilon 2} = C_{\epsilon 1} + r \left(C_{\epsilon 2} - C_{\epsilon 1} \right) \tag{3.5}$$

The coefficient $C^*_{\epsilon 2}$ is no more a constant but dependent on the parameter r. This dependence is what makes the hybridization of the base model possible. This dependence is important as it allows one to link the large scale part of the spectrum to the modelled subgrid scales.

Energy partition as a function of the cutoff

The parameter r is defined as the ratio between the modeled kinetic energy to the total kinetic energy. The kinetic energy ratio parameter r is defined as:

$$r = \frac{k_m}{k} = \frac{1}{k} \int_{\kappa_c}^{\infty} E(\kappa) d\kappa \tag{3.6}$$

Here, $E(\kappa)$ corresponds to the energy density spectrum. The ratio r can be computed from any given energy spectrum. Here, we use the Kolmogorov spectrum given by

$$E_K(\kappa) = C_K \epsilon^{2/3} \kappa^{-5/3} \tag{3.7}$$

[1] Hereon, the subscript 's' refers to a subfilter quantity

with the Kolmogorov constant $C_K = 1.5$. Assuming spectral equilibrium and substituting the spectrum in Eq. 3.6, we obtain

$$r = \frac{1}{\beta_0}\eta_c^{-2/3} \tag{3.8}$$

This ratio corresponds to the ratio the user targets, based on the grid size. The dimensionless parameter η_c is given by:

$$\eta_c = \kappa_c \frac{k^{3/2}}{\epsilon} = \kappa_c L_t \tag{3.9}$$

where L_t refers usually to the integral length scale. The coefficient β_0 is identified as

$$\beta_0 = \frac{2}{3C_K} \tag{3.10}$$

It can be seen that the expression for r is consistent with the DNS limit ($r = 0$ when $\kappa_c \to \infty$). This is not true in the RANS limit ($r = 1$ when $\kappa_c \to 0$) because the Kolmogorov spectrum is invalid in this limit. This motivated Schiestel and Dejoan [64] to propose an empirical relation[2] for r to eliminate this discrepancy:

$$r = \frac{1}{1 + \beta_0 \eta_c^{2/3}} \tag{3.11}$$

A method similar to PITM is Partially Average Navier-Stokes (PANS) [20]. The formalization of this method, though derived using different assumptions, leads to the same set of governing equations as that of PITM, except for a slightly different treatment of turbulent diffusion.

3.1.3 Equivalent-Detached Eddy Simulation

The basic idea of Equivalent-DES is that it bridges DES with PITM, in such a way that the "hybridization function" is not anymore a function of Δ, but of r. The theoretical justification has been given for that in Friess *et al.* [14] where the authors shaped the relationship for the parameter using the concept of H-equivalence where H stands for hybrid. The equivalence is based on the postulate that allows one to bridge two different techniques of hybridization (DES and PITM [64]) of the same system of equations yielding a required condition that has to be satisfied by the DES model (called the Equivalent-DES). As a result, the authors have demonstrated that the DES method is statistically equivalent to the PITM method if the LES lengthscale in ψ is written in terms of r, combining the consistency of PITM and the robustness of DES.

The k-ϵ-based E-DES is given by :

$$\frac{\partial k_s}{\partial t} + \tilde{U}_j \frac{\partial k_s}{\partial x_j} = \mathcal{P}_s - \psi \epsilon_s + \frac{\partial}{\partial x_j}\left[(\nu + \frac{\nu_{t,s}}{\sigma_k})\frac{\partial k_s}{\partial x_j}\right], \tag{3.12}$$

$$\frac{\partial \epsilon_s}{\partial t} + \tilde{U}_j \frac{\partial \epsilon_s}{\partial x_j} = \frac{\epsilon_s}{k_s}(C_{\epsilon 1}\mathcal{P}_s - C_{\epsilon 2}\epsilon_s) + \frac{\partial}{\partial x_j}\left[(\nu + \frac{\nu_{t,s}}{\sigma_\epsilon})\frac{\partial \epsilon_s}{\partial x_j}\right] \tag{3.13}$$

The non-dimensional lengthscale ψ in Eq. 3.12 is given by

$$\psi = \max\left(1; \frac{l_s}{l_{LES}}\right) \quad \text{with} \quad l_s = \frac{k_s^{3/2}}{\epsilon_s}, \quad l_{LES} = \frac{r^{3/2} L_t}{\Psi(r)} \tag{3.14}$$

[2] Other empirical relationships have been reviewed in [13].

Neglecting the resolved dissipation, the integral lengthscale L_t is defined by

$$L_t = \frac{(\overline{k_s} + k_r)^{3/2}}{\overline{\epsilon_s}} \tag{3.15}$$

Here, the transition from RANS to LES is driven by the kinetic energy ratio parameter r, removing its explicit relationship on the grid step. The function $\Psi(r)$ is given by

$$\Psi(r) = 1 + \left(\frac{C_{\epsilon 2}}{C_{\epsilon 1}} - 1\right)\left(1 - r^{\frac{C_{\epsilon 1}}{C_{\epsilon 2}}}\right) \tag{3.16}$$

It is worth mentioning that Friess *et al.* [14] derived three expressions for $\Psi(r)$, under various sets of assumptions. Here, we choose their most complete formulation.

The value of the constants present above remain unchanged and take the values present in the base model. The turbulent eddy viscosity $\nu_{t,s}$ is

$$\nu_{t,s} = C_\mu \frac{k_s^2}{\epsilon_s} \tag{3.17}$$

Friess *et al.* showed that DES is equivalent to TPITM if the DES length scale $L = C_{\mathrm{DES}}\Delta$ is replaced by the appropriate function of the energy ratio r. As a result, DES is also interpretable as a hybrid RANS/temporal LES, which does not require the grid step for the transition from RANS to LES. From the expression for κ_c (Eq. 3.1), r (Eq. 3.11) and DES equivalent length scales, the constant C_{DES} must be replaced by the function

$$f_{\mathrm{DES}} = \frac{1}{\beta_0^{3/2}\pi\psi(r)} \tag{3.18}$$

Recently, Tran *et al.* [76] have applied the E-DES methodology to Menter's shear stress transport (SST) model as the underlying model. We follow here an alternate route starting from the k_s-ϵ_s version of E-DES (for which the H-equivalence has been provided in [14]), leading to the derivation of a k_s-ω_s based E-DES.

3.2 BSL-like model in E-DES framework

The use of k_s-ϵ_s requires additional use of damping functions in the near-wall region. In order to circumvent this, we start from the k_s-ϵ_s version of E-DES and derive a k_s-ω_s based E-DES. In this thesis, the k_s-ω_s BSL variant of the available versions of the k_s-ω_s model is chosen. The k_s-ω_s BSL variant is expected to be advantageous over its counterparts in both the near-wall regions and in regions with low-shear[3].

In this section, the development of Menter's BSL-like model in an E-DES framework is presented. Firstly, the transformation of the E-DES version of the k_s-ϵ_s model to its equivalent k_s-ω_s form is performed. Following which, the E-DES version based on the modified Wilcox k_s-ω_s model is given, this will be called the k_s-ω_s branch. Finally, with the help of the blending function by Menter[45], the transformed E-DES k_s-ϵ_s model and the E-DES Wilcox k_s-ω_s model are blended to obtain an E-DES formulation of Menter's BSL-like model. For simplicity, in this chapter, we will call the

[3]Refer Chapter 1

transformed E-DES version of the k_s-ϵ_s model as the 'k_s-ϵ_s' branch and the E-DES Wilcox k_s-ω_s model as the 'k_s-ω_s' branch.

3.2.1 The k_s-ϵ_s branch

The E-DES k_s-ϵ_s model Eqs. 3.12-3.13 is transformed to its equivalent k_s-ω_s model through the relationship

$$\epsilon_s = \beta^* \omega_s k_s \tag{3.19}$$

The transformation of the model is demonstrated in Appendix A. The resulting transport equations are

$$\frac{\partial k_s}{\partial t} + \tilde{U}_j \frac{\partial k_s}{\partial x_j} = \mathcal{P}_s - \psi_\epsilon \beta^* \omega_s k_s + \frac{\partial}{\partial x_j}\left[(\nu + \sigma_{k_\epsilon}\nu_{t,s})\frac{\partial k_s}{\partial x_j}\right], \tag{3.20}$$

$$\frac{\partial \omega_s}{\partial t} + \tilde{U}_j \frac{\partial \omega_s}{\partial x_j} = \frac{\omega_s}{k_s}\gamma_\epsilon \mathcal{P}_s - \beta_\epsilon \omega_s^2 + \frac{\partial}{\partial x_j}\left[(\nu + \sigma_{\omega_\epsilon}\nu_{t,S})\frac{\partial \omega_s}{\partial x_j}\right] + 2\sigma_{\omega_\epsilon}\frac{1}{\omega_s}\frac{\partial k_s}{\partial x_j}\frac{\partial \omega_s}{\partial x_j} \tag{3.21}$$

with the non-dimensional lengthscale ψ_ϵ given by

$$\psi_\epsilon = \max\left(1; \frac{l_s}{l_{LES}}\right) \quad \text{with} \quad l_s = \frac{k_s^{1/2}}{\beta^*\omega_s}, \qquad l_{LES} = \frac{r_\epsilon^{3/2} L_t}{\Psi_\epsilon} \tag{3.22}$$

Here, the subscript ϵ symbolizes the transformed E-DES k_s-ϵ_s model and the subfilter eddy viscosity $\nu_{t,s}$ is

$$\nu_{t,s} = \frac{k_s}{\omega_s} \tag{3.23}$$

$$\gamma_\epsilon = (C_{\epsilon 1_\epsilon} - 1), \quad \beta_\epsilon = \beta^*(C_{\epsilon 2_\epsilon} - \psi_\epsilon), \quad \sigma_{\omega_\epsilon} = 0.856, \quad \sigma_{k_\epsilon} = 1 \tag{3.24}$$

with

$$\Psi_\epsilon = 1 + \left(\frac{C_{\epsilon 2_\epsilon}}{C_{\epsilon 1_\epsilon}} - 1\right)\left(1 - r_\epsilon^{\frac{C_{\epsilon 1_\epsilon}}{C_{\epsilon 2_\epsilon}}}\right) \tag{3.25}$$

The kinetic energy ratio parameter r_ϵ is given by

$$r_\epsilon = \frac{1}{1 + \beta_{0_\epsilon}\eta_c^{2/3}} \tag{3.26}$$

with $\eta_c = \kappa_c L_t$ and the integral lengthscale L_t is expressed as

$$L_t = \frac{(\overline{k_s} + k_r)^{3/2}}{\beta^* \overline{\omega_s k_s}} \simeq \frac{(\overline{k_s} + k_r)^{3/2}}{\beta^* \overline{\omega_s}\,\overline{k_s}} \tag{3.27}$$

3.2.2 The k_s-ω_s branch

The E-DES k_s-ω_s model is given as:

$$\frac{\partial k_s}{\partial t} + \tilde{U}_j \frac{\partial k_s}{\partial x_j} = \mathcal{P}_s - \psi_\omega \beta^* \omega_s k_s + \frac{\partial}{\partial x_j}\left[(\nu + \sigma_{k_\omega}\nu_{t,s})\frac{\partial k_s}{\partial x_j}\right], \tag{3.28}$$

$$\frac{\partial \omega_s}{\partial t} + \tilde{U}_j \frac{\partial \omega_s}{\partial x_j} = \frac{\omega_s}{k_s}\gamma_\omega \mathcal{P}_s - \beta_\omega \omega_s^2 + \frac{\partial}{\partial x_j}\left[(\nu + \sigma_{\omega_\omega}\nu_{t,s})\frac{\partial \omega_s}{\partial x_j}\right] - \beta^*(1 - \psi_\omega)\omega_s^2 \tag{3.29}$$

The non-dimensional lengthscale ψ_ω is

$$\psi_\omega = \max\left(1; \frac{l_s}{l_{LES}}\right) \quad \text{with} \quad l_s = \frac{k_s^{1/2}}{\beta^*\omega_s}, \qquad l_{LES} = \frac{r_\omega^{3/2} L_t}{\Psi_\omega} \tag{3.30}$$

The subscript ω refers to the Wilcox model. The subfilter eddy viscosity $\nu_{t,s}$ is given by Eq. A.20 and the constants are given by

$$\gamma_\omega = \frac{5}{9}, \quad \beta_\omega = 0.0750, \quad \sigma_{\omega_\omega} = 0.5, \quad \sigma_{k_\omega} = 0.5$$

On the other hand, the function Ψ_ω is expressed as

$$\Psi_\omega = 1 + \left(\frac{C_{\epsilon 2_\omega}}{C_{\epsilon 1_\omega}} - 1\right)\left(1 - r_\omega^{\frac{C_{\epsilon 1_\omega}}{C_{\epsilon 2_\omega}}}\right) \tag{3.31}$$

where $C_{\epsilon 1_\omega} = \gamma_\omega + 1$ and $C_{\epsilon 2_\omega} = \beta_\omega/\beta^* + 1$. The kinetic energy ratio parameter r_ω is given by

$$r_\omega = \frac{1}{1 + \beta_{0_\omega}\eta_c^{2/3}} \tag{3.32}$$

with $\eta_c = \kappa_c L_t$ and the integral lengthscale L_t is given by Eq. 3.27.

3.2.3 E-DES based on Menter's BSL-like model

The idea used by Menter in the construction of the RANS BSL model is put to use here. A blending function is used to blend the k_s-ϵ_s branch with the k_s-ω_s branch such that in the region of the flow which is closest to the wall, the k_s-ω_s branch remains active and changes progressively to the k_s-ϵ_s branch further away from the wall. The blending function F_1 used to perform the blend between the two models is given by

$$F_1 = \tanh(arg_1^4) \tag{3.33}$$

with,

$$arg_1 = \min\left(\max\left(\frac{\sqrt{k_s}}{\beta^*\omega_s y}; \frac{500\nu}{y^2\omega_s}\right); \frac{4\rho\sigma_{\omega_2}k_s}{CD_{k\omega}y^2}\right) \tag{3.34}$$

Eq. 3.28 and Eq. 3.29 are multiplied by F_1 and Eq. 3.20 and Eq. 3.21 are multiplied by $(1 - F_1)$ and the corresponding equations are added together to give the E-DES formulation based on BSL model[4]. The subfilter kinetic energy transport equation takes the form

$$\begin{aligned}\frac{\partial k_s}{\partial t} + \tilde{U}_j\frac{\partial k_s}{\partial x_j} =& \mathcal{P}_s - \underbrace{(F_1\psi_\omega + (1-F_1)\psi_\epsilon)}_{\psi'}\beta^*\omega_s k_s \\ &+ \frac{\partial}{\partial x_j}\left[(\nu + (F_1\sigma_{k_\omega} + (1-F_1)\sigma_{k_\epsilon})\nu_{t,s})\frac{\partial k_s}{\partial x_j}\right]\end{aligned} \tag{3.35}$$

[4]Hereon, the subscript ω represents the terms coming from the k_s-ω_s branch and ϵ represents the terms from the k_s-ϵ_s branch.

and the subfilter specific dissipation rate transport equation takes the form

$$\begin{aligned}\frac{\partial \omega_s}{\partial t} + \tilde{U}_j \frac{\partial \omega_s}{\partial x_j} =& \frac{\omega_s}{k_s}(F_1\gamma_\omega + (1-F_1)\gamma_\epsilon)\mathcal{P}_s - (F_1\beta_\omega + (1-F_1)\beta_\epsilon)\omega_s^2 \\ &+ \frac{\partial}{\partial x_j}\left[(\nu + (F_1\sigma_{\omega_\omega} + (1-F_1)\sigma_{\omega_\epsilon})\nu_{t,s})\frac{\partial \omega_s}{\partial x_j}\right] \\ &+ 2(1-F_1)\sigma_{\omega_\epsilon}\frac{1}{\omega_s}\frac{\partial k_s}{\partial x_j}\frac{\partial \omega_s}{\partial x_j}\end{aligned} \tag{3.36}$$

The terms in the underbrace is the result of the non-dimensional lengthscale ψ' used to achieve the E-DES formulation of the respective RANS models. This is the only additional term that uses the blending function in comparison with the original Menter's BSL model. Considering this term alone, we have

$$\begin{aligned}\psi' = F_1\psi_\omega + (1-F_1)\psi_\epsilon =& F_1 \max\left(1; \frac{k_s^{1/2}}{\beta^*\omega_s L_t}\frac{\Psi_\omega}{r_\omega^{3/2}}\right) \\ &+ (1-F_1)\max\left(1; \frac{k_s^{1/2}}{\beta^*\omega_s L_t}\frac{\Psi_\epsilon}{r_\epsilon^{3/2}}\right)\end{aligned} \tag{3.37}$$

From the above equation, we can infer that within the maximum function, the terms other than the two ratios $\Psi/r^{3/2}$ are alike. As a result, the blending function can be considered within the maximum function.

$$\psi' = \max\left[1; \frac{k_s^{1/2}}{\beta^*\omega_s L_t}\left(F_1\frac{\Psi_\omega}{r_\omega^{3/2}} + (1-F_1)\frac{\Psi_\epsilon}{r_\epsilon^{3/2}}\right)\right] \tag{3.38}$$

From equations 3.48 and 3.32, we notice that the kinetic energy ratio parameter utilize the length-scale Eq. 3.27. As a first approximation, the influence of the F_1 function on the parameter r in the above equation is neglected. That implies that a single length scale and $\beta_0 = \beta_{0_\epsilon} = \beta_{0_\omega}$ coefficient is utilized. The function ψ' then becomes

$$\psi' = \max\left[1; \frac{k_s^{1/2}}{\beta^*\omega_s r^{3/2} L_t}\left(F_1\Psi_\omega + (1-F_1)\Psi_\epsilon\right)\right] \tag{3.39}$$

with the relationship for r specified as

$$r = \frac{1}{1+\beta_0\eta_c^{2/3}} \tag{3.40}$$

with $\eta_c = \kappa_c L_t$ and the integral length-scale expressed as

$$L_t = \frac{(\overline{k_s} + k_r)^{3/2}}{\beta^*\overline{\omega_s}\overline{k_s}} \tag{3.41}$$

The kinetic energy ratio parameter r given above is the target parameter. This parameter is a sensor that is dependent on the local grid and turbulence properties. This is the ratio that the user expects and we shall call this the target kinetic energy ratio or r_t, unless else specified. The ratio observed in the simulation is not necessarily the target ratio, therefore we shall call it the observed ratio, r_o.

Complete model

$$\frac{\partial k_s}{\partial t} + \tilde{U_j}\frac{\partial k_s}{\partial x_j} = \mathcal{P}_s - \psi'\beta^*\omega_s k_s + \frac{\partial}{\partial x_j}\left[(\nu + \sigma_k\nu_{t,s})\frac{\partial k_s}{\partial x_j}\right] \tag{3.42}$$

$$\frac{\partial \omega_s}{\partial t} + \tilde{U_j}\frac{\partial \omega_s}{\partial x_j} = \frac{\omega_s}{k_s}\gamma\mathcal{P}_s - \beta\omega_s^2 + \frac{\partial}{\partial x_j}\left[(\nu + \sigma_\omega\nu_{t,s})\frac{\partial \omega_s}{\partial x_j}\right] + 2(1-F_1)\sigma_{\omega_\epsilon}\frac{1}{\omega_s}\frac{\partial k_s}{\partial x_j}\frac{\partial \omega_s}{\partial x_j} \tag{3.43}$$

with the coefficients $\gamma = F_1\gamma_\omega + (1-F_1)\gamma_\epsilon$, $\beta = F_1\beta_\omega + (1-F_1)\beta_\epsilon$, $\sigma_\omega = F_1\sigma_{\omega_\omega} + (1-F_1)\sigma_{\omega_\epsilon}$, $\sigma_k = F_1\sigma_{k_\omega} + (1-F_1)\sigma_{k_\epsilon}$ and $C_{\epsilon 1_\omega} = \gamma_\omega + 1$ and $C_{\epsilon 2_\omega} = \beta_\omega/\beta^* + 1$ where

$$\begin{aligned} &\gamma_\omega = \frac{5}{9}, \quad \beta_\omega = 0.0750, \quad \sigma_{\omega_\omega} = 0.5, \quad \sigma_{k_\omega} = 0.5 \\ &\gamma_\epsilon = (C_{\epsilon 1} - 1), \quad \beta_\epsilon = \beta^*\left(C_{\epsilon 2} - \psi^{k\epsilon}\right), \quad \sigma_{\omega_\epsilon} = 0.856, \quad \sigma_{k_\epsilon} = 1.0 \end{aligned} \tag{3.44}$$

The non-dimensional lengthscale ψ' is given by

$$\begin{aligned} \psi' = \quad & \max\left[1; \frac{l_s}{r^{3/2}L_t}\left(F_1\Psi_\omega + (1-F_1)\Psi_\epsilon\right)\right] \quad \text{with} \\ & l_s = \frac{k_s^{1/2}}{\beta^*\omega_s}, \quad L_t = \frac{(\overline{k_s} + k_r)^{3/2}}{\beta^*\overline{\omega_s}\overline{k_s}} \end{aligned} \tag{3.45}$$

along with

$$\Psi_\omega = 1 + \left(\frac{C_{\epsilon 2_\omega}}{C_{\epsilon 1_\omega}} - 1\right)\left(1 - r^{\frac{C_{\epsilon 1_\omega}}{C_{\epsilon 2_\omega}}}\right) \tag{3.46}$$

$$\Psi_\epsilon = 1 + \left(\frac{C_{\epsilon 2_\epsilon}}{C_{\epsilon 1_\epsilon}} - 1\right)\left(1 - r^{\frac{C_{\epsilon 1_\epsilon}}{C_{\epsilon 2_\epsilon}}}\right) \tag{3.47}$$

$$r = \frac{1}{1 + \beta_0\eta_c^{2/3}}, \quad \eta_c = \kappa_c L_t \tag{3.48}$$

The subfilter eddy viscosity $\nu_{t,s}$ that appear in the diffusion terms is given by

$$\nu_{t,s} = \frac{k_s}{\omega_s} \tag{3.49}$$

With the coefficients coming from the base models kept unaltered, we have one coefficient, i.e., β_0 in hand that has to be calibrated. The value of the β_0 coefficient should be consistent for both branches. The calibration procedure is shown in the section dedicated to the test cases.

3.3 Explicit algebraic hybrid stress model

Recently, Marstorp *et al.* [41] derived an anisotropic subgrid stress model for LES using the same analogy as for the EARSM by Wallin and Johansson [82] called the explicit algebraic subgrid scale model (EASSM). EASSM is achieved by representing the unknown quantities in terms of the known filtered quantities. The EASSM uses the 2D solution as a first approximation, similar to EARSM by Wallin and Johansson [82]. Temme *et al.* [74] have performed a simulation of the square duct at low Reynolds number and the authors have observed the EASSM model to predict the mean secondary velocity closer to the DNS compared to the linear eddy viscosity models as subgrid scale

model. The EASSM used in [74] consists of the reduced anisotropic tensor for 2D flows. Marstorp *et al.* [41] also mention the 2D tensorial representation to be a reasonable approximation for 3D flows. Recently, numerical simulations were performed using EASSM on the fully developed channel flow at various friction Reynolds numbers by Montecchia *et al.* [50]. Simulations with very coarse grids reveal the EASSM as the subgrid scale model to be less sensitive to the grid step in comparison with the LEVM as the subgrid scale model.

In a hybrid context, the question that arises is the applicability of the weak-equilibrium assumption, i.e., whether or not the vanishing of the transport of the normalized subgrid stress anisotropy is applicable in a hybrid RANS-LES context. To address this, EARSM is applied to a hybrid RANS/LES framework on the following assumption - If the weak equilibrium assumption is valid at the RANS limit and also for modeling the SFS in LES then this assumption should also be valid for an intermediate cutoff (between RANS and LES), giving rise to explicit algebraic hybrid stress model (EAHSM).

A hybrid approach based on an explicit algebraic model for modeling the subfilter stresses has already been utilized in [83, 84] in a seamless approach. The platform sub-filter models utilized in both the references follows the recalibrated model by Hellsten [23].

Presuming the aforementioned equilibrium assumption to be verified for the SFS, our goal is to use a similar methodology by coupling the E-DES based on Menter's BSL-like model developed in the previous section with the explicit algebraic closure developed in Section 2.3.2 of Chapter 2. Once the model calibration and validation is performed, this hybrid methodology using EDES will be extended for buoyancy flows. This will be studied in Chapter 4.

The algebraic expression for the SFS anisotropic tensor $\boldsymbol{a}_s$ consists of higher order terms of the resolved strain-rate tensor $\tilde{\boldsymbol{S}}$ and rotation tensor $\tilde{\boldsymbol{\Omega}}$. The nonlinear SFS stress strain relationship is given as:

$$\boldsymbol{\tau}_s = -2\nu_{t,s}\tilde{\boldsymbol{S}} + \frac{2}{3}k_s\boldsymbol{\delta} + k_s\boldsymbol{a}_s^{(ex)} \tag{3.50}$$

The extra anisotropic tensor has an influence on the resolved velocity through the term $-\frac{\partial \boldsymbol{\tau}_s}{\partial x_j}$ present in the RHS of the filtered momentum equation. The SFS production term is also influenced through the relationship $\mathcal{P}_s = -\boldsymbol{\tau}_s\frac{\partial \tilde{u}_i}{\partial x_j}$.
The algebraic expression for the SFS anisotropic tensor in a general 3D flow is

$$\begin{aligned}\boldsymbol{a}_s =& \beta_3\left((\tau\tilde{\boldsymbol{\Omega}})^2 - \frac{1}{3}II_{\tilde{\Omega}}\boldsymbol{\delta}\right) + \beta_4\tau^2\left(\tilde{\boldsymbol{S}}\tilde{\boldsymbol{\Omega}} - \tilde{\boldsymbol{\Omega}}\tilde{\boldsymbol{S}}\right)\\ &+ \beta_6\left(\tau^3(\tilde{\boldsymbol{S}}\tilde{\boldsymbol{\Omega}}^2 + \tilde{\boldsymbol{\Omega}}^2\tilde{\boldsymbol{S}}) - \frac{2}{3}IV\boldsymbol{\delta} - \tau II_{\tilde{\Omega}}\tilde{\boldsymbol{S}}\right) + \beta_9\tau^4\left(\tilde{\boldsymbol{\Omega}}\tilde{\boldsymbol{S}}\tilde{\boldsymbol{\Omega}}^2 - \tilde{\boldsymbol{\Omega}}^2\tilde{\boldsymbol{S}}\tilde{\boldsymbol{\Omega}}\right)\end{aligned} \tag{3.51}$$

The non-zero β coefficients are

$$\beta_1 = -\frac{N(2N^2 - 7II_{\tilde{\Omega}})}{Q}, \quad \beta_3 = -\frac{12N^{-1}IV}{Q}, \tag{3.52}$$

$$\beta_4 = -\frac{2(N^2 - 2II_{\tilde{\Omega}})}{Q}, \quad \beta_6 = -\frac{6N}{Q}, \quad \beta_9 = \frac{6}{Q} \tag{3.53}$$

where

$$Q = \frac{1}{A_1}\left(N^2 - 2II_{\tilde{\Omega}}\right)\left(2N^2 - II_{\tilde{\Omega}}\right) \tag{3.54}$$

Here, $\tilde{\boldsymbol{S}}$ and $\tilde{\boldsymbol{\Omega}}$ are the filtered strain-rate and rotation tensor respectively given by:

$$\tilde{\boldsymbol{S}} = \frac{1}{2}\left(\tilde{u}_{i,j} + \tilde{u}_{j,i}\right), \quad \tilde{\boldsymbol{\Omega}} = \frac{1}{2}\left(\tilde{u}_{i,j} - \tilde{u}_{j,i}\right) \tag{3.55}$$

The turbulent timescale is defined as

$$\tau = \max\left(\frac{1}{\beta^* \omega_s}; C_\tau \sqrt{\frac{\nu}{\beta^* \omega_s k_s}}\right) \tag{3.56}$$

with the constants $\beta^* = 0.09$ and $C_\tau = 6$ and k_s and ω_s represent the SFS kinetic energy and the specific dissipation rate. N is given by the solution of the third-order equation

$$N^3 - A_3 N^2 - \left(A_1 A_4 II_{\tilde{S}} - 2II_{\tilde{\Omega}}\right) N + 2A_3 II_{\tilde{\Omega}} = 0 \tag{3.57}$$

The solution of the above cubic equation is:

$$N = \begin{cases} \frac{c_1'}{3} + (P_1 + \sqrt{P_2})^{\frac{1}{3}} + sign(P_1 - \sqrt{P_2})|P_1 - \sqrt{P_2}|^{\frac{1}{3}} & P_2 \geq 0, \\ \frac{c_1'}{3} + 2(P_1^2 - P_2)^{\frac{1}{6}} cos\left(\frac{1}{3} arccos\left(\frac{P_1}{\sqrt{P_1^2 - P_2}}\right)\right) & P_2 < 0. \end{cases} \tag{3.58}$$

where,

$$P_1 = \left(\frac{1}{27}c_1'^2 + \frac{A_1 A_4}{6} II_{\tilde{S}} - \frac{2}{3} II_{\tilde{\Omega}}\right) c_1', \tag{3.59}$$

$$P_2 = P_1^2 - \left(\frac{1}{9}c_1'^2 + \frac{A_1 A_4}{3} II_{\tilde{S}} + \frac{2}{3} II_{\tilde{\Omega}}\right)^3 \tag{3.60}$$

with

$$c_1' = A_3 + \frac{C_D}{A_0}\left[max\left(1 + \beta_1^{eq} II_{\tilde{S}}, 0\right)\right] \tag{3.61}$$

and

$$\beta_1^{eq} = -\frac{A_1 N^{eq}}{(N^{eq})^2 - 2II_{\tilde{\Omega}}} \tag{3.62}$$

where $N^{eq} = A_3 + A_4$ and constant C_D

$$C_D = \frac{A_0}{0.18}\left[A_1 - 0.18 A_3\right] \tag{3.63}$$

3.4 Test Cases

In this section, firstly the calibration of the EAHSM model concerning its model coefficient β_0 on the Decay of Isotropic Turbulence (DIT) is presented. This test is one of the simplest case to check the correct behavior of a newly developed subfilter scale turbulence model. Numerical simulations are carried out at two different Taylor Reynolds numbers[5], namely; Comte-Bellot and Corrsin [9] at Re_λ is 71.6 and on the Kang *et al.* [32] at Re_λ is 716.

Once the model has been calibrated, the performance of the EAHSM model is analyzed on the fully developed turbulent channel flow. The channel flow is a widely studied configuration of engineering interest in CFD research with a wealth of numerical analysis and data available in the literature. The simplicity of the geometry makes the channel flow an ideal test case for investigating the behavior of the turbulence model. Numerical simulations are carried out on a moderate friction Reynolds number $\mathrm{Re}_\tau = 550$. Reference data are taken from the DNS of Lee and Moser [39]. One important aspect will be check the model performance on coarse grid resolutions and do a comparison with LES, using the WALE model.

Like in the channel test case, the EAHSM model is used to compute fully developed turbulent flow in a pipe of square cross-section at a friction Reynolds number $\mathrm{Re}_\tau = 600$. The DNS results by Huser and Biringen [27] and Zhang *et al.* [89] are used as reference for this case. It is not a commonly studied configuration despite its simple geometry. The presence of the corners creates a secondary flow which in the previous chapter stood a point of comparison between the linear eddy viscosity models and the EARSM, in a RANS framework.

In the following cases, the resolved velocity field is solved implicitly via a second-order accurate finite-volume scheme while the time advancement is accomplished by a semi-implicit Crank-Nicolson method. This results in a discretely energy conserving numerical scheme. The numerical scheme used to solve the subfilter variables, namely; k_s and w_s corresponds to hybrid approximation.

3.4.1 Calibration on the decay of isotropic turbulence

An isotropic turbulent velocity field is a field with no mean velocity and no mean gradients. The isotropic field is by default homogeneous: invariant in space. Under the action of viscous forces the turbulent field simply decays. Due to the nature of the turbulent field, it is regarded as the most elementary test. Consequently, the importance of this case shall be understood as a first step towards our understanding of the behavior of a turbulence model.

Just like the DES based on Menter's-SST model, the EAHSM formulation has two distinct branches, the transformed k_s-ϵ_s branch and the k_s-ω_s branch, blended by F_1. It is important to recall that the influence of the F_1 function is absent in the β_0 coefficient. The calibration procedure is similar to that followed by Strelets [71] on the DES based on Menter's-SST model. This challenges us to find an optimum value for the β_0 coefficient which is capable of representing the correct energy spectra for the DIT cases, on both branches. By enforcing $F_1 = 1$, the transformed k_s-ϵ_s branch of the EAHSM model is active. This enables us to perform the calibration of the β_0 coefficient exclusively on this branch. On similar terms, the k_s-ω_s branch is active by enforcing $F_1 = 1$. Note that only

[5] Reynolds number $\mathrm{Re}_\lambda = \lambda U/\nu$ corresponding to Taylor micro-scales (λ). Length scales which are larger than the Taylor microscale are not much affected by viscosity. Below the Taylor microscale the turbulent motions are subject to strong viscous forces. The turbulent kinetic energy is dissipated into heat.

the k_s-ϵ_s branch results are presented here for this test case. A similar behavior is observed for the k_s-ω_s branch for the same value of the β_0 coefficient.

To perform the decay of isotropic turbulence, since the models run in a purely LES mode, initial values for the subfilter quantities, namely; k_s and ω_s have to be prescribed which should respect the subfilter part of the respective quantities for a given mesh size Δ. Consequently, the simulation is divided into two phases[6]: the initialization phase (to find the initial values for k_s and ω_s) and the decay phase. For the initialization phase, an initial velocity field is prescribed using the Random Fourier Method (RFM) that provides a synthetic turbulent velocity field enforcing a given model energy spectrum [see Appendix B for the RFM method]. This prescribed velocity field is frozen and the subfilter turbulence model is run until the statistical convergence of the subfilter quantities k_s and ω_s. For the decay phase, the initial values of the subfilter quantities thus obtained in the initialization phase is prescribed. The calibration of the model coefficient is performed by examining the ability of the model to correctly reproduce the energy spectrum in comparison to the available experimental data at various time instances.
The test cases are individually presented in this section. Each test is briefly described, important numerical parameters are looked into, followed by the simulation results.

Comte-Bellot and Corrsin test case

The experiment by Comte-Bellot and Corrsin [9] on the decaying turbulence behind a grid is simulated first. The authors, in their experiments measured data at three different distances $tU_0/M = 42$, 98 and 171 from a grid with mesh size $M = 50.8$ mm and a mean speed near the grid $U_0 = 10$ m.s^{-1}. The Taylor Reynolds number at these locations are $\mathrm{Re}_\lambda = 71.6$, 65.3 and 60.7 respectively. This can be recast for the simulation in terms of time advancement $t_0 = 0$, $t_1 = 56M/U_0$ and $t_2 = 129M/U_0$ by applying Taylor's hypothesis.

Numerical simulations are performed in a triply periodic box $[0, L]^3$ of length $L = \pi/6$. This length for the domain is much larger than the integral length scale in order to avoid spurious effects of periodic boundary conditions. Three different equidistant meshes are used, namely; 16^3 , 32^3 and 64^3 cells. The ratio of the length of the computational mesh-size to the Kolmogorov length scale is provided in Table 3.1. The higher this ratio becomes, the larger is the scale-separation between the largest unresolved scales and the Kolmogorov scales; which will be a good way to test and challenge the SFS model performance. The time-step is specified such that Δt_{CFL} with $\Delta t_{\mathrm{CFL}} = L/(Nu_{rms})$.

The initial velocity field is prescribed according to the data measured at the first downstream position using RFM. According to the experimental data at $tU_0/M = 42$, the kinetic energy and the integral length scale are set respectively to $k = 1.5u_{rms}^2 = 0.074$ m^2.s^{-2} and $L_t = 0.024$ m. Figure 3.1 shows a comparison between the energy spectrum obtained by the analytical expression and the spectrum computed by the constructed velocity field using RFM method on 64^3 cells. The abscissa denotes the wavenumber and the ordinate represents the energy contained. From the spectrum, we can find out in which turbulence scales (or respective wave numbers) the fluctuating kinetic turbulent energy reside. The convergence of the subfilter quantities is confirmed by looking at the temporal evolution of the volume averaged subfilter kinetic energy $< k_s >$ and the temporal evolution of the target and the observed kinetic energy ratio parameter. The converged states for $< k_s >$ and $< r >$ on 96^3 cells at initialization are displayed in figure 3.2. The observed ratio is close to the target ratio which shows the robustness of the EAHSM model. A similar

[6]Common to both cases: Comte-Bellot and Corrsin [9]and Kang *et al.* [32]

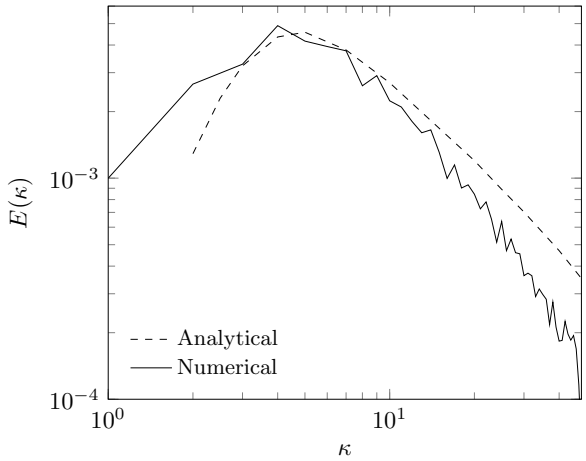

FIGURE 3.1. Initialization phase: Comparison between the constructed spectrum utilizing Equation.. and the numerical result obtained using the RFM method.

initialization is performed for the 32^3 and 64^3 cells (results not shown here). A single point analysis

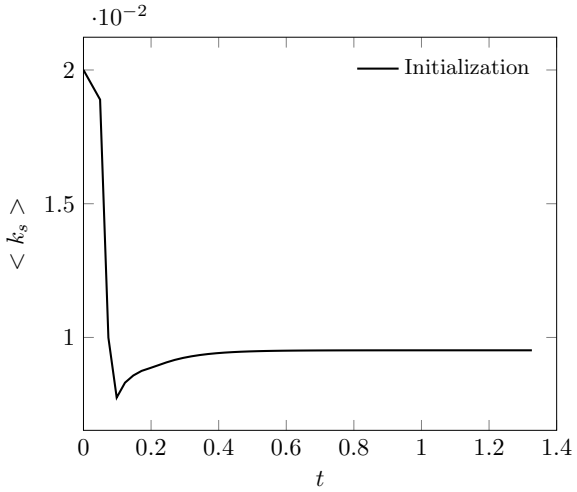

(A) Subfilter kinetic energy

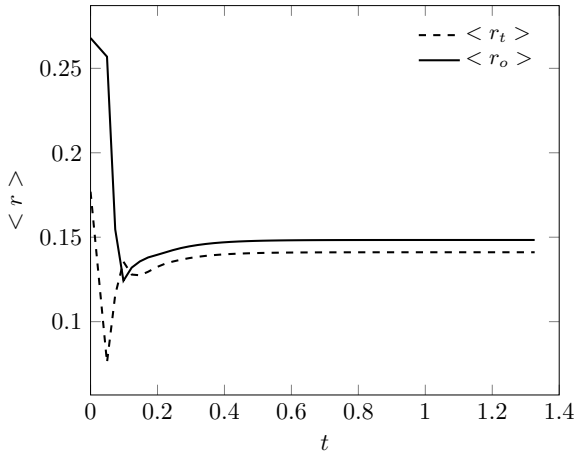

(B) Kinetic energy ratio parameters

FIGURE 3.2. Initialization phase: Convergence of the volume-averaged subfilter kinetic energy (Left) and a comparison between the volume averaged target and the observed kinetic energy ratio parameters (Right).

on the transformed k_s-ϵ_s branch of the EAHSM is performed analytically assuming a steady forcing (constant resolved-velocity gradients). This is obtained by first imposing $F_1 = 0$ followed by volume averaging the governing equations (Eqs. 3.35-3.36) and finding their steady state solution. A steady state solution exists for the models based on the hybrid E-DES method. The fixed point solution for the subfilter kinetic energy is given by

$$< k_s >= \frac{(\beta_\epsilon + \lambda)(l_{LES}S)^2\eta^2\chi}{\lambda(\gamma_\epsilon\lambda + \beta^*\eta\xi)} \tag{3.64}$$

	Box length	η	N	Δ	Δ/η
Comte-Bellot and Corrsin [9]	$\pi/6$	0.029 cm	32	0.0164	56
			64	0.0082	28
			96	0.0041	19
Kang *et al.* [32]	2π	0.011 cm	32	0.1963	1785
			64	0.098	892
			96	0.0654	595

TABLE 3.1. The computational mesh-size to the Kolmogorov length-scale ratio (Δ/η) for the two DIT cases.

where $< k_s >$ is the volume averaged subfilter kinetic energy. In contrast, when a similar exercise is performed on the PITM, the set of equations permit two fixed point solutions. A trivial fixed point $< k_s >=< \omega_s >= 0$, which corresponds to the DNS limit and a non-trivial fixed point when various ratios but $< k_s >,< \omega_s >$ attain steady-state values. It will be interesting to demonstrate that a solution for the PITM method is to have a time-dependent forcing similar to the analysis performed by Girimaji *et al.* [21] on the PANS method. This is not a study conducted in the current thesis. With the initial values, the decay of isotropic turbulence is performed without the frozen turbulence field. The energy spectra for the freely decaying isotropic turbulence at various time instances are shown in figure 3.3. For all three meshes agreement with the analytical spectra is good for the prescribed $\beta_0 = 2/(3C_\kappa) = 0.44$ coefficient, even for the smallest resolved scales also on the coarser grid resolution. Both the branches provide essentially similar results in decaying isotropic turbulence for this value of β_0. The inertial transfer zone for the energy cascade is very short for this case in comparison with standard inertial zones computed at higher Reynolds numbers. Firgure 3.5c is

Kang *et al.* test case

To further support this result and make sure that the EAHSM model can handle demanding LES (at larger Taylor Reynolds number and Δ/η ratio), the DIT of Kang *et al.* [32] is also simulated. In this case, the mesh size of the grid turbulence is $M = 152$ mm and the mean speed near the grid $U_0 = 11.2$ m.s^{-1}. The Taylor micro-scale Reynolds number measured at four different distances $tU_0/M = 20$, 30, 40 and 48 are $\mathrm{Re}_\lambda = 716$, 676, 650 and 626 respectively. Similar to the previous case, this can be recast for the simulation in terms of time advancement $t_0 = 0$, $t_1 = 10M/U_0$, $t_2 = 20M/U_0$ and $t_3 = 28M/U_0$ by applying Taylor's hypothesis. This computation is thus more challenging than the Comte-Bellot and Corrsin in terms of the SFS model, with a Reynolds number that is 10 times larger resulting in a larger inertial region. Numerical simulations are performed in a triply periodic box $[0, L]^3$ with $L = 2\pi$. Three different equidistant meshes are used, namely; 32^3 , 64^3 and 96^3 cells. The initial velocity field is prescribed according to the data measured at the first downstream position using the Random Fourier Method (RFM). Fig. 3.6 shows the comparison between the energy spectrum given by the analytical expression and the numerical result obtained using the RFM method for the 96^3 cells.

For the initialization phase, the convergence of k_s and the temporal evolution of the target and the observed kinetic energy ratio parameter are plotted in Fig. 3.7 again for the 96^3 cells. The results are not shown here for the 32^3 and 64^3 cases.
The computed three-dimensional energy spectra at times $t_0 = 0$, $t_1 = 10M/U_0$, $t_2 = 20M/U_0$ and $t_3 = 28M/U_0$ for the three resolutions are displayed in Fig. 3.8. Despite a larger Δ/η ratio, the agreement is good with the analytical spectra at all times for the three resolutions. Comparison

of the temporal evolution between the target and observed kinetic energy ratio parameter for the three resolutions is displayed in Figure. 3.9. For the 64^3 and 96^3 resolutions, the ratios are in good agreement whereas for the 32^3 there is a small difference. This shows that the EAHSM model is consistent and robust.

Figure. 3.10 shows the time decay of the turbulence for the total kinetic energy, the resolved energy and the subfilter kinetic energy in logarithmic coordinates. The total kinetic energy is the sum of the resolved energy and the subfilter kinetic energy. Thus the test seems to be quite satisfactory and gives credibility to the subgrid-scale version of the EAHSM model. It should be noted however that these values appear optimal for the numerical schemes utilized. From the above test cases, we can conclude that the value of the coefficient $\beta_0 = 2/(3C_\kappa)$ is a good estimate. This value for the model coefficient will remain fixed in the following simulations.

3.4.2 Fully developed turbulent Channel flow

Three dimensional simulations are performed for a fully developed channel flow at a moderate Reynolds number of $Re_\tau = 550$. The 3D geometry of the channel is shown in Figure. 2.3. The distance between the parallel walls of the channel is 2δ with the channel half width δ. Reference data is taken from the DNS of Moser *et al.* [51] at the bulk Reynolds number $Re_b = U_b\delta/\nu = 10000$ where

$$U_b = \frac{1}{2\delta}\int_{-\delta}^{\delta} U(y)\,dy$$

is the bulk velocity and $U(y)$ is the mean streamwise velocity corresponding to $Re_\tau = 550$.

The dimensions of the computational domain are $[0; 2\pi\delta] \times [0; \pi\delta] \times [0; 2\delta]$ in the streamwise, the spanwise and the wall-normal direction, respectively. The computational domain is small in comparison to the DNS ($[0; 8\pi\delta] \times [0; 3\pi\delta] \times [0; 2\delta]$) to reduce the computational cost. The dimensions are sufficiently large to resolve the largest structures of the flow.

Two mesh resolutions 'fine' and 'coarse' are chosen. The fine mesh corresponds to the 'guidelines' mesh requirement for a wall-resolved LES, usually with a $\Delta x^+ = 50$ and $\Delta y^+ = 20$ [63]. A coarse mesh is also considered to compare the predictive capability of EAHSM. The number of mesh points in the coarse mesh is half the number of mesh points in the fine mesh for the streamwise and spanwise directions. Mesh parameters are given in Table 3.2. In the streamwise and spanwise directions, the meshing is uniform with respectively N_x and N_y number of grid points whereas in the wall-normal direction, a non-uniform meshing is used according to the transformation:

$$\forall k \in [1, N_z]\,, z_k = \frac{\delta}{2}\left[1 + \frac{1}{a}\tanh\left[\left(-1 + \frac{2(k-1)}{N_z - 1}\right)\tanh^{-1}(a)\right]\right] \tag{3.65}$$

where the first dimensionless grid point location $z_2^+ = \frac{z_2 R_\tau}{\delta} = 0.5$. The wall-normal mesh distribution remains the same for both resolutions.

Periodic boundary conditions are applied on the streamwise and the spanwise directions. No-slip boundary condition is imposed at the walls whereas in the two homogeneous directions a periodic boundary condition is applied. Since the flow being investigated is fully established, two possible options exist to drive the flow. The first option follows prescribing a constant mass flow rate $Q = \rho U_b A$ at a given section. Here, A is the cross-sectional area of the channel. The bulk velocity U_b is calculated from the bulk Reynolds number. The second option to drive the flow is by prescribing a constant pressure gradient in the streamwise direction. The mean pressure gradient is directly related to the friction velocity u_τ at the wall given by [54]

$$\frac{dP}{dx} = \frac{u_\tau^2}{2\delta}$$

In all our simulations, a constant mass flow rate is fixed. The bulk Reynolds number is thus imposed, and the friction Reynolds number Re_τ is a part of the output of the simulation.
An initial velocity profile is prescribed by superimposing a synthetic field on the mean velocity according to:

$$\mathbf{v}(\mathbf{x}, 0) = (U(z), 0, 0) + \mathbf{v}'(\mathbf{x}, 0) \tag{3.66}$$

with the following law:

$$U^+ = \frac{1}{\kappa}\log(1+0.4z^+) + 7.8(1 - e^{-z^+/11} - \frac{z^+}{11}e^{-\mathbf{z}^+/3}), \tag{3.67}$$

where $U^+ = U(z)/u_\tau$ and $\mathbf{v}'(\mathbf{x},0)$ is a synthetic fluctuating contribution computed from the RFM method with an isotropic turbulent field specified by prescribing $k = k^+ * u_\tau^2$ with the turbulent length scale 1.5δ following the law

$$k^+ = 0.07e^{-z^+/8}(z^+)^2 + 4.5\frac{1 - e^{-z^+/20}}{1 + 4\frac{z^+}{Re_\tau}}, \tag{3.68}$$

conceding the turbulent fluctuations to immediately establish at the beginning of the simulation[11]. This allows one to have a shorter initial transient behavior, to have a fully developed turbulent flow. The initial conditions for the subfilter quantities are: $k_s = 0.1k$ along with a turbulent viscosity ratio $r = \nu_{t,s}/\nu = 10$.

The time step is chosen such that $\Delta t U_b/\Delta x = 0.25$. Time averaging is performed over a period of $60L_x/U_b \approx 21\delta/u_\tau$ after removing the initial time period of $20L_x/U_b \approx 7\delta/u_\tau$, for the flow to be established. At the end of the calculation the statistics are spatially averaged over the two homogeneous (streamwise and spanwise) directions. Computations were also done using the WALE model for both mesh resolutions, as a point of comparison. The results are made dimensionless using $z^+ = zu_\tau/\nu$, $t^+ = \nu/u_\tau^2$, $u^+ = u/u_\tau$ and $k^+ = k/u_\tau^2$.

A good starting point of comparison is by looking at the computed friction Reynolds number by the models. To find the friction Reynolds number, the friction velocity is first computed. The velocity at the wall is zero, respecting the no-slip condition. The velocity at the first node closest to the wall[7] is used to calculate the shear stress at the wall. The molecular viscosity (ν) plays the most important role in this region. The friction velocity is calculated using

$$u_\tau = \sqrt{\nu\frac{du}{dz}} \approx \sqrt{\nu\frac{u_2}{z}}$$

Friction Reynolds number is then calculated by $Re_\tau = u_\tau\delta/\nu$ and Table 3.3 summarizes the friction Reynolds number using the various models.

The mean streamwise velocity normalized by the computed friction velocity for the fine resolution is plotted in Figure. 3.11. From Table 3.3, we can infer that the friction Reynolds number computed by the WALE model is higher on the fine resolution. As a result, the mean-streamwise velocity at the center of the channel for the WALE model is lower. The turbulent kinetic energy has been plotted in Figure. 3.11. For the EAHSM model, it is the sum of the resolved and the subfilter kinetic energies has been plotted whereas only the resolved kinetic energy is represented for the WALE model. The EAHSM model shows a very good agreement with the DNS except in the center of the channel. The mean streamwise velocity and the total kinetic energy profiles for the coarse mesh are plotted in Figure. 3.12. The kinetic energy is overestimated by WALE on coarser meshes, which is a well known behavior that LES exhibits on coarse meshes. The kinetic energy is also slightly over-predicted by the EAHSM model.

The energy distribution between the resolved and modeled scales is examined for the EAHSM

[7] In the wall-normal direction.

Mesh	$N_x \times N_y \times N_z$	Δx^+	Δy^+	Δz_w^+ - Δz_c^+
coarse	$35 \times 43 \times 156$	100	40	0.5 - 15
fine	$69 \times 86 \times 156$	50	20	0.5 - 15
DNS [39]	-	8.9	5.0	0.019 - 4.5

TABLE 3.2. Channel flow simulations at $Re_\tau = 550$. N_x, N_y and N_z are the number of grid points along the streamwise, spanwise and the wall-normal directions, respectively. Δx^+ and Δy^+ are the grid spacings in viscous wall units along the streamwise and the spanwise direction, respectively and Δz_w^+ and Δz_c^+ are the grid spacing in the wall-normal direction at the wall and at the channel centerline.

	WALE	Model 1	Model 2
coarse	525	531	533
fine	567	546	547

TABLE 3.3. Channel flow simulations at $Re_\tau = 550$. Comparison of the computed friction Reynolds number Re_τ for the three models on the two grid resolution. Reference friction Reynolds number corresponds to $Re_\tau = 550$.

model by plotting the target and observed kinetic energy ratio parameters, shown in Figure. 3.13 (left). The figure reveals some important features about the SFS model and the formulation for the target kinetic energy ratio parameter. There is a considerable difference between the target and the observed ratios in the near-wall region. One probable reason could be regarding the high Reynolds number formulation of the model which strongly underestimated subfilter kinetic energy in this region. The subfilter model can be improved by using the low Reynolds number formulation through the introduction of the wall functions. Secondly, we know that at the wall, k_s is zero. Considering the observed r_k to be reliable, the target r_k can be overpredicted. Introducing a limiter for the subfilter length-scale in target r_k given by Eq. 3.48. This limiter will limit the lengthscale from going below the Kolmogorov lengthscales in this region, thereby reducing the target r_k. A different definition of the subgrid length-scale Δ in Eq. 3.48, should improve the near-wall behaviour of the models[66].

A good agreement with DNS results is obtained despite the use of a relatively coarse mesh for the calculations. These results are very similar in comparison to the ones obtained by Montecchia *et al.* [50] at this friction Reynolds number. The performance of the model can be better understood for flows at higher friction Reynolds number. The turbulence model is able to reproduce the correct near wall behavior in terms of the mean streamwise velocity and the position of the kinetic energy peak. Finally, we investigate the influence of the c_2 coefficient. We see no significant differences between the two values of the c_2 coefficient. In the logarithmic region of the flow, the model is functioning as a subfilter model and thus the influence of the subfilter model is less.

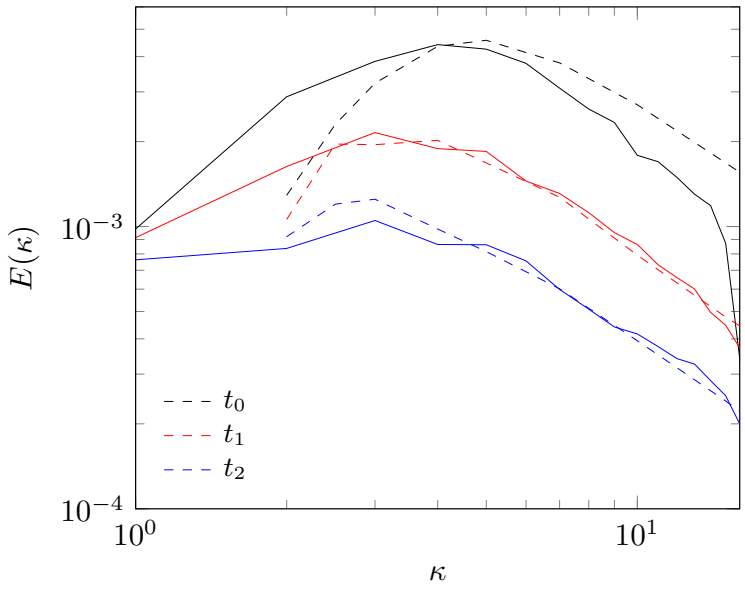

(A) 32^3

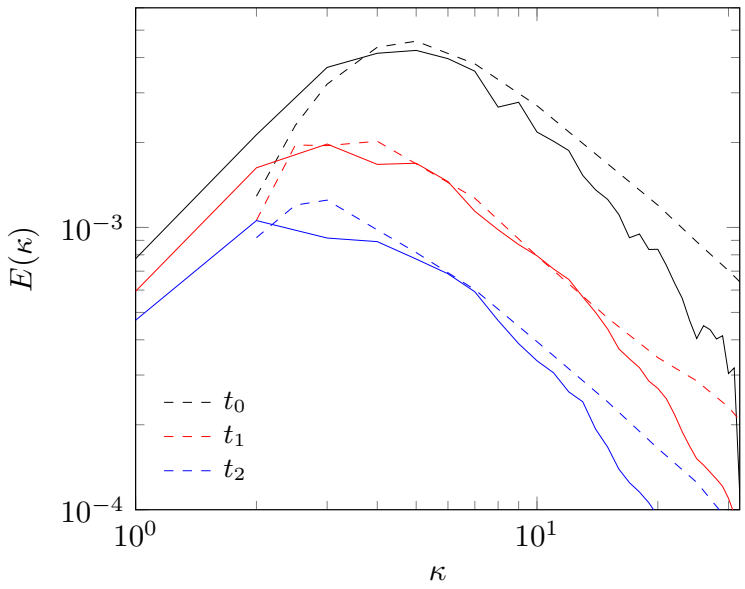

(B) 64^3

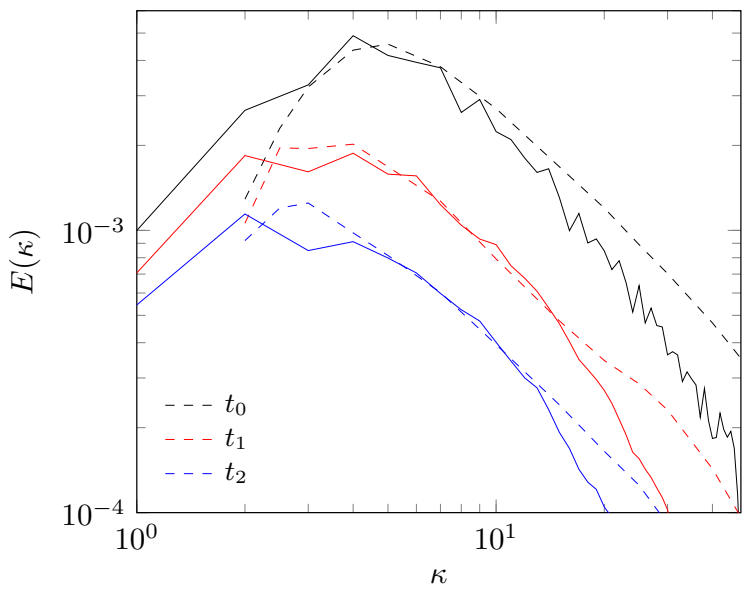

(C) 96^3

FIGURE 3.3 Comparison of the temporal evolution of the energy spectrum

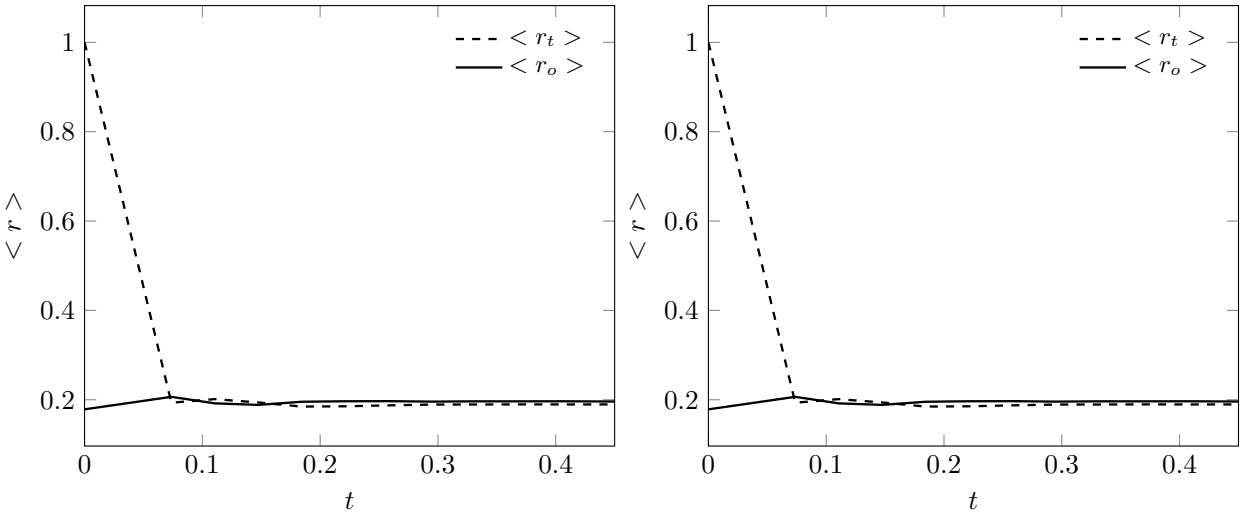

(A) 32^3

(B) 64^3

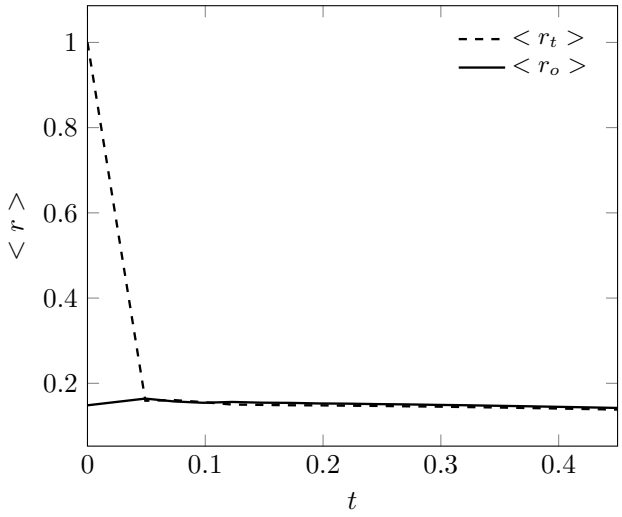

(C) 96^3

FIGURE 3.4. Temporal evolution: Comparison between the target $< r_t >$ and the observed $< r_0 >$ kinetic energy ratio parameter.

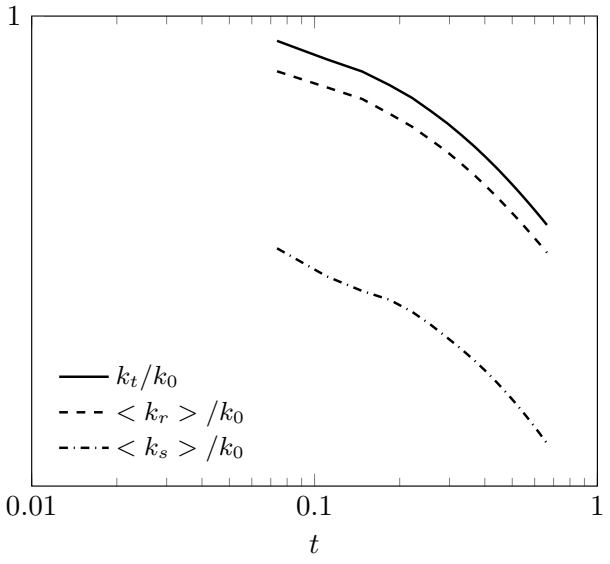

(A) 32^3

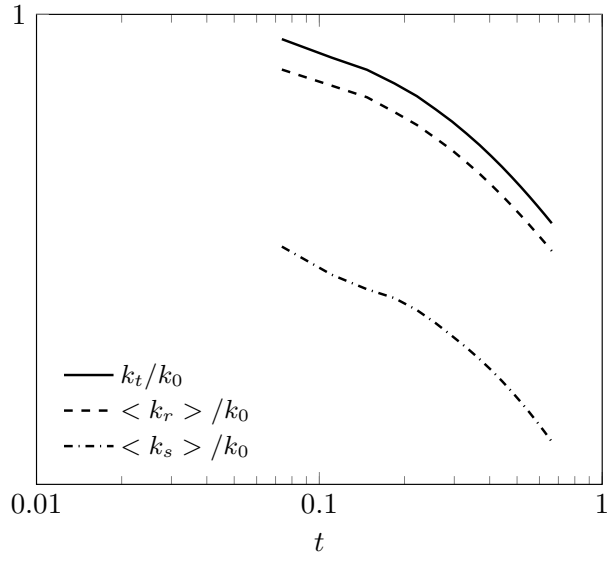

(B) 64^3

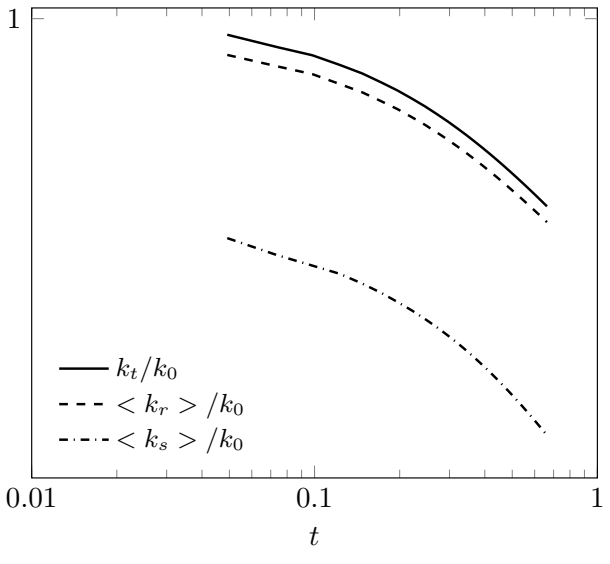

(C) 96^3

FIGURE 3.5. Temporal evolution: Comparison between the target and the observed kinetic energy ratio parameter. The total kinetic energy $k_t =< k_s >$

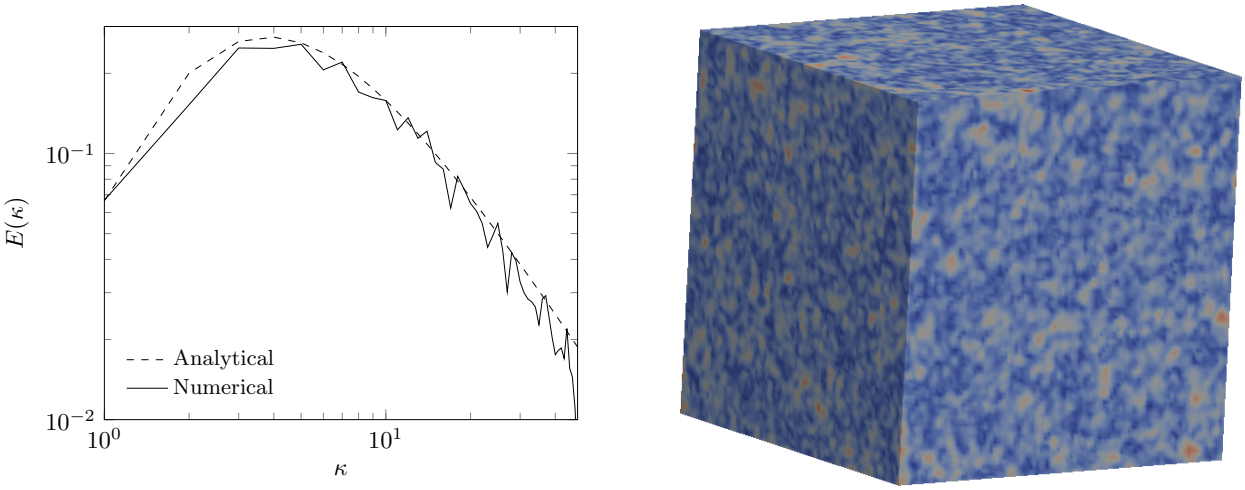

FIGURE 3.6. Initialization phase: Comparison between the constructed spectrum utilizing Equation.. and the numerical result obtained using the RFM method (Left). Norm of the vorticity vector (Right).

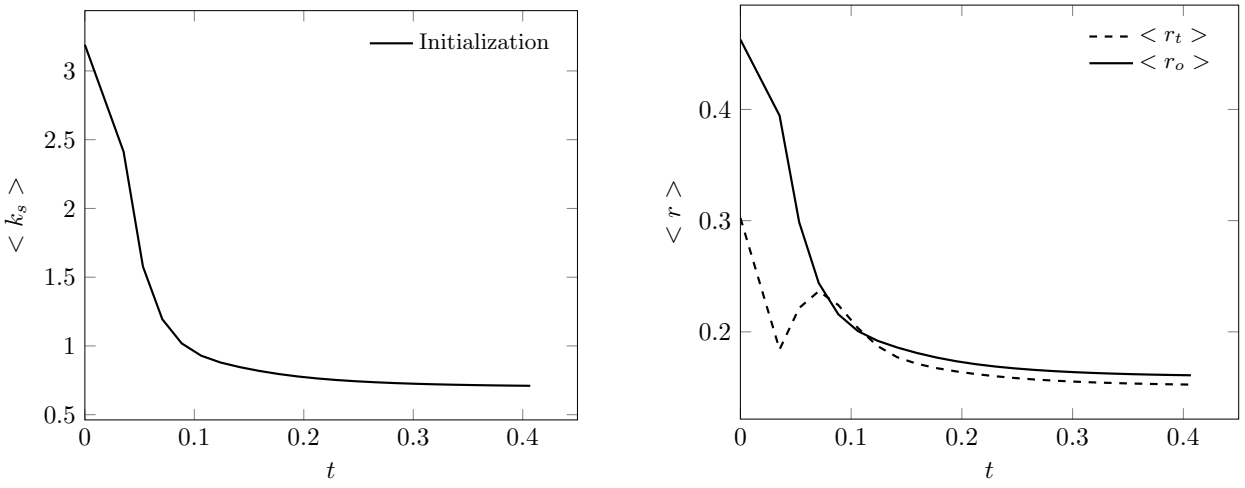

FIGURE 3.7. Initialization phase: Convergence of the volume-averaged sub-filter kinetic energy (Left) and a comparison between the volume averaged target and the observed kinetic energy ratio parameters (Right).

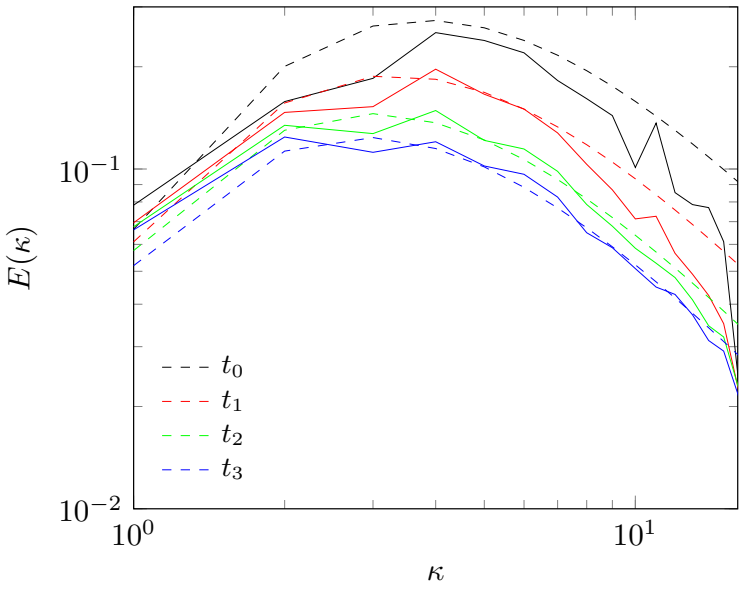

(A) 32^3

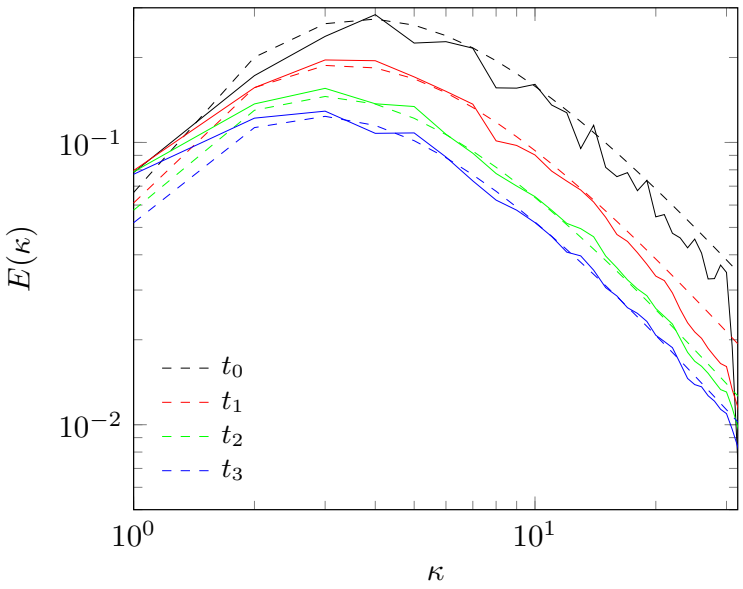

(B) 64^3

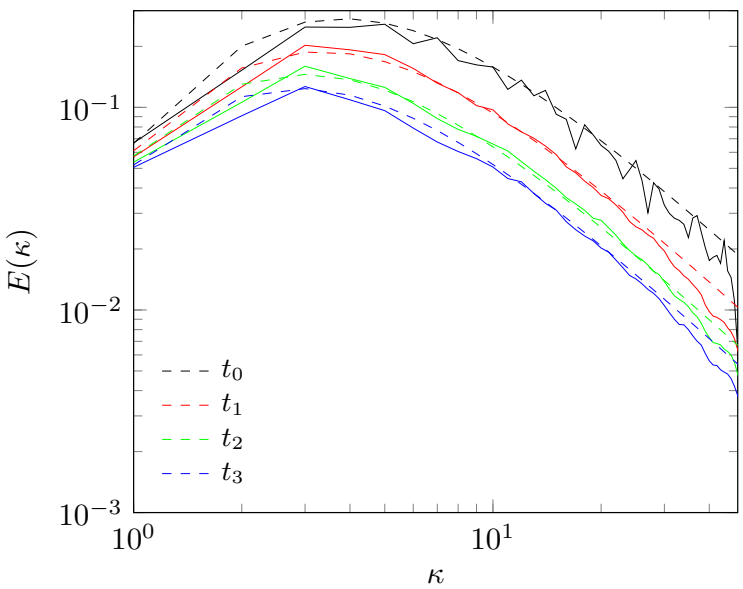

(C) 96^3

FIGURE 3.8 Comparison of the temporal evolution of the energy spectrum

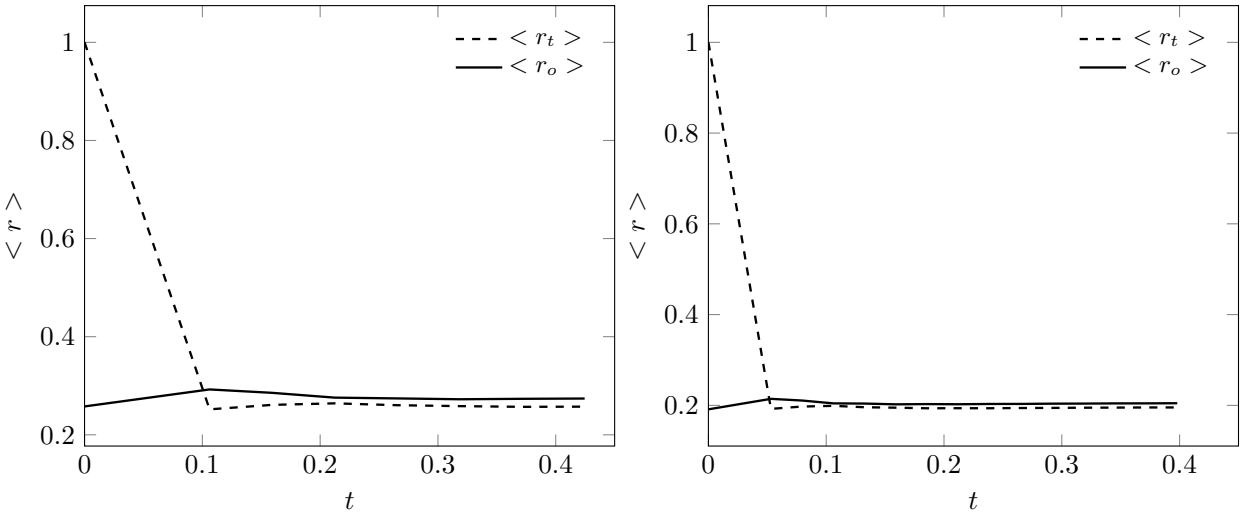

(A) 32^3

(B) 64^3

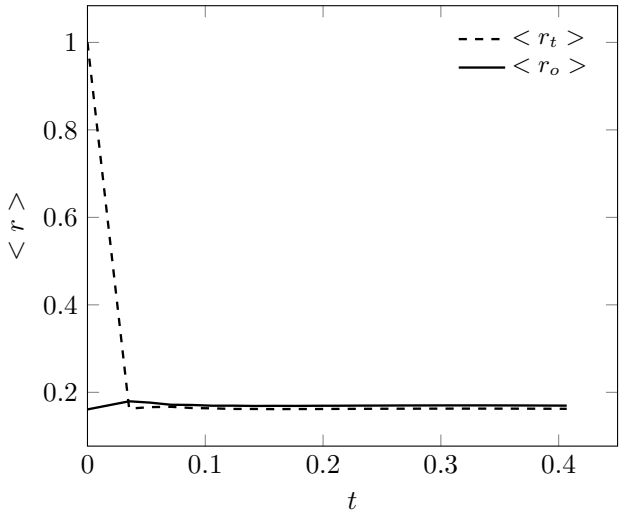

(C) 96^3

FIGURE 3.9. Temporal evolution: Comparison between the target $< r_t >$ and the observed $< r_0 >$ kinetic energy ratio parameter.

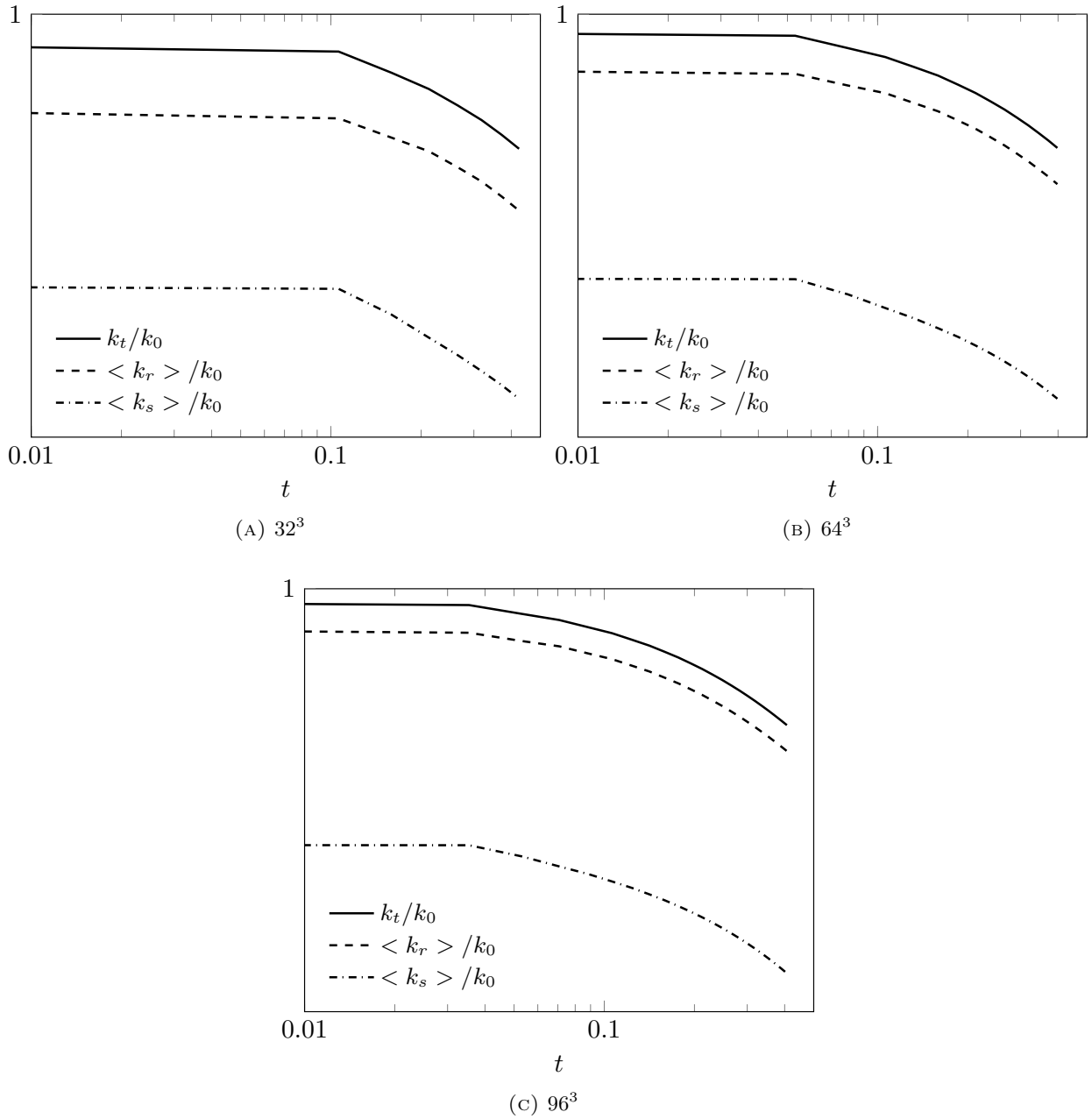

(A) 32^3 (B) 64^3

(C) 96^3

FIGURE 3.10. Temporal evolution: Comparison between the target and the observed kinetic energy ratio parameter. The total kinetic energy $k_t =< k_s > + < k_r >$

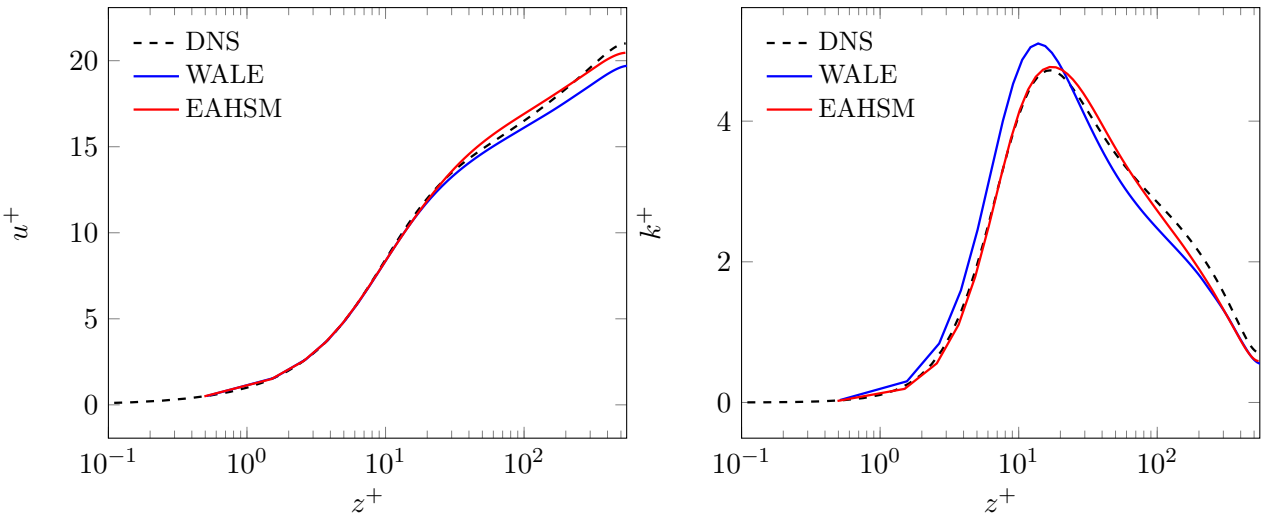

FIGURE 3.11. Periodic channel flow simulation at $Re_\tau = 550$. Fine mesh simulation results obtained from WALE and EAHSM are plotted against the DNS. Profile of the mean streamwise velocity (left). Profile of the total turbulent kinetic energy k_t (right).

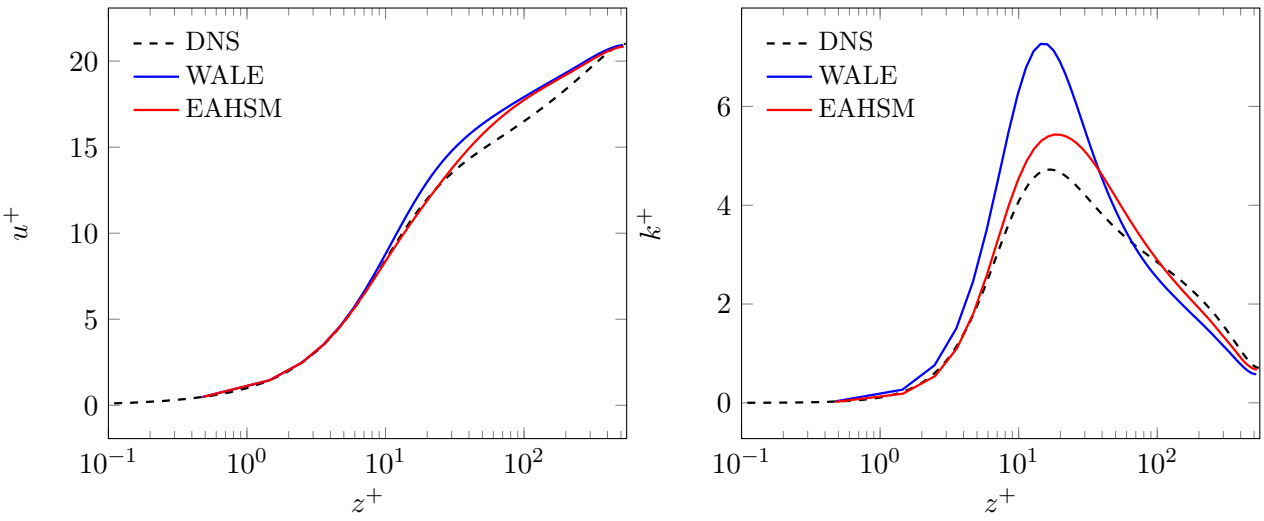

FIGURE 3.12. Periodic channel flow simulation at $Re_\tau = 550$. Coarse mesh simulation results obtained from WALE and EAHSM are plotted against the DNS. Profile of the mean streamwise velocity (left). Profile of the total turbulent kinetic energy k_t (right).

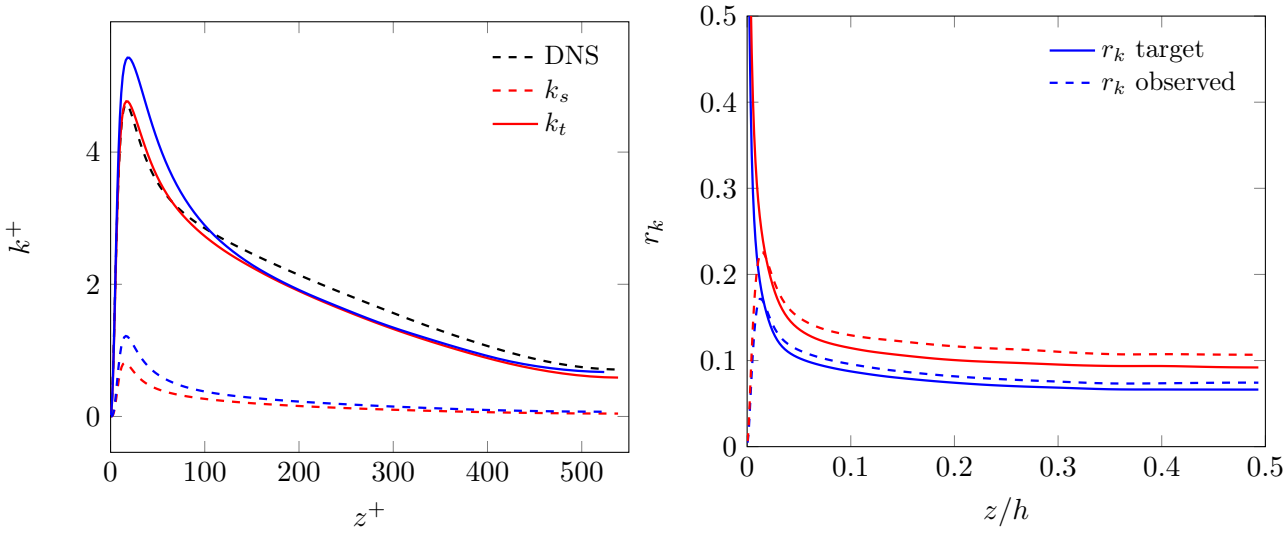

FIGURE 3.13. Periodic channel flow simulation at $Re_\tau = 550$. The profiles of the total and subfilter kinetic energy (left) and target and the observed kinetic energy ratio (right) plotted for the fine (red) and coarse (blue) meshes.

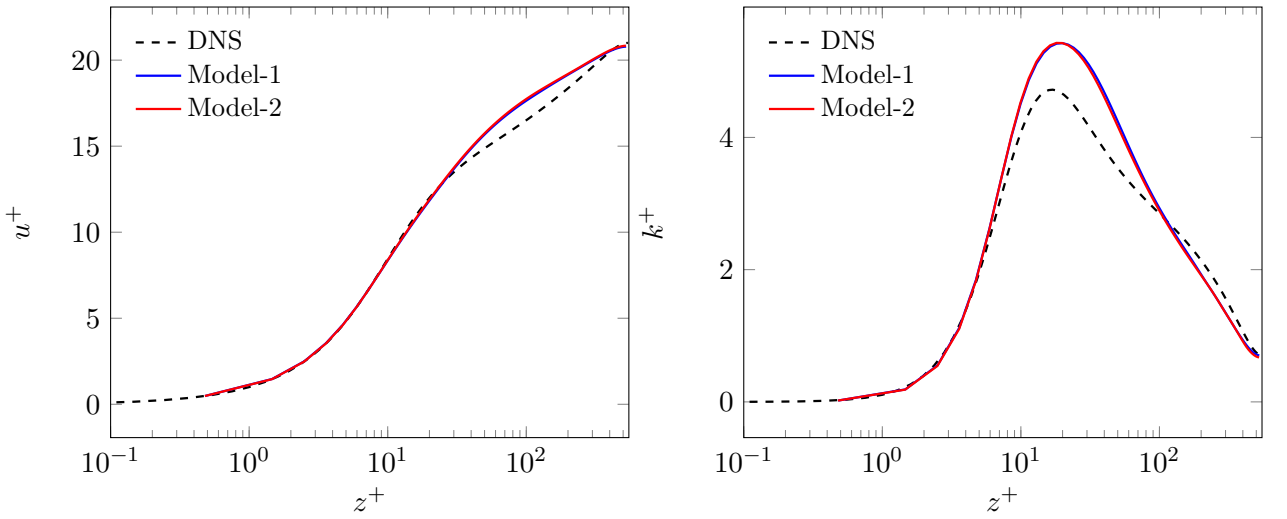

FIGURE 3.14. Periodic channel flow simulation at $Re_\tau = 550$. Profile of the mean streamwise velocity (left). Profile of the total turbulent kinetic energy k_t (right) plotted for the original value of $c_2 = 5/9$ (Model 1) and the modified value $c_2 = 0.539166$ (Model 2).

3.4.3 Fully developed turbulent flow in a Square Pipe

The test case of the fully developed turbulent flow in a square duct constitutes an illustrative case for which the anisotropy between the Reynolds stress components is present and influences the mean flow. In this case, the anisotropy leads to a secondary flow that greatly modifies both the shear stress and the heat transfer at the walls. This may also lead to an increase in the turbulent mixing when dealing for instance with passive scalar transport or variable density flows.

Numerical simulations are performed here in a domain $[0; 2\pi D] \times [0; D] \times [0; D]$ where D is the duct width. Numerical results are compared with direct numerical simulations performed by Huser and Biringer [27] and Zhang *et al.* [89]. The Reynolds number Re_τ based on the friction velocity u_τ and the duct width D is 600 which corresponds approximately to the bulk Reynolds number $\mathrm{Re}_b = u_b D/\nu$ of 10500.

Two meshes are used namely, 'fine' and 'coarse'. As the friction Re_τ for this case is close to the friction Reynolds number for the turbulent channel flow, we consider the same numerical parameters in the streamwise and the two wall-normal directions, given in Table. 3.4. The first dimensionless grid point location in the wall-normal direction is set to $z_2^+ = 1$ using the transformation given for the Channel flow. The coarse mesh has half the number of grid points in the streamwise alone. A Periodic boundary condition is prescribed in the streamwise direction and a no-slip condition is imposed on the four walls. Like for the channel flow. The flow is sustained by prescribing a constant mass flow rate at a cross-section. A synthetic fluctuating field is superimposed on the initial velocity profile using the RFM method, Eqs. 3.66-3.67. An isotropic field is initiated by prescribing $k = k^+ * u_\tau^2$ where k^+ follows the law Eqs. 3.68 along with the turbulent length scale $3D/4$. The initial conditions for the subfilter quantities are: $k_s = 0.1k$ along with a turbulent viscosity ratio $r = \nu_{t,s}/\nu = 10$.

The time step is chosen such that $\Delta t U_b/\Delta x = 0.25$. Time averaging is performed over a period of $200L_x/U_b$ after removing the initial time period of $100L_x/U_b$, for the flow to be established. At the end of the calculation the statistics are spatially averaged along the homogeneous direction. We believe that this should not affect many of the conclusions of this study, except for the secondary flow. The results are made dimensionless using $z^+ = zu_\tau/\nu$, $u^+ = u/u_\tau$, $v^+ = v/u_\tau$.

The friction Reynolds number computed using the friction velocity at the wall on the wall bisector for various models is shown in Table. 3.5. The results presented below focus on the mean streamwise velocity component u and the mean spanwise velocity component v along a corner bisector $y = z$. For the fine mesh results presented in Figure. 3.15, both models have a similar behavior. Both EAHSM and WALE are able to predict the increase in the streamwise velocity near the corner. On the coarse mesh, the EAHSM results are closer to the DNS of Huser & Biringen [27]. The mesh parameters used in the DNS of Huser & Biringen [27] corresponds to a poorly resolved DNS [89]. As the mesh is coarsened, there is an increase in the level of the total kinetic energy.

The secondary flow contours are plotted across a cross-section in Figures. 3.17 and 3.18. A fair degree of symmetry over the quadrants has been obtained but to achieve complete symmetry, a larger sample size for averaging would be necessary for the strength of the secondary velocity is weak. The energy distribution between the resolved and modeled scales is examined for the EAHSM model by plotting the target and observed kinetic energy ratio parameters, shown in Figure. 3.13. There seems to be a slight difference between the two meshes.

Mesh	$N_x \times N_y \times N_z$	Δx^+	Δz_w^+ - Δz_c^+
coarse	$38 \times 98 \times 98$	100	1 - 13
fine	$75 \times 98 \times 98$	50	1 - 13
DNS [27]	$96 \times 100 \times 100$	–	–
DNS [89]	$320 \times 256 \times 256$	11.78	0.216 - –

TABLE 3.4. Simulation on a fully developed flow in a square pipe at $Re_\tau = 600$. Numerical parameters for the two meshes.

	WALE	Model 1	Model 2
coarse	634	613	612
fine	601	591	

TABLE 3.5. Simulation on a fully developed flow in a square pipe at $Re_\tau = 600$. Comparison of the computed friction Reynolds number Re_τ for the three models on the two grid resolution. Reference friction Reynolds number corresponds to $Re_\tau = 600$.

Finally, we investigate the influence of the c_2 coefficient. We see no significant differences in the mean streamwise velocity profile for the two c_2 values (Figure 3.20). For the secondary velocity profile, some differences are seen between the two values for c_2. Since the secondary flow is weak, the convergence of the secondary flow statistics is not yet achieved.

3.5 Conclusion

Main concepts of seamless hybrid RANS/LES methods relevant to the present work were looked upon. Starting from the $k_s - \epsilon_s$ version of E-DES for which the hybrid equivalence has been provided, the derivation of a k_s-ω_s based E-DES has been performed. Menter's blending function is used to obtain a E-DES BSL-like model. Presuming the weak-equilibrium assumption to be verified for the subfilter scales, explicit algebraic closure developed in the previous chapter is coupled with the E-DES based on Menter's BSL-like model.

The calibration of the EAHSM model concerning its model coefficient is done on the decay of isotropic turbulence. Following which tests are performed on the fully developed channel flow and the fully developed flow in a pipe of square cross-section for two grids: fine and coarse. On coarser grids, EAHSM performs fairly better than the WALE model. It has been observed that the target and the observed kinetic energy ratio parameters behave differently close to the wall. Moving towards a low-Reynolds number formulation for the subfilter model and the explicit algebraic relations can be helpful.

In the following chapter, the developed EARSM in chapter 2 and the EAHSM model presented in this chapter will be extended to variable density flows.

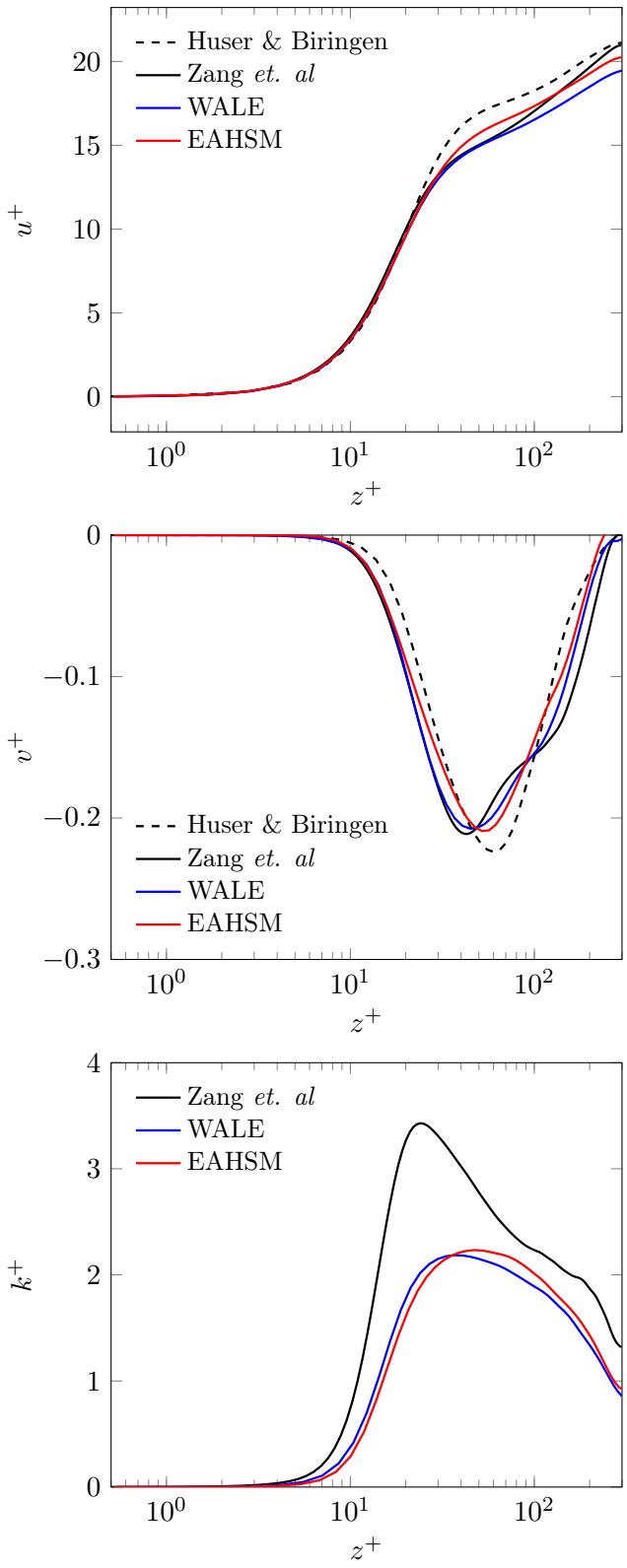

FIGURE 3.15. Periodic flow in a square pipe at $\mathrm{Re}_\tau = 600$. Fine mesh simulation results obtained using WALE and EAHSM.

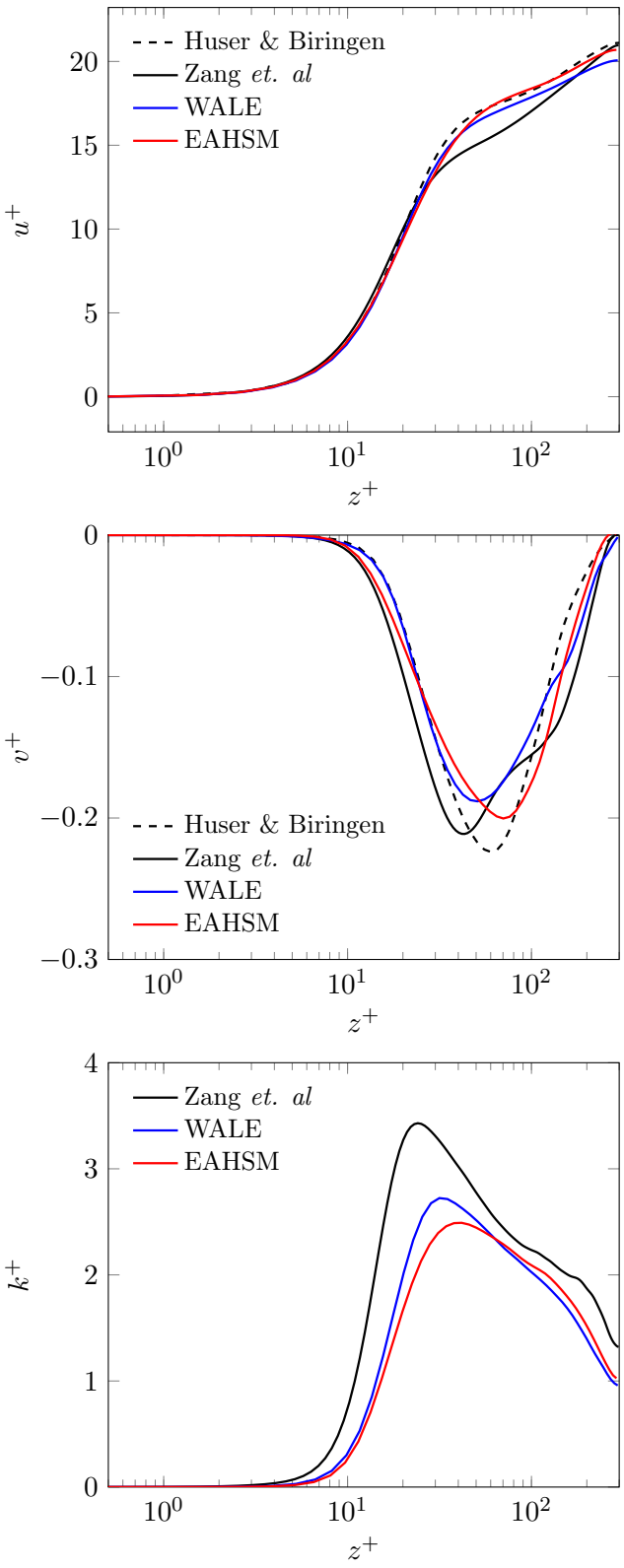

FIGURE 3.16. Periodic flow in a square pipe at $\mathrm{Re}_\tau = 600$. Coarse mesh simulation results obtained using WALE and EAHSM.

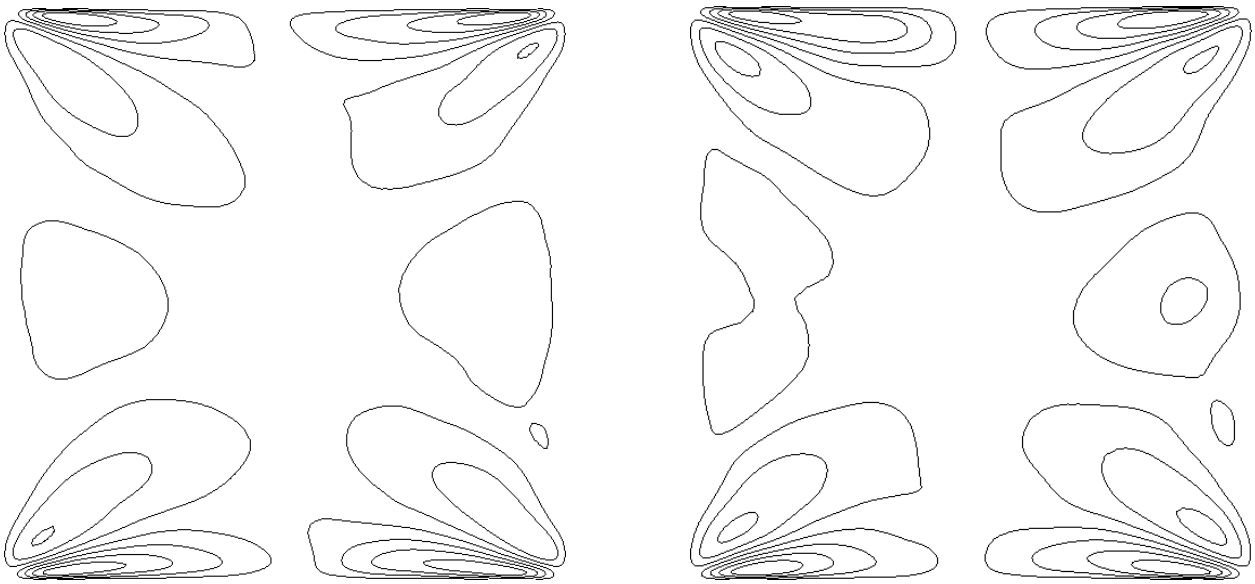

(A) WALE fine (B) EAHSM fine

FIGURE 3.17. Secondary velocity isotachs for the fine mesh.

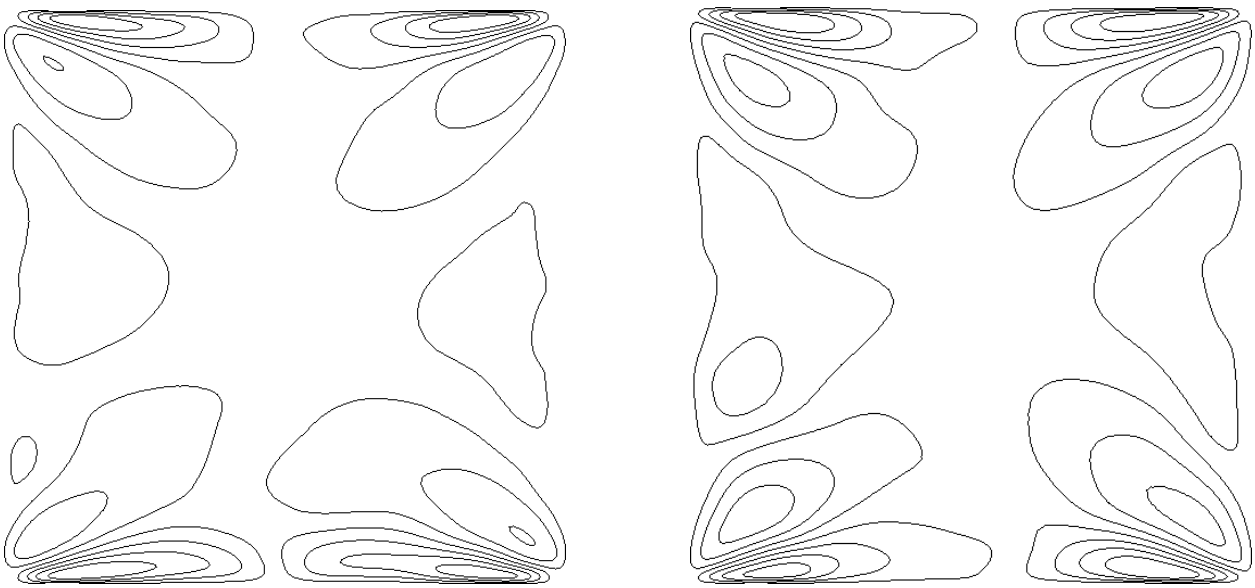

(A) WALE coarse (B) EAHSM coarse

FIGURE 3.18. Secondary velocity isotachs for the coarse mesh

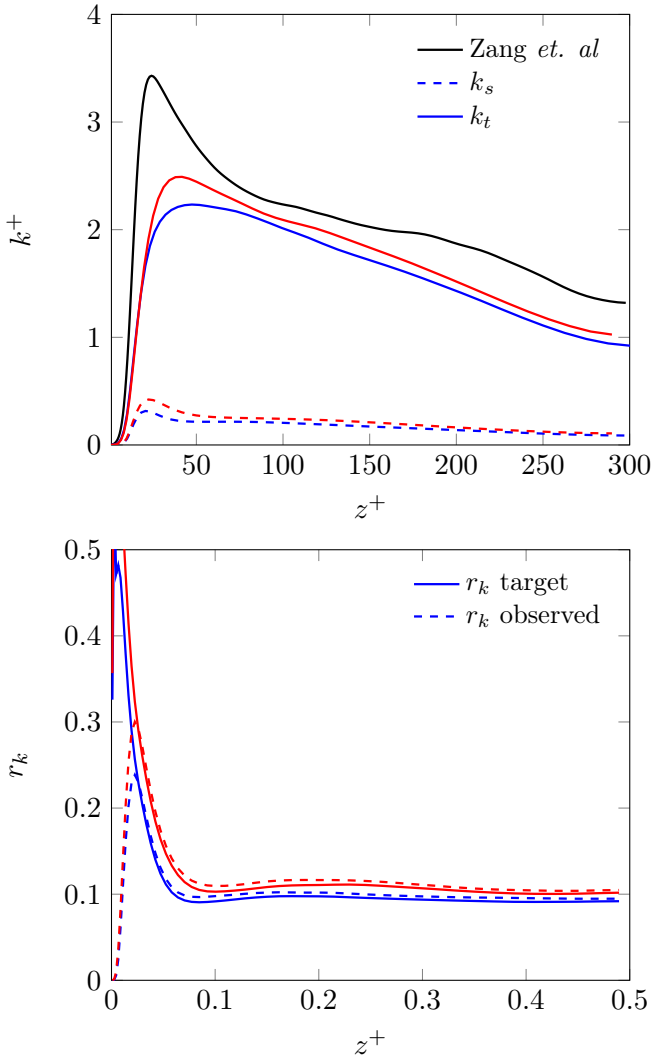

FIGURE 3.19. Fully Developed square duct flow simulation at $Re_\tau = 600$. The profiles of the total and subfilter kinetic energy (top) and target and the observed kinetic energy ratio (bottom) plotted for the fine (red) and coarse (blue) meshes.

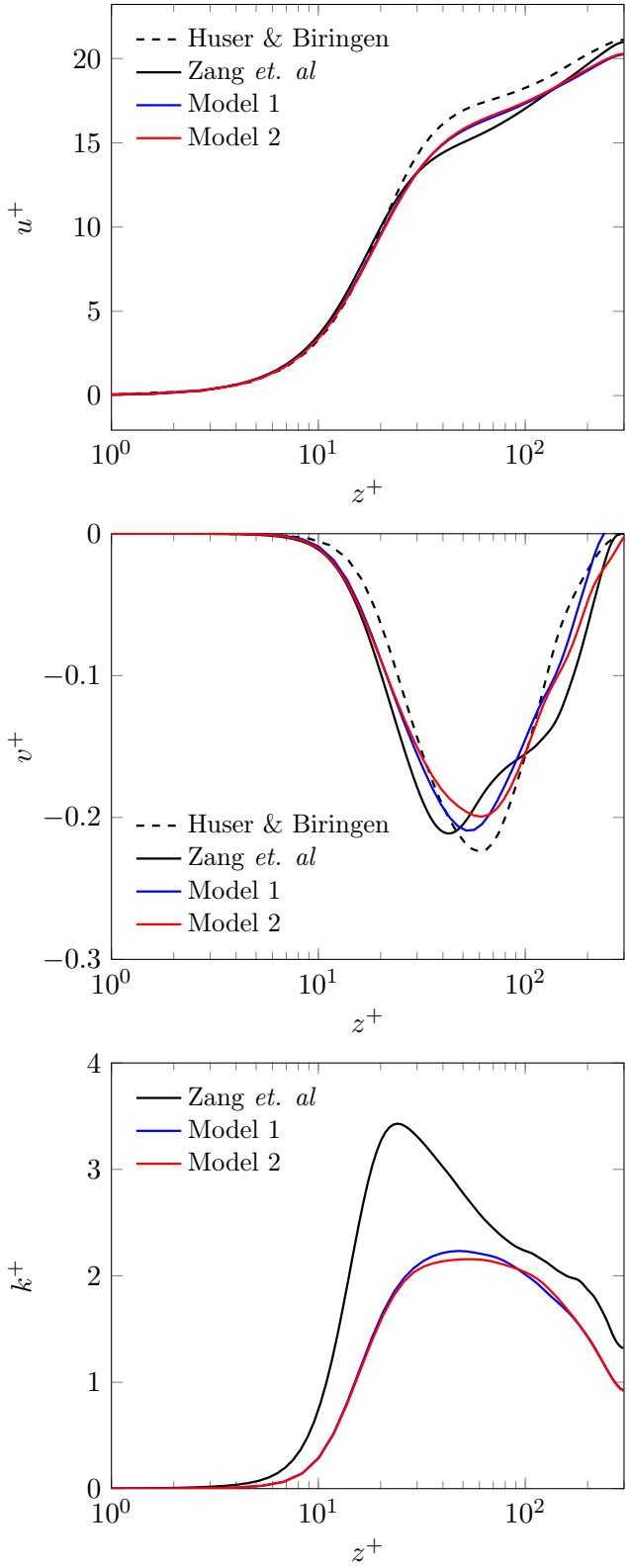

FIGURE 3.20. Fully Developed square duct flow simulation at $Re_\tau = 600$. Profiles of the streamwise and transverse velocities and total turbulent kinetic energy k_t (right) plotted for the original value of $c_2 = 5/9$ (Model 1) and the modified value $c_2 = 0.539166$ (Model 2).

Chapter 4

Extension to variable density flows

In this chapter, we extend the EAHSM model described in Chapter 3 to variable density flows. We restrict in this first step to slightly variable density flows for which the Boussinesq approximation is assumed to be valid. As previously, we first present the derivation of the explicit algebraic model in the RANS framework for both the Reynolds stresses and the scalar flux following a direct solution of the implicit algebraic relationships. The nonlinearity of the coupled expressions for the algebraic expressions is treated through an efficient iteration solution method. The resulting explicit algebraic approach is then extended to the seamless hybrid RANS-LES framework following the same route as presented in Chapter 3. Both the RANS and hybrid RANS-LES algebraic models are assessed in the case of a stable stratification, on the homogeneous mean shear flow and the fully developed channel flow.

4.1 Explicit algebraic Reynolds-stress and scalar flux model

We address in this section explicit algebraic modeling of turbulent fluxes for variable density flows with buoyancy. We restrict in this work to small density differences for which the Boussinesq approximation is assumed to be valid. Using such an approximation, effects of varying density due to temperature or concentration are neglected everywhere in the transport equations except in the buoyancy force. While such a description is restricted to small density differences, this is illustrative of the coupling between momentum and density induced by buoyancy. The resulting transport equations read:

$$\frac{\partial u_i}{\partial x_i} = 0 \tag{4.1}$$

$$\frac{\partial u_i}{\partial t} + u_j \frac{\partial u_i}{\partial x_j} = -\frac{\partial p}{\partial x_i} + \nu \frac{\partial^2 u_i}{\partial x_j \partial x_j} + \varrho(\theta) g_i \tag{4.2}$$

$$\frac{\partial \theta}{\partial t} + u_j \frac{\partial \theta}{\partial x_j} = \kappa \frac{\partial^2 \theta}{\partial x_j \partial x_j} \tag{4.3}$$

where u_i is the velocity field, p the pressure, g_i the gravitational acceleration, κ refers to a molecular diffusivity (heat or species) and θ denotes a scalar that causes density differences. In Eq. 4.2, $\varrho(\theta)$ corresponds to a reduced density variation with respect to a reference state and is defined by

$$\varrho(\theta) = 1 - \beta_\theta \left(\theta - \theta_0\right) \tag{4.4}$$

where β_θ is the expansion coefficient (thermal or compositional). As the transport equation for the scalar is coupled to the momentum transport equation through buoyancy, this refers to an active

scalar. This contrasts with the passive scalar case for which there is no coupling and the scalar is simply advected by the flow.

By using the Reynolds decomposition, $u_i = \overline{u}_i + u_i'$, $p = \overline{p} + p'$ and $\theta = \overline{\theta} + \theta'$ in Eqs. 4.1-4.3 and then taking the average, one arrives at the following Reynolds-averaged version of the governing equations:

$$\frac{\partial \overline{u}_i}{\partial x_i} = 0 \tag{4.5}$$

$$\frac{\partial \overline{u}_i}{\partial t} + \overline{u}_j \frac{\partial \overline{u}_i}{\partial x_j} = -\frac{\partial \overline{p}}{\partial x_i} + \frac{\partial}{\partial x_j}\left(\nu \frac{\partial \overline{u}_i}{\partial x_j} - \overline{u_i' u_j'}\right) + \varrho(\overline{\theta}) g_i \tag{4.6}$$

$$\frac{\partial \overline{\theta}}{\partial t} + \overline{u}_j \frac{\partial \overline{\theta}}{\partial x_j} = \frac{\partial}{\partial x_j}\left(\kappa \frac{\partial \overline{\theta}}{\partial x_j} - \overline{u_j' \theta'}\right) \tag{4.7}$$

where $\varrho(\overline{\theta})$ denotes the reduced averaged density defined by

$$\varrho(\overline{\theta}) = 1 - \beta_\theta \left(\overline{\theta} - \theta_0\right) \tag{4.8}$$

Two terms involving the correlations between the velocity and scalar fluctuations appear. We recall that $\overline{u_i' u_j'}$ correspond the Reynolds stresses. Similarly, $\overline{u_j' \theta'}$ corresponds the turbulent scalar flux arising by the interaction of velocity and fluctuations in the scalar. Both these quantities remain unknown, making the set of equations incomplete.

4.1.1 Transport equation for the turbulent fluxes

As for the Reynolds stresses, one can derive transport equations for the turbulent mass flux. The derivation is not repeated here as it can be found elsewhere. The obtained transport equations for the turbulent fluxes $\overline{u_i' u_j'}$ and $\overline{u_i' \theta'}$ read

$$\frac{\partial \overline{u_i' u_j'}}{\partial t} + \overline{u}_k \frac{\partial \overline{u_i' u_j'}}{\partial x_k} - \mathcal{D}_{ij} = \mathcal{P}_{ij} + \Pi_{ij} - \varepsilon_{ij} + \mathcal{G}_{ij} \tag{4.9}$$

$$\frac{\partial \overline{u_i' \theta'}}{\partial t} + \overline{u}_k \frac{\partial \overline{u_i' \theta'}}{\partial x_k} - \mathcal{D}_{\theta i} = \mathcal{P}_{\theta i} + \Pi_{\theta i} - \varepsilon_{\theta i} + \mathcal{G}_{\theta i} \tag{4.10}$$

where $\mathcal{D}_{\theta i}$, $\mathcal{P}_{\theta i}$, $\Pi_{\theta i}$ and $\varepsilon_{\theta i}$ refer respectively to diffusion, production, pressure redistribution and dissipation of the active scalar turbulent flux. Compared with the passive scalar case, taking into account buoyancy leads to an additional contribution in the transport equation for the turbulent fluxes, namely $\mathcal{G}_{ij}$ in Eq. 4.9 for the Reynolds stresses and $\mathcal{G}_{\theta i}$ in Eq. 4.10 for the turbulent scalar flux. The production term for the Reynolds stresses remains unchanged compared with its expression given in chapter 2 while the production term for the turbulent scalar flux has the following form:

$$\mathcal{P}_{\theta i} = -\overline{u_i' u_k'} \frac{\partial \overline{\theta}}{\partial x_k} - \overline{u_k' \theta'} \frac{\partial \overline{u}_i}{\partial x_k} \tag{4.11}$$

The additional terms in the right hand side of the transport equations for the turbulent fluxes correspond to buoyancy terms that are expressed as

$$\mathcal{G}_{ij} = -\beta_\theta \left(g_i \overline{u_j' \theta'} + g_j \overline{u_i' \theta'}\right), \quad \mathcal{G}_{\theta i} = -2\beta_\theta k_\theta g_i \tag{4.12}$$

where $k_\theta = \frac{1}{2}\overline{\theta'^2}$ is half the scalar variance. For the pressure redistribution term Π_{ij}, the LRR model given in Eq. 1.38 is utilized to which an additional term representing the buoyancy contribution is added [34]

$$\begin{aligned}\Pi_{ij} = &- c_1\frac{\varepsilon}{k}\left(\overline{u_i'u_j'} - \frac{2}{3}k\delta_{ij}\right) - \frac{c_2+8}{11}\left(\mathcal{P}_{ij} - \frac{1}{3}\mathcal{P}_{kk}\delta_{ij}\right) - \frac{30c_2-2}{55}k\left(\frac{\partial\overline{u}_i}{\partial x_j} + \frac{\partial\overline{u}_j}{\partial x_i}\right)\\ &- \frac{8c_2-2}{11}\left(-\overline{u_i'u_k'}\frac{\partial\overline{u}_k}{\partial x_j} - \overline{u_j'u_k'}\frac{\partial\overline{u}_k}{\partial x_i} - \frac{1}{3}\mathcal{P}_{kk}\right) - c_g\left(\mathcal{G}_{ij} - \frac{1}{3}\mathcal{G}_{kk}\delta_{ij}\right)\end{aligned} \tag{4.13}$$

where $k = \overline{u_i'u_i'}/2$ is the turbulent kinetic energy and $\varepsilon = \varepsilon_{ii}/2$ is the dissipation rate. c_1, c_2 and c_g are model coefficients that need to be specified. As in chapter 2, the dissipation rate tensor is assumed to be isotropic and follows Eq. 1.36. The pressure scalar gradient correlation $\Pi_{\theta i}$ and the dissipation vector $\varepsilon_{\theta i}$are modelled as

$$\begin{aligned}\Pi_{\theta i} - \varepsilon_{\theta i} = &- \left(c_{\theta 1} + c_{\theta 5}\frac{k}{\varepsilon k_\theta}\overline{u_k'\theta'}\frac{\partial\overline{\theta}}{\partial x_k}\right)\frac{\varepsilon}{k}\overline{u_i'\theta'}\\ &+ c_{\theta 2}\overline{u_k'\theta'}\frac{\partial\overline{u}_i}{\partial x_k} + c_{\theta 3}\overline{u_k'\theta'}\frac{\partial\overline{u}_k}{\partial x_i} + c_{\theta 4}\overline{u_i'u_k'}\frac{\partial\overline{\theta}}{\partial x_k} + c_{\theta g}\beta_\theta k_\theta g_i\end{aligned} \tag{4.14}$$

where $c_{\theta 1}$, $c_{\theta 2}$, $c_{\theta 3}$, $c_{\theta 4}$, $c_{\theta 5}$, c_g and $c_{\theta g}$ are again the model constants that remain to be specified.

The transport equations for the turbulent kinetic energy k and the scalar variance $2k_\theta$ are obtained from the previous transport equations for the Reynolds stresses and the turbulent scalar flux respectively and read

$$\frac{dk}{dt} - \mathcal{D} = \mathcal{P} - \varepsilon + \mathcal{G} \tag{4.15}$$

$$\frac{dk_\theta}{dt} - \mathcal{D}_\theta = \mathcal{P}_\theta - \varepsilon_\theta \tag{4.16}$$

Here again, as for the Reynolds stresses, taking into account buoyancy leads to the additional term $\mathcal{G}$ in the transport equation for the turbulent kinetic energy. This additional term corresponds to half the trace of Eq. 4.9 and reads

$$\mathcal{G} = \frac{1}{2}\mathcal{G}_{kk} = -\beta_\theta g_k\overline{u_k'\theta'} \tag{4.17}$$

Moving to the transport equation for the scalar variance Eq. 4.16, the first term on the right hand side corresponds to the production term that reads

$$\mathcal{P}_\theta = -\overline{u_k'\theta'}\frac{\partial\overline{\theta}}{\partial x_k} \tag{4.18}$$

The last term on the right hand side in Eq. 4.16 refers to the dissipation term and we follow here [37] by prescribing the ratio $r_\tau = \tau_\theta/\tau$ which corresponds to the ratio of the scalar turbulence time scale, $\tau_\theta = k_\theta/\varepsilon_\theta$, and the characteristic eddy turn over time scale $\tau = k/\varepsilon$. This allows to avoid the need in solving an additional transport equation for the dissipation ε_θ by using the algebraic relation:

$$\varepsilon_\theta = \frac{k_\theta}{r_\tau\tau} \tag{4.19}$$

We will follow here the same methodology described in chapter 2 to deal with the diffusion term $\mathcal{D}_\theta$.

In order to introduce the weak equilibrium assumption for both the Reynolds stresses and the turbulent scalar flux, starting from the previous transport equations for the turbulent fluxes we first need to write transport equations for the corresponding normalized fluxes. We look into details in the following section.

4.1.2 Transport equation for the dimensionless turbulent fluxes

As for the Reynolds stresses, the first step consists thus in writing a transport equation for the normalized scalar flux ξ_i defined by

$$\xi_i = \frac{\overline{u_i'\theta'}}{\sqrt{k k_\theta}} \tag{4.20}$$

Introducing the dimensionless anisotropy tensor a_{ij} in Eq. 4.9 and the normalized scalar flux ξ_i in Eq. 4.10, the transport equations for these quantities read

$$\frac{da_{ij}}{dt} - \frac{1}{k}\left(\mathcal{D}_{ij} - \frac{\overline{u_i'u_j'}}{k}\mathcal{D}\right) = \frac{1}{k}\left(\mathcal{P}_{ij} + \Pi_{ij} - \frac{2}{3}\varepsilon\delta_{ij} + \mathcal{G}_{ij} - \frac{\overline{u_i'u_j'}}{k}\left(\mathcal{P} - \varepsilon + \mathcal{G}\right)\right) \tag{4.21}$$

$$\begin{aligned}\frac{d\xi_i}{dt} - \frac{1}{\sqrt{k k_\theta}}&\left(\mathcal{D}_{\theta i} - \frac{\overline{u_i'\theta'}}{2}\left(\frac{\mathcal{D}}{k} + \frac{\mathcal{D}_\theta}{k_\theta}\right)\right) \\ &= \frac{1}{\sqrt{k k_\theta}}\left(\mathcal{P}_{\theta i} + \Pi_{\theta i} - \varepsilon_{\theta i} + \mathcal{G}_{\theta i} - \frac{\overline{u_i'\theta'}}{2}\left(\frac{\mathcal{P} - \varepsilon + \mathcal{G}}{k} + \frac{\mathcal{P}_\theta - \varepsilon_\theta}{k_\theta}\right)\right)\end{aligned} \tag{4.22}$$

Using the weak-equilibrium assumption, both the advection and diffusion terms will be neglected. In this manner, we will be able to find a system of algebraic equations for the coupled system.

4.1.3 Weak equilibrium assumptions

Using the weak-equilibrium assumption for both the dimensionless anisotropy tensor a_{ij} and the normalized scalar flux ξ_i, the left-hand side of the previous transport equations are removed and the resulting algebraic equations read

$$\frac{\overline{u_i'u_j'}}{k}\left(\mathcal{P} - \varepsilon + \mathcal{G}\right) = \mathcal{P}_{ij} + \Pi_{ij} - \frac{2}{3}\varepsilon\delta_{ij} + \mathcal{G}_{ij} \tag{4.23}$$

$$\frac{\overline{u_i'\theta'}}{2}\left(\frac{\mathcal{P} - \varepsilon + \mathcal{G}}{k} + \frac{\mathcal{P}_\theta - \varepsilon_\theta}{k_\theta}\right) = \mathcal{P}_{\theta i} + \Pi_{\theta i} - \varepsilon_{\theta i} + \mathcal{G}_{\theta i} \tag{4.24}$$

Inserting the mean buoyancy vector Γ_i and the mean scalar gradient Θ_i defined by

$$\Gamma_i = \tau\sqrt{\frac{k_\theta}{k}}\beta_\theta g_i \tag{4.25}$$

$$\Theta_i = \tau\sqrt{\frac{k}{k_\theta}}\frac{\partial\overline{\theta}}{\partial x_i} \tag{4.26}$$

Inserting further a_{ij}, ξ_i, S_{ij} and Ω_{ij} in the definition of the redistribution terms leads to the following expressions

$$\begin{aligned}\frac{\Pi_{ij}}{\varepsilon} &= -c_1 a_{ij} + \frac{4}{5} S_{ij} + \frac{9c_2+6}{11}\left(a_{ik}S_{kj} + S_{ik}a_{kj} - \frac{2}{3}a_{km}S_{mk}\delta_{ij}\right) \\ &\quad + \frac{7c_2-10}{11}\left(a_{ik}\Omega_{kj} - \Omega_{ik}a_{kj}\right) + c_g\left(\Gamma_i\xi_j + \Gamma_j\xi_i - \frac{2}{3}\Gamma_k\xi_k\delta_{ij}\right) \qquad (4.27)\\ \frac{\tau}{\sqrt{kk_\theta}}\left(\Pi_{\theta i} - \varepsilon_{\theta i}\right) &= -\left(c_{\theta 1} + c_{\theta 5}\xi_k\Theta_k\right)\xi_i + \left(c_{\theta 2} + c_{\theta 3}\right)\xi_k S_{ik} \\ &\quad + \left(c_{\theta 2} - c_{\theta 3}\right)\xi_k\Omega_{ik} + c_{\theta 4}\left(a_{ik} + \frac{2}{3}\delta_{ik}\right)\Theta_k + c_{\theta g}\Gamma_i \qquad (4.28)\end{aligned}$$

As a result, the algebraic equations for the Reynolds stress anisotropy tensor a_{ij} and the normalized scalar flux ξ_i read

$$\begin{aligned}N a_{ij} &= -\frac{8}{15}S_{ij} + \frac{7c_2+1}{11}\left(a_{ik}\Omega_{kj} - \Omega_{ik}a_{kj}\right) \\ &\quad - \frac{5-9c_2}{11}\left(a_{ik}S_{kj} + S_{ik}a_{kj} - \frac{2}{3}a_{km}S_{mk}\delta_{ij}\right) \\ &\quad - \left(1-c_g\right)\left(\Gamma_i\xi_j + \Gamma_j\xi_i - \frac{2}{3}\Gamma_k\xi_k\delta_{ij}\right) \qquad (4.29)\\ N_\theta\xi_i &= -\left(c_{\theta S}S_{ik} + c_{\theta\Omega}\Omega_{ik}\right)\xi_k - c_\theta\left(a_{ik} + \frac{2}{3}\delta_{ik}\right)\Theta_k - (2-c_{\theta g})\Gamma_i \qquad (4.30)\end{aligned}$$

The new model constants are defined by $c_{\theta S} = 1 - c_{\theta 2} - c_{\theta 3}$, $c_{\theta\Omega} = 1 - c_{\theta 2} + c_{\theta 3}$ and $c_\theta = 1 - c_{\theta 4}$ while the coefficients N and N_θ are given by

$$\begin{aligned}N &= c_1 - 1 + \frac{\mathcal{P}+\mathcal{G}}{\varepsilon} \\ &= c_1 - 1 - a_{km}S_{km} - \Gamma_k\xi_k \qquad (4.31)\\ N_\theta &= c_{\theta 1} + c_{\theta 5}\xi_k\Theta_k + \frac{1}{2}\left(\frac{\mathcal{P}+\mathcal{G}}{\varepsilon} - 1 + \frac{1}{r}\left(\frac{\mathcal{P}_\theta}{\varepsilon_\theta} - 1\right)\right) \\ &= c_{\theta 1} + \frac{1}{2}\left(\frac{\mathcal{P}+\mathcal{G}}{\varepsilon} - 1 - \frac{1}{r_\tau}\right) + \left(c_{\theta 5} - \frac{1}{2}\right)\xi_k\Theta_k \qquad (4.32)\end{aligned}$$

The set of previous expressions correspond to the most general implicit algebraic formulation. In order to reduce the complexity of the coupled algebraic expressions, we follow in the next section some particular parameter settings considered in [37]. In practice, we will see that focusing only on the two model constants c_2 and $c_{\theta 5}$, a particular set of values allows to greatly simplify the coupled algebraic relationships.

4.1.4 Coupled explicit algebraic relations

As pointed out by Wikström *et al.* [85], the special choice $c_{\theta 5} = 1/2$ greatly reduces the complexity of the algebraic equation. Here, we will adopt the simplifications provided by the parameter choices

$c_2 = 5/9$ as considered in chapter 2 together with $c_{\theta 5} = 1/2$ that leads to

$$Na_{ij} = -\frac{8}{15}S_{ij} + \frac{4}{9}\left(a_{ik}\Omega_{kj} - \Omega_{ik}a_{kj}\right) - (1-c_g)\left(\Gamma_i\xi_j + \Gamma_j\xi_i - \frac{2}{3}\Gamma_k\xi_k\delta_{ij}\right) \tag{4.33}$$

$$N_\theta\xi_i = -\left(c_{\theta S}S_{ik} + c_{\theta\Omega}\Omega_{ik}\right)\xi_k - c_\theta\left(a_{ik} + \frac{2}{3}\delta_{ik}\right)\Theta_k - (2-c_{\theta g})\Gamma_i \tag{4.34}$$

with

$$\begin{aligned} N &= c_1 - 1 + \frac{\mathcal{P}+\mathcal{G}}{\varepsilon} \\ &= c_1 - 1 - a_{km}S_{km} - \Gamma_k\xi_k \end{aligned} \tag{4.35}$$

$$N_\theta = c_{\theta 1} + \frac{1}{2}\left(N - c_1 - \frac{1}{r_\tau}\right) \tag{4.36}$$

Unlike in case of the passive scalar [85], where the equations for a_{ij} and ξ_i can be solved in a sequential way, the equations for a_{ij} and ξ_i in the case of active scalar have to be solved simultaneously due to the terms arising from the buoyancy coupling. As previously, the procedure to solve the implicit equations consists first in assuming that both the coefficients N and N_θ are known.

First, in order to obtain explicit algebraic but still coupled relations from the implicit relations Eqs. 4.33-4.34 we follow the methodology outlined in [22, 28] in order to take benefit from the direct solution described in chapter 2. This methodology consists in rewriting the previous equations for a_{ij} and ξ_i as

$$Na_{ij} = -C_1S_{ij} + \left(a_{ik}\Omega_{kj} - \Omega_{ik}a_{kj}\right) - C_gS^+_{ij} \tag{4.37}$$

$$\left(N_\theta\delta_{ik} + c_{\theta S}S_{ik} + c_{\theta\Omega}\Omega_{ik}\right)\xi_k = -c_\theta\left(a_{ik} + \frac{2}{3}\delta_{ik}\right)\Theta_k - (2-c_{\theta g})\Gamma_i \tag{4.38}$$

where $C_1 = 6/5$, $C_g = 9(1-c_g)/4$ and where the additional tensor S^+_{ij} is defined by

$$S^+_{ij} = \Gamma_i\xi_j + \Gamma_j\xi_i - \frac{2}{3}\Gamma_m\xi_m\delta_{ij} \tag{4.39}$$

As a result, introducing $s \equiv C_1S_{ij}/N$, $s^+ \equiv C_gS^+_{ij}/N$ and $o \equiv \Omega_{ij}/N$, we get formally the same implicit relation for a_{ij} obtained in chapter 2:

$$a = -\tilde{s} + (ao - oa), \quad \tilde{s} = s + s^+ \tag{4.40}$$

Hence, following the direct solution described in chapter 2, we obtain a fully explicit algebraic relation for a_{ij} but still coupled to the normalized scalar flux ξ_i. Next, the resulting expression for a_{ij} can be split into two parts

$$a_{ij} = a^0_{ij} + a^+_{ij} \tag{4.41}$$

where the tensorial basis for the former contribution is independant of the normalized scalar flux. Hence, further substituting the resulting expression for a_{ij} to the equation Eq. 4.38 for ξ_i leads also after some transformations with a^+_{ij} to a fully explicit relation for the normalized scalar flux. A solution strategy is presented in the next section to solve the coupled explicit algebraic relations together with detailed expressions for the explicit algebraic relations.

4.1.5 Coupling strategy

While the splitting introduced previously for the anisotropy tensor allows to obtain explicit algebraic relations for a_{ij} and ξ_i, a solution strategy remains to be specified to solve the coupled relationships. The solution for a_{ij} and ξ_i remains formal as the coefficients N and N_θ remain to be determined. This thus requires an appropriate method to determine these coefficients recalled below for the sake of clarity

$$N = c_1 - 1 - a_{km} S_{km} - \Gamma_k \xi_k \tag{4.42}$$

$$N_\theta = c_{\theta 1} + \frac{1}{2}\left(N - c_1 - \frac{1}{r_\tau}\right) \tag{4.43}$$

Efficient methods have been proposed in [37, 38] to solve Eqs. 4.42-4.42 based on the two limit solutions that correspond to the shear-dominated regime and the buoyancy-dominated regime. While the proposed methods are attractive, the approach is restricted to certain two-dimensional mean flows. In this work, we follow the solution strategy suggested in [22, 28]. As the solution for N_θ is known provided that N is known, we first focus on the solution for N from Eq. 4.42. The solution strategy consists in solving Eq. 4.42 through the following iterative procedure

$$N_n = c_1 - 1 - a_{km}(N_{n-1}) S_{km} - \xi_k(N_{n-1}) \Gamma_k \tag{4.44}$$

The iterative procedure requires a guess N_0 at the first iteration. We select here the analytical solution provided in chapter 2 for the purely shear two-dimensional mean flow case. For the studied cases dealt in this work, the method proves to be very robust and efficient and needs a small number of iterations, in practice $n \leq 4$. The robustness is ensured by introducing a lower limit for the production to dissipation ratio in such a way that N_n remains strictly positive during the iterative sequence. As indicated in [37], this is an important criterion for robustness since it is a necessary condition to avoid a non-singular behavior of the model. The prescribed lower limit used in Eq 4.44 is expressed as

$$\frac{\mathcal{P} + \mathcal{G}}{\varepsilon} \geq 1.1 - c_1 \tag{4.45}$$

The resulting coupling strategy to solve the algebraic relations for the anisotropy tensor and the normalized scalar flux is summarized below

(i) First compute N_n from either the analytical relation ($n = 0$) or from Eq 4.44 ($n \geq 1$)

(ii) Then compute $a^0_{ij}(N_n)$ that depends on S_{ij}, Ω_{ij} and N_n

(iii) Compute the normalized scalar flux $\xi_i(N_n)$ that depends on S_{ij}, Ω_{ij}, Γ_i and N_n

(iv) Then compute $a^+_{ij}(N_n)$ that depends on S_{ij}, Ω_{ij}, Γ_i, ξ_i and N_n

(v) Compute the anisotropy tensor $a_{ij}(N_n) = a^0_{ij}(N_n) + a^+_{ij}(N_n)$ and go back to step *(i)*

The detailed expressions for a^0_{ij}, a^+_{ij} and ξ_i are given hereafter for both two- and three-dimensional mean flows following the direct solution methodology presented in chapter 2 and the algebraic transformations proposed in [22, 28].

Two-dimensional mean flows For two-dimensional mean flows, following [22] we define the traceless analog of S_{ij}^{+} by:

$$S_{ij}^{+(2D)} = \Gamma_i \xi_j + \Gamma_j \xi_i - \Gamma_m \xi_m \delta_{ij}^{(2D)} \tag{4.46}$$

As the strain and vorticity tensors can be treated as two-dimensional, *i.e* $S_{3i} = 0$ and $\Omega_{3i} = 0$, the equation for a_{ij} can be written as:

$$N a_{ij} = -C_1 S_{ij} + (a_{ik}\Omega_{kj} - \Omega_{ik}a_{kj}) - C_g S_{ij}^{+(2D)} - C_g \Gamma_m \xi_m \left(\delta_{ij}^{(2D)} - \frac{2}{3}\delta_{ij}\right) \tag{4.47}$$

Next, defining also the traceless analog of a_{ij} by:

$$a_{ij} = a_{ij}^{(2D)} + \beta_0 \left(\delta_{ij}^{(2D)} - \frac{2}{3}\delta_{ij}\right) \tag{4.48}$$

Then, the equation for a_{ij} Eq. 4.47 can be written as an equation for $a_{ij}^{(2D)}$ and β_0 as:

$$\begin{aligned} N a_{ij}^{(2D)} + N\beta_0 \left(\delta_{ij}^{(2D)} - \frac{2}{3}\delta_{ij}\right) = &- C_1 S_{ij} + (a_{ik}\Omega_{kj} - \Omega_{ik}a_{kj}) - C_g S_{ij}^{+(2D)} \\ &- C_g \Gamma_m \xi_m \left(\delta_{ij}^{(2D)} - \frac{2}{3}\delta_{ij}\right) \end{aligned} \tag{4.49}$$

The coefficient β_0 is determined by equating the three-dimensional tensor groups on both sides of the previous equation and is thus given by:

$$\beta_0 = -\frac{C_g}{N}\Gamma_m \xi_m \tag{4.50}$$

The remaining part is purely two-dimensional and reads:

$$N a_{ij}^{(2D)} = -C_1 S_{ij} + (a_{ik}\Omega_{kj} - \Omega_{ik}a_{kj}) - C_g S_{ij}^{+(2D)} \tag{4.51}$$

This algebraic relation corresponds formally to the relation provided in section 2.3.1 that reads

$$\begin{aligned} (1 - 2II_o)\, a &= -\tilde{s} + (\tilde{s}o - o\tilde{s}) \\ &= -s + (so - os) - s^{+} + (s^{+}o - os^{+}) \end{aligned} \tag{4.52}$$

Substituting $s \equiv C_1 S_{ij}/N$, $s^{+} \equiv C_g S_{ij}^{+(2D)}/N$ and $o \equiv \Omega_{ij}/N$, one gets

$$\begin{aligned} a_{ij}^{(2D)} &= \beta_1 S_{ij} + \beta_4 (S_{ik}\Omega_{kj} - \Omega_{ik}S_{kj}) \\ &\quad + \beta_1^{+} S_{ij}^{+(2D)} + \beta_4^{+} (S_{ik}^{+(2D)}\Omega_{kj} - \Omega_{ik}S_{kj}^{+(2D)}) \end{aligned} \tag{4.53}$$

with

$$\beta_1 = -\frac{C_1 N}{N^2 - 2II_\Omega}\,, \quad \beta_4 = -\frac{C_1}{N^2 - 2II_\Omega}\,, \quad \beta_1^{+} = \frac{C_g}{C_1}\beta_1\,, \quad \beta_4^{+} = \frac{C_g}{C_1}\beta_4 \tag{4.54}$$

As a result, Eq. 4.53 allows to identify the two terms of the splitting $a_{ij} = a_{ij}^{0} + a_{ij}^{+}$. In order to express ξ_i from Eq. 4.34 as a fully explicit algebraic relation, we can write following [22] the

following transformations

$$S_{ij}^{+(2D)}\Theta_j = \left(\Gamma_i\Theta_j + II_{\Theta\Gamma}\delta_{ij}^{(2D)} - \Gamma_j\Theta_i\right)\xi_j \tag{4.55}$$

$$\left(S_{ik}^{+(2D)}\Omega_{kj}\right)\Theta_j = \left(\Gamma_i\Theta_k\Omega_{jk} + \Gamma_m\Theta_k\Omega_{mk}\delta_{ij}^{(2D)} - \Gamma_j\Theta_k\Omega_{ik}\right)\xi_j \tag{4.56}$$

$$\left(\Omega_{ik}S_{kj}^{+(2D)}\right)\Theta_j = \left(\Gamma_k\Theta_j\Omega_{ik} + II_{\Theta\Gamma}\Omega_{ij} - \Gamma_j\Theta_k\Omega_{ik}\right)\xi_j \tag{4.57}$$

Introducing the splitting for a_{ij} and using the above transformations, we get from Eq. 4.34

$$A_{ij}\xi_j = -c_\theta a_{ij}^{0(2D)}\Theta_j - \frac{2}{3}c_\theta\Theta_i - (2 - c_{\theta g})\Gamma_i \tag{4.58}$$

where the matrix A_{ij} is given by

$$A_{ij} = N_\theta\delta_{ij} + c_{\theta S}S_{ij} + c_{\theta\Omega}\Omega_{ij} + c_\theta L_{ij} \tag{4.59}$$

with

$$L_{ij} = \beta_0^+ L_{ij}^{(0)} + \beta_1^+ L_{ij}^{(1)} + \beta_4^+ L_{ij}^{(4)}\,, \quad \beta_0^+ = -\frac{C_g}{3N} \tag{4.60}$$

$$L_{ij}^{(0)} = \Gamma_j\Theta_i \tag{4.61}$$

$$L_{ij}^{(1)} = \Gamma_i\Theta_j + II_{\Theta\Gamma}\delta_{ij}^{(2D)} - \Gamma_j\Theta_i \tag{4.62}$$

$$L_{ij}^{(4)} = \Gamma_i\Theta_k\Omega_{jk} + \Gamma_m\Theta_k\Omega_{mk}\delta_{ij}^{(2D)} - \Gamma_k\Theta_j\Omega_{ik} - II_{\Theta\Gamma}\Omega_{ij} \tag{4.63}$$

In order to use previous results obtained for the passive scalar case [85] to invert the matrix A and following [22], we introduce the traceless two-dimensional $\Gamma\Theta$-strain and $\Gamma\Theta$-rotation rate tensors $\mathring{S}_{ij}$ and $\mathring{\Omega}_{ij}$ as

$$\mathring{S}_{ij} = \frac{1}{2}\left(\Gamma_i\Theta_j + \Gamma_j\Theta_i - II_{\Theta\Gamma}\delta_{ij}^{(2D)}\right)\,, \quad \mathring{\Omega}_{ij} = \frac{1}{2}\left(\Gamma_j\Theta_i - \Gamma_i\Theta_j\right) \tag{4.64}$$

This allows to write the following relation:

$$\Gamma_j\Theta_i = \mathring{S}_{ij} + \mathring{\Omega}_{ij} + \frac{1}{2}II_{\Theta\Gamma}\delta_{ij}^{(2D)} \tag{4.65}$$

Then, we get:

$$L_{ij}^{(0)} = \mathring{S}_{ij} + \mathring{\Omega}_{ij} + \frac{1}{2}II_{\Theta\Gamma}\delta_{ij}^{(2D)} \tag{4.66}$$

$$L_{ij}^{(1)} = -2\mathring{\Omega}_{ij} + II_{\Theta\Gamma}\delta_{ij}^{(2D)} \tag{4.67}$$

$$L_{ij}^{(4)} = -2II_{\Theta\Gamma}\Omega_{ij} + 2II_{\Omega\mathring{\Omega}}\delta_{ij}^{(2D)} \tag{4.68}$$

where $II_{\Omega\mathring{\Omega}}$ is given by

$$II_{\Omega\mathring{\Omega}}\delta_{ij}^{(2D)} = 2\Omega_{ik}\mathring{\Omega}_{kj} = 2\mathring{\Omega}_{ik}\Omega_{kj} \tag{4.69}$$

This allows to express the matrix A as

$$A_{ij} = \tilde{N}_\theta \delta_{ij}^{(2D)} + c_{\theta S} S_{ij} + \tilde{c}_{\theta\Omega} \Omega_{ij} + \mathring{c}_{\theta S} \mathring{S}_{ij} + \mathring{c}_{\theta\Omega} \mathring{\Omega}_{ij} \tag{4.70}$$

$$\tilde{N}_\theta = N_\theta + c_\theta II_{\Theta\Gamma} \left(\frac{\beta_0^+}{2} + \beta_1^+ \right) + 2 c_\theta II_{\Omega\mathring{\Omega}} \beta_4^+ \tag{4.71}$$

$$\tilde{c}_{\theta\Omega} = c_{\theta\Omega} - 2 c_\theta \beta_4^+ II_{\Theta\Gamma} \tag{4.72}$$

$$\mathring{c}_{\theta S} = c_\theta \beta_0^+ \tag{4.73}$$

$$\mathring{c}_{\theta\Omega} = c_\theta \left(\beta_0^+ - 2\beta_1^+ \right) \tag{4.74}$$

This corresponds formally to the result obtained in [22]. The formal solution for the normalized scalar flux is then obtained by inverting the matrix A_{ij}^{-1}. As proposed in [85] for the passive scalar case, this is achieved as a direct consequence of the Cayley-Hamilton theorem and the inverted matrix reads

$$\begin{aligned} A^{-1} &= (det(A))^{-1} \left(tr\{A\} I - A \right) \\ &= (det(A))^{-1} \left(\tilde{N}_\theta \delta_{ij}^{(2D)} - c_{\theta S} S_{ij} - \tilde{c}_{\theta\Omega} \Omega_{ij} - \mathring{c}_{\theta S} \mathring{S}_{ij} - \mathring{c}_{\theta\Omega} \mathring{\Omega}_{ij} \right) \end{aligned} \tag{4.75}$$

with

$$\begin{aligned} det(A) =& \frac{1}{2} \left((tr\{A\})^2 - tr\{A^2\} \right) \\ =& \tilde{N}_\theta^2 - \frac{1}{2} \left(c_{\theta S}^2 II_S + \mathring{c}_{\theta S}^2 II_{\mathring{S}} + \tilde{c}_{\theta\Omega}^2 II_\Omega + \mathring{c}_{\theta\Omega}^2 II_{\mathring{\Omega}} \right) \\ & - c_{\theta S} \mathring{c}_{\theta S} II_{S\mathring{S}} - \tilde{c}_{\theta\Omega} \mathring{c}_{\theta\Omega} II_{\Omega\mathring{\Omega}} \end{aligned} \tag{4.76}$$

As a result, the normalized scalar flux reads

$$\xi_i = - c_\theta A_{ik}^{-1} \left(a_{kj}^0 + \frac{2}{3} \delta_{kj} \right) \Theta_j - (2 - c_{\theta g}) A_{ik}^{-1} \Gamma_k \tag{4.77}$$

Three-dimensional mean flows For three-dimensional mean flows, the explicit solution of Eq. 4.37 is provided in section 2.3.1 that reads

$$\begin{aligned} (1 - 2II_o)\,(1 - \frac{1}{2} II_o) a = & -(1 - \frac{7}{2} II_o)\tilde{s} - 6 I\tilde{V}(o^2 - \frac{1}{3} II_o I) \\ & - (1 - 2II_o)(\tilde{s}o - o\tilde{s}) - 3(\tilde{s}o^2 + o^2\tilde{s} - \frac{2}{3} I\tilde{V} I) - 3(o^2\tilde{s}o - o\tilde{s}o^2) \end{aligned} \tag{4.78}$$

where we have used the notation $I\tilde{V} = tr\{\tilde{s}o^2\}$. As for the two-dimensional case, splitting $\tilde{s}$ and substituting $s \equiv C_1 S_{ij}/N$, $s^+ \equiv C_g S^+_{ij}/N$ and $o \equiv \Omega_{ij}/N$, one gets

$$\begin{aligned}
a_{ij} = &\beta_1 S_{ij} + \beta_3 \left(\Omega_{ik}\Omega_{kj} - \frac{1}{3} II_\Omega \delta_{ij} \right) + \beta_4 (S_{ik}\Omega_{kj} - \Omega_{ik}S_{kj}) \\
&+ \beta_6 \left(S_{ik}\Omega_{kl}\Omega_{lj} + \Omega_{ik}\Omega_{kl}S_{lj} - \frac{2}{3} IV\delta_{ij} \right) + \beta_9 \left(\Omega_{ik}S_{kl}\Omega_{lm}\Omega_{mj} - \Omega_{ik}\Omega_{kl}S_{lm}\Omega_{mj} \right) \\
&+ \beta_1^+ S^+_{ij} + \beta_3^+ IV^+ \left(\Omega_{ik}\Omega_{kj} - \frac{1}{3} II_\Omega \delta_{ij} \right) + \beta_4^+ (S^+_{ik}\Omega_{kj} - \Omega_{ik}S^+_{kj}) \\
&+ \beta_6^+ \left(S^+_{ik}\Omega_{kl}\Omega_{lj} + \Omega_{ik}\Omega_{kl}S^+_{lj} - \frac{2}{3} IV^+\delta_{ij} \right) + \beta_9^+ \left(\Omega_{ik}S^+_{kl}\Omega_{lm}\Omega_{mj} - \Omega_{ik}\Omega_{kl}S^+_{lm}\Omega_{mj} \right)
\end{aligned} \tag{4.79}$$

where the definition for both the coefficients β_i and $\beta_i^+ = C_g\beta_i/C_1$ remains the same except for the coefficient β_3^+ for which the dependance on the invariant IV^+ has been removed and added directly in the previous tensor expression:

$$\beta_3^+ = -\frac{C_g}{C_1}\frac{12N^{-1}}{Q} \tag{4.80}$$

Here again, the above expression allows to identify the two terms of the splitting $a_{ij} = a^0_{ij} + a^+_{ij}$. As for the two-dimensional case, following [22], in order to express ξ_i as a fully explicit algebraic relation, we first write the following transformations:

$$S^+_{ij}\Theta_j = \left(\Gamma_i\Theta_j + II_{\Theta\Gamma}\delta_{ij} - \frac{2}{3}\Gamma_j\Theta_i \right)\xi_j \tag{4.81}$$

$$\left(S^+_{ik}\Omega_{kj}\right)\Theta_j = \left(\Gamma_i\Theta_k\Omega_{jk} - \Gamma_m\Theta_k\Omega_{km}\delta_{ij} - \frac{2}{3}\Gamma_j\Theta_k\Omega_{ik} \right)\xi_j \tag{4.82}$$

$$\left(\Omega_{ik}S^+_{kj}\right)\Theta_j = \left(\Gamma_k\Theta_j\Omega_{ik} + II_{\Theta\Gamma}\Omega_{ij} - \frac{2}{3}\Gamma_j\Theta_k\Omega_{ik} \right)\xi_j \tag{4.83}$$

$$IV^+ \left((\Omega_{ij})^2 - \frac{1}{3} II_\Omega \delta_{ij} \right)\Theta_j = 2 \left((\Omega_{ik})^2\Theta_k - \frac{1}{3} II_\Omega \Theta_i \right)\left((\Omega_{jm})^2\Gamma_m - \frac{1}{3} II_\Omega \Gamma_j \right) \tag{4.84}$$

$$\left(IV^+\delta_{ij}\right)\Theta_j = 2 \left(\Gamma_k\Theta_i(\Omega_{kj})^2 - \frac{1}{3}\Gamma_j\Theta_i II_\Omega \right)\xi_j \tag{4.85}$$

$$\begin{aligned}
\left(\Omega_{ik}S^+_{km}(\Omega)^2_{mj}\right)\Theta_j = &\left(\Omega_{ik}\Gamma_k\Theta_m(\Omega_{jm})^2 + \Omega_{ij}\Gamma_m\Theta_k(\Omega_{mk})^2\right)\xi_j \\
&- \frac{2}{3}\Omega_{ik}\Gamma_p\xi_p\Theta_j(\Omega_{kj})^2
\end{aligned} \tag{4.86}$$

$$\begin{aligned}
\left((\Omega)^2_{ik}S^+_{km}\Omega_{mj}\right)\Theta_j = &-\left((\Omega)^2_{ik}\Gamma_k\Theta_m(\Omega_{mj})^2 + (\Omega)^2_{ij}\Gamma_m\Theta_k\Omega_{km}\right)\xi_j \\
&- \frac{2}{3}(\Omega)^2_{ik}\Gamma_p\xi_p\Theta_j\Omega_{kj}
\end{aligned} \tag{4.87}$$

Introducing the splitting for a_{ij} and using the above transformations, we get from Eq. 4.34

$$A_{ij}\xi_j = -c_\theta a^0_{ij}\Theta_j - \frac{2}{3}c_\theta\Theta_i - (2 - c_{\theta g})\Gamma_i \tag{4.88}$$

where the matrix A is again given by

$$A_{ij} = N_\theta\delta_{ij} + c_{\theta S}S_{ij} + c_{\theta\Omega}\Omega_{ij} + c_\theta L_{ij} \tag{4.89}$$

with

$$L_{ij} = \beta_1^+ L_{ij}^{(1)} + \beta_3^+ L_{ij}^{(3)} + \beta_4^+ L_{ij}^{(4)} + \beta_6^+ L_{ij}^{(6)} + \beta_9^+ L_{ij}^{(9)} \tag{4.90}$$

$$L_{ij}^{(1)} = \Gamma_i \Theta_j + II_{\Theta\Gamma}\delta_{ij} - \frac{2}{3}\Gamma_j\Theta_i \tag{4.91}$$

$$L_{ij}^{(3)} = 2\left((\Omega_{ik})^2\Theta_k - \frac{1}{3}II_\Omega\Theta_i\right)\left((\Omega_{jm})^2\Gamma_m - \frac{1}{3}II_\Omega\Gamma_j\right) \tag{4.92}$$

$$L_{ij}^{(4)} = \Gamma_i\Theta_k\Omega_{jk} - \Gamma_m\Theta_k\Omega_{km}\delta_{ij} - \Gamma_k\Theta_j\Omega_{ik} - II_{\Theta\Gamma}\Omega_{ij} \tag{4.93}$$

$$\begin{aligned} L_{ij}^{(6)} &= \Gamma_i\Theta_k(\Omega)_{jk}^2 + \Gamma_k\Theta_m(\Omega)_{mk}^2\delta_{ij} + \Gamma_k\Theta_j(\Omega)_{ik}^2 + II_\Omega(\Omega)_{ij}^2 \\ &\quad - \frac{4}{3}\left(\Gamma_j\Theta_k(\Omega)_{ik}^2 + \Gamma_k\Theta_i(\Omega)_{kj}^2\right) + \frac{4}{9}\Gamma_j\Theta_i II_\Omega \end{aligned} \tag{4.94}$$

$$L_{ij}^{(9)} = \Omega_{ik}\Gamma_k\Theta_m(\Omega_{jm})^2 + \Omega_{ij}\Gamma_m\Theta_k(\Omega_{mk})^2 + (\Omega)_{ik}^2\Gamma_k\Theta_m(\Omega_{mj})^2 + (\Omega)_{ij}^2\Gamma_m\Theta_k\Omega_{km} \tag{4.95}$$

As for the previous two-dimensional case, in order to use results obtained for the passive scalar case, the matrix A_{ij} is rewritten as:

$$A_{ij} = \tilde{N}_\theta\delta_{ij} + M_{ij}\,, \quad M_{ij} = c_{\theta S}S_{ij} + c_{\theta\Omega}\Omega_{ij} + c_\theta\tilde{L}_{ij} \tag{4.96}$$

The coefficient $\tilde{N}_\theta$ and the traceless matrix $\tilde{L}_{ij}$ are defined by :

$$\tilde{N}_\theta = N_\theta - \frac{c_\theta}{3}L_{kk}\,, \quad \tilde{L}_{ij} = L_{ij} - \frac{1}{3}L_{kk}\delta_{ij} \tag{4.97}$$

Following [85] for the passive scalar case, the inverted matrix can be obtained as a direct consequence of the Cayley-Hamilton theorem and reads

$$A_{ij}^{-1} = \frac{1}{det(A)}\left(\left(\tilde{N}_\theta^2 - \frac{II_M}{2}\right)\delta_{ij} - \tilde{N}_\theta M + M^2\right) \tag{4.98}$$

with

$$det(A) = \tilde{N}_\theta\left(\tilde{N}_\theta^2 - \frac{II_M}{2}\right) + \frac{III_M}{3}\,, \quad II_M = tr\{M^2\}\,, \quad III_M = tr\{M^3\} \tag{4.99}$$

The normalized scalar flux then reads

$$\xi_i = -c_\theta A_{ik}^{-1}\left(a_{kj}^0 + \frac{2}{3}\delta_{kj}\right)\Theta_j - (2 - c_{\theta g})A_{ik}^{-1}\Gamma_k \tag{4.100}$$

4.1.6 The k-ω BSL model for buoyancy flows

In order to close the turbulence model, additional equations are necessary to provide the turbulence characteristic scales. Following Chapter 2, the BSL k-ω model is used for which the governing transport equations read as:

$$\frac{dk}{dt} = \mathcal{P} + \mathcal{G} - \beta^*\omega k + \frac{\partial}{\partial x_j}\left[(\nu + \sigma_k\frac{k}{\omega})\frac{\partial k}{\partial x_j}\right] \tag{4.101}$$

$$\frac{d\omega}{dt} = \frac{\omega}{k}\left(\gamma\mathcal{P} + \alpha\mathcal{G}\right) - \beta\omega^2 + \frac{\partial}{\partial x_j}\left[(\nu + \sigma_\omega\frac{k}{\omega})\frac{\partial\omega}{\partial x_j}\right] + 2(1 - F_1)\sigma_{\omega_2}\frac{1}{\omega}\frac{\partial k}{\partial x_j}\frac{\partial\omega}{\partial x_j} \tag{4.102}$$

We recall that the production terms due to the shear stresses and the buoyancy, denoted by $\mathcal{P}$ and $\mathcal{G}$ respectively are expressed as

$$\mathcal{P} = -\overline{u_i' u_j'} \frac{\partial \overline{u}_i}{\partial x_j}, \quad \mathcal{G} = -\beta_\theta g_i \overline{u_i' \theta'} \tag{4.103}$$

These terms are dependent on the closure of the Reynolds stresses and the turbulent mass flux. When the k-ω BSL model is coupled with EASFM, the production terms include the explicit algebraic relationships derived in the previous section.

The model constants σ_k, γ, α, β, σ_ω and σ_{ω_2} are defined with the use of a blending function, F_1 following Eq. 1.24 by

$$\phi = F_1 \phi_1 + (1 - F_1)\phi_2 \tag{4.104}$$

where ϕ represents the coefficients σ_k, γ.. in the BSL model and ϕ_1 and ϕ_2 are the respective coefficients from the k-ω branch and the k-ϵ branch. An additional coefficient α arises from the buoyancy contribution in the ω equation. Here, we recall the values of the coefficients for the two branches:
$\sigma_{k1} = 0.5$, $\gamma_1 = 5/9$, $\alpha_1 = -1$, $\beta_1 = 0.0750$ and $\sigma_{\omega 1} = 0.5$.
$\sigma_{k2} = 1.0$, $\gamma_2 = 0.44$, $\alpha_2 = 0.44$, $\beta_2 = 0.0828$, and $\sigma_{\omega 2} = 0.856$

4.1.7 Transport equation for the scalar variance

The k-ω BSL model for buoyancy flows described in the previous section allows to provide the turbulence time scale $\tau = k/\epsilon$ and, using Eq. 4.19, needs to be complemented by a closed form of the transport equation Eq. 4.16 the scalar variance $2k_\theta$ to provide the remaining scalar turbulence time scale $\tau_\theta = k_\theta/\epsilon_\theta$. Following [38, 79] and the same previous methodology to express the turbulent diffusivity involved in the diffusive turbulent flux, the transport equation for the scalar variance reads:

$$\frac{dk_\theta}{dt} = \mathcal{P}_\theta - \varepsilon_\theta + \frac{\partial}{\partial x_j}\left[(\kappa + \frac{1}{\sigma_{k_\theta}}\frac{k}{\omega})\frac{\partial k_\theta}{\partial x_j}\right] \tag{4.105}$$

with $\sigma_{k_\theta} = 2$. The production term $\mathcal{P}_\theta$ involves the algebraic expression for the turbulent scalar flux and reads

$$\mathcal{P}_\theta = -\overline{u_k' \theta'} \frac{\partial \overline{\theta}}{\partial x_k} \tag{4.106}$$

From Eq. 4.19, the dissipation rate ε_θ is determined through the algebraic relation

$$\varepsilon_\theta = \frac{k_\theta}{r_\tau \tau} \tag{4.107}$$

where the ratio $r_\tau = \tau_\theta/\tau$ corresponds to the ratio of the scalar turbulence time scale, $\tau_\theta = k_\theta/\varepsilon_\theta$ to the characteristic eddy turn over time scale $\tau = k/\varepsilon$. Following [37, 79], a constant value $r_\tau = 0.55$ is specified for the time scale ratio.

4.1.8 Diffusion correction

Examination of the weak equilibrium assumption for the normalized turbulent heat fluxes was performed by Vanpouille *et al.* [78] on the channel flow. The authors reported the failure of the weak equilibrium assumption specifically in the core of the channel. The diffusion plays a crucial role in these regions where the production to dissipation ratio is small and consequently a correction is necessary for considering its effects.

Following [79], we first extend the diffusion correction Eq. 2.52 described in Chapter 2 in the absence of buoyancy by accounting also for the production arising from the buoyancy term. As a result, the correction now reads

$$c_1' = A_3 + \frac{C_D}{A_0} \max\left(1 - \frac{\mathcal{P}+\mathcal{G}}{\epsilon}, 0\right) \tag{4.108}$$

where we use the same value for the constant C_D determined in Chapter 2. During the iterative procedure described in section 4.1.5, the production to dissipation ratio involved in the above correction uses the analytical solution provided in Chapter 2 for the purely shear two-dimensional case only at the first iteration while the complete expression is used for subsequent iterations.

Moving to the turbulent scalar flux, the diffusive correction was extended by Högström *et al.* [26] for the passive scalar case using the same reasoning. We put to use this correction for the active scalar case by also considering the buoyancy contribution through the production term $\mathcal{G}$. The proposed diffusion correction for the turbulent scalar flux follows the methodology described in Chapter 2 for the anisotropy tensor and, following [26], consists in modeling the missing diffusion term in Eq. 4.22 as

$$\mathcal{D}_{\theta i} - \frac{\overline{u_i'\theta'}}{2}\left(\frac{\mathcal{D}}{k} + \frac{\mathcal{D}_\theta}{k_\theta}\right) = -c_{D\theta}\sqrt{\frac{k_\theta}{k}}\xi_i\mathcal{D} \tag{4.109}$$

As in Chapter 2, the diffusive flux of k is further approximated by assuming the equilibrium relation that reads here by taking into account the additional production term due to buoyancy, $\mathcal{D} \simeq \epsilon - \mathcal{P} - \mathcal{G}$. This allows to express the right-hand side of Eq. 4.109 as

$$c_{D\theta}\sqrt{\frac{k_\theta}{k}}\xi_i\mathcal{D} = c_{D\theta}\epsilon\sqrt{\frac{k_\theta}{k}}\xi_i\left(1 - \frac{\mathcal{P}+\mathcal{G}}{\epsilon}\right) \tag{4.110}$$

As a result, the diffusion correction for the turbulent scalar flux consists of replacing the $c_{\theta 1}$ coefficient by $c_{\theta 1}'$ with

$$c_{\theta 1}' = c_{\theta 1} + c_{D\theta} \max\left(1 - \frac{\mathcal{P}+\mathcal{G}}{\epsilon}, 0\right) \tag{4.111}$$

Here again, as in Chapter 2, the limiter is added to prevent the model from approaching to a singular behavior for large production to dissipation ratio. Following the methodology described in Chapter 2 to prescribe C_D, the determination of $c_{D\theta}$ should require a careful examination of the resulting eddy diffusivity in some particular situations together with a calibration with some reference turbulent Schmidt or Prandtl number. In order to exhibit some effective eddy diffusivity

κ_t, the turbulent scalar flux is rewritten as

$$\begin{aligned}\overline{u_i'\theta'} &= -\tau k D_{ij}\frac{\partial\overline{\theta}}{\partial x_j} - \tau k_\theta(2-c_{\theta g})A_{ik}^{-1}\beta_\theta g_k \\ &= -\tau k\frac{D_{ll}}{3}\frac{\partial\overline{\theta}}{\partial x_i} - \tau k\left(D_{ij}-\frac{D_{ll}}{3}\delta_{ij}\right)\frac{\partial\overline{\theta}}{\partial x_j} - \tau k_\theta(2-c_{\theta g})A_{ik}^{-1}\beta_\theta g_k\end{aligned} \tag{4.112}$$

where D_{ij} is the dispersion tensor defined as

$$D_{ij} = c_\theta A_{ik}^{-1}\left(a_{kj}^0 + \frac{2}{3}\delta_{kj}\right) \tag{4.113}$$

The first term on the right-hand side of Eq. 4.112 corresponds formally to an eddy diffusivity term that is expressed usually as

$$\overline{u_i'\theta'} = -\frac{\nu_t}{\mathrm{Pr}_t}\frac{\partial\overline{\theta}}{\partial x_i} \tag{4.114}$$

Hence, using $\nu_t = C_\mu\tau k$ with the commonly assumed value $C_\mu = 0.09$, the turbulent Prandtl number Pr_t may identify to

$$\mathrm{Pr}_t = \frac{3C_\mu}{D_{ll}} \tag{4.115}$$

It is beyond the scope of this work to provide a detailed discussion about the resulting effective turbulent Prandtl number for buoyant flows. Nevertheless, we just provide here a rough estimate in the passive scalar case that allows to greatly simplify the analysis. In this case, assuming further $c_{\theta S} = c_{\theta\Omega} = 0$, allows to express the turbulent Prandtl number as

$$\mathrm{Pr}_t = \frac{3C_\mu N_\theta}{2c_\theta} \tag{4.116}$$

When the strain rate goes to zero, the model behaves:

$$N_\theta(\sigma\to 0) = (\tilde{c}_{\theta 1} - \frac{1}{2})\left(\frac{r+1}{r}\right), \tag{4.117}$$

where we have introduced the following expression for the coefficient $c_{\theta 1}$ proposed by Wikström [85]:

$$c_{\theta 1} = \tilde{c}_{\theta 1}\left(\frac{r+1}{r}\right) \tag{4.118}$$

As a result, using the values $\tilde{c}_{\theta 1} = 1.6$ and $r = 0.55$ proposed in [37, 85] and used in this work leads to $\mathrm{Pr}_t \simeq 0.4$. Hence, as in Chapter 2 without diffusion correction, the resulting effective turbulent Prandtl number is too small and leads to an overestimation of the eddy diffusivity. Introducing the diffusion correction and using the commonly adopted value $\mathrm{Pr}_t = 0.9$ leads to $c_{D\theta} = 3.567$. This value corresponds roughly to half of that proposed by Högström *et al.* [26] following a calibration procedure on the turbulent channel flow case.

4.2 Validation of EARSM for buoyancy flows

In this section, we evaluate the performance of the developed EASFM model on two test cases. The values for the coefficients that appear in the model have to be specified. In this preliminary study, we do not intend to investigate on the model coefficients and consider the values prescribed by Lazeroms *et al.* [37]. The corresponding values are reported in Table 4.1.

C_g	$\tilde{c}_{\theta 1}$	$c_{\theta 2}$	$c_{\theta 3}$	$c_{\theta 4}$	$c_{\theta 5}$	$c_{\theta g}$	r_τ
0.3	1.6	1	0	0	0.5	0.75	0.55

TABLE 4.1. Values of model constants. The values of EARSM model constants without scalar transport remain the same as those presented in Chapter 2

The behavior of the model is first assessed on the case of stably stratified homogeneous shear flow at Richardson numbers $Ri = 0$, 0.2, 0.25 and 0.3 for a turbulent Reynolds number $Re_t = 191$. We find that the resulting model is robust and performs well for the current choice of model coefficients which supports the findings of Lazeroms *et al.* [37]. It is worth pointing out that performing a calibration study on the model coefficients will be required for turbulent flows with unstable stratification. Simulations are performed for the developed flow in a stably stratified turbulent channel at friction Richardson number's $Ri_\tau = 60$, 120 and 480 for friction Reynolds number $Re_\tau = 550$. The DNS results obtained by Garcia-Villalba and Del Alamo [17] is used as the reference for this case.

In the following cases, the velocity field is solved implicitly via a second-order accurate finite-volume scheme while the time advancement is accomplished by a semi-implicit Crank-Nicolson method. The numerical scheme used to solve the scalar variables (θ, k and ω) corresponds to a MUSCL-like approximation. Implementation of the algebraic expressions for both the Reynolds stresses and the scalar flux follows the same methodology described in Chapter 2 that consist in formulating the model in terms of an effective eddy diffusivity that is treated implicitly together with an additional correction that is treated fully explicitly:

$$\overline{u_i' u_j'} - \frac{2}{3} k \delta_{ij} = -2\nu_t S_{ij} + a_{ij}^{(ex)} \tag{4.119}$$

$$\overline{u_i' \theta'} = -\kappa_t \frac{\partial \overline{\theta}}{\partial x_i} + \overline{u_i' \theta'}^{(ex)} \tag{4.120}$$

where κ_t refers to the (isotropic) eddy diffusivity defined in the previous section.

We would like to recall that throughout this work, no particular attention towards the near-wall region has been given. Regardless of this, we obtain good results for the test cases considered. Improvements in the near-wall performance of the model can be achieved by utilizing wall functions for both the turbulence model and the coefficients present in the explicit algebraic relations.

4.2.1 Homogeneous mean shear flow

A homogeneous turbulence sustained by a uniform mean shear together with a stable stratification is one of the simplest shear flows. The physical configuration of which is shown in Figure. 4.1. As the direct consequence of homogeneity, in the absence of transport Eq 4.101 for the kinetic energy

reduces to an ordinary differential equation

$$\frac{dk}{dt} = \mathcal{P} + \mathcal{G} - \epsilon$$

where we recall that $\mathcal{P}$ is the production due to shear stress, $\mathcal{G}$ is the production due to buoyancy and ϵ is the dissipation rate.

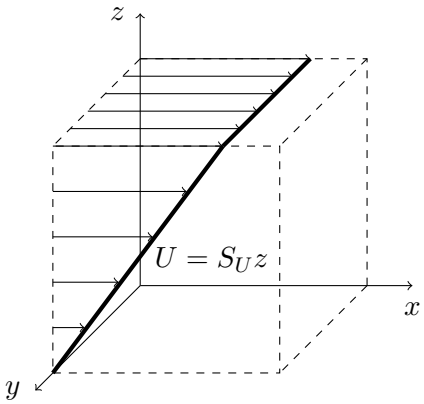

FIGURE 4.1. Configuration of homogeneous shear turbulence

Following [37], to assess the validity of the explicit algebraic model, in this test we prescribe uniform and constant values for both the mean velocity gradient $S_U = dU/dz$ and the mean scalar gradient $S_\Theta = d\Theta/dz$. The strength of the stratification is usually estimated by the gradient Richardson number given by

$$R_i = \beta_\theta g \frac{d\Theta}{dz} \left(\frac{dU}{dz} \right)^{-2}$$

The case $R_i = 0$ corresponds to the non-stratified situation for which the buoyancy term $\mathcal{G}$ is absent and the turbulent kinetic energy grows exponentially as the production and dissipation are not balanced. For non-zero Richardson number, the buoyancy force has a stabilizing effect by damping turbulence. In this case, the production term due to buoyancy is non-zero resulting in the reduction of turbulent kinetic energy as the stratification gets stronger. For a particular level of stratification, the total production balances dissipation allowing the kinetic energy to reach a steady value. Beyond this level that refers to a critical gradient Richardson number R_{ic}, the effects of stratification are so strong that turbulence decays.

The model performance above and below the critical gradient Richardson number is assessed here numerically with a prescribed mean velocity gradient S_U and a mean scalar gradient S_Θ along the vertical direction. Four different Richardson numbers, $R_i = 0$, 0.2, 0.25 and 0.3 are specified by modifying the value of β_θ. The numerical simulations start with an initial turbulent Reynolds number $Re_t = \sqrt{2k} L_t/\nu = 191$ with $L_t = k^{3/2}/\epsilon = 0.63$ and the shear number $S^* = S_U k/\epsilon$ is initially set to 1.

The temporal evolution of the normalized kinetic energy for the four prescribed Richardson numbers together with the total production to dissipation ratio are plotted in Figure. 4.2. As the strength of the stratification increases, the term $\mathcal{G}$ acts as a destruction term and the ratio $(\mathcal{P} + \mathcal{G})/\epsilon$ reduces. We observe here that for a Richardson number equal to 0.25, a balance between total production

due to shear and buoyancy and dissipation is nearly recovered together with a non-zero steady state value for the kinetic energy. Hence, as in [37], the critical Richardson number predicted by the algebraic model corresponds to the estimate $R_{ic} = 0.25$ obtained by Miles [49] using linear stability analysis for stably stratified inviscid shear flows.

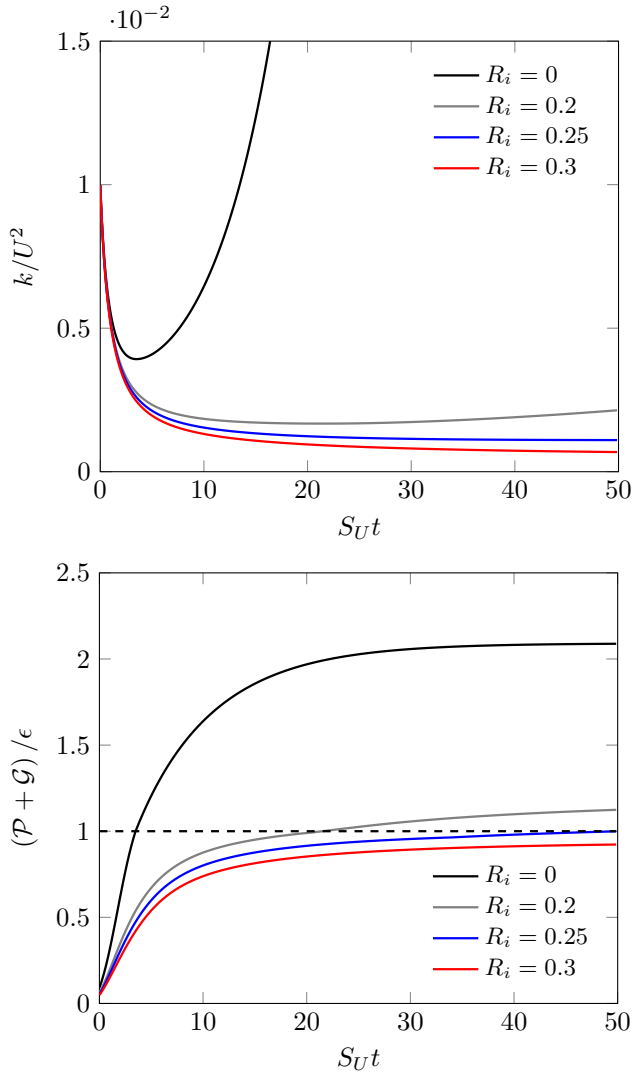

FIGURE 4.2. Time evolution of the turbulent kinetic energy (left) and the total production to dissipation ratio (right) for different Richardson numbers.

4.2.2 Fully developed turbulent channel flow

In this section, we move to the fully developed turbulent channel flow with a stable stratification. The friction Reynolds number is $Re_\tau = 550$ and corresponds to the case considered and described in chapter 2. Assuming that θ plays the role of the temperature, a stable stratification is achieved by imposing a constant temperature difference between the two walls with the highest temperature at the top wall. We follow here the same procedure described in chapter 2 to get a fully developed turbulent flow at a prescribed bulk Reynolds number. We consider three friction Richardson numbers corresponding to $Ri_\tau = 60$, 120 and 480 with $Pr = \nu/\kappa = 0.7$ and we prescribe here their

corresponding bulk Reynolds numbers $Re_b = 11219$, 11882 and 14760 according to the DNS data provided by Garcia-Villalba and Del Alamo [17]. The friction Richardson number is defined by

$$Ri_\tau = \frac{\beta_\theta g \Delta\bar{\theta} h}{u_\tau^2}$$

Two-dimensional numerical simulations are performed in a domain $[0; 2\pi\delta] \times [0; \delta]$ corresponding to the streamwise and the wall-normal directions respectively. In the streamwise direction, the meshing is uniform whereas in the wall-normal direction a non-uniform meshing is used according to the transformation given by Eq 2.55. The numerical parameters follows Section 2.4.1, also given in Table. 3.2. A no-slip boundary condition is prescribed at the walls. The flow is periodic in the streamwise direction and a constant mass flow rate is prescribed at a cross-section (as done previously in Chapters 2 and 3) using the bulk velocity U_b to drive the flow. The results are made dimensionless using $z^+ = zu_\tau/\nu$, $u^+ = u/u_\tau$ and using the temperature difference between the two walls $\Delta\bar{\theta}$.

Before moving to the stratified case, we first examine briefly the non-stratified case which was also investigated by Garcia-Villalba and Del Alamo [17]. The bulk Reynolds number in this case is $Re_b = 10140$. The non-stratified case corresponds formally to the passive scalar case studied by Wikström *et al.* [85] for which the algebraic expression for the Reynolds stresses does not depend on the turbulent scalar flux and the solution for N and N_θ discussed in section 4.1.5 can be obtained without any iterative procedure. The mean streamwise velocity and the mean scalar profiles are reported in figure. 4.3 together with the streamwise and the wall-normal component of the turbulent scalar flux in figure. 4.4. As reported in [37, 85], without diffusion correction, the mean scalar profile is overpredicted in the centre of the channel. The use of the diffusion correction described in section 4.1.8 allows to improve the mean scalar profile and to obtain a similar profile compared with predictions reported in [37] with a standard eddy diffusivity model. On the other hand, despite the fact that the streamwise component of turbulent scalar flux is underpredicted, probably due to the adopted values for the model constants and the lack of a dedicated near-wall treatment, the values are non-zero and this contrasts to a standard eddy diffusivity model.

We now move to the stratified case by focussing first on the mean streamwise velocity profile. In figure. 4.5, the mean velocity profile is plotted for the friction Richardson numbers $Ri_\tau = 60$, 120 and 480. Close to the wall, the mean velocity profiles for the three cases are have a similar velocity gradients. The flow in this region is least affected by the strength of stratification. An increase in the Richardson number increases the mean velocity in the core of the channel. This region can be identified as the region where the turbulent shear stresses are suppressed by the effects of buoyancy. With an increase in stratification one can see an increase in the centerline velocity. Consequently, the flow at the center of the channel undergoes relaminarization. There is an underprediction of the mean velocity at the center of the channel in comparison to the DNS. The benefit in using diffusion correction appears to be unnecessary and even counter-productive at least for intermediate Richardson numbers and in the center of the channel. We recall here that the correction described in section 4.1.8 has been proposed following a straightforward analogy with the unstratified case presented in Chapter 2 and this would requires a more careful analysis or a Richardson-dependent diffusion correction coefficient.

The mean temperature profile is also affected by stratification. Close to the wall the temperature gradient is reduced as Richardson number increases. The mean temperature profile is shown for the three cases in figure. 4.6. The temperature gradient gets steeper towards the center of the channel as Ri_τ increases. Like for the mean velocity profile, the model closeness with DNS is better for

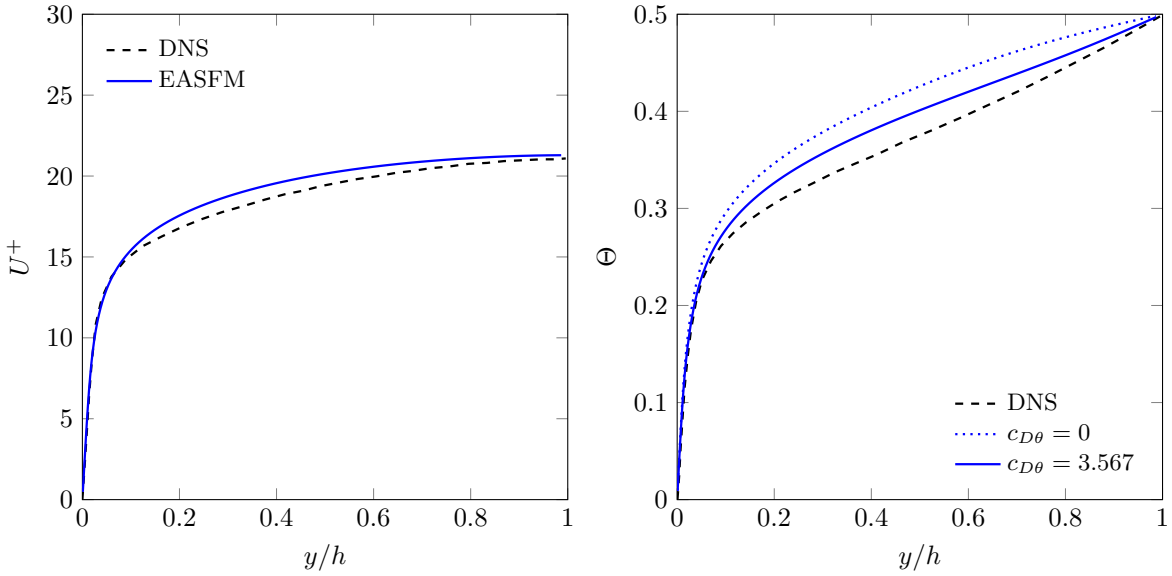

FIGURE 4.3. Mean velocity (left) and temperature (right) profiles for the non-stratified case. The dashed curves represent the DNS of Garcia-Villalba and Del Alamo [17].

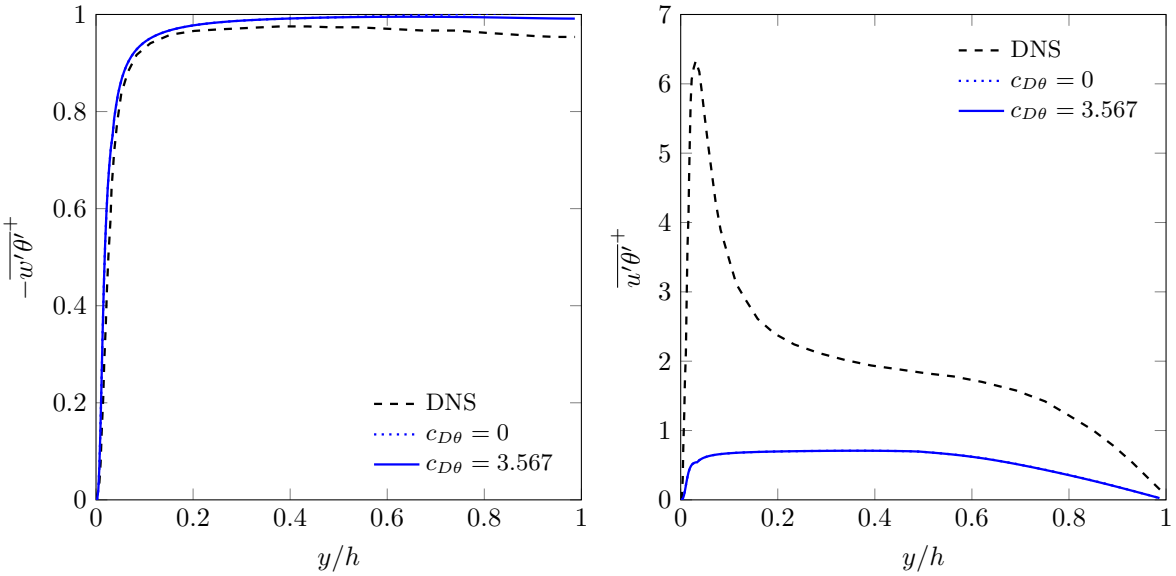

FIGURE 4.4. Wall-normal (left) and streamwise (right) component of the turbulent scalar flux for the non-stratified case. The dashed curves represent the DNS of Garcia-Villalba and Del Alamo [17].

increased levels of stratification. Here again, the benefit in using diffusion correction appears to be unnecessary and even counter-productive, especially in the center of the channel where the scalar gradient is not well predicted.

The kinetic energy profile is plotted in figure. 4.7. The peak of the turbulent kinetic energy is underpredicted along with the location of the peak, a behavior observed similarly in Chapter 2. Introducing wall functions will improve the model behavior in this region. The kinetic energy

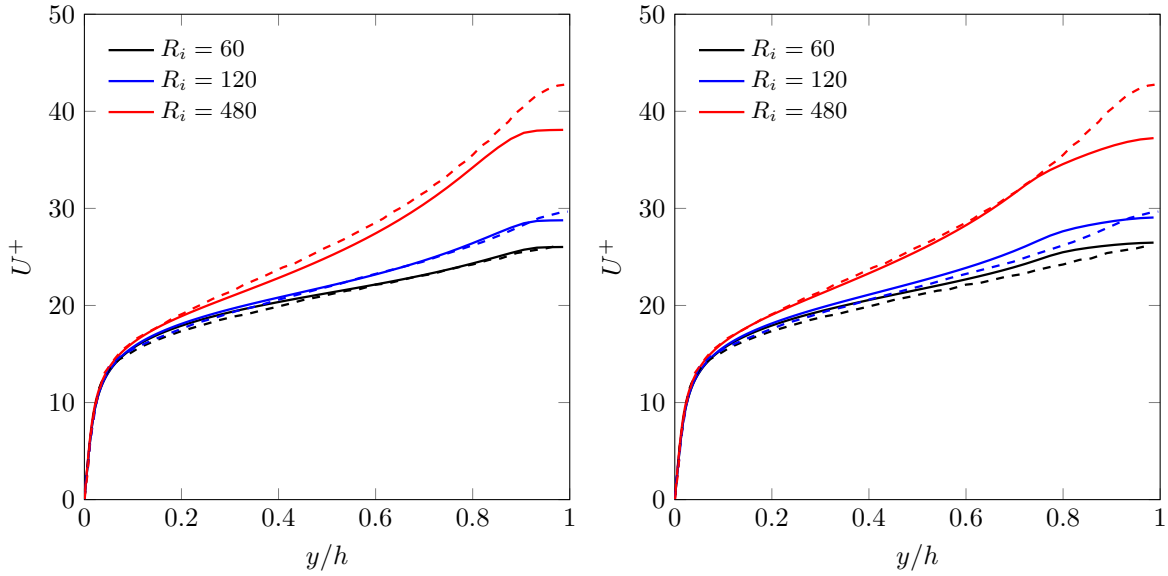

FIGURE 4.5. The mean velocity profile without (left) and with (right) diffusion correction for the three Richardson numbers. The dashed curves represent the DNS of Garcia-Villalba and Del Alamo [17].

attains almost a constant value for $0.1 < y/h < 0.5$. It can be inferred from figure. 4.8 that the total production balances dissipation for $0.1 < y/h < 0.5$. The kinetic energy is overestimated for most part of the channel. There is a rapid decrease in the total production to dissipation ratio towards the center of the channel and has a negative value. This shows the dominant effects of buoyancy over the usual turbulent behavior of the flow observed for $Ri_\tau = 0$. Although the profiles do not match with the DNS [17], the model still captures the pronounced effects that increasing Ri_τ has on the flow. This behavior of the model agrees with [37].

4.3 Explicit algebraic hybrid stress and scalar flux model

In Section 3.3, the validity of the weak-equilibrium assumption, in a hybrid RANS/LES framework, was discussed. The following hypothesis was put forth : if the weak-equilibrium assumption is valid for subgrid scale closures in LES, as well as at the RANS limit, then it should be valid in between. When accounting for scalar turbulent fluxes, the same assumption can be made : Eqs.4.23 and 4.24 can be formally applied to the subfilter scales.
As a result, the relationships presented in Sec. 4.1.4 and 4.1.5 can be formally applied in the framework of seamless hybrid RANS/LES.
In that framework, the subfilter stresses are defined using Eq.3.50 and subfilter scalar fluxes $\widetilde{u_i'\theta}$ are defined as :

$$\widetilde{u_i'\theta} = \xi_i \sqrt{k_s k_{\theta s}} \tag{4.121}$$

where k_s is the subfilter turbulent kinetic energy and $k_{\theta s}$ is the subfilter equivalent of the scalar variance, rigorously defined as:

$$k_{\theta s} = \widetilde{\theta'\theta'}$$

Their transport equations are detailed hereafter. The normalized scalar flux vector $\boldsymbol{\xi}$ is detailed in Sec.4.3.3, as well as the SFS anisotropic tensor $\boldsymbol{a_s}$.

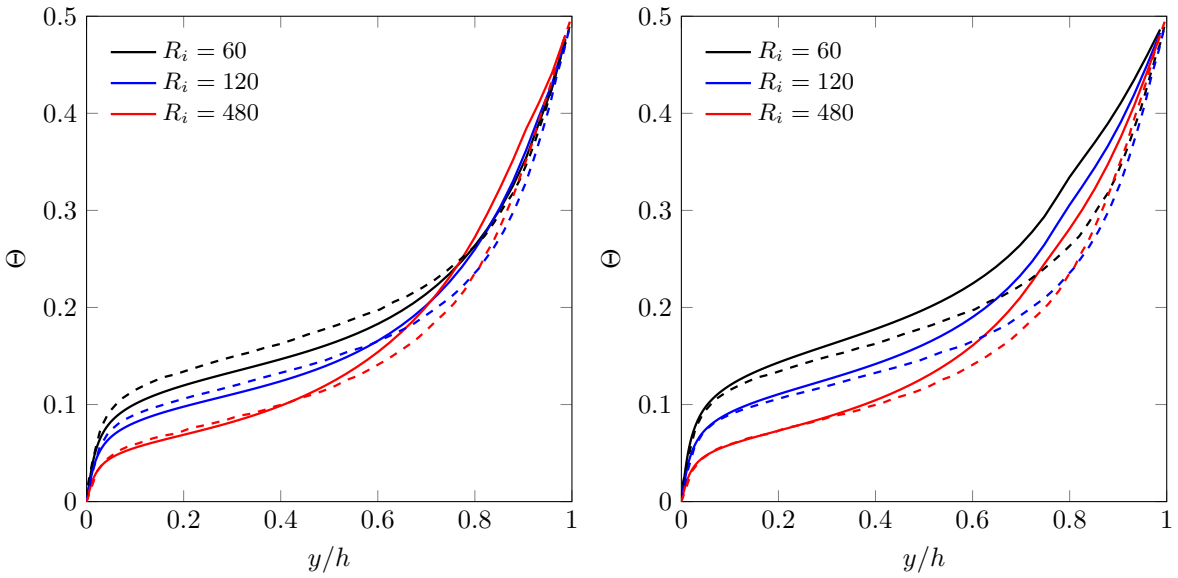

FIGURE 4.6. The mean temperature profile without (left) and with (right) diffusion correction for the three Richardson numbers. The dashed curves represent the DNS of Garcia-Villalba and Del Alamo [17].

4.3.1 Transport equation for k_s and ω_s

$$\frac{dk_s}{dt} = \mathcal{P}_s + \mathcal{G}_s - \beta^* \omega_s k_s + \frac{\partial}{\partial x_j}\left[(\nu + \sigma_k \frac{k_s}{\omega_s})\frac{\partial k_s}{\partial x_j}\right] \tag{4.122}$$

$$\frac{d\omega_s}{dt} = \frac{\omega_s}{k_s}(\gamma \mathcal{P}_s + \alpha \mathcal{G}_s) - \beta \omega_s^2 + \frac{\partial}{\partial x_j}\left[(\nu + \sigma_\omega \frac{k_s}{\omega_s})\frac{\partial \omega_s}{\partial x_j}\right] + 2(1-F_1)\sigma_{\omega_2}\frac{1}{\omega_s}\frac{\partial k_s}{\partial x_j}\frac{\partial \omega_s}{\partial x_j} \tag{4.123}$$

As in RANS mode, the production terms due to the shear stresses and the buoyancy, denoted by $\mathcal{P}_s$ and $\mathcal{G}_s$ respectively are expressed as

$$\mathcal{P}_s = -\tau_{ijs}\frac{\partial \widetilde{u}_i}{\partial x_j}, \quad \mathcal{G}_s = -\beta_\theta g_i \widetilde{u_i'\theta'} \tag{4.124}$$

All the constants in Eqs.4.122 and 4.123 have the same values as in RANS mode (see Sec.4.1.6). The function F_1 is defined by Eqs.3.33 and 3.34.

4.3.2 Transport equation for $k_{\theta s}$

Similar to what is done for k_s, one must adapt the sink term in the transport equation for $k_{\theta s}$, in order to account for the cutoff induced by the seamless hybrid RANS/LES.
Applying Equivalent DES to $k_{\theta s}$ raises the question of a specific energy ratio for scalar turbulence, that we would call r_θ, and that would be defined as :

$$r_\theta = \frac{\overline{k_{\theta s}}}{\overline{k_{\theta s}} + k_{\theta res}} \tag{4.125}$$

But this would require to build specific subfilter length/time scales. As a consequence, we will use the dynamic energy ratio r. Yet we assumed, at the RANS level (see Eq. 4.107), that the dissipation

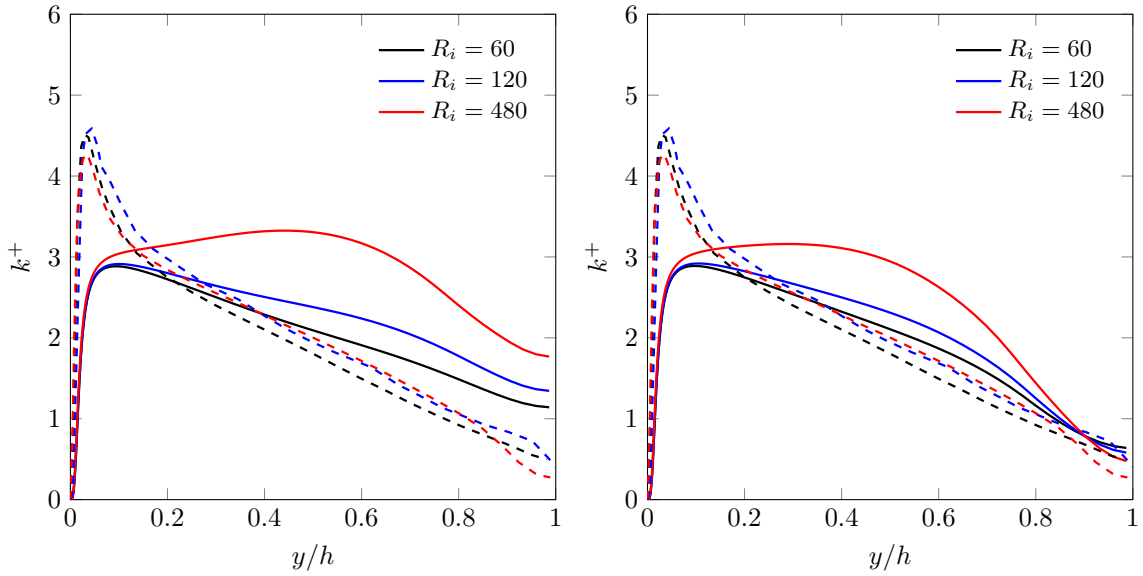

FIGURE 4.7. The turbulent kinetic energy profile without (left) and with (right) diffusion correction for the three Richardson numbers. The dashed curves represent the DNS of Garcia-Villalba and Del Alamo [17].

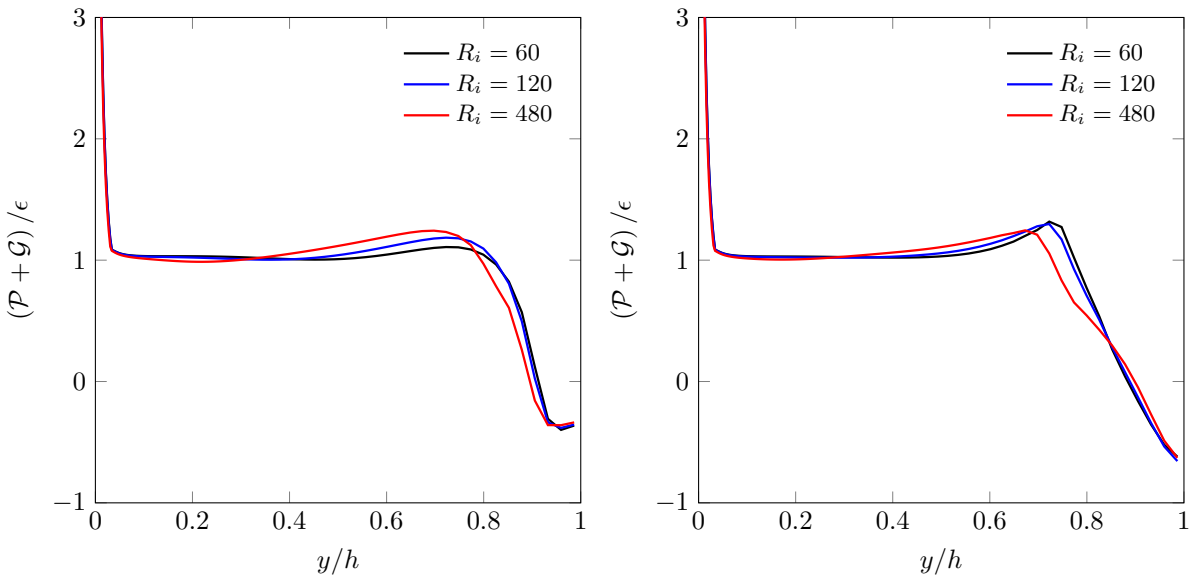

FIGURE 4.8. Total production to dissipation ratio without (left) and with (right) diffusion correction in the wall normal direction for the three Richardson numbers.

of the scalar, ε_θ is defined such as the ratio between scalar and dynamic eddy turnover time scales, is an imposed constant, called r_τ.
We recall here that, in purely dynamic Equivalent DES, one adds a cœfficient ψ in front of the subfilter dissipation term, in the transport equation of k_s:

$$\psi = \max\left(1; \frac{l_S}{l_{LES}}\right), \tag{4.126}$$

where :

$$l_S = \frac{k_S^{3/2}}{\varepsilon_S} \quad \text{et} \quad l_{LES} = \frac{r^{3/2} k_{tot}^{3/2}}{\Psi(r)\varepsilon_{tot}} \ , \tag{4.127}$$

where $\Psi(r)$ can, for instance, be given by Equation 3.25.
Now, we build a scalar-specific coefficient ψ_θ, that has to be placed in front of the scalar subfilter dissipation $\varepsilon_{\theta s}$, in the transport equation of $k_{\theta s}$.
A conceptual problem is raised here : it is not always possible to build a length scale with k_θ et ε_θ, for dimensional reasons. For exemple, if θ is temperature, it is clearly impossible to build a length scale from $k_{\theta s}$ and $\varepsilon_{\theta s}$.
Nevertheless, for any kind of scalar, $\varepsilon_{\theta s}$ will always have the dimension of $k_{\theta s}$ divided by time, since the former is a term of the transport equation of the latter. In other words, for any scalar θ, the ratio $k_{\theta s}/\varepsilon_{\theta s}$ is a time scale.
Following Tran *et al.* [76] in the dynamic framework, one can build ψ from the comparison of time scales, instead of length scales :

$$\psi = \max\left(1; \frac{t_S}{t_{LES}}\right) \ , \tag{4.128}$$

with:

$$t_S = \frac{k_S}{\varepsilon_S} \quad \text{and} \quad t_{LES} = \frac{r k_{tot}}{\Psi(r)\varepsilon_{tot}} \ . \tag{4.129}$$

It is straightforward to build ψ_θ following the same approach as above.

$$\psi_\theta = \max\left(1; \frac{t_{\theta,S}}{t_{\theta,LES}}\right) \ , \tag{4.130}$$

with:

$$t_{\theta s} = \frac{k_{\theta s}}{\varepsilon_{\theta s}} \quad \text{and} \quad t_{\theta LES} = \frac{r k_{\theta,tot}}{\Psi(r)\varepsilon_{\theta,tot}} \ . \tag{4.131}$$

We heuristically assume that $\Psi(r)$ used for k_s can be used for scalar turbulence (see Eq. 3.25). Introducing the scalar to dynamic time ratio:

$$r_\tau = \frac{k_\theta/\varepsilon_\theta}{k/\varepsilon}, \tag{4.132}$$

and its subfilter counterpart $r_{\tau s}$, one can define $t_{\theta s}$ and $t_{\theta LES}$ from dynamic turbulent variables (assuming $\varepsilon_{tot} \approx \varepsilon_s$):

$$\psi_\theta = \max\left(1; \frac{r_{\tau s}}{r_\tau}\frac{k_s}{r k_{tot}}\Psi(r)\right) \ . \tag{4.133}$$

The subfilter time scale ratio $r_{\tau,S}$ may for instance be defined from Jimenez *et al.* (2015) [30] in the purely LES framework:

$$r_{\tau s} \approx Pr \tag{4.134}$$

or from a blending between r_τ and the expression above, using the energy ratio r.

For the scalar we do not perform any blending between two second scales (unlike what we do for the dynamic subfilter quantities ε_s and ω_s), we simply use the coefficient ψ_θ defined by Eq. 4.133, leading to:

$$\frac{dk_{\theta s}}{dt} = \mathcal{P}_{\theta s} - \psi_\theta \varepsilon_{\theta s} + \frac{\partial}{\partial x_j}\left[(\nu + \frac{1}{\sigma_{k_\theta}}\frac{k_s}{\omega_s})\frac{\partial k_{\theta s}}{\partial x_j}\right] \tag{4.135}$$

where the subfilter production term $\mathcal{P}_{\theta s}$ reads

$$\mathcal{P}_{\theta s} = -\widetilde{u_k'\theta'}\frac{\partial\widetilde{\theta}}{\partial x_k} \tag{4.136}$$

4.3.3 Explicit algebraic coupled subfilter closure

In the general 3D flow case, the algebraic expression for the SFS anisotropic tensor $\boldsymbol{a}_s$ reads

$$\begin{aligned}
a_{ijs} = &\beta_1\tilde{S}_{ij} + \beta_3\left(\tilde{\Omega}_{ik}\tilde{\Omega}_{kj} - \frac{1}{3}II_{\tilde{\Omega}}\delta_{ij}\right) + \beta_4(\tilde{S}_{ik}\tilde{\Omega}_{kj} - \tilde{\Omega}_{ik}\tilde{S}_{kj}) \\
&+ \beta_6\left(\tilde{S}_{ik}\tilde{\Omega}_{kl}\tilde{\Omega}_{lj} + \tilde{\Omega}_{ik}\tilde{\Omega}_{kl}\tilde{S}_{lj} - \frac{2}{3}IV\delta_{ij}\right) + \beta_9\left(\tilde{\Omega}_{ik}\tilde{S}_{kl}\tilde{\Omega}_{lm}\tilde{\Omega}_{mj} - \tilde{\Omega}_{ik}\tilde{\Omega}_{kl}\tilde{S}_{lm}\tilde{\Omega}_{mj}\right) \\
&+ \beta_1^+\tilde{S}^+_{ij} + \beta_3^+IV^+\left(\tilde{\Omega}_{ik}\tilde{\Omega}_{kj} - \frac{1}{3}II_{\tilde{\Omega}}\delta_{ij}\right) + \beta_4^+(\tilde{S}^+_{ik}\tilde{\Omega}_{kj} - \tilde{\Omega}_{ik}\tilde{S}^+_{kj}) \\
&+ \beta_6^+\left(\tilde{S}^+_{ik}\tilde{\Omega}_{kl}\tilde{\Omega}_{lj} + \tilde{\Omega}_{ik}\tilde{\Omega}_{kl}\tilde{S}^+_{lj} - \frac{2}{3}IV^+\delta_{ij}\right) + \beta_9^+\left(\tilde{\Omega}_{ik}\tilde{S}^+_{kl}\tilde{\Omega}_{lm}\tilde{\Omega}_{mj} - \tilde{\Omega}_{ik}\tilde{\Omega}_{kl}\tilde{S}^+_{lm}\tilde{\Omega}_{mj}\right)
\end{aligned} \tag{4.137}$$

where the β_i and the β_i^+ coefficients are expressed as in Sec.4.1.5. The tensors $\tilde{\boldsymbol{S}}$ and $\tilde{\boldsymbol{\Omega}}$ are defined by Eq.3.55.
The algebraic expression for the SFS scalar flux $\boldsymbol{\xi}_s$ reads :

$$\xi_{is} = -c_\theta A^{-1}_{ik}\left(a_{kjs}^{(0)} + \frac{2}{3}\delta_{kj}\right)\Theta_{js} - (2 - c_{\theta g})A^{-1}_{ik}\Gamma_{ks} \tag{4.138}$$

where

$$\Gamma_{is} = \tau\frac{k_{\theta s}}{k_s}\beta_\theta g_i \quad \text{and} \quad \Theta_{is} = \tau\frac{k_s}{k_{\theta s}}\frac{\partial\tilde{\theta}}{\partial x_i}$$

Globally, the coupling strategy is identical to what is done in RANS mode (see Sec.4.1.5), except that :

- Averaged quantities are replaced with filtered quantities.
- Closure model variables are replaced with their subfilter scale counterpart.

4.4 Test cases

The behavior of the proposed explicit algebraic hybrid stress and scalar flux model is here assessed through the same previous test cases addressed in section 4.2 in a RANS framework, namely the homogeneous shear flow and the fully developed turbulent channel flow both with stable stratification. As in section 4.2, a full calibration of the model constants is beyond the scope of this study and we focus here on a rather qualitative evaluation of the seamless hybrid model by using the set of model coefficient values given previously.

The numerical simulations are performed using the P^{2}REMICS software. In the following cases, the velocity field is solved implicitly via a second-order accurate finite-volume scheme on a staggered mesh while the time advancement is accomplished by a semi-implicit Crank-Nicolson method. This

results in a discretely energy conserving scheme. The numerical scheme used to solve the scalars corresponds to a MUSCL like scheme.

4.4.1 Homogeneous mean shear flow

In this section, we investigate the behavior of the explicit algebraic hybrid stress and scalar flux model in the situation of the homogeneous mean shear flow described previously in section 4.2.1 in a RANS framework. Compared with the previous RANS simulations for which the integral length scale or the turbulent kinetic energy can evolve freely, the size L of the computational domain enforces here upper bounds that correspond to the order of the box size L for the integral length scale and to the order of $S_U L$ for the velocity fluctuations [56]. While this contrasts with unbounded calculations that use remeshing procedures together with periodic boundary conditions [60], such a confined configuration exhibits also a violent growth of the kinetic energy during the transient regime and the subsequent statistically steady state has been extensively studied as it seems to be representative of some real situations.

Numerical simulations are performed in a box $[0, L]^3$ with $L = 2\pi$. This is much larger than the prescribed initial value for the integral length scale in order to avoid confinement effects during the transient regime. Following [55], the linear background profiles for the mean velocity and the mean temperature are imposed by adding respectively forcing terms f_{Ui} and f_θ to the transport equations for the resolved velocity and the resolved temperature as

$$f_{Ui} = \frac{S_U y - \langle u \rangle_{xy}}{\tau} e_1 \,, \quad f_\theta = \frac{S_\theta y - \langle \theta \rangle_{xy}}{\tau} \tag{4.139}$$

where τ denotes here the forcing time scale usually taken as the time step and the notation $\langle \cdot \rangle_{xy}$ refers to the horizontal average. Periodic boundary conditions apply in the horizontal x- and y-directions while the following boundary conditions apply on the horizontal surfaces:

$$u = S_U z \,, \quad v = w = 0 \,, \quad \theta = S_\theta z \tag{4.140}$$

The initial velocity field is prescribed by using the Random Fourier Method introduced in Chapter 3 with a parameterization of the model energy spectrum that follows the prescribed kinetic energy and integral length scale given in Section 4.2.1. In the same way, following the procedure described in 3, the initial values for the subfilter quantities k_s and ω_s are obtained by running the subfilter turbulence model until a statistically steady state. Two different equidistant meshes are used, namely 32^3 and 64^3 cells. The time step is specified such that $\Delta t = 0.5/(N S_U)$.

The temporal evolution of the normalized kinetic energy k/U^2 for three Richardson numbers, $Ri = 0$, 0.2 and 0.3 is reported in Figure 4.9 for the two mesh resolutions. As in Section 4.2.1, three distinct regimes are obtained according to the value of the Richardson number. As observed in direct numerical simulations [29, 55], the case $R_i = 0$ leads to an initial phase for which kinetic energy decays, that may result from isotropic initial conditions, followed by an exponential-like growth and subsequently followed by a statistically steady state regime characterized by large oscillations in the kinetic energy [56] owing to finite box size effects.Moving to the high Richardson number case $R_i = 0.3$ leads as expected to a decay in the kinetic energy. The value found here for the critical Richardson number $R_{ic} \simeq 0.1$ differs substantially from the estimate $R_{ic} = 0.25$ obtained through linear inviscid stability analysis [49] and from RANS numerical experiments performed in Section 4.2.1. On the other hand, this agrees with direct numerical simulation results, for which

$0.04 < R_{ic} < 0.17$ for instance in [29], that exhibit a strong dependence of the critical Richardson number on Reynolds and shear numbers. A detailed discussion about the critical Richardson number issue is beyond the scope of this work and we will just refer to [29] that suggests that the linear result of Miles [49] fails to be valid for nonlinearly evolving uniform shear flows.

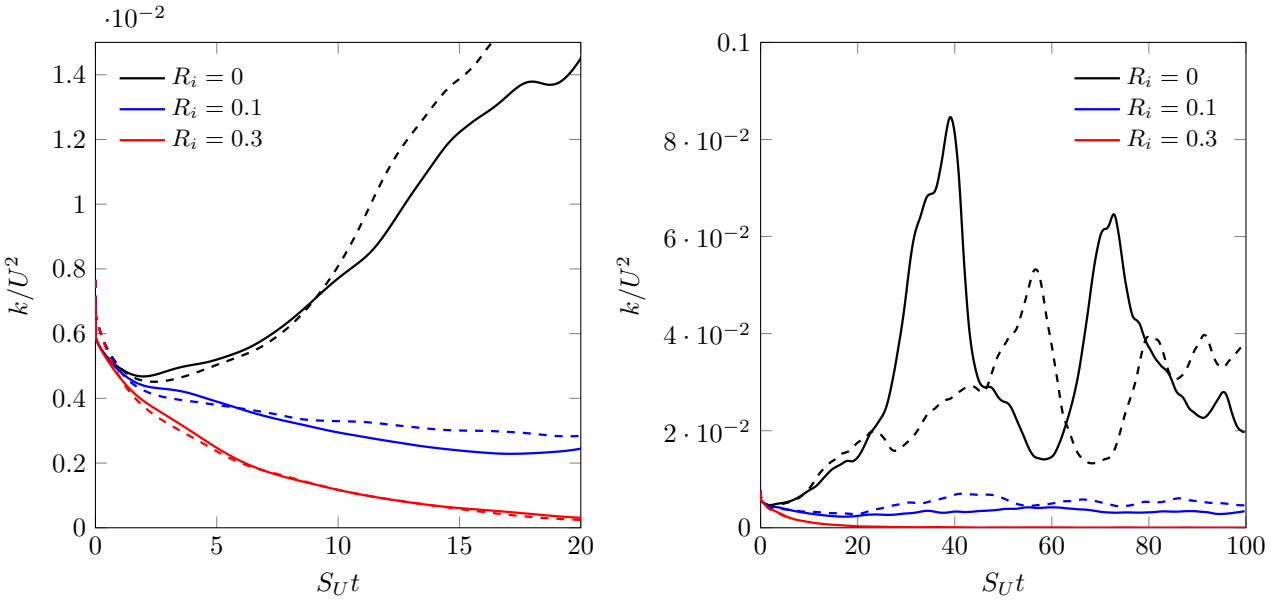

FIGURE 4.9. Time evolution of the turbulent kinetic energy for different Richardson numbers with $N = 32$ (solid lines) and $N = 64$ (dashed lines).

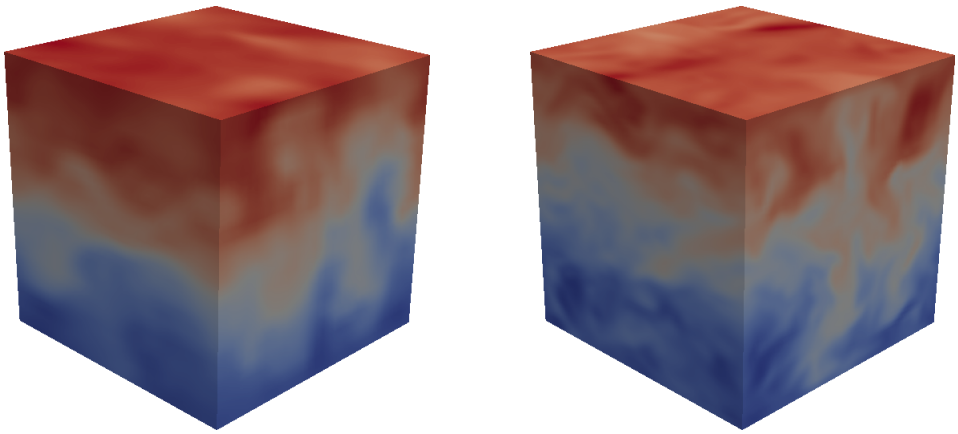

FIGURE 4.10. Snapshots of the streamwise resolved velocity for $N = 32$ (left) and $N = 64$ (right) for $R_i = 0$ at $S_U t = 20$.

4.4.2 Fully developed turbulent channel flow

We now investigate in this section the behavior of the seamless hybrid RANS-LES model on the fully developed turbulent channel flow with a stable stratification described previously in a RANS framework. The physical description of the test case is not repeated here and we refer to Section 4.2.2. As the friction Reynolds number is $Re_\tau = 550$, we adopt here the fine mesh used in Chapter 3 for the same case without stratification and we refer to Section 3.4.2 for more details regarding

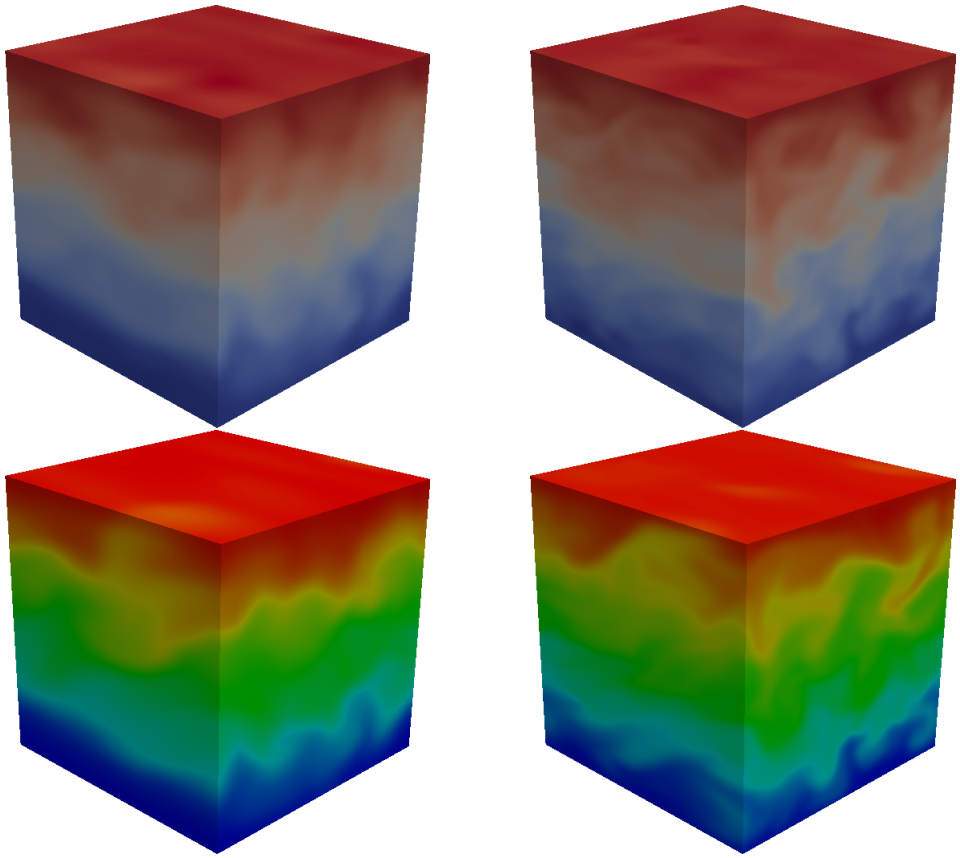

FIGURE 4.11. Snapshots of the streamwise resolved velocity (top) and the resolved scalar (bottom) for $N = 32$ (left) and $N = 64$ (right) for $R_i = 0.1$ at $S_U t = 20$.

numerical settings. We also provide in this section LES results using the WALE model together with an eddy-diffusivity model that relates the subfilter scalar flux to the resolved scalar gradient through a turbulent Prandtl number Pr_t with $\mathrm{Pr}_t = 1$.

As in Section 3.4.2, the dimensions of the computational domain are $[0; 2\pi\delta] \times [0; \pi\delta] \times [0; 2\delta]$ in the streamwise, the spanwise and the wall-normal direction, respectively. We acknowledge that this computational domain is small in comparison to the DNS that corresponds to $[0; 8\pi\delta] \times [0; 3\pi\delta] \times [0; 2\delta]$. Nevertheless, relaminarization that has mainly motivated the use of large computational domains in [16, 17] has not been observed in our simulations and this greatly reduces the computational cost. The mesh resolution is recalled in Table 4.2 together with the mesh resolution used in DNS.

As previously performed in the RANS framework in Section 4.2.2, we first examine the non-stratified case. We focus again on the mean streamwise velocity and the mean scalar profiles that are reported in figure. 4.12 together with the streamwise and the wall-normal component of the turbulent scalar flux in figure. 4.13. Contrary to the mean velocity profile that appears to be better reproduced by the hybrid model as already observed in Chapter 3, the mean scalar profile shows no clear improvement compared with a simple eddy-diffusivity model. In the same way, the turbulent scalar fluxes predicted by the models are close to each other and are in a good agreement with DNS results. However, it must be pointed out that the turbulent scalar flux reported for the hybrid approach takes into account the modeled part while only the resolved part is reported for the WALE model. Even if it is premature to conclude, this is probably due to the particular setting of model constants

Mesh	$N_x \times N_y \times N_z$	Δx^+	Δy^+	Δz_w^+ - Δz_c^+
fine	$69 \times 86 \times 156$	50	20	0.5 - 15
DNS [17]	-	9	4.1	- 6.7

TABLE 4.2. Stably stratified channel flow simulations at $Re_\tau = 550$. N_x, N_y and N_z are the number of grid points along the streamwise, spanwise and the wall-normal directions, respectively. Δx^+ and Δy^+ are the grid spacings in viscous wall units along the streamwise and the spanwise direction, respectively and Δz_w^+ and Δz_c^+ are the grid spacing in the wall-normal direction at the wall and at the channel centerline.

($c_{\theta S} = c_{\theta \Omega} = 0$) that leads to an algebraic subfilter closure that behaves like an eddy-diffusivity approach in this case.

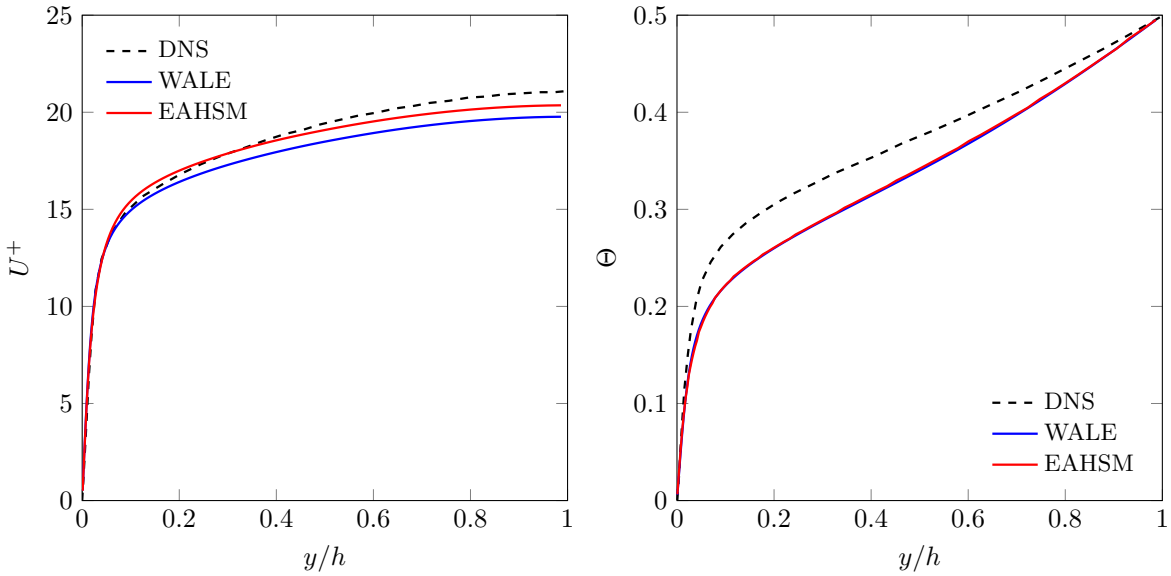

FIGURE 4.12. Mean velocity (left) and temperature (right) profiles for the non-stratified case. The dashed curves represent the DNS of Garcia-Villalba and Del Alamo [17].

When moving to the stratified case, the numerical simulation results reported in Figures 4.14-4.16 for the mean streamwise velocity and the mean scalar profiles and in Figure 4.21 for snapshots of the resolved velocity and the resolved scalar follow the tendencies observed previously in a RANS framework. The stable stratification leads to a higher velocity in the centre of the channel compared with the unstratified case due to a damping of the turbulent shear stresses.

From a quantitative point of view, the agreement with DNS reference results [16, 17] is less satisfactory compared with the unstratified case carried out in Chapter 3. The computed friction Reynolds numbers reported in Table 4.3 reflect this behavior with a mismatch that increases with the Richardson number.

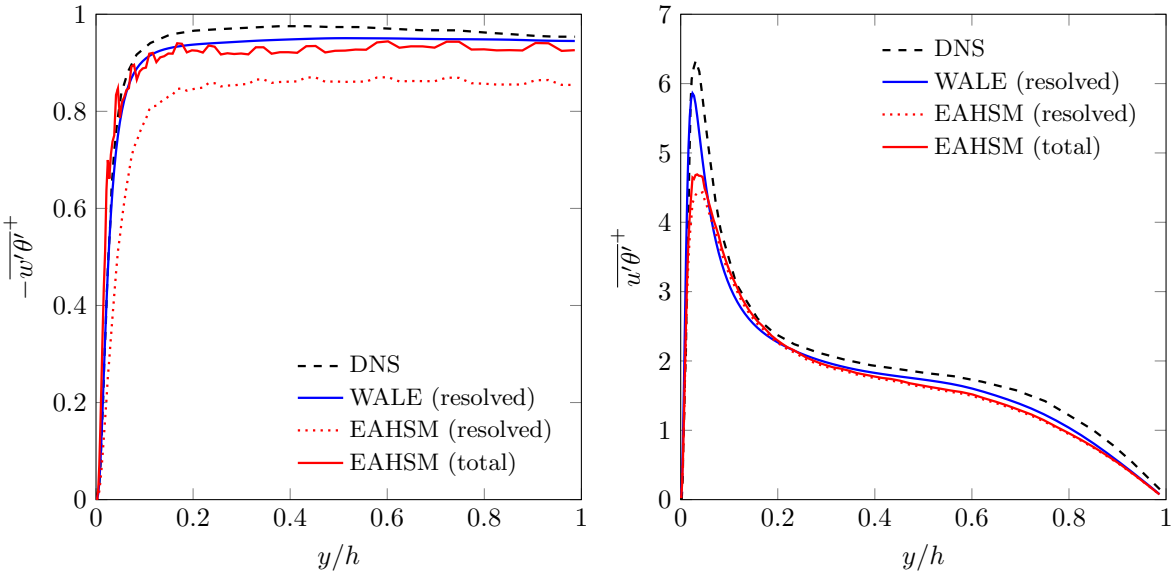

FIGURE 4.13. Wall-normal (left) and streamwise (right) component of the turbulent scalar flux for the non-stratified case. The dashed curves represent the DNS of Garcia-Villalba and Del Alamo [17].

R_i	WALE	EAHSM	DNS
0	573 - 13.4	556 - 14.3	550 - 16.4
60	585 - 7.4	565 - 7.7	550 - 6.9
120	588 - 6.0	568 - 6.3	550 - 5.4
480	608 - 4.3	582 - 4.2	550 - 3.3

TABLE 4.3. Comparison of the computed friction Reynolds and Nusselt numbers Re_τ / Nu for the three Richardson numbers.

We observe as previously in the non-stratified case that both the WALE and EAHSM models produce very similar results and here seem to tend to underestimate turbulence damping in the centre of the channel while the near-wall behavior is better reproduced. As a result, the mean stream velocity and the mean scalar gradient in the wall-normal direction are underpredicted in the core of the channel as illustrated in Figures 4.14-4.16.

Moving to the turbulent kinetic energy and the root-mean-square of the scalar fluctuations that are shown in Figures 4.17-4.19, both the WALE and EAHSM models tend to underpredict the level of fluctuations in the channel centre. This discrepancy is probably due to the presence of internal gravity waves outlined in [16, 17] in the core region of the channel as suggested by the high level of the root-mean-square of the scalar fluctuations. It appears here premature to identify precisely the reasons that cause the internal gravity waves to be poorly described for such high stratification levels. Nevertheless, we just mention here that relatively small computational domains may constrain internal gravity waves [16]. Moreover, it is also important to keep in mind that neither the WALE model nor the EAHSM model account for internal gravity waves. This calls for further work that would consist of numerical simulations using larger computational domains and on the interest in

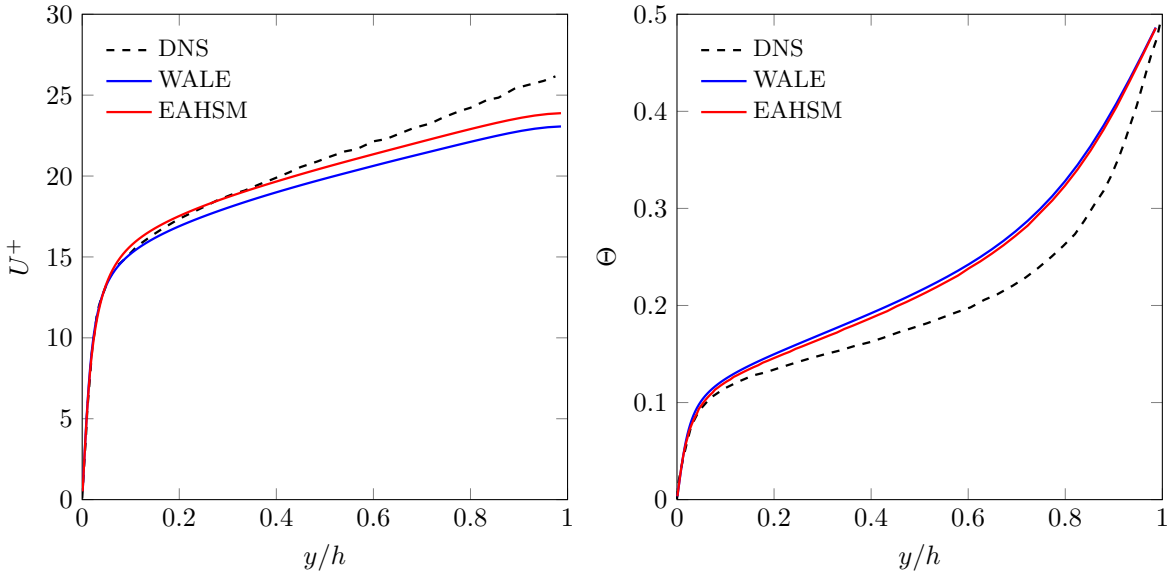

FIGURE 4.14. Mean velocity (left) and mean temperature (right) profile - $R_i = 60$.

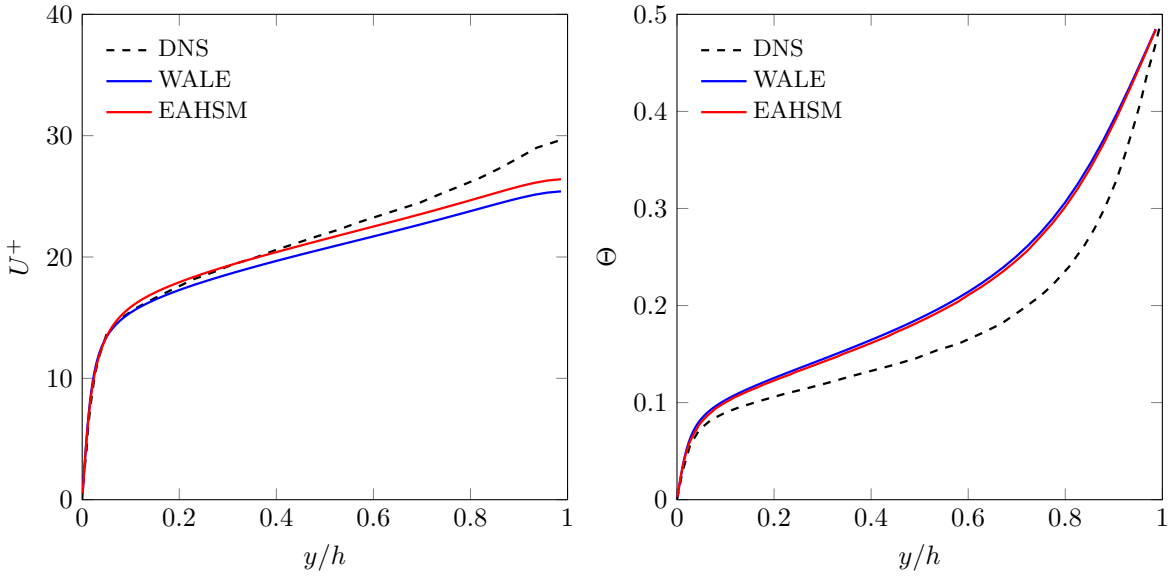

FIGURE 4.15. Mean velocity (left) and mean temperature (right) profile - $R_i = 120$.

introducing internal waves modeling in algebraic models (see for instance [81]).

The underestimation of the fluctuations, at high Richardson numbers, is also illustrated by Figure 4.20, that shows target and observed r_k, as well as observed scalar variance ratio (as defined by Eq. 4.125). Both ratios (scalar and kinetic) exhibit bumps near $y/h \approx 0.8$ at $Ri = 480$, which is consistent with what was said above, about internal gravity waves.

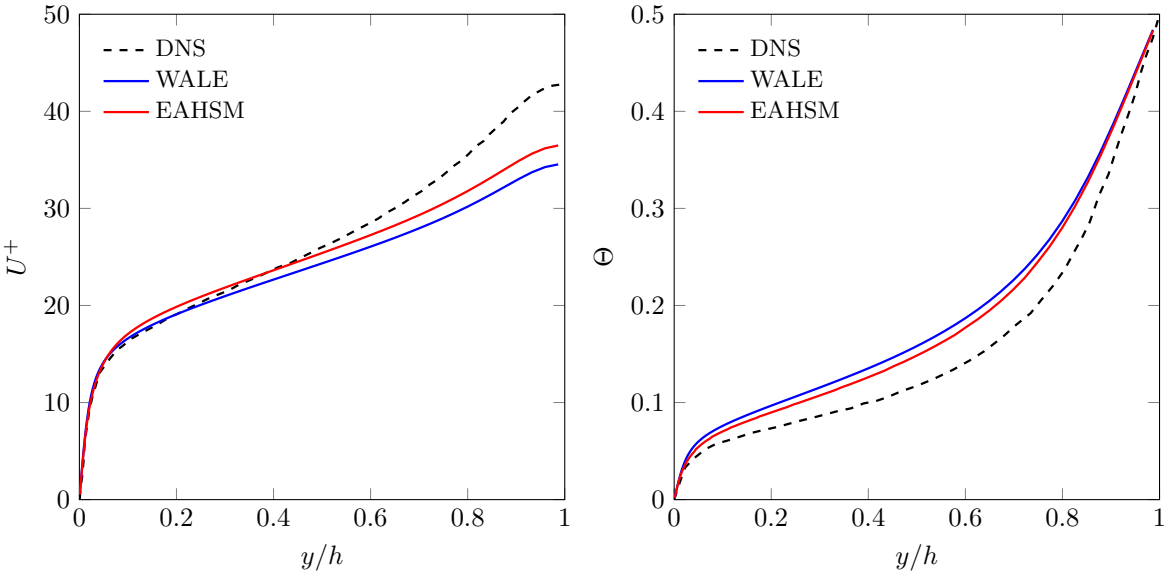

FIGURE 4.16. Mean velocity (left) and mean temperature (right) profile - $R_i = 480$.

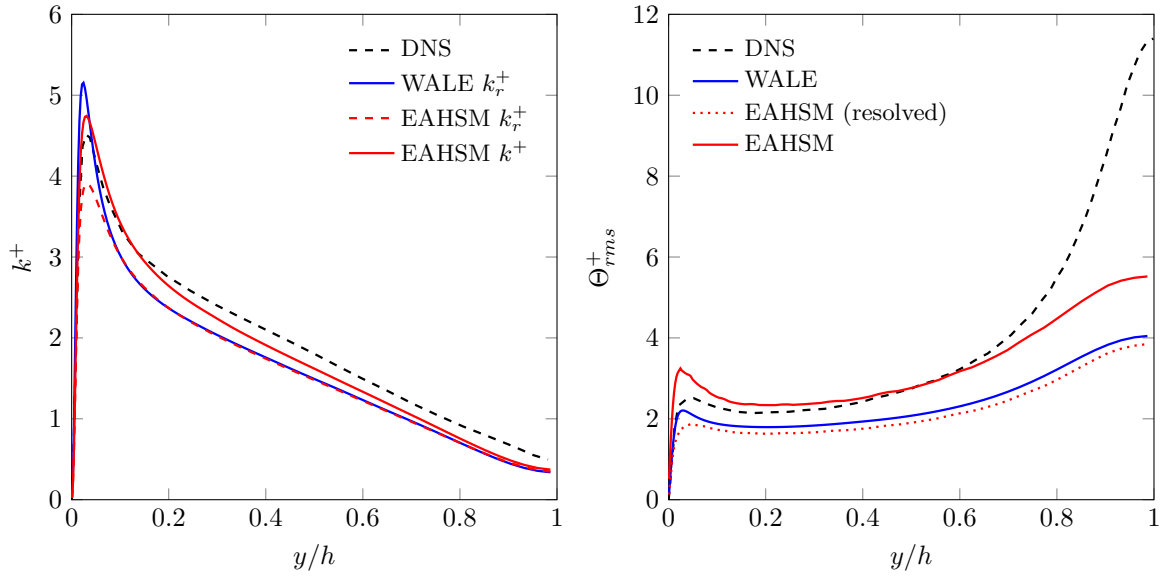

FIGURE 4.17. Turbulent kinetic energy (left) and scalar variance (right) profile - $R_i = 60$.

4.5 Conclusion

In this chapter we deal with slightly variable density flows for which the Boussinesq approximation is assumed to be valid. Derivation of the explicit algebraic model for both the Reynolds stresses and the scalar flux following a direct solution of the implicit algebraic relationship has been presented in a RANS framework. An efficient iteration solution strategy has been specified to solve the coupled algebraic expressions. Like in Chapter 2, the BSL model is used to close the turbulence model.
The model behavior is accessed on the homogeneous mean shear flow with the default values for the

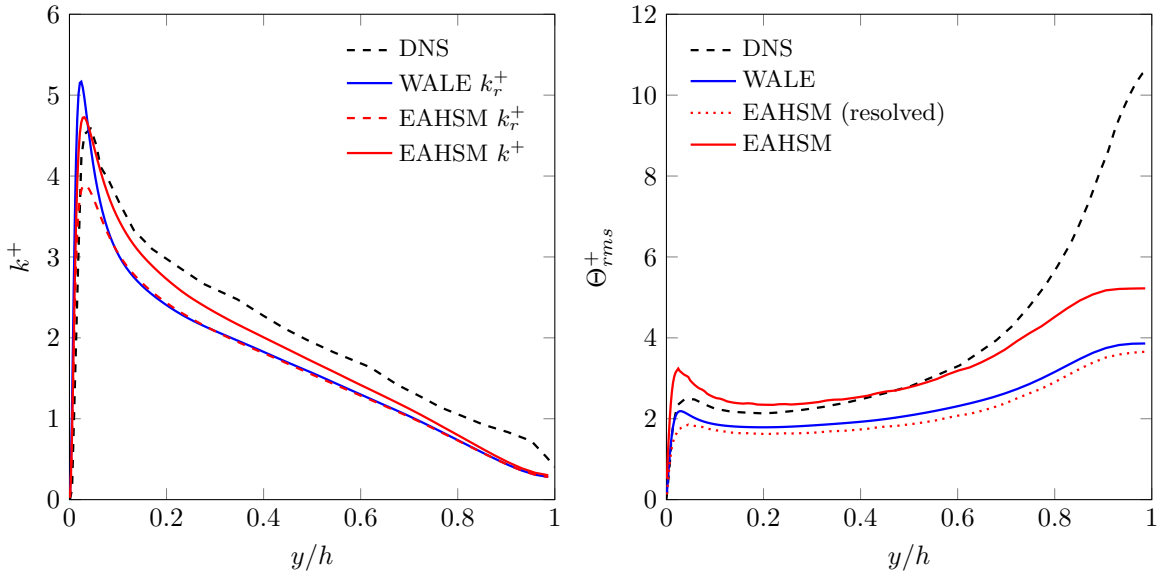

FIGURE 4.18. Turbulent kinetic energy (left) and scalar variance (right) profile - $R_i = 120$.

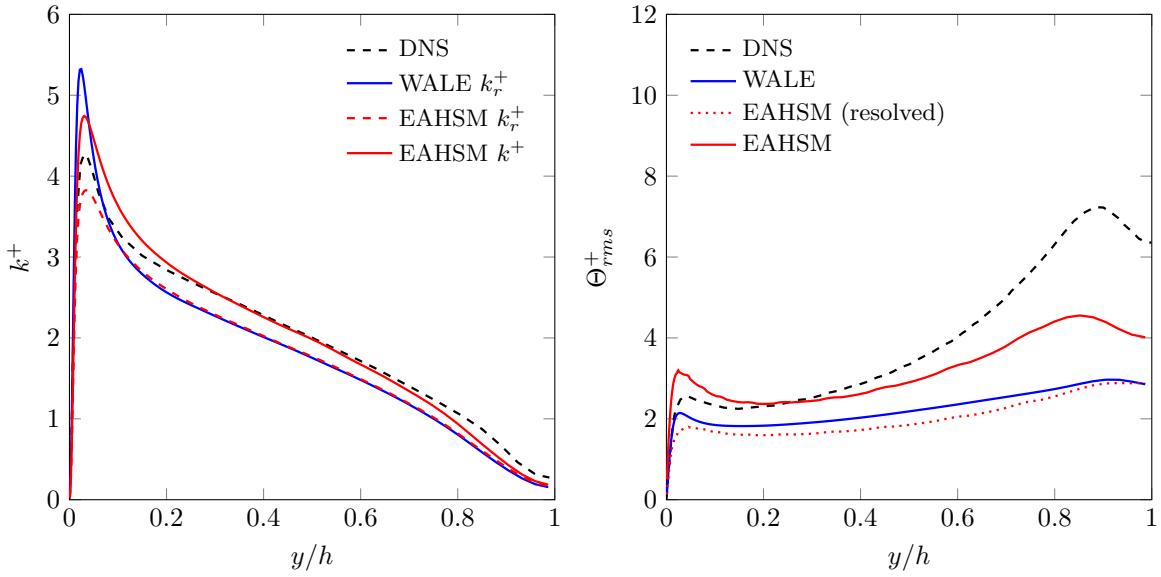

FIGURE 4.19. Turbulent kinetic energy (left) and scalar variance (right) profile - $R_i = 480$.

model coefficients. The total production due to shear and buoyancy balances dissipation with a non-zero steady state value for the kinetic energy for a Richardson number equal to 0.25. This verifies the correct behavior of the model. Some discrepancies are observed for the mean temperature profile on the stably stratified turbulent channel.

Following the validation of EARSM for buoyancy flows, the explicit algebraic approach is then extended to the seamless hybrid RANS-LES framework following the same route as presented in Chapter 3. The behavior of the proposed explicit algebraic hybrid stress and scalar flux model is accessed on the same stably stratified cases.

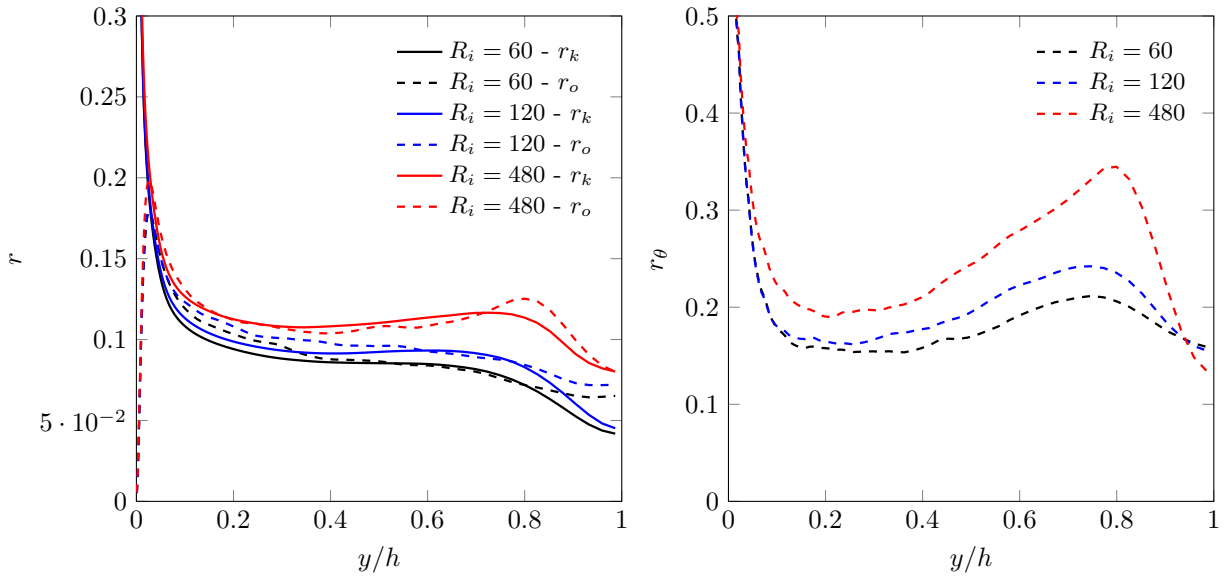

FIGURE 4.20. Target and observed kinetic energy ratio (left) and observed scalar variance ratio (right) for the three Richardson numbers.

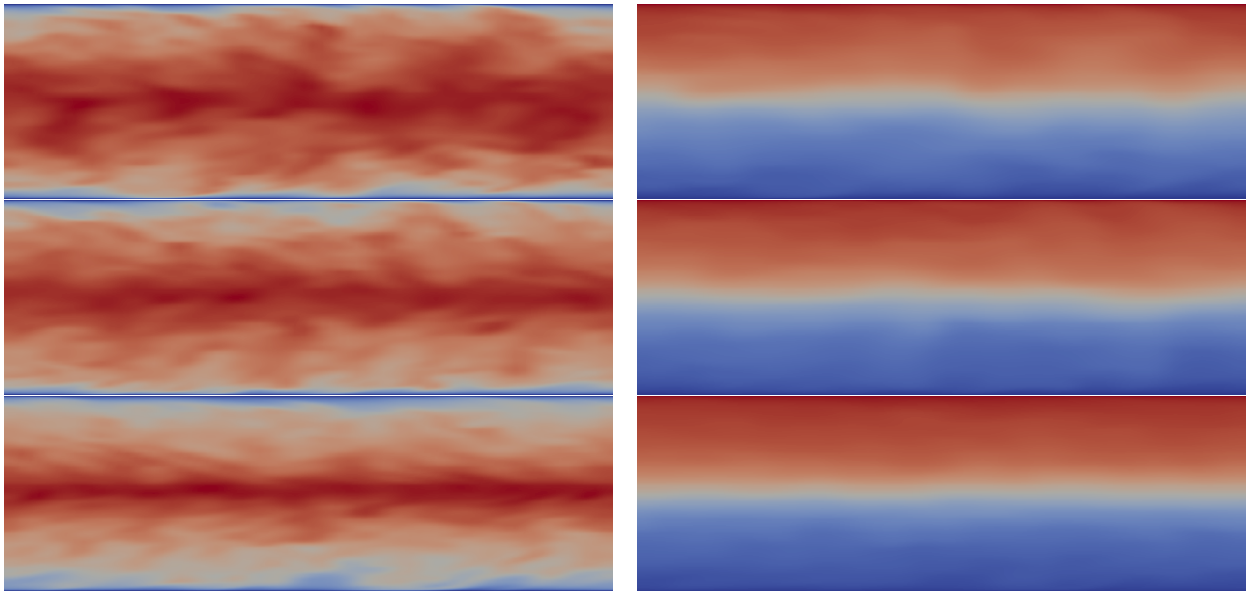

FIGURE 4.21. Instantaneous resolved streamwise velocity (left) and resolved temperature (right) predicted by the EAHSFM model for the three Richardson numbers $R_i = 60$ (top), 120 (middle) and 480 (bottom).

Chapter 5

General conclusions

The present thesis is a contribution to explicit algebraic models, in the hybrid RANS/LES framework, including passive and active scalar transport.

The development of explicit algebraic Reynolds stress model in a RANS framework has first been revisited. A direct solution method instead of using a particular tensor basis projection method has been put to use to arrive at an explicit algebraic relation. However, coupling EARSM with the two-equation model usually requires a full calibration of the model coefficients. It has been shown that modifying the diffusion terms in the kinetic energy and specific dissipation rate transport equations along with the calibration of a coefficient from the parent Reynolds stress model eliminates the need for a complete recalibration of the coefficients in the platform two-equation model. In the developed model, no particular treatment of the near wall region has been considered except for the use of a Kolmogorov limiter in the turbulent time scale. Validation of EARSM has been performed on the fully developed channel flow and the fully developed flow in a pipe of square cross-section. The resulting EARSM is able to capture the secondary flow arising due to the presence of the corners unlike the linear eddy viscosity models.

The next step has been to generalize the obtained EARSM to the seamless hybrid RANS/LES framework. The main concepts of seamless hybrid RANS/LES methods relevant to the present work were looked upon. Starting from the $k_s - \epsilon_s$ version of E-DES for which the hybrid equivalence has been provided, the derivation of a k_s-ω_s based E-DES has been performed. Menter's blending function has been used to obtain a E-DES BSL-like model. Presuming the weak-equilibrium assumption to be verified for the subfilter scales, explicit algebraic closure developed in the previous chapter has been coupled with the E-DES based on Menter's BSL-like model, leading to an Explicit Algebraic Hybrid Stress Model (EAHSM). The calibration of the EAHSM model's coefficients has been against the decay of isotropic turbulence. Following which tests zere performed on the fully developed channel flow and the fully developed flow in a pipe of square cross-section using two grids: fine and coarse. On coarser grids, EAHSM performs fairly better than the WALE model. It has been observed that the target and the observed kinetic energy ratio parameters are significantly different, close to the wall. To circumvent this issue, a low-Reynolds number formulation for the subfilter model and the explicit algebraic relations could be helpful.

The final challenge of the present work, was to deal with slightly variable density flows for which the Boussinesq approximation is assumed to be valid. As a first step, the explicit algebraic model for both the Reynolds stresses and the scalar flux following a direct solution of the implicit algebraic relationship has been derived in a RANS framework. An efficient iteration solution strategy has been specified to solve the coupled algebraic expressions. Like in Chapter 2, the BSL model has been used to close the turbulence model.
The model behavior is assessed on the homogeneous mean shear flow with the default values for the

model coefficients. The total production due to shear and buoyancy balances dissipation with a non-zero steady state value for the kinetic energy for a Richardson number equal to 0.25. This verifies the correct behavior of the model. Some discrepancies are observed for the mean temperature profile on the stably stratified turbulent channel.
Following the validation of EARSM for buoyancy flows, the explicit algebraic approach has then been extended to the seamless hybrid RANS-LES framework following the same route as presented in Chapter 3. The behavior of the proposed explicit algebraic hybrid stress and scalar flux model is assessed on the same stably stratified cases as in the RANS context.

Eventually, the work presented in this thesis opens the way to further developments that are listed below:

- The algebraic models studied in this work were used without a dedicated near-wall treatment except the limiter given by Equation 2.7 for the turbulent time scale. It is expected that more accurate results can be obtained for wall-bounded flows by using near-wall corrections in both the RANS and hybrid RANS-LES framework. In the latter case, this could offer the possibility to use coarser meshes. This could be accomplished by adopting for instance the near-wall correction proposed in [79] for the platform model together with elliptic blending approaches for the algebraic turbulent fluxes.

- The EASFM model together with the coupling strategy to solve for the Reynolds-stresses and the turbulent scalar flux presented in Chapter 3 gives satisfactory results and appears be very robust using the values prescribed in [37] for the model coefficients. It could be instructive to perform a sensitivity study on the model coefficients on other situations of interest (unstable stratification, natural convection) and assess the robustness of the coupling strategy.

- The hybrid seamless RANS-LES calculations have been performed using the rough estimate provided by the Kolmogorov spectrum and resulting in Equation 3.11 for the kinetic energy ratio. On the other way, the dissipation term for the subfilter scalar variance transport equation was assumed to be independant of the cut-off. It could be interesting to study the role played by the energy spectrum function used to estimate the kinetic energy ratio, especially for variable density flows, and to study the interest in introducing a cut-off dependence through an Equivalent-DES like description of the scalar variance dissipation. Another interesting perspective would be to introduce some limiters for the turbulence length scale involved in the kinetic energy ratio following similar arguments as proposed for IDDES approaches [66].

- The test cases presented in this work mainly deal with periodic wall-bounded flows for which turbulence is prescribed at the beginning of the simulation and is then sustained in the near-wall region. It could be interesting to adapt forcing techniques originally proposed for zonal hybrid RANS-LES methods to the seamless hybrid RANS-LES approach described in this work. In this frame, the volumetric forcing proposed in [11] appears to be very attractive. It could reduce for instance the "log layer mismatch" frequently observed in hybrid RANS-LES simulations that use very coarse meshes [66] or it could be useful to sustain turbulence for other situations of interest for which turbulence at boundaries play a major role rather than at the beginning of the simulation (turbulent jet, ...).

- Finally, the algebraic approaches described in this work for incompressible and slightly variable density flows can be extended following the methodology proposed in [22] and followed in this work to account for truly variable density flows possibly with significant mean or subfilter dilatation.

Appendix A

Transformation of k_s-ε_s to its equivalent k_s-ω_s model

The E-DES version of the k-ε model reads:

$$\frac{Dk_s}{Dt} = \mathcal{P}_s - \psi\epsilon_s + \frac{\partial}{\partial x_j}\left[(\nu + \frac{\nu_{t,s}}{\sigma_k})\frac{\partial k_s}{\partial x_j}\right], \tag{A.1}$$

$$\frac{D\epsilon_s}{Dt} = \frac{\epsilon_s}{k_s}\left(C_{\epsilon 1}\mathcal{P}_s - C_{\epsilon 2}\epsilon_s\right) + \frac{\partial}{\partial x_j}\left[(\nu + \frac{\nu_{t,s}}{\sigma_\epsilon})\frac{\partial \epsilon_s}{\partial x_j}\right] \tag{A.2}$$

The relationship between the dissipation rate and the specific dissipation rate is usually given as $\varepsilon = \beta^*\omega k$ in a RANS framework. We assume this relationship to be valid for the subfilter scales:

$$\epsilon_s = \beta^*\omega_s k_s \tag{A.3}$$

with β^* as the constant of proportionality. Differentiating the above equation with respect to time leads to:

$$\frac{d\varepsilon_s}{dt} = \beta^*\omega_s\frac{dk_s}{dt} + \beta^* k_s\frac{d\omega_s}{dt} \tag{A.4}$$

Inserting equation A.1 and equation A.2 in the above equation leads to:

$$\frac{d\omega_s}{dt} = \frac{1}{\beta^* k_s}\left[\beta^*\omega_s\left(C_{\epsilon 1}\mathcal{P}_s - C_{\epsilon 2}\beta^*\omega_s k_s\right) + \frac{\partial}{\partial x_j}\left((\nu + \frac{\nu_{t,s}}{\sigma_\epsilon})\frac{\partial \epsilon_s}{\partial x_j}\right)\right] \tag{A.5}$$

$$- \frac{\omega_s}{k_s}\left[\mathcal{P}_s - \psi\beta^*\omega_s k_s + \frac{\partial}{\partial x_j}\left((\nu + \frac{\nu_{t,s}}{\sigma_k})\frac{\partial k_s}{\partial x_j}\right)\right] \tag{A.6}$$

By rearranging the terms, we obtain

$$\frac{d\omega_s}{dt} = \left(C_{\epsilon 1} - 1\right)\frac{\omega_s}{k_s}\mathcal{P}_s - \beta^*(C_{\epsilon 2} - \psi)\omega_s^2 + \frac{1}{\beta^* k_s}\left[\frac{\partial}{\partial x_j}\left((\nu + \frac{\nu_{t,s}}{\sigma_\epsilon})\frac{\partial \epsilon_s}{\partial x_j}\right)\right] \tag{A.7}$$

$$- \frac{\omega_s}{k_s}\left[\frac{\partial}{\partial x_j}\left((\nu + \frac{\nu_{t,s}}{\sigma_k})\frac{\partial k_s}{\partial x_j}\right)\right] \tag{A.8}$$

Considering the first diffusive term on the right hand side of the previous equation:

$$I_1 = \frac{1}{\beta^* k_s}\left[\frac{\partial}{\partial x_j}\left((\nu + \frac{\nu_{t,s}}{\sigma_\epsilon})\frac{\partial \epsilon_s}{\partial x_j}\right)\right] \tag{A.9}$$

$$= \frac{1}{\beta^* k_s}\left[\frac{\partial}{\partial x_j}\left((\nu + \frac{\nu_{t,s}}{\sigma_\epsilon})\frac{\partial(\beta^*\omega_s k_s)}{\partial x_j}\right)\right] \tag{A.10}$$

$$= \frac{1}{\beta^* k_s}\left[\frac{\partial}{\partial x_j}(\nu + \frac{\nu_{t,s}}{\sigma_\epsilon})\left(\beta^* k_s\frac{\partial \omega_s}{\partial x_j} + \beta^*\omega_s\frac{\partial k_s}{\partial x_j}\right)\right] \tag{A.11}$$

$$= \frac{1}{k_s}\left[\frac{\partial}{\partial x_j}\left((\nu + \frac{\nu_{t,s}}{\sigma_\epsilon})k_s\frac{\partial \omega_s}{\partial x_j}\right)\right] + \frac{1}{k_s}\left[\frac{\partial}{\partial x_j}\left((\nu + \frac{\nu_{t,s}}{\sigma_\epsilon})\omega_s\frac{\partial k_s}{\partial x_j}\right)\right] \tag{A.12}$$

$$= \frac{\partial}{\partial x_j}\left((\nu + \frac{\nu_{t,s}}{\sigma_\epsilon})\frac{\partial \omega_s}{\partial x_j}\right) + \frac{2}{k_s}(\nu + \frac{\nu_{t,s}}{\sigma_\epsilon})\frac{\partial \omega_s}{\partial x_j}\frac{\partial k_s}{\partial x_j} + \frac{\omega_s}{k_s}\left[\frac{\partial}{\partial x_j}\left((\nu + \frac{\nu_{t,s}}{\sigma_\epsilon})\frac{\partial k_s}{\partial x_j}\right)\right] \tag{A.13}$$

The second diffusive term on the right hand side of equation A.7:

$$I_2 = \frac{\omega_s}{k_s}\left[\frac{\partial}{\partial x_j}\left((\nu + \frac{\nu_{t,s}}{\sigma_k})\frac{\partial k_s}{\partial x_j}\right)\right] \tag{A.14}$$

As in the development of the BSL model in [45], we consider $\sigma_\epsilon = \sigma_k$. This implies that the last term on the right hand side of equation A.13 and I_2 cancel out each other resulting in:

$$I = I_1 - I_2 = \frac{\partial}{\partial x_j}\left[(\nu + \frac{\nu_{t,s}}{\sigma_\epsilon})\frac{\partial \omega_s}{\partial x_j}\right] + \frac{2}{k_s}(\nu + \frac{\nu_{t,s}}{\sigma_\epsilon})\frac{\partial \omega_s}{\partial x_j}\frac{\partial k_s}{\partial x_j} \tag{A.15}$$

The second term in the right hand side of Eq. A.15 corresponds to the cross-diffusion term. In a RANS framework, the effects of molecular viscosity in the cross-diffusion term was negligible as demonstrated in the case of free shear layers by Menter [45]. Similarly, we assume the effects of molecular viscosity in the cross-diffusion term to be negligible. Substituting $\nu_{t,s} = (k_s/\omega_s)$ in the cross-diffusion term of Eq. A.15 leads to:

$$I = \frac{\partial}{\partial x_j}\left[(\nu + \sigma_{\omega_\epsilon}\nu_{t,s})\frac{\partial \omega_s}{\partial x_j}\right] + 2\sigma_{\omega_\epsilon}\frac{1}{\omega_s}\frac{\partial k_s}{\partial x_j}\frac{\partial \omega_s}{\partial x_j} \tag{A.16}$$

By substituting Eq. A.16 into the Eq. A.7, we have the resulting transformed equation. The resulting k_s-ω_s model reads

$$\frac{Dk_s}{Dt} = \mathcal{P}_s - \psi_\epsilon\beta^*\omega_s k_s + \frac{\partial}{\partial x_j}\left[(\nu + \sigma_{k_\epsilon}\nu_{t,S})\frac{\partial k_s}{\partial x_j}\right], \tag{A.17}$$

$$\frac{D\omega_s}{Dt} = \frac{\omega_s}{k_s}\gamma_\epsilon\mathcal{P}_s - \beta_\epsilon\omega_s^2 + \frac{\partial}{\partial x_j}\left[(\nu + \sigma_{\omega_\epsilon}\nu_{t,S})\frac{\partial \omega_s}{\partial x_j}\right] + 2\sigma_{\omega_\epsilon}\frac{1}{\omega_s}\frac{\partial k_s}{\partial x_j}\frac{\partial \omega_s}{\partial x_j} \tag{A.18}$$

with the non-dimensional lengthscale ψ_ϵ given by

$$\psi_\epsilon = \max\left(1; \frac{l_s}{l_{LES}}\right) \quad \text{with} \quad l_s = \frac{k_s^{1/2}}{\beta^*\omega_s}, \qquad l_{LES} = \frac{r_\epsilon^{3/2}L_t}{\Psi_\epsilon} \tag{A.19}$$

Here, the subscript ϵ symbolizes the transformed E-DES k_s-ϵ_s model and the turbulent eddy viscosity $\nu_{t,s}$ is

$$\nu_{t,S} = \frac{k_s}{\omega_s} \tag{A.20}$$

$$\gamma_\epsilon = \left(C_{\epsilon 1_\epsilon} - 1\right), \quad \beta_\epsilon = \beta^* \left(C_{\epsilon 2_\epsilon} - \psi^{k\epsilon}\right), \quad \sigma_{\omega_\epsilon} = 0.856, \quad \sigma_{k_\epsilon} = 1.0 \tag{A.21}$$

with

$$\Psi_\epsilon = 1 + \left(\frac{C_{\epsilon 2_\epsilon}}{C_{\epsilon 1_\epsilon}} - 1\right)\left(1 - r_\epsilon^{\frac{C_{\epsilon 1_\epsilon}}{C_{\epsilon 2_\epsilon}}}\right) \tag{A.22}$$

Appendix B

Random Fourier Modes method

The Random Fourier Modes (RFM) method consists in writing the synthetic fluctuating velocity as:

$$\boldsymbol{u}'(\vec{x},t) = 2\sum_{n=1}^{N} \hat{u}^n \cos(\boldsymbol{\kappa}^n \cdot (\vec{x} - \boldsymbol{u}_c t) + \psi_n)\boldsymbol{\sigma}^n \tag{B.1}$$

where $\hat{u}^n$, ψ_n and $\boldsymbol{\sigma}^n$ correspond respectively to the amplitude, the phase and the direction of the Fourier mode n associated with the wave vector $\boldsymbol{\kappa}^n$. The convective velocity $\boldsymbol{u}_c$, needs to be a constant in space to avoid a decorrelation of the velocity field. The wave vector $\boldsymbol{\kappa}^n$ is picked randomly on a sphere of radius $\kappa_n = |\boldsymbol{\kappa}^n|$ to ensure statistical isotropy. From spherical coordinates $(\kappa_n, \varphi_n, \theta_n)$, its components are written as:

$$\kappa_1^n = \kappa_n \sin(\theta_n)\cos(\varphi_n) \tag{B.2}$$
$$\kappa_2^n = \kappa_n \sin(\theta_n)\sin(\varphi_n) \tag{B.3}$$
$$\kappa_3^n = \kappa_n \cos(\theta_n) \tag{B.4}$$

where θ_n, $0 \leq \theta_n \leq \pi$ and φ_n, $0 \leq \varphi_n \leq 2\pi$ are random angles defined for each mode n. Requiring that the probability of a randomly selected direction of a wave vector to be the same for all dS on the shell of the sphere of radius κ_n leads to:

$$p(\kappa_n)d\kappa_n = \frac{dS}{4\pi\kappa_n^2} \tag{B.5}$$
$$p(\theta_n)d\theta_n p(\varphi_n)d\varphi_n = \frac{\kappa_n d\theta_n \kappa_n \sin(\theta_n) d\varphi_n}{4\pi\kappa_n^2} \tag{B.6}$$

On the other hand, writing the divergence free condition leads to:

$$\nabla \cdot \boldsymbol{u}'(\vec{x},t) = -2\sum_{n=1}^{N} \hat{u}^n \sin(\boldsymbol{\kappa}^n \cdot (\vec{x} - \boldsymbol{u}_c t) + \psi_n)\boldsymbol{\kappa}^n \cdot \boldsymbol{\sigma}^n \tag{B.7}$$

This requires the vectors $\boldsymbol{\kappa}^n$ and $\boldsymbol{\sigma}^n$ to be orthogonal for each mode n. The unit vector $\boldsymbol{\sigma}^n$ is then defined by the random angle α_n, $0 \leq \alpha_n \leq 2\pi$, in the plane $(\boldsymbol{\xi}^n, \boldsymbol{\eta}^n)$ as

$$\boldsymbol{\sigma}^n = \cos(\alpha_n)\boldsymbol{\xi}^n + \sin(\alpha_n)\boldsymbol{\eta}^n \tag{B.8}$$

The unit vector $\boldsymbol{\xi}^n$ can be arbitrarily prescribed such that $\boldsymbol{\xi}^n \cdot \boldsymbol{\kappa}^n = 0$, for instance

$$\xi_1^n = \cos(\varphi_n)\cos(\theta_n) \tag{B.9}$$
$$\xi_2^n = \sin(\varphi_n)\cos(\theta_n) \tag{B.10}$$
$$\xi_3^n = -\sin(\theta_n) \tag{B.11}$$

Then the unit vector $\boldsymbol{\eta}^n$ is determined from the cross product $\boldsymbol{\eta}^n = \boldsymbol{\kappa}^n \times \boldsymbol{\xi}^n$ leading to

$$\eta_1^n = -\sin(\varphi_n) \tag{B.12}$$
$$\eta_2^n = \cos(\varphi_n) \tag{B.13}$$
$$\eta_3^n = 0 \tag{B.14}$$

As a result, the unit vector $\boldsymbol{\sigma}^n$ is given by

$$\sigma_1^n = \cos(\varphi_n)\cos(\theta_n)\cos(\alpha_n) - \sin(\varphi_n)\sin(\alpha_n) \tag{B.15}$$
$$\sigma_2^n = \sin(\varphi_n)\cos(\theta_n)\cos(\alpha_n) + \cos(\varphi_n)\sin(\alpha_n) \tag{B.16}$$
$$\sigma_3^n = -\sin(\theta_n)\cos(\alpha_n) \tag{B.17}$$

The probability density functions for the parameters φ_n, θ_n, α_n and ψ_n are given in Table (B.1).

Pdf	Interval
$P(\varphi_n) = 1/(2\pi)$	$0 \leq \varphi_n \leq 2\pi$
$P(\theta_n) = \sin(\theta_n)/2$	$0 \leq \theta_n \leq \pi$
$P(\alpha_n) = 1/(2\pi)$	$0 \leq \alpha_n \leq 2\pi$
$P(\psi_n) = 1/(2\pi)$	$0 \leq \psi_n \leq 2\pi$

TABLE B.1. Probability density functions for the random variables

Finally, the amplitude $\hat{u}^n$ is determined from a modeled energy spectrum $E_s(\kappa)$ as follows:

$$\hat{u}^n = \sqrt{E_s(\kappa_n)\delta\kappa_n} \tag{B.18}$$

where $\delta\kappa_n$ denotes the wave number step of the nth Fourier mode in the interval $[\kappa_1, \kappa_N]$.
The smallest wave number κ_1 is given by $\kappa_1 = f\kappa_e$ where κ_e denotes the wave number at which the energy spectrum reaches its maximum and f is a constant which is less than 1. On the other hand, the highest wave number κ_N is given by $\kappa_N = 1.5 \max \kappa_c(r)$. Here, the cut-off wavenumber $\kappa_c(r)$ is given as $\kappa_c(r) = 2\pi/(C_g\Delta)$, depending on the grid size. The constant C_g depends on the numerical scheme used. This method employs a set of wave numbers which is fixed in time. The number of modes is discretised either by using a linear or a logarithmic distribution as attributed below. But the integration is performed from $n = 0$ upto n corresponding to $\kappa^n = \kappa_c(r)$ which varies spatially so that the number of modes linked to the large-scale structure vary spatially.
For a linear discretization, κ_n and $\delta\kappa_n$ are simply given by:

$$\delta\kappa_n = \frac{\kappa_N - \kappa_1}{N}, \quad \kappa_n = \kappa_1 + n\delta\kappa_n \tag{B.19}$$

A better discretization in the lower wave number range corresponding to the larger energy-containing eddies can be obtained by using a logarithmic discretization [2]:

$$\delta\kappa_n = \frac{\log(\kappa_N) - \log(\kappa_1)}{N}, \quad \kappa_n = \exp(\log(\kappa_1) + n\delta\kappa_n) \tag{B.20}$$

B.1 Model spectrum

Here, the general expression for the energy spectrum to determine $E_s(\kappa)$ is given by:

$$E_s(\kappa) = C\varepsilon^{2/3}\kappa^{-5/3} f_L(\kappa L_e) f_\eta(\kappa\eta) \tag{B.21}$$

The non-dimensional function $f_L(\kappa L_e)$ determines the shape of the energy containing scales. This function corresponds to 1 for $\kappa L_e \to +\infty$. Here, L_e corresponds to the size of the most energy-containing eddies.
On the other hand, $f_\eta(\kappa L_\eta)$ determines the shape of the dissipation range and it tends to unity for $\kappa L_\eta \to 0$. Here, η corresponds to the Kolmogorov scales.
In the inertial subrange, both $f_L(\kappa L_e), f_\eta(\kappa L_\eta) \to 1$ and the original Kolmogorov spectrum is recovered. Here, the coefficient C is the Kolmogorov constant. The functions $f_L(\kappa L_e)$ and $f_\eta(\kappa L_\eta)$ are given by,

$$f_L(\kappa L_e) = \left[\frac{\kappa L_e}{((\kappa L_e)^2+1)^{1/2}}\right]^{\frac{5}{3}+p_0} \tag{B.22}$$

The choice of $p_0 = 4$ corresponds to the Von Kármán Pao spectrum.

$$f_\eta(\kappa\eta) = exp\left(-2(\kappa\eta)^2\right) \tag{B.23}$$

The specification of $f_\eta(\kappa L_\eta)$ is followed as in the work of Laffite *et al.* [33]. By substituting $f_L(\kappa L_e)$ and $f_\eta(\kappa L_\eta)$ in Eq.(B.21), the following model spectrum is obtained.

$$E_s(\kappa) = C\varepsilon^{2/3}\kappa^{-5/3}\frac{(\kappa L_e)^{17/3}}{\left[((\kappa L_e)^2+1)^{1/2}\right]^{17/6}} exp\left(-2(\kappa L_\eta)^2\right) \tag{B.24}$$

Usually, L_e is related to the integral length scale L while L_η refers to the Kolmogorov length scale:

$$L_e = \alpha_L L\,, \quad L = \frac{k^{3/2}}{\epsilon}\,, \quad L_\eta = \left(\frac{\nu^3}{\epsilon}\right)^{1/4} \tag{B.25}$$

The spectrum can be rearranged as follows

$$E_s(\kappa) = \alpha_E k L_e \frac{(\kappa L_e)^4}{\left[((\kappa L_e)^2+1)^{1/2}\right]^{17/6}} exp\left(-2(\kappa L_\eta)^2\right) \tag{B.26}$$

where α_L and α_E are constants. The coefficient α_E is determined through the definition of the kinetic energy:

$$k = \int_0^\infty E(\kappa) d\kappa \tag{B.27}$$

Following Lafitte, for small κL_η the function f_η tends to unity and by introducing the change of variables $y = (\kappa L_e)^2$ one obtains

$$k = \frac{\alpha_E}{2} k \int_0^\infty \frac{y^{3/2}}{[1+y]^{17/6}} dy \tag{B.28}$$

As a result we get

$$\alpha_E = \frac{2}{3}\frac{55}{9\sqrt{\pi}}\frac{\Gamma(5/6)}{\Gamma(1/3)} \tag{B.29}$$

On the other hand, the coefficient α_L can be found from the integral length scale definition for isotropic turbulence

$$\frac{4}{3\pi}kL = \int_0^\infty \frac{E_s(\kappa)}{\kappa} d\kappa \tag{B.30}$$

Neglecting again the function f_η and using the same change of variables, one gets

$$\alpha_L = \frac{\Gamma(1/3)}{\sqrt{\pi}\Gamma(5/6)} \tag{B.31}$$

B.2 Model spectrum for the decay of isotropic turbulence

The above energy spectrum is utilized for the initialization of the synthetic fluctuating field for both the fully developed channel flow and the fully developed flow in a square pipe. Meanwhile, the energy spectrum used for calibrating the model coefficient on the decay of isotropic turbulence is as follows:

$$\begin{aligned} E_s(\kappa) =& C_\kappa \varepsilon^{2/3} \kappa^{-5/3} \left[\frac{\kappa L_e}{\left[(\kappa L_e)^{\alpha_2} + \alpha_1 \right]^{1/\alpha_2}} \right]^{\frac{5}{3}+\alpha_3} \\ & \exp^{-\alpha_4 \kappa \eta} \left[1 + \alpha_5 \left(\frac{1}{\pi} \arctan\left(\alpha_6 \log_{10}(\kappa\eta) + \alpha_7 \right) + \frac{1}{2} \right) \right] \end{aligned} \tag{B.32}$$

with the value of the parameters: $C_\kappa = 1.613$, $\alpha_1 = 0.39$, $\alpha_2 = 1.2$, $\alpha_3 = 4.0$, $\alpha_4 = 2.1$, $\alpha_5 = 0.522$, $\alpha_6 = 10.0$ and $\alpha_7 = 12.58$. This energy spectrum corresponds to the three-dimensional spectrum provided in [32]. These values for the parameters has been found in [32] through the comparison of the spectrum with the measured experimental data.

Bibliography

[1] C Dennis Barley et al. "Analysis of buoyancy-driven ventilation of hydrogen from buildings". In: *International Conference on Hydrogen Safety, San Sebastian*. 2007.

[2] W. Béchara, C. Bailly, and P. Lafon. "Stochastic approach to noise modeling for free turbulent flows". In: *AIAA Journal* 32.3 (1994), pp. 455–463.

[3] Ahmed Bentaib, Nicolas Meynet, and Alexandre Bleyer. "ISP-49 on Hydrogen Combustion." In: *NEA/CSNI/R(2011) 9* (2011).

[4] Ahmed Bentaib, Nicolas Meynet, and Alexandre Bleyer. "Overview on hydrogen risk research and development activities: methodology and open issues". In: *Nuclear Engineering and Technology* 47.1 (2015), pp. 26–32.

[5] Ahmed Bentaib, Nicolas Meynet, and Alexandre Bleyer. *Research and development with regard to severe accidents in pressurised water reactors: Summary and outlook.* 2017.

[6] JR Carlson et al. "Computation of turbulent wake flows in variable pressure gradient". In: *Computers & fluids* 30.2 (2001), pp. 161–187.

[7] René-Daniel Cécora et al. "Differential Reynolds-stress modeling for aeronautics". In: *AIAA Journal* 53.3 (2014), pp. 739–755.

[8] Bruno Chaouat. "The state of the art of hybrid RANS/LES modeling for the simulation of turbulent flows". In: *Flow, Turbulence and Combustion* 99.2 (2017), pp. 279–327.

[9] G. Comte-Bellot and S. Corrsin. "Simple Eulerian time correlation of full-and narrow-band velocity signals in grid-generated, "isotropic" turbulence". In: *Journal of Fluid Mechanics* 48.2 (1971), pp. 273–337.

[10] Lars Davidson and Shia-Hui Peng. "Hybrid LES-RANS modelling: a one-equation SGS model combined with a k-ω model for predicting recirculating flows". In: *International Journal for Numerical Methods in Fluids* 43.9 (2003), pp. 1003–1018.

[11] B. De Laage De Meux. "B. Modélisation des écoulements turbulents en rotation et en présence de transferts thermiques par approche hybride RANS/LES zonale". PhD thesis. PhD thesis, 2012.

[12] PA Durbin. "Application of a near-wall turbulence model to boundary layers and heat transfer". In: *International Journal of Heat and Fluid Flow* 14.4 (1993), pp. 316–323.

[13] Atabak Fadai-Ghotbi et al. "A seamless hybrid RANS-LES model based on transport equations for the subgrid stresses and elliptic blending". In: *Physics of Fluids* 22.5 (2010), p. 055104.

[14] C Friess, R Manceau, and TB Gatski. "Toward an equivalence criterion for hybrid RANS/LES methods". In: *Computers & Fluids* 122 (2015), pp. 233–246.

[15] Jochen Fröhlich and Dominic Von Terzi. "Hybrid LES/RANS methods for the simulation of turbulent flows". In: *Progress in Aerospace Sciences* 44.5 (2008), pp. 349–377.

[16] Manuel García-Villalba and Juan C del Álamo. "Turbulence and internal waves in a stably-stratified channel flow". In: *High Performance Computing in Science and Engineering'08*. Springer, 2009, pp. 217–227.

[17] Manuel Garcia-Villalba and Juan C Del Alamo. "Turbulence modification by stable stratification in channel flow". In: *Physics of Fluids* 23.4 (2011), p. 045104.

[18] TB Gatski and T Jongen. "Nonlinear eddy viscosity and algebraic stress models for solving complex turbulent flows". In: *Progress in Aerospace Sciences* 36.8 (2000), pp. 655–682.

[19] Thomas B Gatski and Charles G Speziale. "On explicit algebraic stress models for complex turbulent flows". In: *Journal of fluid Mechanics* 254 (1993), pp. 59–78.

[20] Sharath S Girimaji. "Partially-averaged Navier-Stokes model for turbulence: A Reynolds-averaged Navier-Stokes to direct numerical simulation bridging method". In: *Journal of Applied Mechanics* 73.3 (2006), pp. 413–421.

[21] Sharath S Girimaji, Eunhwan Jeong, and Ravi Srinivasan. "Partially averaged Navier-Stokes method for turbulence: Fixed point analysis and comparison with unsteady partially averaged Navier-Stokes". In: *Journal of Applied Mechanics* 73.3 (2006), pp. 422–429.

[22] I.A. Grigoriev et al. "Capturing turbulent density flux effects in variable density flow by an explicit algebraic model". In: *Physics of Fluids* 27 (2015).

[23] Antti Hellsten. "Some improvements in Menter's k-omega SST turbulence model". In: *29th AIAA, Fluid Dynamics Conference*. 1998, p. 2554.

[24] Antti Hellsten and Seppo Laine. "Explicit algebraic Reynolds-stress modelling in decelerating and separating flows". In: *Fluids 2000 Conference and Exhibit*. 2000, p. 2313.

[25] Antti Hellsten et al. *New Two-equation Turbulence Model for Aerodymamics Applications*. Helsinki University of Technology, 2004.

[26] Carl-Maikel Hogstrom, Stefan Wallin, and Arne V Johansson. "Passive scalar flux modelling for CFD". In: *TSFP DIGITAL LIBRARY ONLINE*. Begel House Inc. 2001.

[27] Asmund Huser and Sedat Biringen. "Direct numerical simulation of turbulent flow in a square duct". In: *Journal of Fluid Mechanics* 257 (1993), pp. 65–95.

[28] Werner M.J. Lazeroms. Igor A. Grigoriev. "Direct solution for the anisotropy tensor in explicit algebraic Reynolds stress models." In: *Methodological Note* (2015), pp. 191–200.

[29] Frank G Jacobitz, Sutanu Sarkar, and Charles W Van Atta. "Direct numerical simulations of the turbulence evolution in a uniformly sheared and stably stratified flow". In: *Journal of Fluid Mechanics* 342 (1997), pp. 231–261.

[30] C Jiménez et al. "Subgrid scale variance and dissipation of a scalar field in large eddy simulations". In: *Physics of Fluids* 13.6 (2001), pp. 1748–1754.

[31] Adam Jir-Uuml et al. "Computational study of the high-lift A-airfoil". In: *Journal of aircraft* 38.4 (2001), pp. 769–772.

[32] Hyung Suk Kang, Stuart Chester, and Charles Meneveau. "Decaying turbulence in an active-grid-generated flow and comparisons with large-eddy simulation". In: *Journal of Fluid Mechanics* 480 (2003), pp. 129–160.

[33] Bailly C. Laurendeau E. Lafitte A. Le Garrec T. "Turbulence Generation from a Sweeping-Based Stochastic Model." In: *AIAA Journal* 52.2 (2014).

[34] BE Launder. "On the effects of a gravitational field on the turbulent transport of heat and momentum". In: *Journal of Fluid Mechanics* 67.3 (1975), pp. 569–581.

[35] Brian Edward Launder, G Jr Reece, and W Rodi. "Progress in the development of a Reynolds-stress turbulence closure". In: *Journal of fluid mechanics* 68.3 (1975), pp. 537–566.

[36] Brian Edward Launder and BI Sharma. "Application of the energy-dissipation model of turbulence to the calculation of flow near a spinning disc". In: *Letters in heat and mass transfer* 1.2 (1974), pp. 131–137.

[37] WMJ Lazeroms et al. "An explicit algebraic Reynolds-stress and scalar-flux model for stably stratified flows". In: *Journal of Fluid Mechanics* 723 (2013), pp. 91–125.

[38] WMJ Lazeroms et al. "Efficient treatment of the nonlinear features in algebraic Reynolds-stress and heat-flux models for stratified and convective flows". In: *International Journal of Heat and Fluid Flow* 53 (2015), pp. 15–28.

[39] Myoungkyu Lee and Robert D Moser. "Direct numerical simulation of turbulent channel flow up to $Re_\tau \approx 5200$". In: *Journal of Fluid Mechanics* 774 (2015), pp. 395–415.

[40] L Lorentzen and I Lindblad. "Application of two-equation and EARSM turbulence models to high lift aerodynamics". In: *17th Applied Aerodynamics Conference*. 1999, p. 3181.

[41] Linus Marstorp et al. "Explicit algebraic subgrid stress models with application to rotating channel flow". In: *Journal of Fluid Mechanics* 639 (2009), pp. 403–432.

[42] Florian Menter, Martin Kuntz, and Roland Bender. "A scale-adaptive simulation model for turbulent flow predictions". In: *41st aerospace sciences meeting and exhibit*. 2003, p. 767.

[43] Florian R Menter. "Influence of freestream values on k-omega turbulence model predictions". In: *AIAA journal* 30.6 (1992), pp. 1657–1659.

[44] Florian R Menter. "Two-equation eddy-viscosity turbulence models for engineering applications". In: *AIAA journal* 32.8 (1994), pp. 1598–1605.

[45] Florian R Menter. "Zonal two equation kw turbulence models for aerodynamic flows". In: *23rd fluid dynamics, plasma dynamics, and lasers conference*. 1993, p. 2906.

[46] FR Menter. "Influence of freestream values on k-omega turbulence model predictions". In: *AIAA journal* 30.6 (1992), pp. 1657–1659.

[47] FR Menter, AV Garbaruk, and Y Egorov. "Explicit algebraic Reynolds stress models for anisotropic wall-bounded flows". In: *Progress in Flight Physics* 3 (2012), pp. 89–104.

[48] FR Menter and M Kuntz. "Adaptation of eddy-viscosity turbulence models to unsteady separated flow behind vehicles". In: *The aerodynamics of heavy vehicles: trucks, buses, and trains*. Springer, 2004, pp. 339–352.

[49] John W Miles. "On the stability of heterogeneous shear flows". In: *Journal of Fluid Mechanics* 10.4 (1961), pp. 496–508.

[50] Matteo Montecchia et al. "Taking large-eddy simulation of wall-bounded flows to higher Reynolds numbers by use of anisotropy-resolving subgrid models". In: *Physical Review Fluids* 2.3 (2017), p. 034601.

[51] Robert D Moser, John Kim, and Nagi N Mansour. "Direct numerical simulation of turbulent channel flow up to $Re_\tau = 590$". In: *Physics of fluids* 11.4 (1999), pp. 943–945.

[52] Franck Nicoud and Frédéric Ducros. "Subgrid-scale stress modelling based on the square of the velocity gradient tensor". In: *Flow, turbulence and Combustion* 62.3 (1999), pp. 183–200.

[53] S.B. Pope. "A more general effective-viscosity hypothesis". In: *Journal of Fluid Mechanics* 72 (02 1975), pp. 331–340.

[54] Stephen B Pope. *Turbulent flows*. IOP Publishing, 2001.

[55] Vincent Prat et al. "Shear mixing in stellar radiative zones-II. Robustness of numerical simulations". In: *Astronomy & Astrophysics* 592 (2016), A59.

[56] A. Pumir. "Turbulence in homogeneous shear flows". In: *Physics of Fluids* 8.11 (1996), pp. 3112–3127.

[57] J-F Qiu, S Obi, and TB Gatski. "Evaluation of extended weak-equilibrium conditions for fully developed rotating channel flow". In: *Flow, Turbulence and Combustion* 80.4 (2008), pp. 435–454.

[58] Osborne Reynolds. "On the dynamical theory of incompressible viscous fluids and the determination of the criterion". In: *Philosophical Transactions of the Royal Society of London. A* 186 (1895), pp. 123–164.

[59] W. Rodi. "A new algebraic relation for calculating Reynolds stressese". In: *Z. Angew. Math. Mechs* 56 (1976), pp. 219–221.

[60] Michael M Rogers and Parviz Moin. "The structure of the vorticity field in homogeneous turbulent flows". In: *Journal of Fluid Mechanics* 176 (1987), pp. 33–66.

[61] T Rung et al. "Turbulence closure model constraint derived from stress-induced secondary flow". In: *AIAA journal* 38.9 (2000), pp. 1756–1758.

[62] Pierre Sagaut. *Large eddy simulation for incompressible flows: an introduction*. Springer Science & Business Media, 2006.

[63] Pierre Sagaut. *Multiscale and multiresolution approaches in turbulence: LES, DES and hybrid RANS/LES methods: applications and guidelines*. World Scientific, 2013.

[64] Roland Schiestel and Anne Dejoan. "Towards a new partially integrated transport model for coarse grid and unsteady turbulent flow simulations". In: *Theoretical and Computational Fluid Dynamics* 18.6 (2005), pp. 443–468.

[65] M Shur et al. "Detached-eddy simulation of an airfoil at high angle of attack". In: *Engineering Turbulence Modelling and Experiments 4*. Elsevier, 1999, pp. 669–678.

[66] Mikhail L Shur et al. "A hybrid RANS-LES approach with delayed-DES and wall-modelled LES capabilities". In: *International Journal of Heat and Fluid Flow* 29.6 (2008), pp. 1638–1649.

[67] Joseph Smagorinsky. "General circulation experiments with the primitive equations: I. The basic experiment". In: *Monthly weather review* 91.3 (1963), pp. 99–164.

[68] Philippe R Spalart. "Comments on the feasibility of LES for wings, and on a hybrid RANS/LES approach". In: *Proceedings of first AFOSR international conference on DNS/LES*. Greyden Press. 1997.

[69] PRaA Spalart and S1 Allmaras. "A one-equation turbulence model for aerodynamic flows". In: *30th aerospace sciences meeting and exhibit*. 1992, p. 439.

[70] Charles G Speziale, Sutanu Sarkar, and Thomas B Gatski. "Modelling the pressure–strain correlation of turbulence: an invariant dynamical systems approach". In: *Journal of fluid mechanics* 227 (1991), pp. 245–272.

[71] M Strelets. "Detached eddy simulation of massively separated flows". In: *39th Aerospace sciences meeting and exhibit*. 2001, p. 879.

[72] Chenglong Tang et al. "Explosion characteristics of hydrogen–nitrogen–air mixtures at elevated pressures and temperatures". In: *international journal of hydrogen energy* 34.1 (2009), pp. 554–561.

[73] Dale B Taulbee. "An improved algebraic Reynolds stress model and corresponding nonlinear stress model". In: *Physics of Fluids A: Fluid Dynamics* 4.11 (1992), pp. 2555–2561.

[74] Nils Temme, Martin Niemann, and Jochen Fröhlich. "Comparison of isotropic and anisotropic subgrid scale models in Large Eddy Simulations of a backward-facing step and square duct flow". In: *PAMM* 16.1 (2016), pp. 585–586.

[75] Hendrik Tennekes, John Leask Lumley, JL Lumley, et al. *A first course in turbulence*. MIT press, 1972.

[76] TT Tran et al. "A hybrid temporal LES approach. Application to flows around rectangular cylinders". In: *Proceedings of 9th ERCOFTAC International Symposium on Engineering Turbulence Modelling and Measurements, Thessaloniki, Greece*. 2012.

[77] Paul G Tucker and Lars Davidson. "Zonal k–l based large eddy simulations". In: *Computers & Fluids* 33.2 (2004), pp. 267–287.

[78] D Vanpouille, B Aupoix, and E Laroche. "Development of an explicit algebraic turbulence model for buoyant flows–Part 1: DNS analysis". In: *International Journal of Heat and Fluid Flow* 43 (2013), pp. 170–183.

[79] David Vanpouille. "Développement de modèles de turbulence adaptés à la simulation des écoulements de convection naturelle à haut nombre de Rayleigh". PhD thesis. Toulouse, ISAE, 2013.

[80] AG Venetsanos et al. "Source, dispersion and combustion modelling of an accidental release of hydrogen in an urban environment". In: *Journal of hazardous materials* 105.1-3 (2003), pp. 1–25.

[81] D Violeau. "Explicit algebraic Reynolds stresses and scalar fluxes for density-stratified shear flows". In: *Physics of fluids* 21.3 (2009), p. 035103.

[82] Stefan Wallin and Arne V Johansson. "An explicit algebraic Reynolds stress model for incompressible and compressible turbulent flows". In: *Journal of Fluid Mechanics* 403 (2000), pp. 89–132.

[83] Jack Weatheritt and Richard D Sandberg. "Hybrid Reynolds-Averaged/Large-Eddy Simulation Methodology from Symbolic Regression: Formulation and Application". In: *AIAA Journal* (2017), pp. 3734–3746.

[84] M Weinmann, RD Sandberg, and C Doolan. "Tandem cylinder flow and noise predictions using a hybrid RANS/LES approach". In: *International Journal of Heat and Fluid Flow* 50 (2014), pp. 263–278.

[85] P.M. Wikström, S. Wallin, and A.V. Johansson. "Derivation and investigation of a new explicit algebraic model for the passive scalar flux". In: *Physics of Fluids* 12.3 (2000), pp. 688–702.

[86] D. C. Wilcox. "Formulation of the $k-\omega$ turbulence model revisited." In: *American Institute of Aeronautics and Astronautics Journal* 46.11 (2008), pp. 2823–2838.

[87] David C Wilcox. "Reassessment of the scale-determining equation for advanced turbulence models". In: *AIAA journal* 26.11 (1988), pp. 1299–1310.

[88] David C Wilcox et al. *Turbulence modeling for CFD*. Vol. 2. DCW industries La Canada, CA, 1998.

[89] Hao Zhang et al. "Direct numerical simulation of a fully developed turbulent square duct flow up to Re_τ= 1200". In: *International Journal of Heat and Fluid Flow* 54 (2015), pp. 258–267.